

Vacuum Deposited Organic and Composite Charge Transport Layers for Photovoltaic Devices

Nina Klein
Wolfson College

A thesis submitted for the degree of
DPhil in Materials at the University of Oxford

Abstract

This thesis studies the mechanisms by which charge transport layers influence photovoltaic device performance.

Organic hole transport layers of pentacene (Ptn) are employed in quantum dot (QD) photovoltaic devices to improve performance. Device operation mechanisms are studied through current-voltage (IV) testing, complemented by Kelvin Probe measurements of QD and Ptn layer Fermi levels. The results reveal that space-charge effects initially cause s-shaped IV curves and identify Ptn-QD energy level alignment as critical to subsequently lifting these extraction limits. Atmospheric treatments of air and nitrogen are compared, demonstrating that performance improvements stem from Ptn oxidation. Photonic UV-exposure treatments are trialled to control oxidation processes, but are not found to be effective. Overall, the studies show that Ptn performs two primary enhancement roles: electron blocking which minimises rear contact recombination, and hole extracting which balances carrier collection. A 50 nm Ptn layer gives improved performances over control devices, increasing the short circuit current (J_{sc}) from 9.2 to 12.9 mA/cm^2.

Gold (Au) and silver (Ag) nanoparticles (NPs) are added to organic layers of tris(8-hydroxyquinolinato)aluminium (Alq3) to create composite electron transport layers with modified optoelectronic properties. The NPs are characterised by AFM and UV-VIS-NIR spectroscopy, demonstrating that the evaporated metal nominal thickness controls the NP size and plasmonic absorption wavelength. The Alq3 electronic structure is altered by NP-organic interactions which create gap states and induce charge transfer. Kelvin Probe measurements of composite layers reveal that Au NPs cause larger Fermi level (E_f) shifts of 0.2 eV compared to 0.1 eV for Ag NPs. Device photocurrent changes are investigated by wavelength filtered IV testing and photoluminescence measurements. Photocurrents are found to be increased by direct NP plasmonic absorption, but reduced by NP-induced Alq3 exciton quenching. Carrier transport mechanisms are investigated through AC impedance testing, which shows NP trapping effects are outweighed by the creation of low resistance pathways. Both modified organic and direct NP pathways contribute to substantial transport improvements with increasing NP nominal thickness. The cathode metal is varied to demonstrate that interface Fermi level pinning causes extraction limits which are lifted with increasing NP nominal thickness. Au NPs induce larger interface and transport improvements at lower nominal thicknesses than Ag NPs.

Composite electron transport layers, of Au NPs and Alq3, are employed in planar heterojunction organic photovoltaic devices to enhance efficiencies. The elimination of s-shaped IV characteristics with NP additions is investigated further by Kelvin Probe measurements and Mott-Schottky analysis. These studies demonstrate that Fermi level pinning at the cathode interface initially limits extraction and that NP-organic interactions cause gap state creation and filling which lifts both energy and transport related extraction limits. Comparisons to NP-only devices, without Alq3 layers, show s-shaped IV curves remain, proving that direct NP pathways are not simply circumventing extraction limits. Device absorption and EQE spectrums are measured, revealing that NP optical effects have a negligible impact on photovoltaic performance. NP electronic effects influence device carrier dynamics, which are characterised through AC impedance equivalent circuit modelling, in addition to dark and intensity dependent IV testing. NPs improve both bulk and interface transport with increasing NP nominal thickness. At high nominal thicknesses, however, these gains are outweighed by concurrent recombination increases. Both modified organic and direct NP pathways contribute to each of these mechanisms, although losses originate predominantly from direct NP effects. Devices with and without Alq3 layer are compared, showing that Alq3 enhances efficiencies by performing buffer layer roles and mitigating NP losses.

Acknowledgements

This research was funded by the Engineering and Physical Sciences Research Council and the Department of Materials. Wolfson College and the Institute of Materials, Minerals and Mining provided funds for conference travel. I'm grateful to all the above for their financial generosity supporting this work and my continuing education.

I'm thankful for the supervision and guidance Prof Andrew Watt and Prof Hazel Assender provided throughout this DPhil degree. I'm particularly appreciative of Andrew's boundless enthusiasm for science, his careful eye for our safety and his kind heart making every challenge easier to face. The lab and research group built by Andrew's hard work enabled these studies to be undertaken. I'm especially grateful for Hazel's calm practicality in all circumstances and rigorous scientific approach: always asking the right questions to make our work more honest. The time and energy Hazel gave to reviewing and improving my work is deeply appreciated.

Many other members of the University also contributed their considerable expertise to various parts of this project. In particular, thanks go to Richard Turner for his extensive laboratory knowledge and to the Oxford Materials Characterisation Service team for providing training and access to equipment. Special thanks are particularly due to the workshop team: Laurie Walton, Pete Flaxman and Bob Lloyd, who took me under their wing and helped me build The HOF. I'm also grateful to my college advisor Prof Moritz Riede for setting an example of how to be a balanced and effective academic.

To all members of the Watt and Assender research groups over the years, thank you for making the trips to Begbroke worth it even when experiments went awry! I especially thank Dr Nanlin Zhang, Yujiro Tazawa and Wing Chung Liu, for assisting with experimental work for this research. I'm also honoured to have met and worked with: Dr Cheng Cheng, Dr Thomas Cosnahan, Daniel Gregory, Dr Assia Kasdi, Dr Peter Kovacik, Dr Darren Neo, Dr Vincent Tobin, Dr Inji Yeom and Zhanet Zaharieva.

Of course, many people outside the lab also contributed to the completion of this work. I'm so glad to have had the Qroo: Tom Coxon, Karwei So, James Holt-Martyn, Gemma Tidman and Marc Sarazin, to share the ups and downs of DPhil life with, thank you all for making Wolfson College the best one! To all members of the incredibly welcoming OW! ultimate frisbee team, thank you for keeping my body as well as my mind occupied and healthy whilst at Oxford.

I’m grateful also to Jack Tunmore, for being a founding member of Team Nina and making sure I popped the Oxford bubble frequently. To Anna Clements, thank you so much for being my fellow fractal warrior, as well as being more than just a frisbee friend. I’m so glad we lingered in the joyful foolishness of DPhils together! Enormous thanks go to Dr Joe O’Gorman, for continually humouring me despite the laughable amount of actually good puns and always appearing with jelly beans and cocoa at the right moments. I absolutely would not have got this far without you along for the ride, ppkk.

The final thanks go to my family, for supporting me in so many ways. David and Avril, I’m so grateful for you welcoming me into your lives and providing peaceful surrounds for thesis writing. To my brother Nathan and grandma Muriel, thank you for your words of calm encouragement and your belief in me throughout. Last but certainly not least, Mum and Dad, my deepest thanks and eternal gratitude for always being there for me in every way. Your love and support over all the years are what have made this work possible.

Statement of Originality

This thesis is an account of work carried out by the author in the Materials Department at the University of Oxford under the supervision of Prof Hazel Assender and Prof Andrew Watt. Where the work of others has been drawn upon this is duly acknowledged in the text, and a list of references is presented at the end of the thesis. No part of this thesis has been submitted towards the completion of another degree at The University of Oxford or elsewhere.

Table of Contents

Abstract ..... **i**

Acknowledgements ..... **iii**

Statement of Originality ..... **v**

Table of Contents ..... **vi**

List of Abbreviations ..... **ix**

Chapter 1: Introduction **1**

1.1 Sustainable Energy **1**

1.1.1 Current Challenges and Solutions *1*

1.1.2 Organic Photovoltaics Opportunities *4*

1.2 Background to Organic Photovoltaics **9**

1.2.1 Organic Semiconductors *9*

1.2.2 Photovoltaic Devices *13*

1.3 Motivation **19**

1.3.1 Charge Transport Layers for Performance Enhancement *19*

1.3.2 Thesis Aims and Outline *28*

Chapter 2: Equipment and Methods **31**

2.1 Deposition System Design **31**

2.1.1 Vacuum Thermal Evaporation *31*

2.1.2 Deposition System: The HOF *33*

2.2 Fabrication Procedures **41**

2.3 Characterisation Methods **42**

Chapter 3: Organic Charge Transport Layers in Quantum Dot Photovoltaic Devices **48**

3.1 Introduction **48**

3.1.1 Quantum Dot Photovoltaics *48*

3.1.2 Utilising Charge Transport Layers *50*

3.1.3 S-Shaped IV Curves *53*

3.1.4 Approach *54*

3.2 Experimental **54**

3.3 Device Architecture **55**

3.3.1 Pentacene Deposition *55*

3.3.2 Quantum Dot Device *58*
3.4 Electron Blocking Role **59**
3.5 Energy Level Alignment **61**
3.5.1 IV Curve Characteristics *61*
3.5.2 Atmospheric Treatments *62*
3.5.3 Photonic Treatments *68*
3.6 Hole Extracting Role **72**
3.6.1 Pentacene Thickness Effects *72*
3.6.2 Extraction Mechanisms *75*
3.7 Conclusions **78**
Chapter 4: Metal Nanoparticles in Organic Charge Transport Layers **81**
4.1 Introduction **81**
4.1.1 Metal Nanoparticles *81*
4.1.2 Metal-Organic Interactions *84*
4.1.3 Organic Non-Volatile Memory *89*
4.1.4 Approach *94*
4.2 Experimental **95**
4.3 NP Characterisation **96**
4.3.1 Optics *96*
4.3.2 Morphology *99*
4.3.3 Electronics *104*
4.4 Device Electronics **106**
4.4.1 Device Architecture *106*
4.4.2 Transport Modification by NPs *107*
4.4.3 Interface Modification by NPs *123*
4.5 Device Optoelectronics **132**
4.5.1 Photoresponse *132*
4.5.2 Collection Changes with NPs *133*
4.5.3 Generation Changes with NPs *134*
4.5.4 NP Related Losses *137*
4.6 Conclusions **140**
Chapter 5: Hybrid Charge Transport Layers in Organic Photovoltaic Devices **145**
5.1 Introduction **145**

5.1.1 Metal NPs in Organic Photovoltaics *145*
5.1.2 Evaporated NPs in Transport Layers *148*
5.1.3 Hypotheses and Approach *152*
5.2 Experimental **153**
5.3 Device Architecture **154**
5.4 Device Operation **156**
5.4.1 Collection Limited Controls *156*
5.4.2 NP Performance Enhancements *161*
5.5 Role of NPs **166**
5.5.1 Performance Limit Lifted *166*
5.5.2 Transport Improves Performance *174*
5.5.3 Generation Improves Performance *180*
5.5.4 Recombination Impairs Performance *186*
5.5.5 Net Performance Balance *191*
5.6 Role of Alq3 ..... **192**
5.7 Conclusions **194**
Chapter 6: Conclusions and Future Work **199**
6.1 Conclusions **199**
6.2 Future Work **203**
References **207**
Appendices **242**
A. Appendix to Chapter 4 ..... **242**
A.1 AC Impedance ECM Results *242*
B. Appendix to Chapter 5 ..... **247**
B.1 AC Impedance ECM Results *247*
B.2 Universal PV-Interface Fitting Test *253*

List of Abbreviations

Φ	energy barrier
6T	alpha-sexithiophene
AC	alternating current
AFM	atomic force microscopy or microscope
Ag	silver
Al	aluminium
Alq3	tris(8-hydroxyquinolinato)aluminium
Au	gold
BCP	bathocuproine
BHJ	bulk heterojunction
BPhen	bathophenanthroline
C, *C*	capacitor, capacitance
CPE	constant phase element
CTL	charge transport layer
DC	direct current
ECM	equivalent circuit model
E_f	Fermi level
EQE	external quantum efficiency
ETL	electron transport layer
FF	fill factor
HJ	heterojunction
HOMO	highest occupied molecular orbital
HTL	hole transport layer
I	current
IPES	inverse photoemission spectroscopy
IR	infra-red
ITO	indium tin oxide
IV	current-voltage
J	current density
J_0	dark saturation current
$J_{ph}(D)$	photocurrent extracted from dark IV curves
$J_{ph}(F)$	photocurrent extracted from filtered IV curves

$J_{ph}(L)$	photocurrent extracted from light IV curves
J_{sc}	short circuit current
LSPR	localised surface plasmon resonance
LUMO	lowest unoccupied molecular orbital
MAI	methylammonium iodide
MoO_3	molybdenum(VI) oxide
M-S	Mott-Schottky
n	diode ideality factor
N_2	nitrogen
N_{ms}	apparent dopant density
NP	nanoparticle
ONVM	organic non-volatile memory
OPV	organic photovoltaic
P3HT	poly(3-hexylthiophene-2,5-diyl)
PbS	lead sulphide
PCE	power conversion efficiency
PEDOT:PSS	poly(3,4-ethylenedioxythiophene)-poly(styrenesulfonate)
PHJ	planar heterojunction
PL	photoluminescence
Ptn	pentacene
PV	photovoltaic
QCM	quartz crystal monitor
QD	quantum dot
R, R	resistor, resistance
R-C	resistor-capacitor
R-CPE	resistor-constant phase element
$R_{iv}(D)$	average resistance extracted from dark IV curves
$R_{iv}(L)$	average resistance extracted from light IV curves
R_{oc}	open circuit resistance
R_p	parallel resistance, in R-C or R-CPE combination
RR	rectification ratio
R_s	series resistance
R_{sh}	shunt resistance
SEM	scanning electron microscopy

SubPc	boron subphthalocyanine chloride
TEM	transmission electron microscopy
UPS	ultraviolet photoelectron spectroscopy
UV	ultraviolet
V_{bi}	built-in voltage
V_{ms}	apparent built-in voltage
V_{oc}	open circuit voltage
V_{ph}	photovoltage
WF	work function
XPS	X-ray photoemission spectroscopy
XRD	X-ray diffraction
Z	impedance
ZnO	zinc oxide

Chapter 1: Introduction

1.1 Sustainable Energy

1.1.1 Current Challenges and Solutions

Energy is an essential component of modern life and global demand is projected to increase 30 % by 2040 [1]. Currently, most energy is generated from fossil fuels, which is problematic for a myriad of reasons. Pollution has devastating effects on both planetary and human health, and uneven resource distribution creates political tensions. A primary issue is the emission of greenhouse gasses which cause climate change [2]. A CO_2 level of 350 ppm is required to stabilise the climate and avoid irreversible impacts on humanity and nature [3], however, currently recorded levels stand at 408 ppm [4]. This has led to significant global warming, with averages temperatures now 1 °C above pre-industrial levels [5].

The impacts of climate change are being felt today, with the most devastating consequences being borne by people who are already the most vulnerable on the planet (Figure 1-1) [6] [7] [8]. The necessary transition from dirty fossil fuels to clean renewable energy is underway, but it must be rapidly accelerated to avoid catastrophic climate change. The severity of the situation and the benefits to be gained by acting have led to an unprecedented level of global cooperation. At the COP21 conference in 2015, 195 countries signed a legally binding agreement, promising to reduce emissions and limit warming below 2 °C [9].



Figure 1-1: In 2016, climate change combined with the El Niño weather event to produce a global drought affecting over 400 million people [8]. The photograph above shows people in India experiencing the severe water supply crisis. Image by Indranil Mukherjee of the Associated Free Press [10].

The implementation of renewable energy is often assessed in terms of the energy trilemma. Ideally, new technologies would deliver energy: 1) from sustainable sources; 2) with security of supply; 3) at an affordable cost. Solar, wind, hydro, tidal and geothermal power each offer a different combination of compromises across these areas. The contribution of sustainable sources to the energy mix is growing (Figure 1-2): renewable technologies currently supply 13% of global energy demand [11] which is projected to rise to 40 % by 2040 [1]. Various challenges associated with a substantial transition to renewables, however, remain to be resolved [12]. These include addressing the intermittent nature of the source and integrating with existing infrastructure and technologies. Therefore, research and investment are required to develop storage solutions, upgrade the grid network and electrify heat and transport.

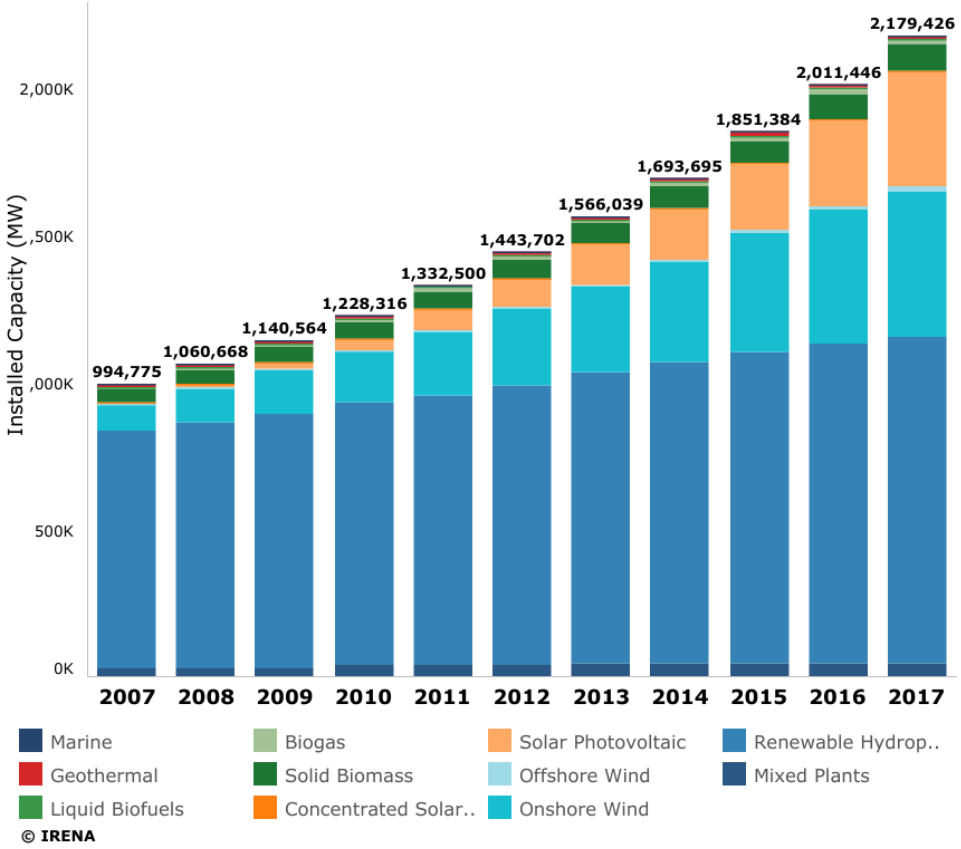


Figure 1-2: The global trend in cumulative installed capacity of renewable energy from 2007 to 2017 [13].

Of all the renewable sources, solar energy is the most abundant. Photovoltaic (PV) panels on only 0.4 % of the earth's surface would satisfy global energy demand [14], assuming the installation of complementary grid and storage technologies. The energy trilemma can be used to evaluate the potential of solar PV as follows. 1) The source is inherently sustainable, although panel materials should be considered with scarcity and recycling in mind. 2) There are few safety or supply risks if storage is used to compensate intermittency and seasonality. 3) PVs based on silicon are already commercially successful, having reached grid parity at less than $1 per Watt [15].

PV generation has grown at a rate of 46 % per year since 1990 [11] and is forecast to be the largest source of renewable capacity by 2040 [1]. This rapid deployment has been driven by a phenomenon known as Swanson's Law: for every doubling in installed capacity, the module

cost reduces by 20 % (Figure 1-3) [16] [17]. To date, the largest operational PV farm has a 1,000 MW capacity to power 350,000 homes in India [18]. Saudi Arabia's first ever utility-scale renewables development recently set a record low power price agreement of 2.34 US-cents per kWh [19]. Therefore, harvesting the sun's unlimited power through large-scale PV deployment could be the solution to providing clean, affordable energy for all.

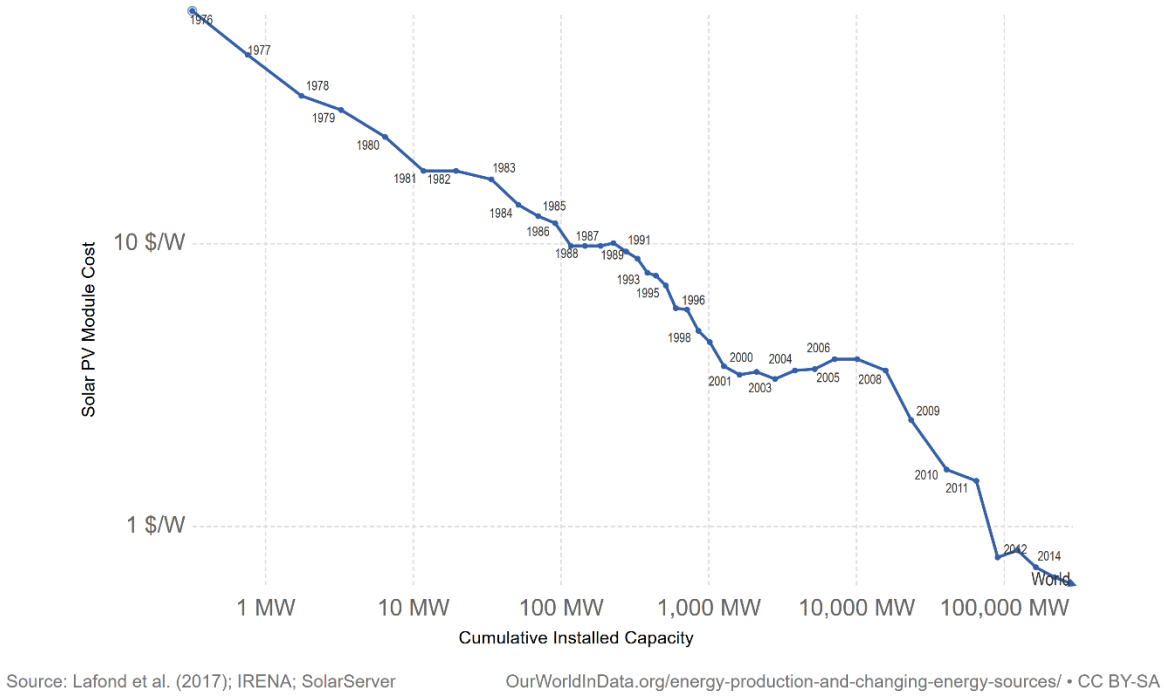


Figure 1-3: A graph of Swanson's Law, showing the reduction in PV module cost as the cumulative installed capacity increases [20].

1.1.2 Organic Photovoltaics Opportunities

A multitude of different PV technologies have been developed over the years. Their efficiency improvements are tracked by the ubiquitous NREL chart (Figure 1-4) [21]. Whilst power conversion efficiencies (*PCE*s) are important when assessing the commercial viability of a technology, the module costs and operating lifetime must also be considered [22]. Each unique PV embodiment will fulfil these three performance criteria to different extents.

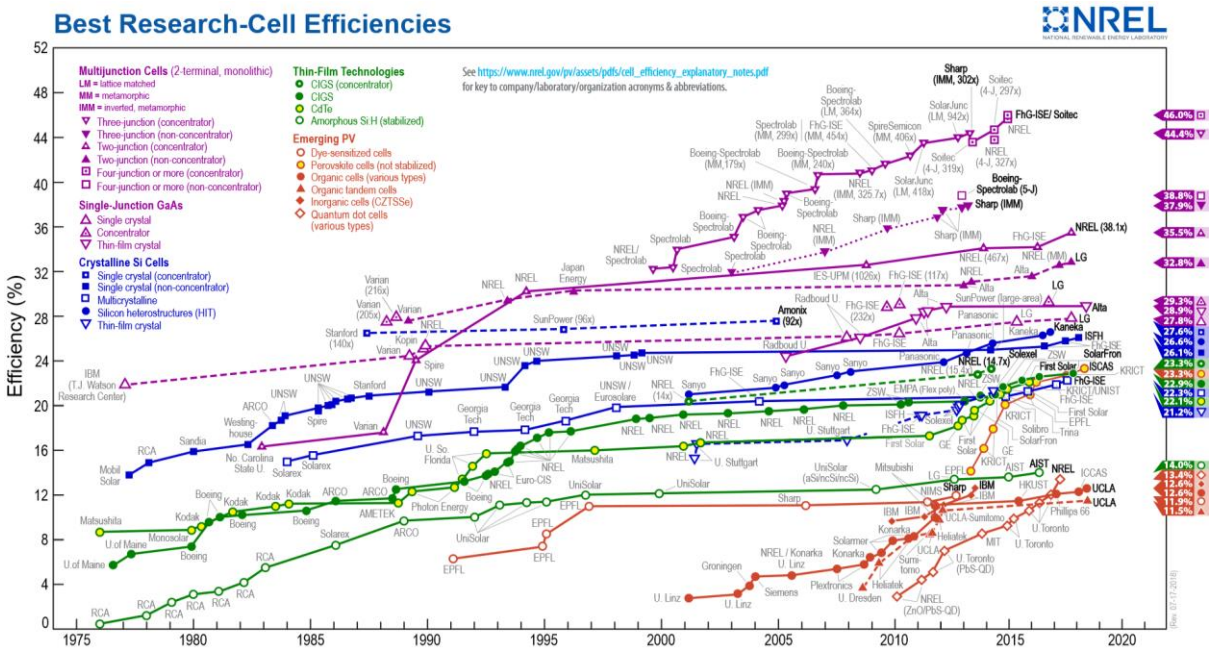


Figure 1-4: The NREL chart, tracking improvements in the certified efficiencies of various PV technologies under research [21].

Silicon-based PVs, for example, were initially developed for niche extra-terrestrial applications, but commercial deployment is now widespread [23]. Modules operate at around 16 % efficiency, over the course of a 25 year warranty lifetime [24] [25]. Improved scientific understanding has driven *PCE* increases [26]. In parallel, innovative manufacturing engineering has substantially reduced module costs, although fabrication processes are intrinsically very demanding [27].

Perovskites are a new class of PV materials, which were found to have very favourable carrier transport properties [28]. Laboratory device performances have increased at an unprecedented rate: after only 5 years certified PCEs are now pushing 23 % [21] [29]. Whilst low production costs are anticipated [30], concerns remain over the use of toxic lead and limited operational stabilities [31]

Quantum dots (QDs) are another promising PV material, discussed in detail subsequently (Section 3.1.1). Moderate *PCE*s over 13 % have already been achieved in labs [32] and scalable

ambient processing techniques can reduce manufacturing costs [33]. The PV devices investigated in Chapter 3 employ QD active layers. However, this thesis focuses primarily on organic photovoltaics (OPVs): an emerging technology with certified *PCE*s currently over 12 % [21] [34].

The unique selling point of OPVs is their low cost. Further work, however, is required to improve efficiencies and lifetimes to commercial standards [35]. The mechanical flexibility of organic materials allows fabrication using roll-to-roll processes, enabling high-throughput low-cost mass production [36] [37]. Another advantage is OPVs following in footsteps of organic light emitting diode (OLED) and organic field effect transistor (OFET) commercialisation [38] [39]. The pre-existing understanding of organic semiconductor science and device production techniques can be utilised to accelerate the development of OPVs. Additionally, OPVs can be integrated with these technologies to produce devices for flexible off-grid applications.

Organics are especially suited to PV applications because, as direct bandgap materials, they have high absorption coefficients of 10^5 cm^{-1} [40]. This is also advantageous for materials consumption, as thin devices of only 50 – 200 nm can absorb all incident light [41]. Additionally, it is possible to design the chemistry of organic molecules to tailor their optoelectronic properties for specific device applications.

Organic materials, however, also have some drawbacks related to their electronic properties. Low thin film mobilities can limit carrier collection, restricting the *PCE*s achievable [41]. Interactions with the ambient environment can degrade performance, shortening the operational lifetime of devices [42] [43]. Therefore, further research and development of OPVs is required for commercial success. Improved scientific understanding may provide methods to counter the

low mobilities. Engineering approaches are commonly applied to overcome stability issues by encapsulating devices within protective barrier coatings [44].

A popular platform for OPVs research is devices based on solution-processed polymers. Polymeric single-junction OPVs have achieved reported *PCE*s of 13.1 % [45]. Device embodiments are commonly a two-phase mixed layer, called a bulk heterojunction (BHJ), with a carefully controlled morphology advantageous for photocarrier generation and extraction [46]. The work in this thesis, however, utilises vacuum deposited small molecule organics. The highest *PCE* reported for evaporated single-junction OPVs is 8.4 % [47]. Performance innovations in evaporated devices often stem from complex architectures with multifunctional layers [48] [49] [50].

The vacuum deposited device embodiment has unique advantages which give it commercial potential. In the OLED field, for example, vacuum deposited small molecules are the standard state-of-the-art technology [51]. Small molecule organics benefit from precise chemical structures and thus well-defined optoelectronic properties [41] [52]. Whilst solution-processed polymers have superior mixed-layer morphology control, sequential multilayer deposition is challenging as orthogonal solvents are necessary [53]. On the other hand, vacuum deposition of small molecules enables the easy fabrication of multilayer architectures, with precisely controlled parameters and a high material purity [37]. This facilitates the creation of multi-junction PV devices, as individual sub-cells are simply deposited sequentially [54]. Multi-junction architectures can improve performances though complementary sub-cell materials broadening the spectral absorption range. Until a very recent report of an impressive 17.3 % *PCE* [55], the solution processed tandem *PCE* record of 13.1 % had not exceeded that of single-junction devices [56]. For evaporated multi-junction devices, record *PCEs* of 13.2 % have been

achieved [57]. Small molecule vacuum processed devices can therefore achieve comparable *PCEs* and have additional benefits which may lead to even higher efficiencies in future.

OPVs are rapidly becoming commercially competitive. Levelised cost of electricity calculations suggest mass-produced OPVs, with an efficiency of 5 % and a lifetime of 3 -5 years, would be cost competitive with fossil fuel generation sources [22]. Heliatek is a German company commercialising small molecule vacuum deposited OPVs [58]. Having set the record 13.2 % efficiency for multi-junctions discussed above, they raised € 80 million in funding to open an industrial scale manufacturing line by 2020. OPVs therefore represent a versatile technology, with the potential to provide affordable renewable energy, which would benefit from further scientific research (Table 1-1).

Strengths	**Weaknesses**
• Low-cost potential • Tuneable optoelectronics • Low energy fabrication • Scalable continuous production • Low material consumption • Mechanical flexibility • Lightweight • Ease of integration	• Low efficiency • Environmental degradation • Short lifetime • Economic payback time • Unproven environmental impact
Opportunities	**Threats**
• Low energy payback time • Building-integrated power generation • Consumer electronics integration • Generation from passive surfaces • Novel PV-based products	• Efficiency targets not met • Lifetime targets not met • Competing PV cost reduction • Barrier technology limits • Emerging energy technologies

Table 1-1: A SWOT analysis for OPV technologies. Adapted from Brabec et al. [59].

1.2 Background to Organic Photovoltaics

1.2.1 Organic Semiconductors

• Optoelectronic Properties

The molecular bonding of organics determines their optoelectronic properties; absorption and conductivity being key for OPVs. Semiconducting behaviour stems from the presence of unsaturated double bonds [60]. Each carbon atom has one valence electron in a perpendicular p_z orbital, in addition to three forming sigma-bonds in a planar sp_2 configuration. Adjacent p_z orbitals can overlap forming a delocalised pi-bonding system. The in-phase (or out-of-phase) configuration gives bonding (or antibonding) orbitals with lower (or higher) energies.

A structure of alternating single and double bonds produces a conjugated system, which is essential for OPV molecules [61]. The occupied bonding HOMO (highest occupied molecular orbital) and unoccupied antibonding LUMO (lowest unoccupied molecular orbital) pi-orbitals create the optical gap; their energy offset determines the wavelengths of light absorbed (Figure 1-5). The delocalisation of electrons throughout the pi-system gives extended carrier transport along the molecule, provided the orbitals are partially filled. Aspects of the electronic structure can be modified by physical properties of the thin film [62]. Disorder slightly shifts the HOMO and LUMO levels of some molecules, effectively broadening the energy levels through the creation of tail states (Figure 1-5). Defects can alter the molecular bonding, creating gap states at intermediate energies between the HOMO and LUMO levels (Figure 1-5).

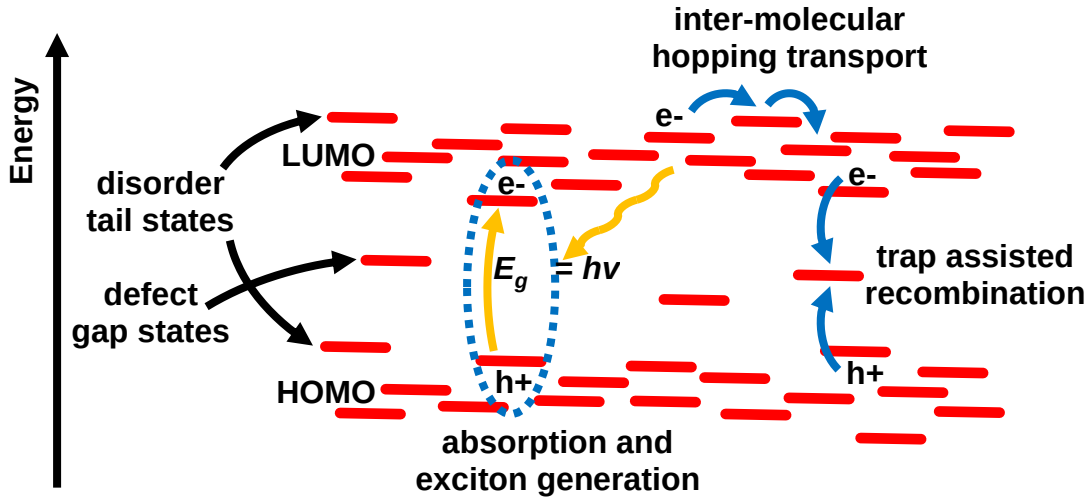


Figure 1-5: A schematic energy level diagram of an organic semiconductor, showing the HOMO and LUMO level as individual states alongside the tail and gap states. The processes of bandgap energy (E_g) absorption, transport and recombination are also depicted.

Organics are a versatile class of materials, due to their tunable optoelectronic properties. This is possible because the band structure is controlled by the nature of the conjugated system. Various approaches are used to modify the organic properties for specific performance needs [62]. Molecules can be synthesised with different backbone structures or chemical compositions. Additionally, additives, which alter carrier densities through doping, or processing treatments, to modify molecular packing, can be employed. On the other hand, unintentional additions also affect the optoelectronic properties. Impurity species may: change the chemical structure or modify the molecular packing, creating localised charge trapping sites [63]. In particular, environmental oxygen and moisture are known to degrade PV performance [42] [43].

Another feature of organics which gives unique optoelectronic properties stems from their weak intermolecular bonding and low dielectric constants. These properties limit the degree of electrical delocalisation, causing the generation of a Frenkel exciton upon photon absorption [64] (Figure 1-5). A Frenkel exciton is a molecularly localised electron-hole pair which are strongly coulombically bound. This tight binding causes the pair to recombine if they are not

transferred to separate molecules, significantly limiting the excitonic lifetime. The specific structure and dielectric properties of the organic therefore dictate the exciton diffusion length possible before recombination occurs.

• Thin Film Transport

Organics generally form thin films with amorphous or nanocrystalline structures, where the bonding between molecules consists of weak van der Waals interactions [61]. These features produce the characteristic physical properties of low melting points and flexibility, as well as dictating the electronic properties by causing specific carrier transport mechanisms to operate [62]. Whilst charges move freely within the molecularly delocalised conjugated system, tunnelling processes are necessary to cross the gaps between adjacent molecules. The electronic localisation and lack of long-range order cause site-to-site hopping transport mechanisms to operate (Figure 1-5), rather than the coherent band transport found in highly ordered crystal structures [65].

The transport mechanism is a thermally activated hopping process, which can be assisted or inhibited by an external field [66]. The tunnelling probability depends on the overlap of the adjacent molecular pi-orbital and electron wavefunction. Therefore, the molecular packing and interaction characteristics determine the carrier transport properties. This is the origin of the lower mobilities, around 10^{0} - 10^{-8} $cm^{2}V^{-1}s^{-1}$, measured for organic thin films [41]. Additionally, the disorder broadening of the energy levels causes carrier density dependent mobilities, due to relaxation processes through tail states. Transport is also disrupted by bandgap states, created by impurities or defects, which trap carriers and cause recombination (Figure 1-5).

• Interface Formation

Schottky-Mott theory is used to determine whether a Schottky junction or ohmic contact forms at a metal-semiconductor interface (Figure 1-6) [67] [68]. The key factors governing interface formation are the energy offset between the metal work function (WF) and organic Fermi level and the carrier type and density of the organic material. Upon contact, electrical equilibrium is established by charge transfer. The band bending is given by the built-in interface potential and the organic surface states [69] [70] [71]. Any resulting barrier is then given by the difference between the WF and transport energy level. Doping can be used to convert Schottky barriers into tunnelling junctions: increasing the carrier density reduces the spatial extent of band bending.

The disordered electronic structure of organics, here again, influences their properties: the substantial additional tail and gap states can dominate interface formation characteristics [61]. These states must be filled when establishing electrical equilibrium. Therefore, it is common to observe interface Fermi levels pinned at states in the bandgap [72] [73]. Any barrier is then independent of the original energy level offsets; instead depending on the specific nature of the interface states. In this regard, strong interactions with metals can sometimes introduce additional structural and electrochemical complexities [74] [75]. During deposition, metals atoms can migrate into the underlying organic, disrupting the molecular packing. Chemical reactions can also occur, producing organometallic species. These phenomena produce additional electronics states in the bandgap which govern interface formation characteristics (Figure 1-6).

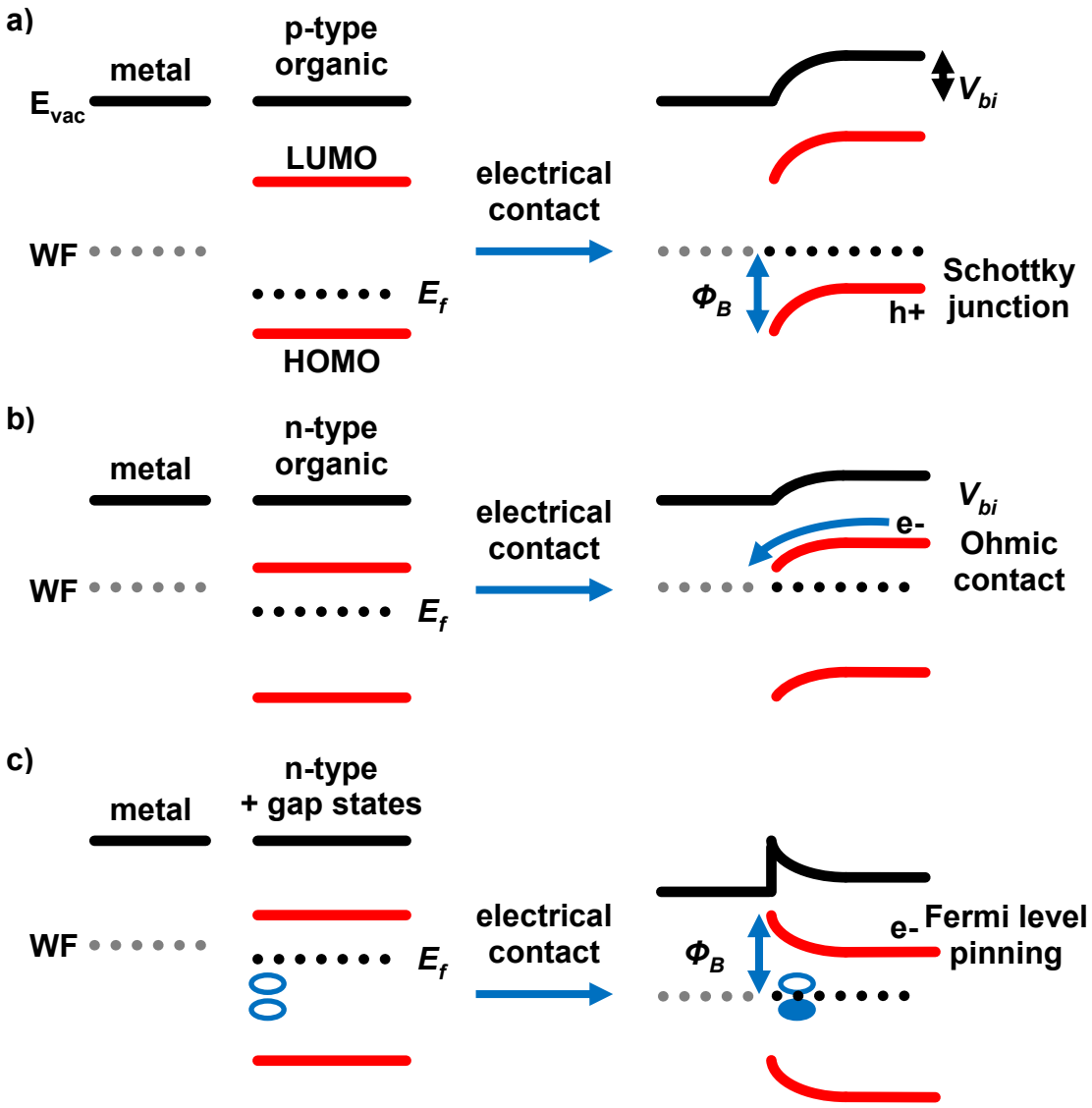


Figure 1-6: Energy level diagrams showing interface formation characteristics and barriers (Φ_B) for different a-b) organic material types and c) metal-organic interactions.

1.2.2 Photovoltaic Devices

• Operation Principles

OPVs achieve photovoltaic conversion through a complex multi-step process (Figure 1-7) [64] [76]. The various device layers facilitate specific aspects of the overall mechanism. Understanding the optoelectronic phenomena involved is central to overcoming performance limitations. The individual steps are as follows:

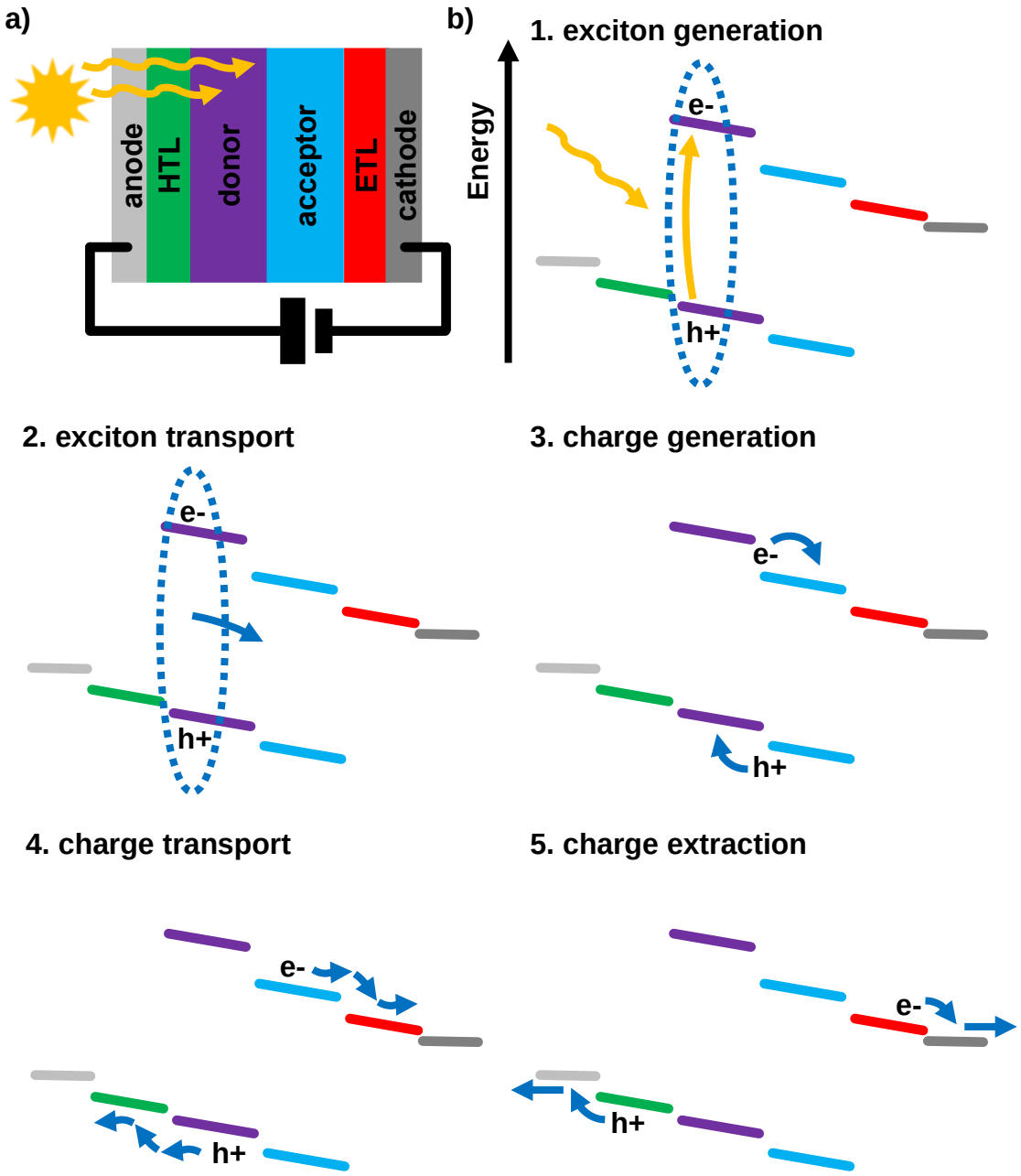


Figure 1-7: An OPV device a) layer structure and b) energy level diagrams depicting the steps of the photovoltaic conversion process: 1. exciton generation, 2. exciton transport, 3. charge generation, 4. charge transport and 5. charge extraction.

1. Exciton generation

The active layer absorbs a photon with sufficient energy to promote an electron across the bandgap. The maximum energy harvestable is determined by the overlap of the incident solar spectrum and device absorption characteristics [77] [78]. The reflecting back contact produces

an optical field distribution across the layer stack [79]. Whilst organics absorb strongly, their absorption bands are often narrow, causing poor responsivity across the spectral range.

2. Exciton transport

Organic absorption creates an exciton which then diffuses through the active layer. The bound electron-hole pair's strong Coulomb interactions promote geminate recombination. This limits exciton lifetimes to nanoseconds and so diffusion lengths are typically only 5-10 nm [41]. Traversing larger absorption layer thicknesses therefore results in significant geminate recombination losses.

3. Charge generation

The Coulomb interactions produce exciton binding energies of 0.2-1.0 eV, which require fields of 10^6 Vcm^{-1} for dissociation [40]. The electric field across a typical OPV device is not sufficient, so a donor-acceptor heterojunction (HJ) layer structure is required [80]. At the HJ interface, the energy level offsets overcome the binding energy, enabling charge separation. Energy offsets of 0.3 eV can effectively generate free charges, avoiding geminate recombination losses [41]. The mechanistic details, however, are a topic of intense research.

4. Charge transport

The free charges then drift through the active layers, driven by the built-in field from the different electrode WFs. Despite separate transport through donor and acceptor layers, the low mobility of organics [41] causes carrier losses as electrons and holes may recombine before reaching the electrodes. Radiative recombination occurs through band-to-band transitions,

which are required to maintain thermodynamic balance. Trap-assisted recombination via mid-gap states will also occur, due to structural defects or impurities [63]. Additionally, charge transport may be hampered by space-charge effects. Charge accumulation opposing the built-in field is caused by long transport distances, unbalanced mobilities and energetic barriers [81].

5. Charge extraction

Finally, charges are extracted to the external circuit via the electrodes, where interface characteristics play a crucial role. Interface energy barriers significantly degrade performances and direct active layer contact can quench excitons causing carrier losses [82]. Therefore, charge transport layers (CTLs) are commonly employed at the interface to improve charge extraction characteristics.

• Performance Characterisation

The current-voltage (IV) characteristics of devices are measured in the dark and under illumination, to extract key operation parameters (Figure 1-8). Standard testing conditions are used to give comparable data: samples are illuminated by the AM 1.5 spectrum at 100 $mWcm^{-2}$, which approximates the terrestrial solar spectrum [83]. The energy level structure of the device, with different electrode WFs aligned to the donor and acceptor transport levels, creates energy barriers for minority carrier injection. This produces the rectifying IV curves observed and enables carrier collection for photovoltaic power generation [61].

The key operation parameters are as follows. The photocurrent at short circuit conditions (J_{sc}) gives the maximum number of photocarriers extracted per unit area. The J_{sc} depends on the incident photon flux, alongside the device absorption characteristics and any subsequent carrier collection losses [76]. The photovoltage at open circuit conditions (V_{oc}) gives the maximum

potential difference generated from the offset between the electron and hole quasi-Fermi levels. The exact origins of the V_{oc} value are debated, however, it stems from the gap between the donor HOMO and acceptor LUMO, while being influenced by the electrode WFs and reduced by recombination [84]. The fill factor (*FF*) describes the quality of the IV characteristics, as it depends on the position of the maximum power point, given by J_M and V_M. It indicates the collection efficiency of the device and as such is strongly affected by recombination processes [81]. The overall efficiency of the device converting incident illumination into electrical power, the *PCE*, is calculated from these three parameters and the illuminating power, P_{in}.

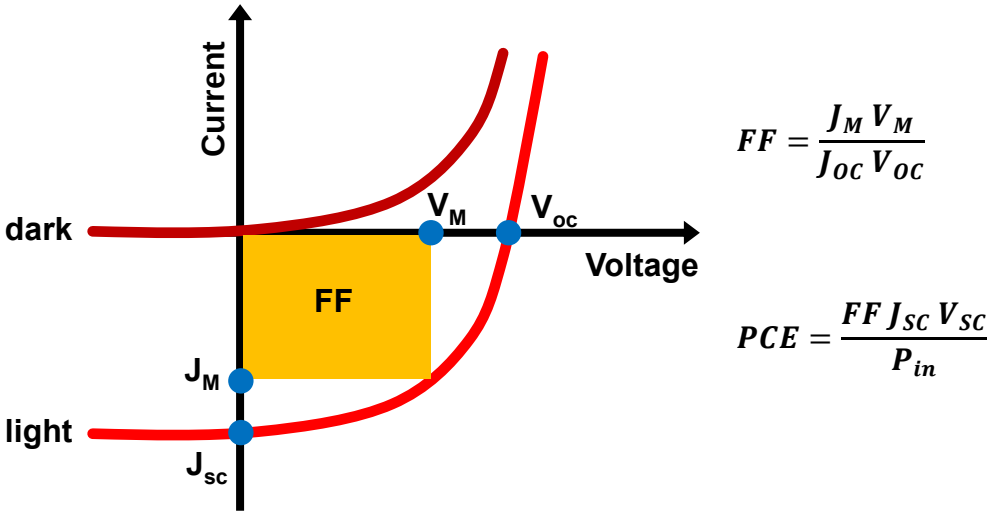


Figure 1-8: Typical PV device IV characteristics with key parameters indicated, alongside equations for the *FF* and *PCE*.

PV device operation can be modelled using an equivalent circuit model (ECM) composed of: a diode, a photocurrent source and resistor elements (Figure 1-9) [40]. The series resistor gives the series resistance (R_s), which describes the overall device resistance to carrier transport and is influenced by the layer stack design. A high R_s reduces the *FF* by changing the slope of the IV curve around the V_{oc} point. The parallel resistor gives the shunt resistance (R_{sh}) and represents pathways for leakage currents often caused by fabrication defects. A low R_{sh} reduces the *FF* by changing the slope of the IV curve around the J_{sc} point.

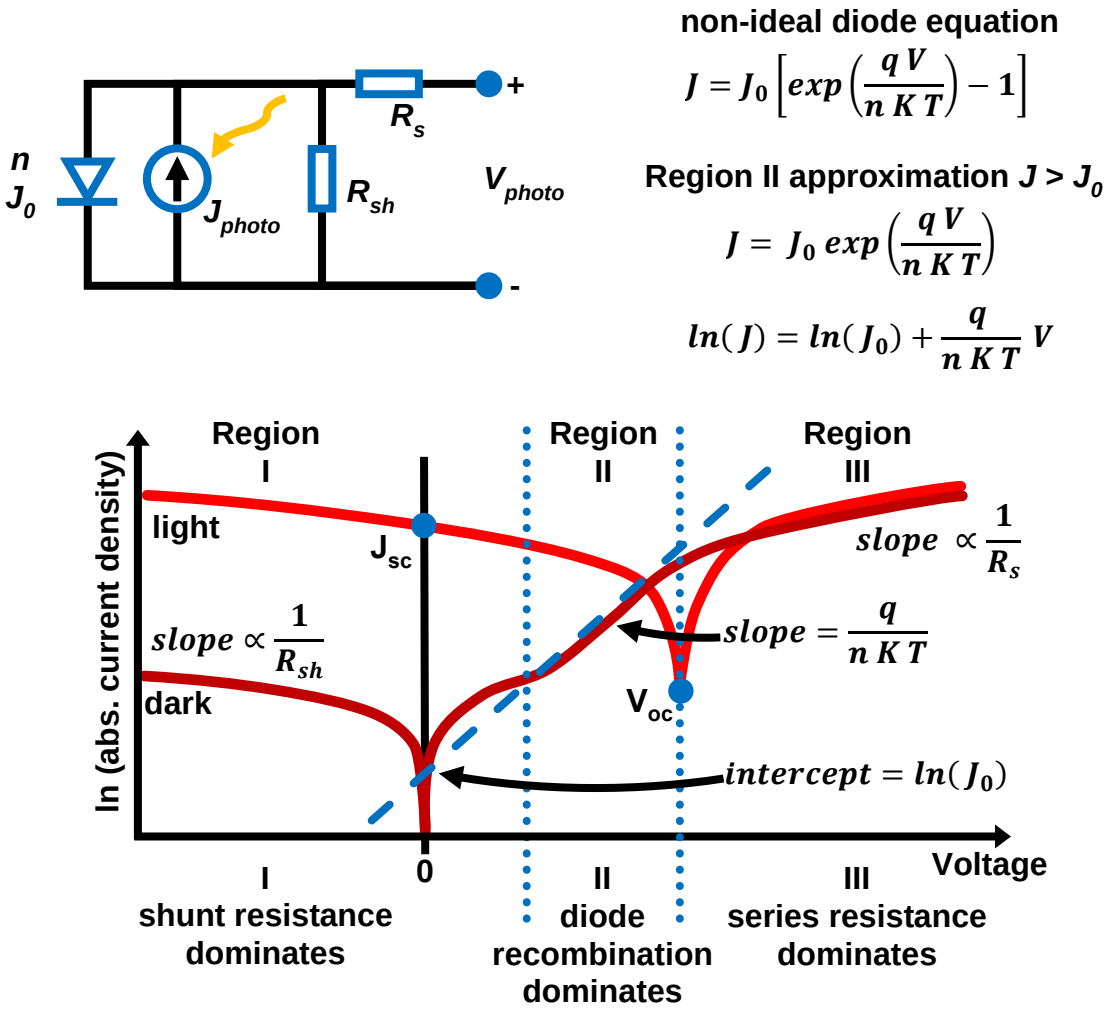


Figure 1-9: The ECM of PV operation alongside the associated diode equations, which correspond to the semi-log plot of dark IV characteristics shown below.

Semi-log plots of dark IV curves show the three distinct regions used to extract the different operation parameters (Figure 1-9). For the diode component, the diode ideality factor (*n)* and dark saturation current (J_0) values are derived from modelling with the non-ideal diode equation [81]. Linear fitting in region II gives *n* which indicates the dominant recombination mechanisms occurring [85] and J_0 which provides a general measure of the amount of recombination [86]. The R_s and R_{sh} values are calculated from the reciprocal of the slope of a linear-linear IV curve in regions III and I respectively [87].

1.3 Motivation

1.3.1 Charge Transport Layers for Performance Enhancement

The inclusion of CTLs is a versatile route for enhancing the performance of PV devices. Primarily, they facilitate charge extraction from the active layer to the electrodes, however, they also perform various secondary roles. Traditionally, silicon PVs do not require CTLs; commercial modules use n- or p-doped regions to achieve ohmic electrode contact. However, recent reports suggest employing distinct CTLs, of common OPV materials, could improve module costs and performances [88]. CTLs are key to the success of perovskite PVs, especially small molecule organic hole transport layers (HTLs) of spiro-OMeTAD (2,2',7,7'-Tetrakis[N,N-di(4-methoxyphenyl)amino]-9,9'-spirobifluorene) which has: a high hole mobility, good visible transparency and favourable processing characteristics [89]. Similarly, for OPVs CTLs are critical to the high performances now achieved [90] [91] [92]. The various roles performed by CTLs in OPV devices are now outlined.

• Electrical Enhancement Mechanisms

A key function of CTLs is to provide a selective contact, which extracts majority carriers and prevents minority carrier and exciton recombination at the electrodes (Figure 1-10). Bad alignment between the electrode WF and organic HOMO or LUMO, hinders charge transport and extraction. CTLs are used to provide intermediate energy levels which facilitate majority charge collection [93] [94]. To avoid resistive losses, organic CTLs are often doped to improve their conductivity [95] [96] [97]. Non-selective direct contact between the electrode and active layer leads to charge and exciton recombination. CTLs with offset transport energy levels and wider bandgaps are therefore used to block undesirable carrier transport to the electrodes [98] [99] [100].

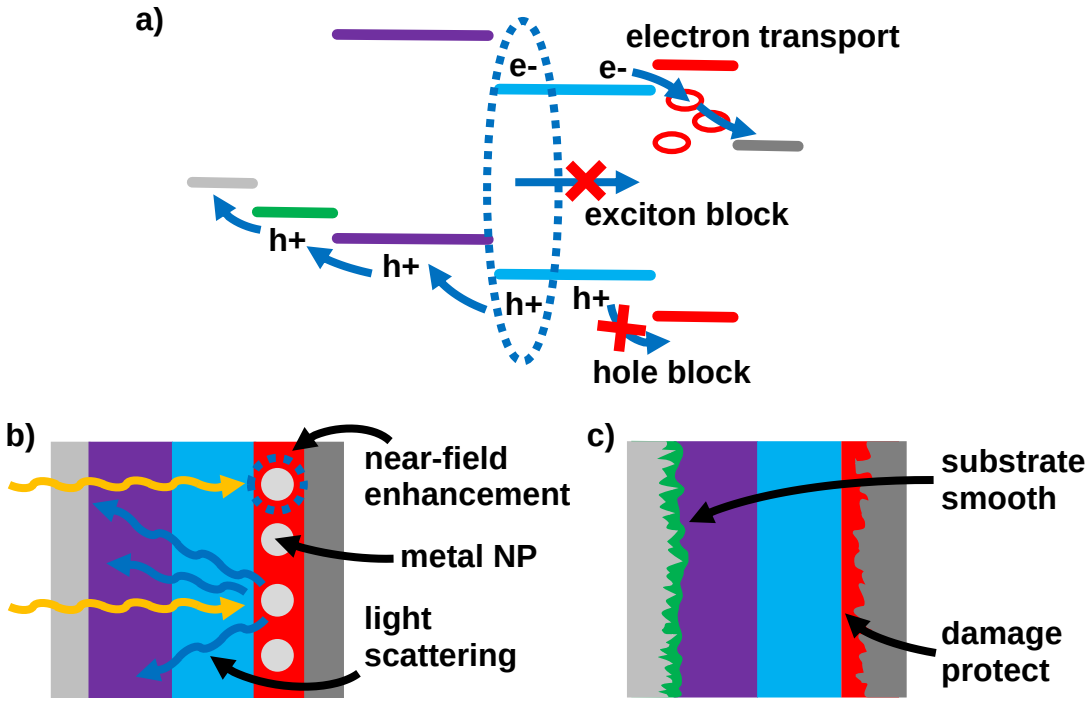


Figure 1-10: Examples of CTL enhancement mechanisms: a) selective contact formation, b) optically active metal nanoparticles (NPs) and c) physical buffer layers.

CTLs are also used to directly adjust the electrode WF, reducing energy barriers to extraction and increasing the built-in voltage (V_{bi}). CTLs containing polar species create interface dipoles, which shift the energy alignment to form ohmic contacts [101] [102]. For cathodes with poor electron selectivity, the alignment can be modified by shallow WF CTL materials [103] [104]. Metal-organic interface interactions are complex and not fully understood, they can lead to Schottky barrier formation at electrodes [105] [106] [74]. These extraction barriers can be mitigated by doping CTLs to form quasi-ohmic tunnel junctions [73] [107] or gap state creation in the CTL providing a transport route circumventing the barrier [108]. Fermi level pinning barriers, formed by complex interactions at the metal cathode interface, can be relieved by CTLs which suppress surface state formation in the active layer [109] [110].

• Optical Enhancement Mechanisms

Thin film interference effects in OPVs can lead to non-optimised optical fields causing absorption losses. CTLs are therefore utilised as optical spacers: their thickness is varied (sometimes by just 10s of nm [92]) to maximise the spatial distribution of the field in the photoactive layer. Effective optical spacer layers are positioned at the reflecting back electrode, are transparent in the visible region and have a low refractive index [111] [112].

OPVs are often restricted by the absorption-diffusion trade-off: organics are poor conductors, so the necessary transport distances limit the layer thickness for absorption [113]. Plasmonic species, such as metal nanoparticles (NPs), have been embedded in CTLs to enhance absorption without increasing device thicknesses (Figure 1-10) [114] [115]. This is primarily achieved by scattering light into the photoactive layer to increase the optical path length. Additionally, near-field plasmonic effects may contribute to absorption increases.

• Structural Enhancement Mechanisms

Leakage pathways in the architecture of OPVs can cause significant recombination losses. CTLs can be employed as a smoothing layer to prevent shorting, for example, due to rough indium tin oxide (ITO) electrodes (Figure 1-10) [116] [117]. CTLs also provide protection from other physical and chemical interactions. As a buffer layer, they shield the underlying organic from metal electrode deposition damage (Figure 1-10) [109] [118]. They also act as a barrier to environmental ingress, as oxygen and moisture degrade the optoelectronic properties of organics which limits the ambient stability of devices [119] [120] [121].

• Specific Material Examples

An individual CTL may perform several of the roles outlined above simultaneously. Various material classes are employed in OPV devices, each with associated benefits and drawbacks (Table 1-2). The features of a few commonly employed CTLs will now be outlined.

Class	Materials	Key Features
Metals	Ca, Ba, Mg	• Shallow WF modifies energy level alignment • High conductivity electron transport • Air and moisture sensitive
Metal salts	LiF, Cs2CO3	• Ionic dipole modifies energy level alignment • Diffuse to n-dope underlying organics • Diffusion can degrade device lifetime
Metal oxides	**p-type:** WO3 MoO3 V2O5	• Highly selective contact for holes • Enhance device stability • Form smooth uniform layers • Thick layers cause high series resistance
	n-type: ZnO TiO_2	• Highly selective contact for electrons • Optical spacer layer • Enhance device stability • UV light-soaking required for carrier collection
Organics	**Polymers:** PEDOT:PSS PANI	• Selective contact and energy level alignment • Conductivity limits thickness, unless doped • Tune electronic properties via chemical structure • Solution processing may require orthogonal solvents
	Small molecules: BCP, Alq3 NPB, Ptn	• Selective contact and energy level alignment • Conductivity limits thickness, unless doped • Tune electronic properties via chemical structure • Well defined molecular structure and high purity
	Conjugated polyelectrolytes: PFN	• Molecular dipole modifies energy level alignment • Tune electronic properties via chemical structure • Soluble in environmentally friendly polar-solvents
Plasmonics	Au, Ag Nanoparticles Nanostructures	• Scattering or LSPR to enhance absorption • Tune optical properties via composition and geometry • Direct active layer contact can quench excitons

Table 1-2: A summary of various materials employed as CTLs in OPV devices [90] [91] [92].

A ubiquitous CTL in OPVs is the solution processed polymer poly(3,4-ethylenedioxythiophene)-poly(styrenesulfonate) (PEDOT:PSS) [122] [123] [124] [125] [126]. It forms smooth films on ITO, reducing shorts, and has good transparency in the visible region,

minimising parasitic absorption in its position at the front of the device. Its energy levels modify the ITO WF, to assist hole extraction, and high conductivities are achieved through PSS doping. However, it is acidic and can etch the underlying ITO which degrades device performance [127].

A material often used to replace PEDOT:PSS in conventional devices in MoO_3 [128] [129] [130] [131] [132]. Thermal evaporation produces smooth uniform films with high transparency. Its deep WF forms an effective hole selective contact and layers also enhance device stability. Thickness optimisation is often undertaken, for effective coverage of underlying layers without unnecessary series resistance increases [133] [134].

ZnO [135] [136] [111] [137] and TiO_x [138] [79] [139] [140] [141] are both solution processable electron transport layers (ETLs). Visible region transparency and a low refractive index make them efficient optical spacer layers. They have a high electron selectivity but require UV light-soaking for effective carrier transport and extraction [142] [143]. Therefore, they are often located on ITO in inverted architectures to improve electron collection [144]. For QD PVs, studied in Chapter 3, ZnO and TiO_x ETLs additionally form an intrinsic part of the device architecture. They create the p-n junction depletion region with the QD layer, which facilitates photocarrier generation and collection [145] [146]. QD PVs, and their associated CTLs, are discussed specifically in the introduction to Chapter 3 (Section 3.1.2).

• Thesis Relevant Embodiments

This thesis investigates CTLs composed of evaporated small molecule organics and metal NPs. Recent reports of these embodiments will now be highlighted, to demonstrate their utility in OPVs and hence the interest in understanding their operation mechanisms.

Given the division of OPVs as a field, evaporated CTLs are less common than their solution processed counterparts, nevertheless, they have certain advantages. CTLs are inherently adjacent to active layers, so dry processing helps to easily minimise inter-layer interactions [37] [91]. The well-controlled thicknesses and possibility for co-evaporation doping, are also beneficial when employing low conductivity organics [37] [95] [90].

Many OPV devices now contain evaporated organic ETLs before the top metal electrode. The current evaporated OPV efficiency record of 8.4%, was achieved in part by carefully optimising the BCP (bathocuproine) ETL thickness which strongly influenced performance [47]. The most commonly used materials are BCP [147] [148] [149] [150] and BPhen (bathophenanthroline) [151] [152] [153] [154], although Alq3 (tris(8-hydroxyquinolinato)aluminium) [155] [156] and C60 (buckminsterfullerene) [157] [158] are reported with reasonable frequency (Figure 1-11). Forming an exciton blocking selective contact is a key role of these layers, which also often function as optical spacers.

Providing protection from metal electrode evaporation is also an important role. ETLs passivate metal-organic interfacial interactions, which would otherwise create recombination centres at the active layer surface [110]. Whilst thick layers provide effective protection, issues arise as low conductivities increase the device series resistance [159]. Novel ETLs have demonstrated that improved homogeneity allows thinner layers to remain effective [160]. The electrode protection role can contribute to the transport mechanism in ETLs. The metal-organic interaction creates bandgap states which facilitate electron transport [161] [162]. Alternatively, doping can be used to improve conductivity and lift thickness limitations [95].

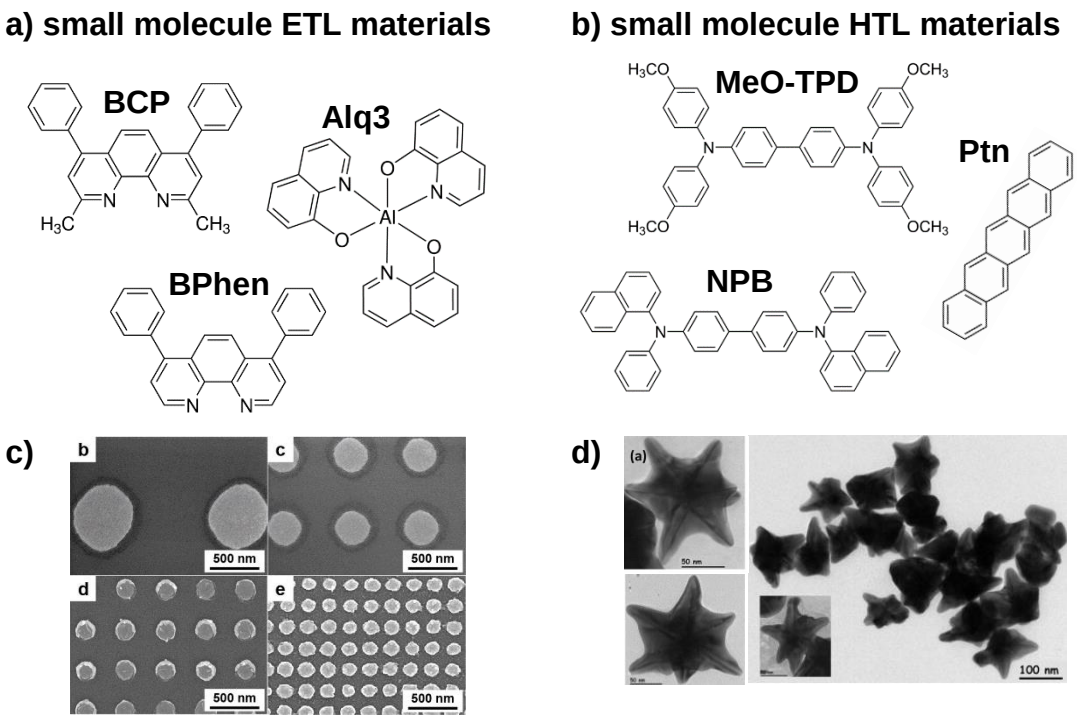


Figure 1-11: The molecular structures of small molecule organics typically used as a) ETLs and b) HTLs [163]. c) Scanning electron microscopy (SEM) images of laser interference lithography fabricated Ag NPs [164]. d) Transmission electron microscopy (TEM) images of colloidally synthesised Au nanostars [165].

Recent ETL studies often explore dual-material layers. LiF is commonly combined with organics, to create a shallow WF cathode which enhances electron collection, alongside a deep HOMO which blocks holes [166]. Additional enhancement mechanisms have also been observed: charge transfer from the fluorine dopes the organic for electron transport [167] and the organic provides an additional interface with the active layer for exciton dissociation [168]. Other combinations have been explored, including p-type MoO_3 which with BCP extended the device lifetime though improved environmental protection [169]. Blending wide-gap ETL materials with electron conducting fullerenes has been shown to enhance performances and also increase lifetimes by suppressing crystallisation [170] [171].

High efficiencies and good device stabilities have been achieved with dual-material ETLs in polymer BHJ architectures. Combining BCP with the conjugated polyelectrolyte PFN (Poly [(9,9-bis(3'-(N,N-dimethylamino)propyl)-2,7-fluorene)-alt-2,7-(9,9–dioctylfluorene)]) has

produced very high efficiencies of over 10 % [172]. Efficiencies of 8 % were achieved with a TmPyPB (1,3,5-Tri(m-pyridin-3-ylphenyl)benzene) and LiF combination, the devices retained 90 % of their initial *PCE* after 72 hours of ambient exposure [108]. ETL studies in small molecule planar heterojunction (PHJ) architectures generally achieve lower *PCE*s around 3 %, however, as control *PCE*s can be below 0.5 % the increases are still significant [170] [169] [110].

Evaporated organic HTLs are less common than ETLs, due to the prevalence of PEDOT:PSS and MoO_3 for solution and vacuum processed OPVs respectively. Various small molecule p-type materials are employed, common choices are MeO-TPD (N,N,N',N'-tetrakis(4-Methoxy-phenyl)benzidine) and NPB (N,N′-Di(1-naphthyl)-N,N′-diphenyl-(1,1′-biphenyl)-4,4′-diamine) [173] [174] (Figure 1-11). The HTLs primarily perform a selective contact role, similar to that described above for ETLs. The addition of an organic HTL combined with MoO_3 has achieved reasonable *PCE*s around 5 % in small molecule PHJ devices [175]. In addition to reducing recombination and creating an ohmic contact, this dual-material approach provides another exciton dissociation interface with the active layer [176].

HTL performance depends critically on the HOMO level position. It must be deep enough to provide a large V_{bi} for collection, but not so deep that it creates a hole transport barrier [177]. Recent reports suggest the LUMO requirements may be less stringent. Novel narrow bandgap HTLs have been shown to improve the performance of a PHJ device from 3.98 % to 4.92 % [178]. The materials still have bandgaps wider than the donor, so exciton blocking operates effectively. However, their LUMOs match that of the donor, suggesting electron blocking is a less important HTL role.

A detailed review of metal NPs in OPVs is given in the introduction of Chapter 5 (Section 5.1.1). The following paragraphs therefore only highlight notable recent examples from the field. Incorporating metal NPs within CTLs is advantageous as it avoids direct active layer contact which causes recombination [179]. Studies generally involve tuning the NP material and geometry, to manipulate the optical interaction with the active layer [115].

Thermally evaporating both gold (Au) and silver (Ag) NPs into CTLs, has been used to broaden scattering across the visible wavelengths, through the different plasmonic resonances of Au and Ag [180]. Both the size and location of thermally evaporated NPs can be controlled using laser interference lithography (Figure 1-11). Applying this technique with Ag NPs produced a *PCE* of 10.72 %, one of the highest reported for plasmonic OPVs [164]. Solution-based synthesis methods allow complex NP geometries (such as nanostars) to be produced (Figure 1-11) [165], which can achieve high *PCE*s of around 9% in devices [181] [182].

The embodiment most relevant to this thesis is directly evaporated NPs within an organic CTL. For this embodiment, the highest reported *PCE* is 4.87 %, which was improved from 3.36 % for the control small molecule PHJ device [183]. The Ag NPs in the BCP ETL mostly improved electron extraction, which is somewhat unusual as optical effects generally dominate NP enhancement mechanisms. Whilst electronic effects are sometimes observed with NP additions, metal-organic electrochemical interactions are not fully understood [105] [106] [74], especially considering the increased reactivity of NPs [184].

A recent report employed both a plasmonic NP CTL and a dual-material CTL, in a polymer BHJ architecture [185]. The ETL of BCP and LiF provided a selective contact with good energy alignment, whilst the HTL of PEDOT:PSS with Au and Ag NPs increased the active layer optical path length. A volume ratio of 25:75 Au:Ag increased the visible wavelength scattering,

improving the *PCE* from 4.36 to 5.36 % with NP additions. However, integrating metal NPs with OPVs can sometimes be challenging. Adding Ag NPs beneath a pentacene (Ptn) HTL was found to increase ITO leakage currents and reduced the *PCE*, despite improving the device's resistance to illumination-induced degradation [186].

The literature reports described above, show various types of CTLs can successfully improve the efficiency of PV devices through a variety of mechanisms. CTLs based on evaporated organics can play multiple performance enhancing roles and are suitable for deposition on active layers. Additionally, electrochemical interactions at their metal-organic interfaces are of mechanistic interest. Metal NPs represent a versatile method of enhancing absorption in thickness limited organic layers. Again, a deeper understanding of the electronic effects of NP-organic interactions would be valuable. This thesis therefore studies these embodiments as outlined below.

1.3.2 Thesis Aims and Outline

• Aims

The overall intention of this research is to develop the mechanistic understanding of performance enchantment strategies for PV devices. To that end, experiments explore various device architectures, layer structures and material combinations. CTLs are investigated because they are a key method of overcoming extraction limitations which often restrict device performances. Additionally, CTLs potentially contribute performance gains through multiple other mechanisms. The properties of the CTLs are therefore modified, in order to understand and improve the various roles played in PV operation. Metal NPs are studied in CTLs, because they have been shown and understood to improve light management, but also may enhance PV performance through other mechanisms which have not been researched as extensively.

Additionally, the electrochemical interactions of metals and organics, especially involving NP structures, encompass a plethora of phenomena of mechanistic interest. The nature of the metal NPs is therefore varied, in order to understand and control their influence on the CTL properties and PV device performance. The introduction of each results chapter outlines specific research motivations in the context of the relevant individual fields.

• Outline

This introduction has demonstrated the urgent real-world need for renewable energy and shown the potential benefits of developing OPV technologies. The underlying organic semiconductor and device physics was explained, to give an understanding of PV operation mechanisms and enable the conception of improvement strategies. State-of-the-art approaches to PV performance enhancement were presented, alongside the current mechanistic understanding. The equipment and methods chapter explains the basic physics of the vacuum thermal evaporation processing technique and characterisation methods employed. It describes the process of designing and building the deposition system used to produce samples for this research. The general experimental parameters, applicable to the fabrication and characterisation of all samples, are also provided.

In Chapter 3, a Ptn HTL is used to improve charge extraction in QD PV devices, through various mechanisms. Post-fabrication photonic and atmospheric treatments are explored, to modify the interface energetics. In Chapter 4, Au and Ag NPs, of 1-5 nm nominal thickness, are fabricated within an Alq3 ETL to manipulate the optoelectronic properties. Single layer device architectures are characterised to understand the interaction and operation mechanisms, taking into account both optical and electronic effects. In Chapter 5, composite ETLs, of Au NPs and Alq3, are employed to improve charge extraction in OPV devices, through multiple mechanisms. NPs, of 0.5-5 nm nominal thickness, are tested in full PV devices, to explore the

effects of NPs on PV operation, both the resulting improvements and losses are considered. The thesis concludes, by reviewing the contribution of this work to improving the scientific understanding in various areas related to OPVs. It also identifies aspects which could be taken further to: enhance performances, expand mechanistic understanding or apply emerging concepts in alternative embodiments.

Chapter 2: Equipment and Methods

2.1 Deposition System Design

2.1.1 Vacuum Thermal Evaporation

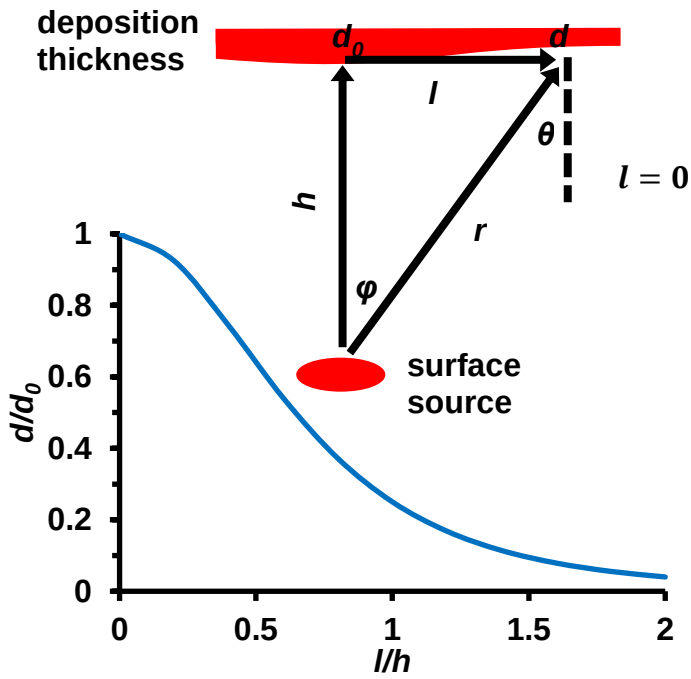
This thesis reports studies of organic thin films and metal NPs, both fabricated by vacuum thermal evaporation deposition. This technique enables multilayer and composite structures to be produced, with precise control over film thickness and composition [37]. Alternatively, organic and NP layers can be created by solution processing. This technique operates by applying a suspension to the substrate, then removing the solvent to leave behind a layer of deposited material. However, inter-layer solvent interactions can limit the production of multilayer structures [37]. Solution processing is therefore less suitable for the proposed programme of research.

The process of vacuum thermal evaporation can be broken down into three stages as the name suggests. Firstly *vacuum*: the chamber is pumped out to achieve a high vacuum level. This is necessary to extend the mean free path of evaporated species, enabling them to reach the substrate. For example, at atmospheric pressure species can travel approximately 50 nm before a collision, whereas at a vacuum level of 10^{-6} Torr this distance is extended to 25 m [187]. Secondly *thermal*: a power supply then passes a large DC current through a resistive element, which heats up the evaporant material. Heating can be direct, via a boat source, to provide high temperatures for metal evaporation. Alternatively, it may be indirect, via crucible and basket sources, for low-temperature organic material evaporation.

Thirdly *evaporation*: the material then evaporates or sublimes from the source, and upon reaching the substrate condenses to form a thin film. The evaporant species travel and deposit

with a line of sight type mechanism. This means substrates can be covered or uncovered by shutters, to control the layer thickness deposited. Additionally, patterned masks can create specific film geometries, however, spreading at mask edges can occur if there is an offset between the mask and the substrate [188].

The film thickness across the deposition surface varies due to the material evaporating from the source in multiple directions. The deposition variation (eq. v) can be determined from the cosine law (eq. i), describing the evaporant plume shape of a surface source, and the setup geometry (eq. ii-iv) (Figure 2-1) [189]. Key parameters in the equations are: h the source to substrate throw distance, l the position on the surface and d the film thickness at that position. To maximise the substrate homogeneity (d/d_0), the l:h ratio should be small. This can be achieved by positioning sources more centrally under substrates or reducing the substrate size (decreasing l) and making the throw distance larger (increasing h). All the different features of vacuum thermal evaporation outlined above should be considered when designing a deposition system.



$$d = \frac{M\,cos\varphi\,cos\theta}{\pi\,\rho\,r^2} \quad \textbf{(eq. i)}$$

$$l = 0 \text{ gives: } d_0 = \frac{M}{\pi\,\rho\,h^2} \quad \textbf{(eq. ii)}$$

$$cos\varphi = cos\theta = \frac{h}{r} \quad \textbf{(eq. iii)}$$

$$r^2 = h^2 + l^2 \quad \textbf{(eq. iv)}$$

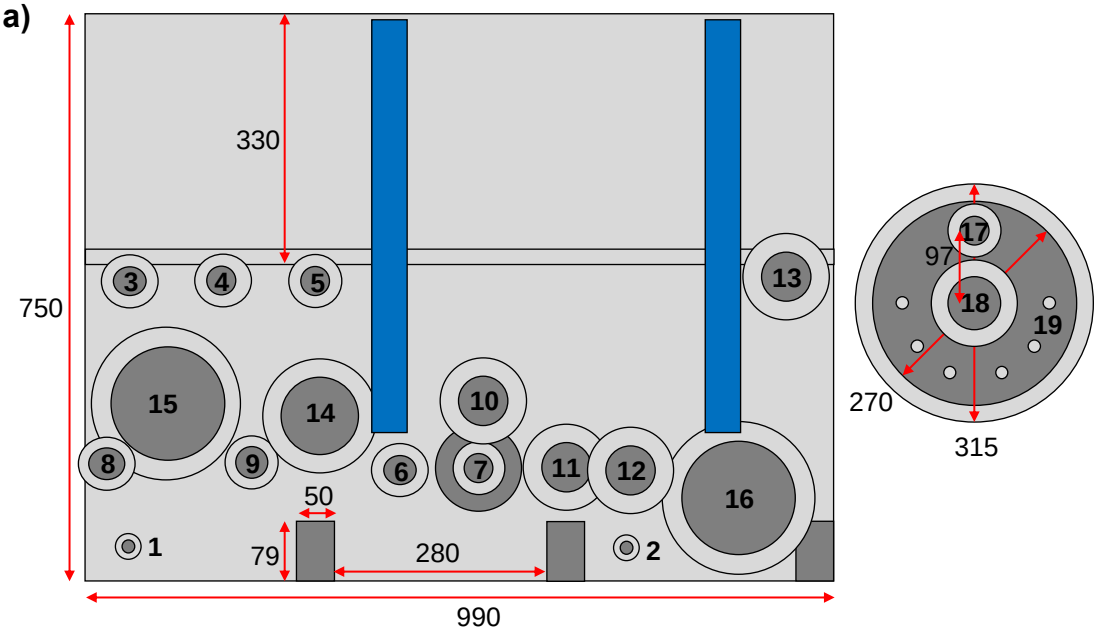
$$\frac{d}{d_0} = \frac{1}{\left(1 + \left(\frac{l}{h}\right)^2\right)} \quad \textbf{(eq. v)}$$

Figure 2-1: A schematic diagram illustrating the experimental setup geometry, alongside the associated equations used to derive the deposition thickness for a surface source. The deposition homogeneity (d/d_0) is plotted against the l:h ratio (l/h) as per eq. v. The equation parameters are as follows: h the source to substrate throw distance, l the position on the surface, d the film thickness at that position, r the radial throw distance, φ the emission angle, θ the receiving angle, M the evaporant mass and p the deposition density. Adapted from Ohring et.al [189].

2.1.2 Deposition System: The HOF

As part of this DPhil project, a new deposition system was custom designed and built to meet the needs of the research programme (Figure 2-2, Figure 2-3, Figure 2-4 and Figure 2-5). To achieve high-performance PV devices and study the effects of organic CTL and metal NP incorporation, specific equipment capabilities are required (Table 2-1). The deposition system must be able to fabricate complex layer architectures, with carefully controlled film formation parameters. Ideally, it should also enable rapid device variable testing, to accelerate the research and development cycle. These requirements called for a sophisticated system, capable of fabricating several different multi-layer devices in one run and precisely applying additives to individual layers.

a)



b)

Port	System Part
2	vent valve
3	QCM
4	shallow source or thermocouple
5	shallow source or thermocouple
6	vacuum gauge

Port	System Part
10	turbo pump
11	deep source
13	shallow source x 2
18	shuttering
19	substrate thermocouple

c)

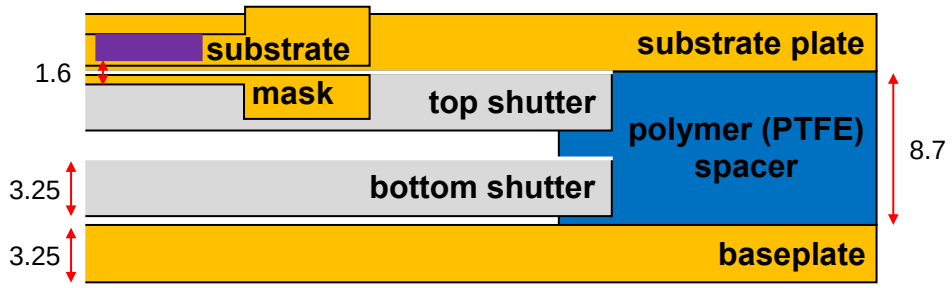


Figure 2-2: Diagrams showing various aspects of the design process for the deposition system, with measurements shown in mm units. a) A projection view of the external chamber layout, showing the positions of various ports and the pneumatic lifters; alongside a top-down view of the external chamber lid layout, showing the positions of various ports. b) A table specifying the port number used for various system components. c) A zoomed-in cross-sectional view of the two-level shuttering system located inside the chamber beneath the lid.

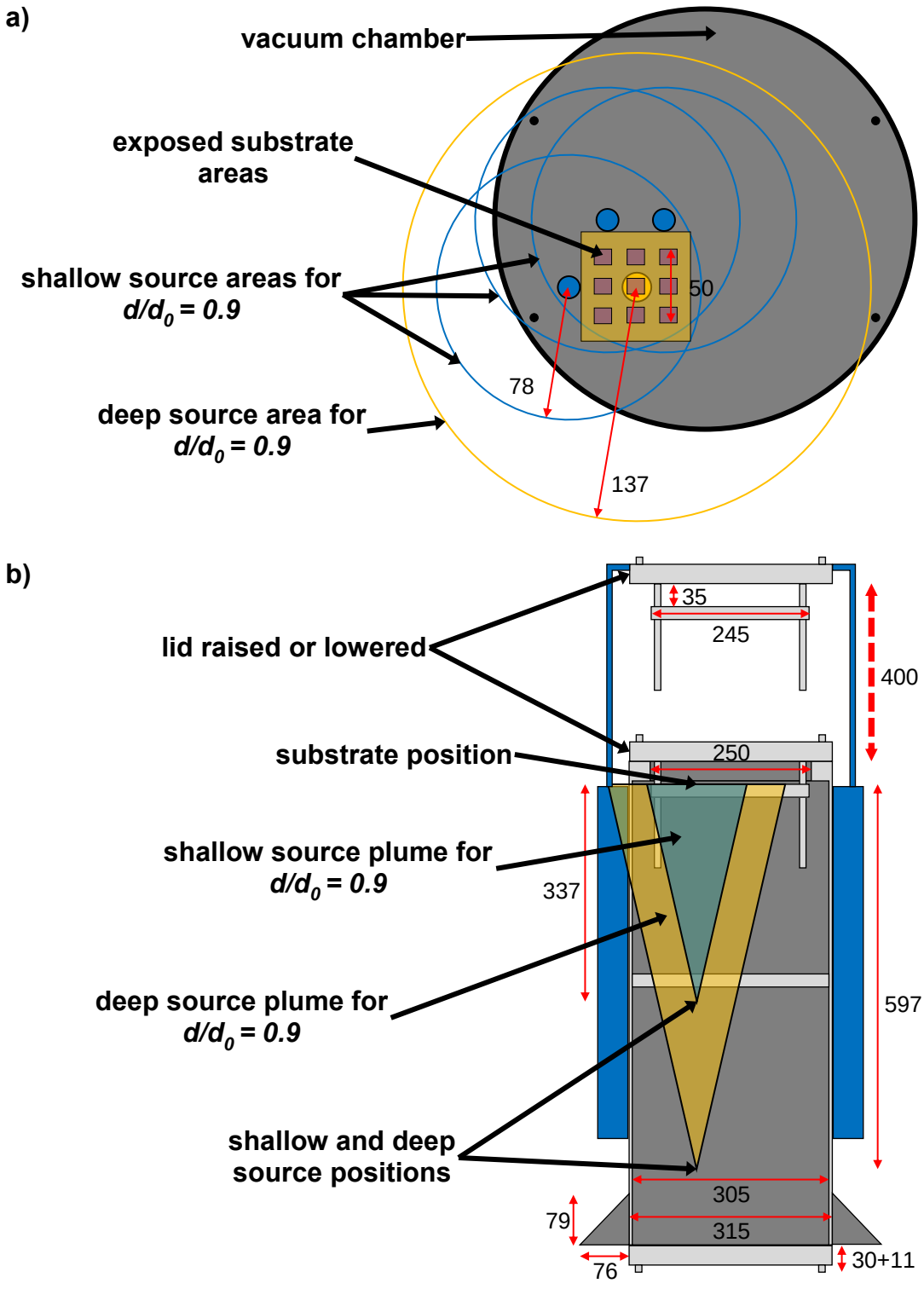


Figure 2-3: Diagrams showing various aspects of the design process for the deposition system, with measurements shown in mm units. a) A top-down view of the internal chamber geometry, showing the source homogeneity areas with respect to the exposed substrate positions. b) A cross-sectional view of the internal chamber geometry, showing the evaporant plume homogeneity for both shallow and deep source positions, alongside a demonstration of the pneumatic lid lifting mechanism.

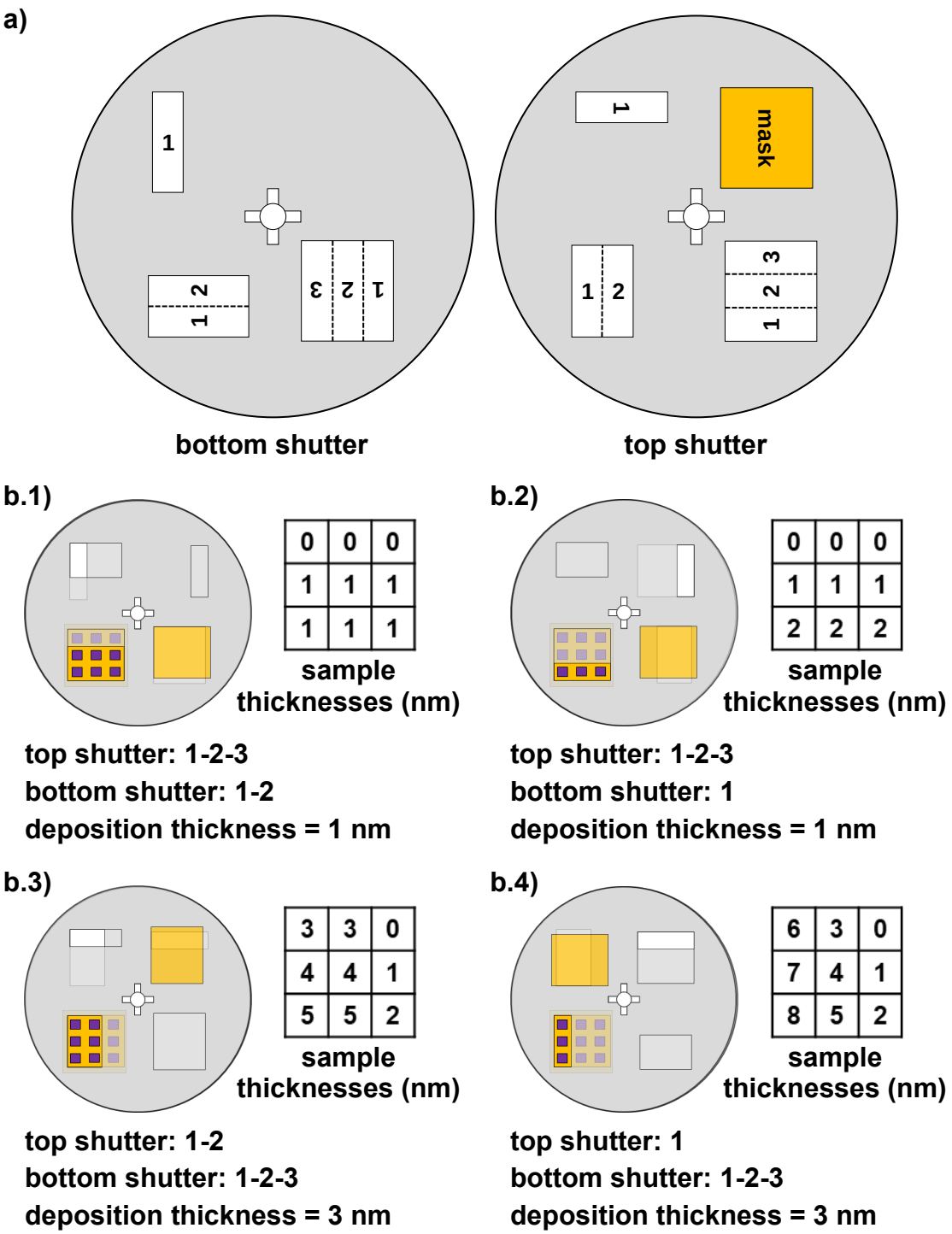


Figure 2-4: Diagrams showing various aspects of the design process for the deposition system. a) The masking geometry of the top and bottom levels in the shuttering system. b.1-4) An example of a four-step deposition sequence with shuttering positions to produce nine different sample thicknesses.

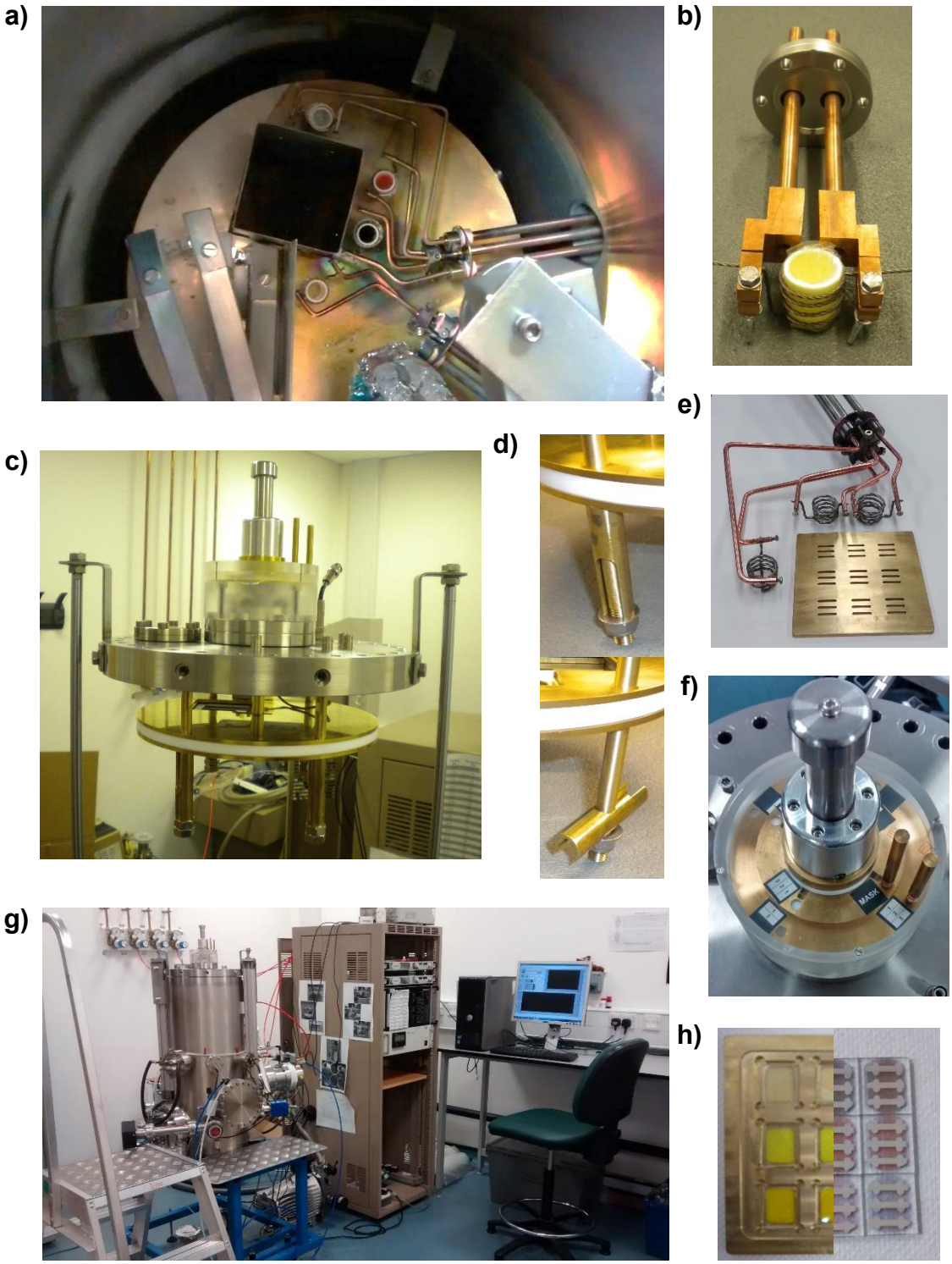


Figure 2-5: Photographs of various aspects of the experimental setup of the deposition system. a) A top-down view of the source and QCM positioning. b) The custom-built connectors for the deep source. c) The internal and external components of the shuttering system, elevated by the pneumatic lifting system. d) A demonstration of the height adjustment mechanism, for the internal portion of the shuttering system. e) The custom-built connectors for the shallow sources positioned around the top contact mask. f) The external portion of the shuttering system, used for mask manipulation, identification and alignment. g) The deposition lab setup showing: the chamber on its stand, the vacuum system, the gas supply systems, the power supply units and the computer monitoring. h) The substrate holder and substrates showing the top contact deposition pattern.

Research Requirement		Detail
A	Complex device architectures	• Multiple layers of different materials with specific geometries
B	Study organic CTL inclusion	• Systematic nominal thickness variable testing • Fair comparison to controls without CTL
C	Study metal NP additive	• Explore NP size effects by varying nominal thickness • Fair comparison to controls without NPs
D	Rapid testing cycles	• Multiple variables and samples in single batch • Fast device fabrication turnaround time
E	Sample consistency	• Sample-to-sample variation within a batch can occur due to experimental accuracy or control limitations
F	Sample comparability	• Batch-to-batch variations can occur due to different experimental or environmental conditions
G	High performance devices	• Avoid environmental exposure and impurity introduction

Table 2-1: The experimental requirements of the research programme, which were used to design the deposition system specifications.

The system specifications were drawn up by considering the sample types necessary to answer the research questions of this thesis (Table 2-1). The various features of the system were then designed to meet these needs and integrate with the re-purposed vacuum chamber forming the body of the system (Table 2-2, Table 2-3 and Table 2-4). The two most important features are the shuttering system and the multiplicity of sources. The components were either handmade in the materials workshop or ordered from specialist suppliers (K. J. Lesker, RS, Testbourne, Inficon). The individual parts were then built into the chamber and the system was tested to ensure performance standards were achieved. The geometric tooling factor for the quartz crystal monitor (QCM) was established by depositing organic (or metal) layers of various thicknesses for a given tooling factor. The QCM thickness was compared to the actual thickness measured by ellipsometry (or surface profilometry for metals), allowing the correct tooling factor to be identified.

Multiple Sources	
Multiple organic, inorganic and metal sources • 4 crucible and basket sources for organic or inorganic evaporation • 2 tungsten-boat sources for metal evaporation • baffles positioned between sources	
Strategic source-substrate geometry • central metal source for device area uniformity (although throw-distance issues meant not used eventually) • organic and metal source positions to optimise evaporant plume (lateral location and throw-distance to give approx. ±5 % thickness variation)	
System Feature	**Requirements Enabled**
Sufficient sources to deposit: NP, charge transport, active and electrode layers	**A, B, C**
Optimised evaporant plume alignment increases homogeneity across substrates	**C, E**
Baffles between sources minimise cross contamination	**F, G**
Full material range enables entire device stack in single pump-down cycle	**D, G**

Table 2-2: The deposition system features related to the evaporation sources, the specific research requirements they satisfy are indicated.

Shuttering System	
Multiple substrates and pixels • 3-by-3 matrix arrangement of 9 substrates • 3 pixels per substrate so 27 devices per testing cycle • adjustable height substrate holder for ergonomics and throw distance	
Various substrate shuttering configurations • 8 unique mask geometries in a two-level system • specific substrate selection and top contact patterning available • controlled by dual-axis rotary-linear motion feedthrough • external mechanism for mask identification and positioning alignment	
System Feature	**Requirements Enabled**
9 samples per batch with identical processing conditions	**D, F**
Multiple pixels per substrate improves testing statistics	**B, C, D**
Masking gives 9 unique thickness samples for comparison	**B, C, D**
Top contact pattern mask enables entire device stack in single pump-down cycle	**D, G**
Variable height substrate holder maximises throw distance for deposition homogeneity	**C, E**
Minimum gap between top contact mask and substrate reduces spreading	**A**
Locating mechanism for shutter rotation gives accurate mask alignment	**E**

Table 2-3: The deposition system features related to the shuttering system, the specific research requirements they satisfy are indicated.

General Functionalities	Requirements Enabled
Chamber Features	
Stable and reinforced frame for chamber • customised to incorporate rotary vacuum pump • with wheels for improved mobility	**-**
Pneumatic lid lifting mechanism • easy chamber opening to access substrates and sources	**-**
Air cooling of chamber and QCM • stable environmental conditions throughout deposition process	**F**
Vacuum Features	
Scroll and turbo pumps alongside knife-edge seals and copper gaskets • fast pump-down to high vacuum 10^{-6} Torr base pressure	**D, G**
Viton gasket and knife-edge seals on chamber opening • maintain high vacuum capability with re-usable seal	**G**
Source and Substrate Features	
Ceramic crucible and wire basket sources • uniform material heating and increased component lifetime	**B, F**
Tungsten-boat sources • high-temperature capability for metal evaporation	**C**
Feedthroughs, cables and power supplies selection • rated to match source specifications to ensure full heating capacity	**-**
Control and Monitoring Features	
QCM at fixed position near substrate • appropriate and consistent deposition monitoring via Q-pod	**B, C, F**
Temperature measurement via k-type thermocouples • additional process monitoring of substrate and sources available	**F**
LabVIEW programme for monitoring and control • source power control for consistent ramping procedure • rate, thickness, current, pressure and temperature recording	**F**

Table 2-4: The general features of the deposition system, the research requirements each one satisfies are indicated.

Whilst building the system, and indeed conducting different types of experiments, various aspects of the design were modified as needed. The individual substrate size was reduced, enabling the total number of substrates per batch to be increased from 4 to 9. When fully organic PV studies began, the crucible thermocouples were removed, and the port was used for crucible sources instead. The deep crucible source was found to have an excessive throw distance; requiring substantially more material evaporation to produce a given film thickness. This was problematic for aluminium (Al) evaporation, as an oxide crust grew to cover the crucible

opening before the desired film thickness was deposited. Therefore, the deep crucible source was not used in experiments, despite its favourable central alignment with respect to the substrates. Instead, an additional tungsten-boat source was added at the standard source height, with as favourable a substrate alignment as possible. Additionally, whilst proportional-integral-derivative (PID) rate control functionality was available it was not utilised, due to run-to-run variations in evaporation characteristics which required human decisions in the feedback cycle. Finally, the roughing pump was upgraded from a rotary to a scroll model, this was beneficial for pump-down times and contamination levels.

The deposition system was known colloquially as ‘The HOF’. This was in part for the bulky build it shares with actor David Hasselhoff, but primarily in recognition of the truth in Prof Douglas Hofstadter’s self-referential maxim [190]:

Hofstadter's Law: It always takes longer than you expect, even when you take into account Hofstadter's Law.

2.2 Fabrication Procedures

Sample fabrication always begins with substrate preparation. ITO coated glass (Präzisions Glas & Optik or Delta Technologies) was patterned by etching in a hydrochloric and nitric acid solution. Alternatively, glass microscope slides (Fisher Scientific) were used as-received. The substrates were ultrasonically cleaned at 50 °C successively in: deionised water and detergent, deionised water, acetone, and isopropanol. This was followed by a 10-minute oxygen plasma treatment to remove organic contaminants.

Over-layers were then deposited by vacuum thermal evaporation (custom system), and sometimes spin-coating (Ossila), to complete the sample architecture (Figure 2-6). The

experimental sections of the individual chapters describe the specific materials and parameters used to construct the devices in each case.

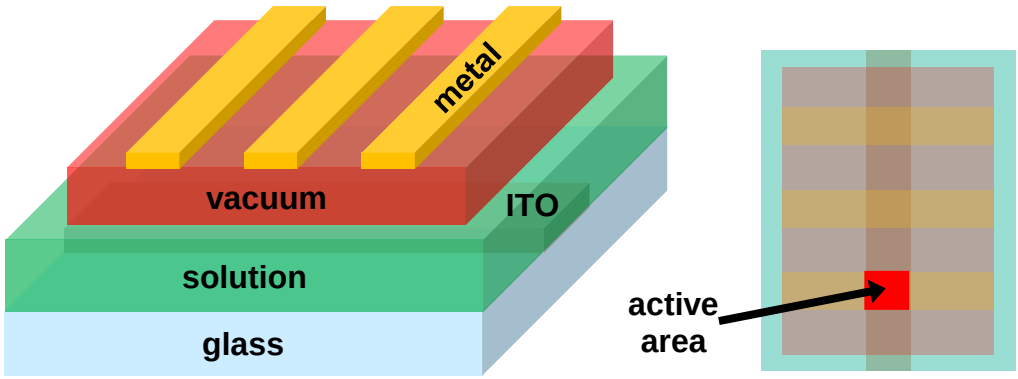


Figure 2-6: A schematic diagram of the device geometry showing the structure of the: substrate, solution or vacuum processed over-layers and metal top contact. Each sample contains three pixels for electrical testing, the active area of one is highlighted in the figure.

Vacuum thermal evaporation of all layers was conducted at a base pressure of 10^{-6} Torr and the full device stack was deposited without breaking vacuum. A QCM and Q-pod (Inficon) were used to track the deposition rate and nominal thickness. The deposition flux reaching the substrates was controlled by an adjacent mechanical shutter with multiple geometries, enabling various substrate exposure configurations. The top electrode was patterned via shadow masking, so the overlap between the metal and the ITO defined the device active area, called a pixel.

2.3 Characterisation Methods

The general experimental set-ups and operation principles of the techniques used to characterise samples are outlined below. The experimental sections of the individual chapters detail any specific testing parameters used in addition to those laid out below.

• UV-VIS-NIR Spectroscopy

Absorption spectroscopy measures the optical transmission of a sample across a wide wavelength range: from the UV to the near-IR. For thin films and composite layers, absorption measurements were conducted on an Agilent Cary 5000 Series UV-VIS-NIR spectrophotometer. Baselines were set for 100% transmission (no sample) and 0% transmission (blackout card) and the transmission was calculated with respect to a reference sample of the pristine substrate. The layer absorption could then be conventionally calculated using Beer's law:

$$Absorbance\ (a.u.) = -log[\ Transmittance\ ] \qquad \text{Equation 2-1}$$

• Reflectance Spectroscopy

An integrating sphere measures the reflectivity of samples with respect to optical standards, which are assumed to give 100% reflection characteristics. The absorption of full PV devices was measured using an Ocean Optics ISP-REF Integrating Sphere and an Ocean Optics USB2000 spectrometer. In addition to the metallic electrode, a mirror reflectance standard was used as a backing behind the sample to ensure no transmission occurred. Therefore, the device absorption could be calculated by subtracting only the reflection [191]:

$$Absorption\ (\%) = 100 - Reflection\ (\%) \qquad \text{Equation 2-2}$$

$$\text{assuming: } Transmission\ (\%) = 0$$

• Photoluminescence (PL) Spectroscopy

PL testing gives information about the radiative recombination processes occurring. The sample is excited by an external light source and the subsequent band to band optical transitions are

measured as the emitted photoluminescence. A Thorlabs S3FC405 fibre coupled laser source provided photoexcitation of Alq3 at a wavelength of 405 nm. The PL of the NP-organic composite sample was then detected using a Thorlabs RP23 probe.

• X-ray Diffractometry (XRD)

The crystal structure of organic materials can be probed using X-ray diffraction measurements. Atomic periodicity increases the diffracted beam intensity at specific scanning angles where the lattice spacing induces constructive interference. A Rigaku MiniFlex X-ray diffractometer was used to characterise Ptn thin films. The intensity peaks were indexed and the corresponding interplanar spacing was calculated, to identify the presence of specific crystalline phases.

• Atomic Force Microscopy (AFM)

AFM is a technique capable of imaging surfaces at a resolution of a few nanometres, with especially high accuracy in the Z-direction. As a cantilever probe scans the surface, the deflection of a laser beam, reflected from the top of the probe, is measured to track the topological features. An Agilent 5400 AFM was used to image the NP-organic composite surface in non-contact tapping mode with an RTESPA-150 probe (Bruker). Image analysis was conducted using Gwyddion software to identify individual NPs and measure their geometries.

• Kelvin Probe Microscopy

Kelvin Probe measurements are conducted by electrically contacting the probe to the sample surface. Any potential difference between the two materials causes a current to flow. An increasing bias is then applied until no current flows between the sample and probe. At this point, the applied bias (V_{sp}) balances the sample-probe potential difference (eV_{sp}), where e is

the elementary charge. The probe Fermi level ($E_{f,\ probe}$) is calibrated against known references samples. Therefore, the absolute Fermi level of the sample can be calculated ($eV_{sp} + E_{f,\ probe}$).

A KP Technology Scanning Kelvin Probe System 2001 was used for Fermi level determination. At each scanning position on the sample, 25 measurements were taken for averaging. A calibration curve of reference samples (Al 4.1 eV and Au 5.1 eV) was used to calculate absolute Fermi level values. All Kelvin probe measurements were conducted by Mr Yujiro Tazawa or Mr Wing Chung Liu, both fellow DPhil students in the research group.

• Current-Voltage Testing

The device IV characteristics were measured under N_2 flowing at 2 to 3 L/min using a Keithley 2400 Source Meter. An ABET Technologies SunLite solar simulator provided 20 to 100 mW/cm^2 AM1.5 solar spectrum illumination through adjustment of the source height. All illumination intensities were calibrated by an ABET Technologies 15151-KG5 Si reference cell.

Under 100 mW/cm^2 illumination, the standard PV characteristics, of *PCE*, *FF*, J_{sc} and V_{oc}, were obtained. IV testing under dark conditions and fitting of semi-log and linear plots was used to derive the operation parameters R_s, R_{sh}, n and J_0. The forward and reverse voltage sweeps were averaged to produce the IV characteristics. The methods used to extract device parameters from IV characteristics are described in the introduction (Section 1.2.2). The variation in photoresponse with illumination intensity was also analysed to probe recombination dynamics. The scaling factor of the relationship between intensity and photocurrent or photovoltage provides the device parameter alpha or beta respectively [192]. These parameters indicate recombination processes operating in the device due to space-charge (alpha) or trapping (beta) effects.

• External Quantum Efficiency (EQE) Testing

EQE measurements provide information at a quantum level about the device optical absorption and carrier extraction capabilities. The number of incident photons is compared to the number of extracted electrons, at a given wavelength. This is achieved by measuring the device photocurrent across multiple wavelengths under known illumination characteristics. The EQE spectrums of PV devices were determined under illumination from a halogen lamp using an Oriel Cornerstone 130 monochromator. The current was detected by a Keithley 6845 picoammeter and testing was carried out under N_2 as before. Calibration of the photon flux was undertaken using a Newport 818 UV enhanced silicon photodetector and a Newport 918 IR germanium photodetector.

• AC Impedance Testing

The AC impedance response of devices was evaluated with an Agilent E4980A option 001 precision LCR meter. A 30 mV AC probe signal was used for all measurements, which were carried out under N_2 as before. Both impedance-frequency and impedance-voltage testing was conducted, at various bias voltages and across a range of frequencies. The impedance-frequency characteristics were measured under illumination to match PV operating conditions. Data analysis was conducted using the EIS Spectrum Analyzer software available from http://www.abc.chemistry.bsu.by/vi/analyser/. The data was fitted with equivalent circuit models (ECMs) composed of resistor elements (R) and constant phase elements (CPE) (non-ideal capacitor elements) representing specific device processes [109]. Changes in the resistance (*R*) or capacitance (*C*) values and their frequency dependence, were used to identify any modifications to device operation. The impedance-voltage characteristics were measured in the dark, to minimise the number of free carriers in the depletion region, allowing Mott-Schottky (M-S) analysis to be undertaken [193]. The applied bias was varied to modify the

depletion region width and so change the capacitance. Values for the apparent built-in voltage (V_{ms}) and apparent dopant density (N_{ms}) could then be extracted from capacitance-voltage plots. The calculations assumed a dielectric constant of 3.

Chapter 3: Organic Charge Transport Layers in Quantum Dot Photovoltaic Devices

3.1 Introduction

The Introduction Chapter outlined the various benefits CTLs can confer on PV device operation. Chapter 3 explores using Ptn HTLs to improve the efficiency of QD PV devices through a variety of operation mechanisms. This introduction begins by outlining the appeal of QD materials for PV applications. It then discusses literature reports of QD PVs with CTLs, in order to elucidate possible mechanisms for performance enhancements. Finally, it explains the phenomenon of s-shaped IV curves, which are commonly encountered when characterising novel PV architectures.

3.1.1 Quantum Dot Photovoltaics

QDs are semiconducting nanocrystals with unique optoelectronic properties induced by quantum confinement effects. To manipulate the optical bandgap and energy level positions, the QD size can be varied up to the Bohr Radius which defines the threshold for exciton confinement (Figure 3-1) [194]. QDs for PVs are composed of metal chalcogenides, such as PbS or CdSe, as their narrow bulk bandgap and large Bohr radius enable wide absorption tuning. Hot-injection synthesis methods enable the nucleation and growth of highly crystalline and monodisperse QDs [195] [196]. Organic ligands are employed as surfactants to produce a colloidal QD suspension. Thin films for device applications are then fabricated via solution processing methods, such as spin-coating [197] [198]. A ligand exchange step is included to incorporate short-chain ligands which improve thin film transport properties [199]

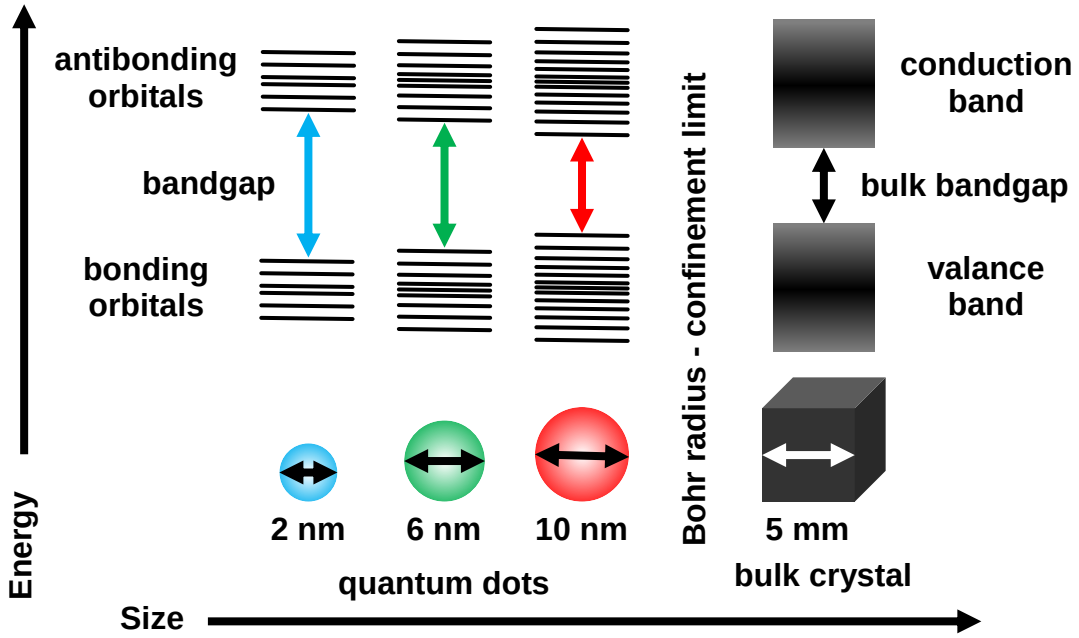


Figure 3-1: The changing electronic structure of QDs: from bulk crystal band structure to nanocrystal quantised energy levels. Adapted from Cox at al. [200].

QD PVs are a promising emerging technology, with certified efficiencies now reaching over 13% [21] [201] [32]. QDs are an appealing photoactive layer material because their optoelectronic properties are tuneable [202] [203]. Additionally, device fabrication is compatible with low-cost mass-manufacturing techniques [204].

PV operation has been improved substantially by device architecture innovations [205]. A depleted HJ architecture was developed to overcome limitations of the QD-metal Schottky junction embodiment [206] [207]. At the front of the device, n-type metal oxides form a depletion region junction with the QD layer, enabling increased photocarrier generation and collection. A similar concept is applied in quantum junction architectures; here QDs are also the n-type material, allowing the energy levels of both layers to be fine-tuned [208].

Device transport improvements have been achieved through using ligands to alter QD interactions and surface chemistry [209]. Halide species can effectively passivate trap states, improving carrier mobilities and air stability [210] [211] [212]. Additionally, different halides

are utilised to induce n- or p-type transport characteristics [213]. Bi-functional organic ligands enable QD crosslinking to reduce inter-dot distances and increase thin film mobilities [214]. Whilst these architecture and processing developments improve carrier generation and transport in QD PVs, device performances are often still limited by inefficient charge collection from the QDs to the electrodes [215].

3.1.2 Utilising Charge Transport Layers

To increase extraction efficiencies, therefore, CTLs are often employed. PV operation can be enhanced by a range of CTL functions; based on electrical, optical and structural effects (Section 1.3.1). This chapter studies the influence of Ptn HTLs on QD PV device performance. A variety of HTL embodiments have been demonstrated in QD devices including: ligand treatments of QD layers [212] and interlayers of transition metal oxides [216] or semiconducting polymers [217]. Studies emphasise materials selection considerations, as appropriate energy level alignment is required to facilitate QD to electrode charge transfer [218].

Given the prevalence of depleted HJ device architectures, ETLs of ZnO and TiO_2 are common in QD PVs. In addition to their role as a HJ material, they also operate as a selective contact which provides preferential electron extraction [219]. To enhance this ETL function, different dopants for TiO_2 have been explored [220]. The band alignment with adjacent QD layers was adjusted using Zr or Sb, to enable efficient barrier-free extraction. Similarly, for ZnO I ions have been used to modify the carrier concentration and band structure [221]. An increased V_{bi} enhanced collection from the QD layer, improving the *PCE* from 10.1 % to a then-record of 10.8 %. These reports emphasise the importance of CTL electronic structure for effective integration in QD PVs. In addition to ETLs, HTLs are also important to achieve balanced extraction in high-performance devices [221].

Advances in QD energy level control have led to EDT (ethanedithiol) ligands being used to create p-type QD based HTLs. Band alignment engineering is used to facilitate hole extraction whilst blocking electron transport, forming a selective contact [212]. This approach has increased *PCE*s from 6.0 % to 8.3 % with impressive long-term unencapsulated air stability. HTLs of PbS-EDT are now used routinely for state-of-the-art QD PVs, achieving certified efficiencies over 10 % [222]. MoO_3 is an alternative HTL material, which gives ohmic contact to QD thin films. At the QD interface, dipole formation gives favourable band bending for hole extraction into MoO_3 [223]. The presence of bandgap states can then enhance hole transport to the electrode. MoO_3 HTLs can also inhibit energy barrier formation at the QD-metal anode interface [224]. The deep MoO_3 Fermi level shifts the electrode WF, providing improved hole extraction to various different anode materials.

Organic thin films are also employed as effective HTLs in QD PVs. Polymer HTLs primarily function as a selective contact, therefore, energy level alignment is critical to avoid transport barriers [218]. This hole selectivity has been shown to reduce recombination at the metal electrode, leading to *PCE* increases from 4.2 % to 5.1 %. Hole extraction increases may also stem from the creation of an additional depletion region at the QD-organic interface. In addition to the selective contact role, organics may be an exciton generation layer which increases device absorption [217]. Polymer HTLs have been shown to contribute additional photocarriers, provided they have suitable energy levels compared to the QD active layer.

Recently, a poly(3-hexylthiophene-2,5-diyl) (P3HT) HTL was enhanced, using dopants and an O_2 plasma treatment, to achieve a 7.8 % *PCE* with 20 days ambient stability [225]. The device performance and stability were superior with P3HT compared to a MoO_3 HTL. A hybrid organic-inorganic HTL has demonstrated improved performance over individual PEDOT:PSS

or MoO_3 layers [226]. The PEDOT:PSS contributed an appropriate Fermi level for hole extraction and improved the active layer coverage to reduce leakage currents. Additionally, the conduction band of the MoO_3 effectively blocked electrons to reduce recombination.

P3HT has been shown by Neo et al. to be an effective HTL enhancing collection from PbS QDs [227]. Improvements to carrier transport, energy level alignment and morphology were demonstrated. Here Ptn is proposed as an alternative to P3HT due to its analogous and advantageous properties (Figure 3-2). Ptn has similar energy levels to P3HT [228], which should facilitate favourable interface energetics, and has a higher hole mobility [229], which should improve carrier collection. Additionally, as a vacuum-processable material, Ptn is deposited under dry conditions, removing the need to consider solvent interactions with the underlying solution processed QD layers [230].

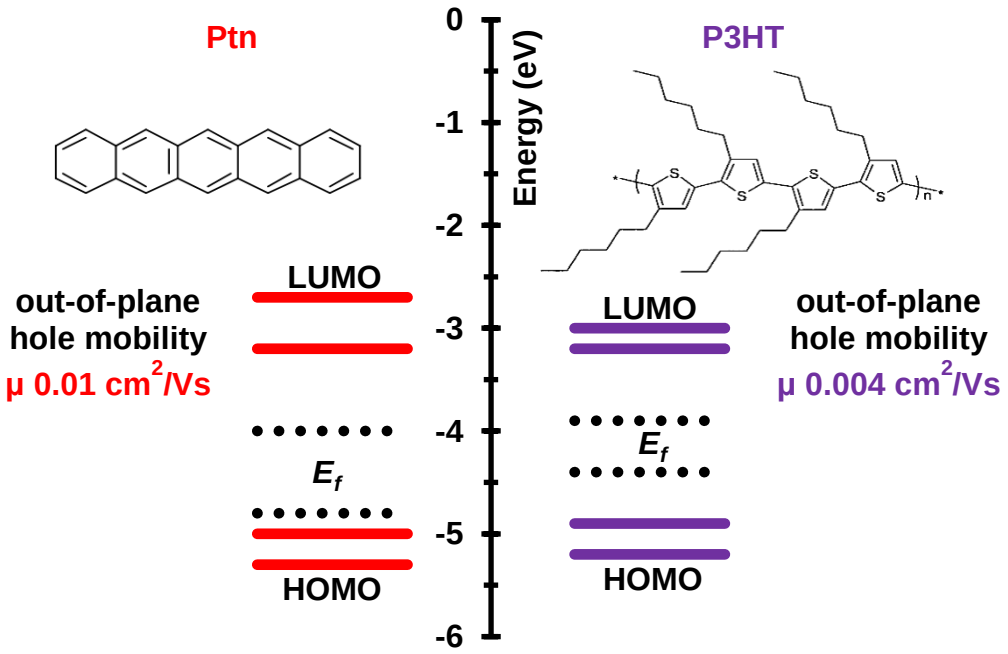


Figure 3-2: A comparison of the structure and properties of organic HTL materials Ptn (left) [231] and P3HT (right) [232]. The energy level schematic shows upper and lower bounds to reflect the range of values reported in the literature.

3.1.3 S-Shaped IV Curves

Adding CTLs sometimes degrades device performance, due to modified energetic or transport properties. S-shaped IV curves are frequently reported for novel PV architectures [233] [234] [235]. This feature is described as a reverse diode because space-charge limits act in opposition to the primary HJ diode [236] [237] [238]. Various mechanisms cause these extraction limits: from imbalanced mobilities [238] and poorly conducting layers [239] [240], to unfavourable band bending at electrodes [237] and energy level offsets to extraction layers [241].

In PV devices, energy barriers or transport restrictions cause generated photocarriers to accumulate locally creating a space-charge [238] [240] [236]. The resulting electric field sets up a counter voltage which blocks carrier extraction [238] [81]. This produces S-shaped IV curves as the space-charge modifies the device's net field which reduces the photocurrent (Figure 3-3) [81] [236]. Space-charge effects cause a small net field below V_{oc}, which limits extraction resulting in low photocurrents. The applied bias can eventually overcome the space-charge field, lifting the extraction limits to give larger photocurrents at more negative voltages.

S-shaped IV curves indicate that specific energetic properties or transport processes are restricting device operation and causing resultant extraction limits. Energetic barriers, due to unfavourable energy level offsets [241] or band bending [237], cause a space-charge accumulation adjacent to the interface. Transport restrictions, due to low mobilities [238] or thick layers [239], cause a similar space-charge accumulation within the limiting layer. Reports explicitly demonstrate transport-induced s-shaped IV curves for devices without any energetic barriers [238] [239].

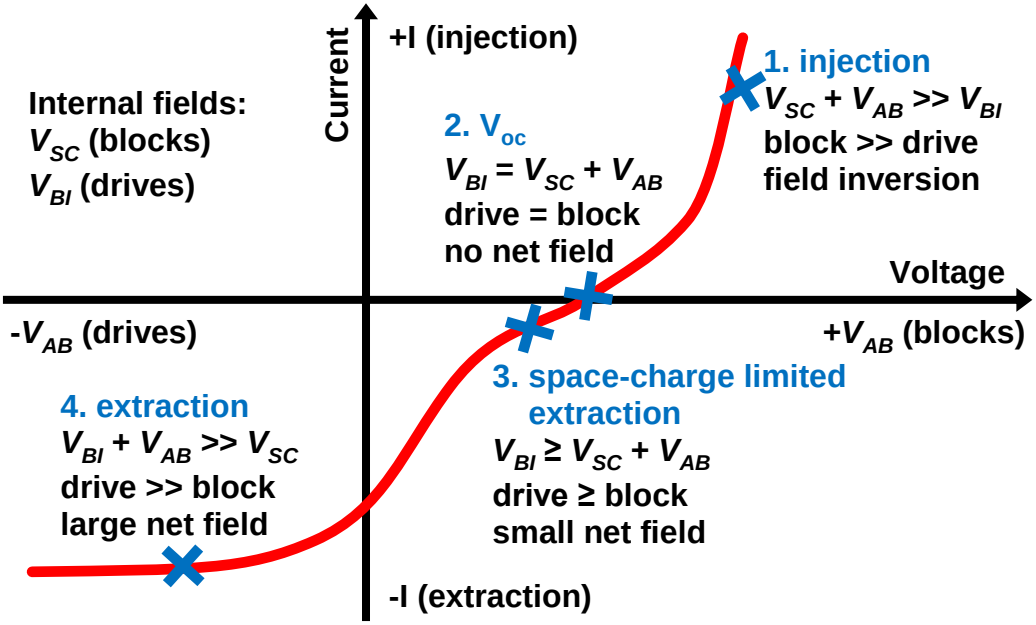


Figure 3-3: An s-shaped IV curve showing the net field components (built-in voltage (V_{BI}), space-charge field (V_{SC}) and applied bias (V_{AB})) and the resulting photocurrent characteristics at specific external biases.

3.1.4 Approach

In this chapter, Ptn is employed as a HTL to enhance QD PV device performance. Thermal evaporation parameters are controlled to produce Ptn layers with the thin film phase crystal structure. The importance of energy level alignment to achieving the maximum PV performance is illustrated. To optimise interface energetics between Ptn and QD layers, atmospheric and photonic treatments are explored. Device characterisation is undertaken to elucidate two key mechanisms modifying the PV operation process. Firstly, the Ptn acts as an electron blocking layer, minimising rear contact recombination. Secondly, the Ptn acts as a hole extracting layer, balancing carrier collection.

3.2 Experimental

The Equipment and Methods chapter (Section 2.2) describes fabrication procedures common to all embodiments. For this chapter, the synthesis and processing of the ZnO and QD materials was conducted by Dr Nanlin Zhang, a member of the research group. ZnO nanocrystals and 1.3

eV PbS QDs with a solution-phase ligand exchange to MAI (methylammonium iodide) were synthesised following the method of Neo et al. [227]. The ZnO was deposited by spin-coating at 2000 rpm for 20 seconds, followed by annealing in air for 10 minutes at 100 °C. The PbS QDs were then spin-coated at 2000 rpm for 60 seconds. Device fabrication was completed using a deposition system designed and built for this research project (Section 2.1.2). The deposition sequence was: Ptn 0 to 100 nm at 0.4 Å/sec (99.9% sublimed, Sigma-Aldrich); Au 50 nm at 0.1 Å/sec for the first 10 nm and thereafter at 0.4 Å/sec (99.99%, Testbourne).

The Equipment and Methods chapter (Section 2.3) also describes all characterisation methods used. The QD PV device active area is 0.0128 cm^2 and silver conductive paint (RS) was applied to the Au electrode area contacting the electrical testing pins. Throughout the chapter, error values represent the standard deviation from 6 pixels across 2 substrates. An exception is the 50, 75, 100 nm Ptn thickness study, where the error values represent the standard deviation across 3 pixels on each substrate. The thin film absorption was determined from UV-VIS-NIR transmission measurements. For X-ray diffraction (XRD) analysis, the interplanar spacing was calculated as the average of all indexed peaks. For IV characterisation, the voltage was swept between -0.4 V and +1 V with a step size of 0.023 V and delay time of 100 ms. For Kelvin Probe analysis, 25 measurements were taken at each of 6 different scanning positions across 2 substrates.

3.3 Device Architecture

3.3.1 Pentacene Deposition

Ptn is ubiquitous in the field of organic electronics and is deployed in a multitude of devices, from transistors [242] to PVs [243]. Device performance depends critically on the Ptn crystal structure, which determines the electrical and optical properties exhibited [244]. Ptn layers are

fabricated by vacuum thermal evaporation, which is controlled to produce well-ordered films with good charge transport properties [245].

Various processing conditions determine the resulting Ptn crystal structure (Figure 3-4). For device applications, the preferred crystal structure is the thin film phase produced by single-phase layered growth [245]. To avoid bulk phase formation, the film is kept below a critical thickness which varies with temperature [246]. Additionally, the substrate material's chemical reactivity and surface roughness influences both the molecular orientation and film morphology [245]. Ptn can grow on QD substrates with a well-defined planar interface and grain size influenced by the capping ligand [247].

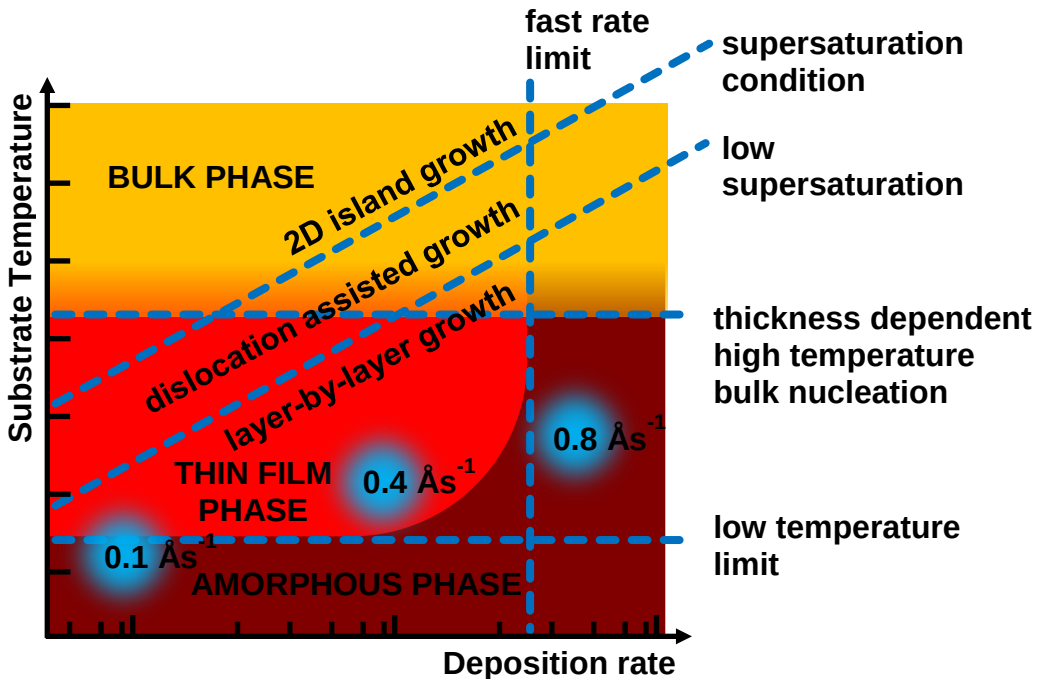


Figure 3-4: A schematic phase diagram for Ptn layer deposition, showing the influence of processing conditions on crystal structure and growth mode. Adapted from Ruiz et al. [245]. The approximate regions likely to be associated with each sample tested below are indicated as diffuse blue circles labelled with the deposition rate.

Investigations were undertaken to determine the processing conditions suitable for device fabrication. Ptn layers 50 nm thick were deposited at rates of 0.1, 0.4 and 0.8 Ås^{-1}. Whilst for these specific depositions the substrate temperature was not measured, it was measured for

subsequent similar depositions and the maximum recorded temperature was 55 °C. Given the 50 nm layer thickness, this should prevent bulk phase nucleation occurring [246]. The measured evaporation source temperatures were 198, 208 and 219 °C for the 0.1, 0.4 and 0.8 $Å s^{-1}$ depositions respectively. Additionally, the samples were fabricated in sequence with the lowest rate first and the highest rate last. In combination, these conditions could have caused the substrate temperature to increase for the higher deposition rate samples.

The XRD spectra reveal the resulting Ptn crystal structure differences (Figure 3-5). A 0.4 $Å s^{-1}$ deposition rate produces multiple crystalline peaks, with a d_{001} interplanar spacing of 1.53 ± 0.01 nm. This demonstrates thin film phase formation (d_{001} of 1.54 nm) and the absence of any bulk phase growth (d_{001} of 1.45 nm) [245]. Deposition rates of 0.1 and 0.8 $Å s^{-1}$ show small or no crystalline peaks, suggesting amorphous growth dominates. The approximate phase diagram regions likely to be associated with each sample are indicated above (Figure 3-4). The absorption spectrum (Figure 3-6) exhibits the expected optical bandgap at 1.86 eV, alongside symmetric ring-stretching vibrational mode peaks at shorter wavelengths [248]. Therefore, deposition conditions have been identified to produce Ptn layers with appropriate electrical and optical properties for use in QD PVs.

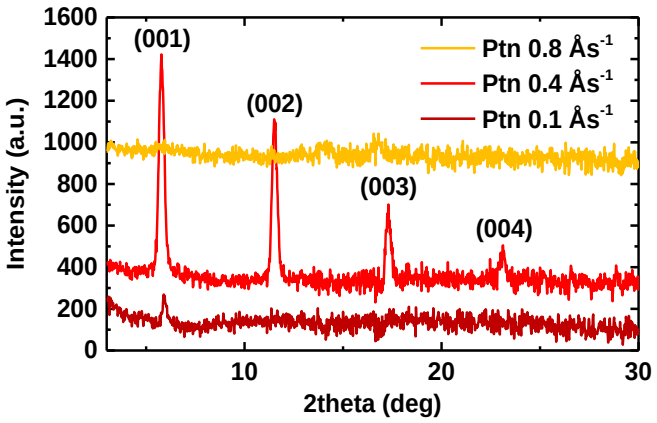


Figure 3-5: The XRD spectra of Ptn layers, evaporated at different deposition rates, with an approximately equal thickness of 50 nm. The traces are offset for clarity and the thin film phase crystalline peaks are indexed.

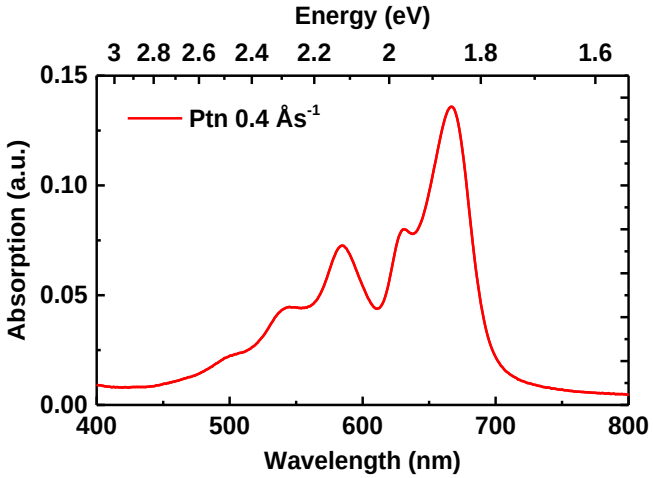


Figure 3-6: The Ptn layer absorption spectrum, displaying the characteristic optical bandgap and higher energy vibronic progression peaks.

3.3.2 Quantum Dot Device

The QD devices in this chapter (Figure 3-7), are based on a PbS-MAI absorber layer which forms a Schottky junction with the ZnO ETL. An inverted architecture is employed to improve the device stability and photocarrier extraction efficiency [146] [249]. Devices were fabricated with (Ptn-QD) and without (QD-only) a 50 nm Ptn layer evaporated at 0.4 $Ås^{-1}$. Ptn has appropriate energy level positions and a high out-of-plane mobility, to enable hole collection from the QD layer and transport to the anode for extraction [231] [250].

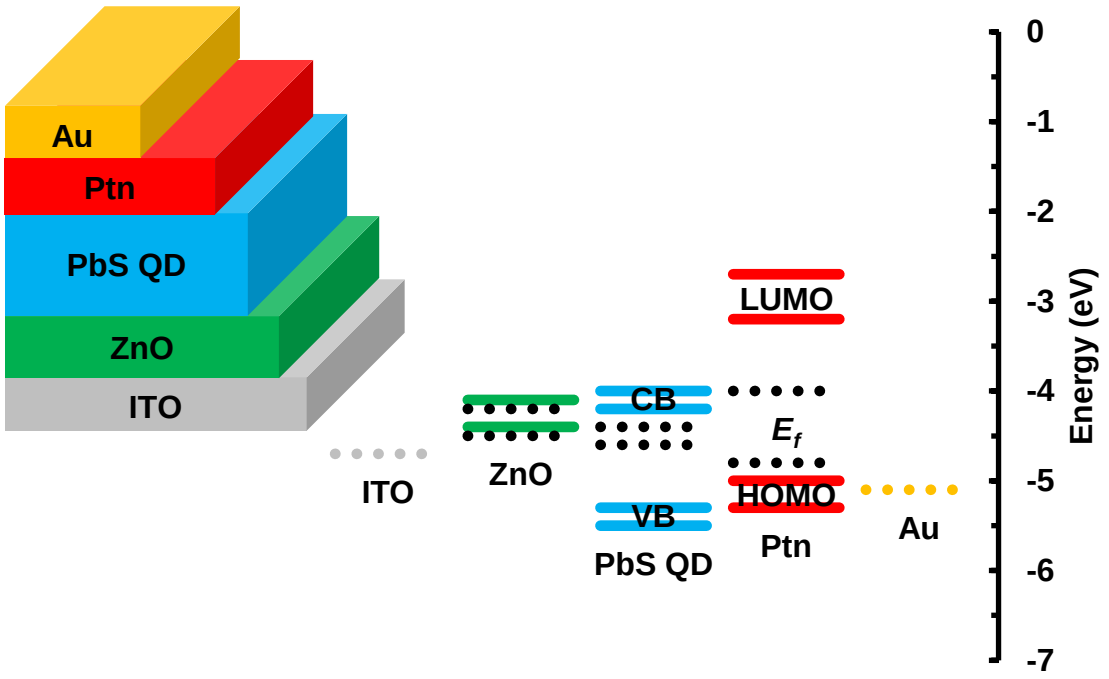


Figure 3-7: A schematic of the device architecture (left) and the energy level positions under vacuum level alignment (right), where an upper and lower bound are shown for the conduction band (CB), valence band (VB), HOMO, LUMO and Fermi level (E_f) to reflect the range of values reported in the literature.

3.4 Electron Blocking Role

Testing the devices immediately after fabrication (day 0) reveals substantially different PV parameters (Table 3-1). The QD-only device exhibits a standard rectifying IV curve (Figure 3-8), indicating that PV operation processes function effectively in the control device structure. The overall performance of the Ptn-QD device, however, is limited by an s-shape in the IV curve (Figure 3-8), which is discussed subsequently (Section 3.5). This feature significantly restricts the fourth quadrant photoresponse, causing a *FF* of 0.22 which indicates a low carrier collection efficiency [81].

day 0	***PCE* (%)**	**J_{sc} (mA/cm^2)**	**V_{oc} (V)**	***FF***	**J_0 (mA/cm^2)**
QD-only	2.4 ± 0.8	9.4 ± 0.3	0.46 ± 0.04	0.55 ± 0.15	$7.5 \times 10^{-3} \pm 5.6 \times 10^{-3}$
Ptn-QD	1.4 ± 0.1	12.8 ± 0.3	0.50 ± 0.01	0.22 ± 0.02	$1.5 \times 10^{-5} \pm 0.2 \times 10^{-5}$

Table 3-1: The average PV parameters from IV testing of devices without (QD-only) or with (Ptn-QD) a Ptn HTL.

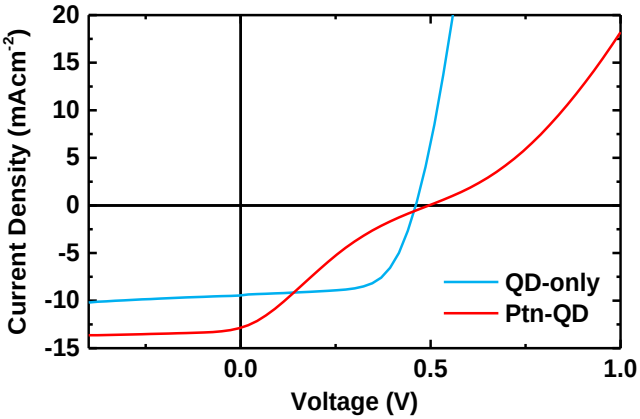


Figure 3-8: Representative IV curves of devices without (QD-only) or with (Ptn-QD) a Ptn HTL. The device structure is ITO-ZnO-QD-(Ptn)-Au.

The Ptn-QD device does, however, present considerable J_{sc} increases alongside slight improvements to the V_{oc} value. This suggests incorporating a Ptn HTL can increase the number of carriers extracted by the electrodes, despite collection limitations existing in the device. Dark IV measurements (Figure 3-9) reveal the recombination related parameter J_0 is reduced by more than two orders of magnitude for Ptn-QD devices (Table 3-1) [86]. This indicates that the HTL is acting to suppress recombination in the device. Thus, the carrier population available for collection is increased, as reflected in the larger J_{sc} measured.

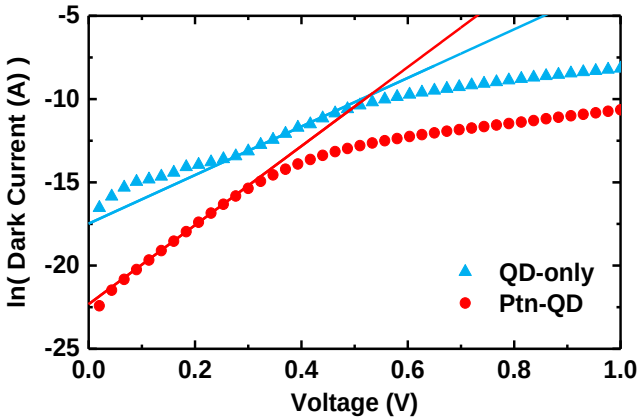


Figure 3-9: Representative dark IV data of devices without (QD-only) or with (Ptn-QD) a Ptn HTL. Linear fits used to extract J_0 are shown.

A possible mechanism for this process is the Ptn layer performing an electron blocking role (Figure 3-10) [251]. Without Ptn, electrons generated in the QD layer may diffuse towards the anode and recombine with holes present there [252]. With Ptn, the shallow Ptn LUMO compared to the QD conduction band creates an energy barrier [213] [247]. This restricts electron transport to the anode and so suppresses the recombination pathway enabling increased hole extraction [252]. These results therefore suggest that the Ptn acts as an electron blocking layer minimizing rear contact recombination.

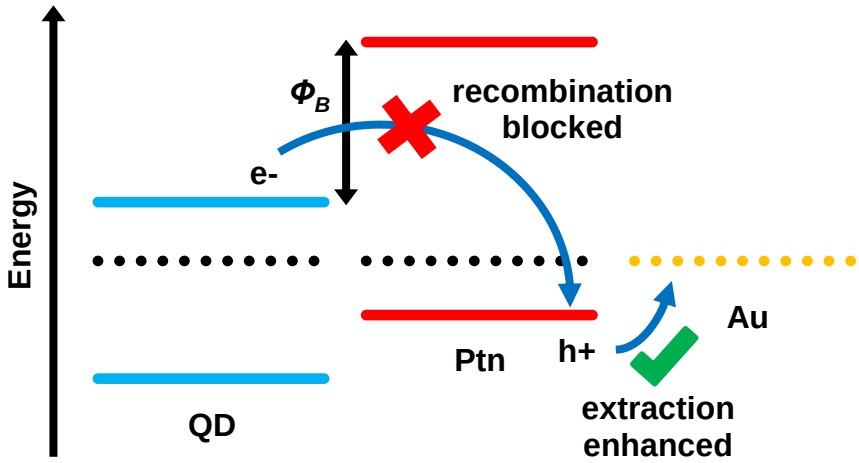


Figure 3-10: An energy level schematic illustrating the electron blocking performance enhancement mechanism in Ptn-QD devices, where the electron energy barrier (Φ_B) at the Ptn HTL prevents recombination.

3.5 Energy Level Alignment

3.5.1 IV Curve Characteristics

The s-shaped IV curves of Ptn-QD devices immediately after fabrication indicate that extraction limits are causing a space-charge accumulation [81], as discussed previously (Section 3.1.3). This could be due to the additional Ptn layer restricting carrier transport [238] or causing an unfavourable energy level alignment [241], as will be explored subsequently. After several days' storage under dark ambient conditions, the IV characteristics of the Ptn-QD devices were measured again. The s-shape was found to be absent and classic PV rectifying characteristics

prevailed instead. This indicates that some aspect of the storage procedure is improving specific energy or transport related PV operation processes [81].

Organic materials undergo physiochemical interactions with the ambient environment, causing alterations to their energetic structure and carrier dynamics [42] [43]. These property modifications often negatively affect PV performances, so devices are generally kept under inert atmospheres [44]. In the present case, however, improvements are achieved with ambient atmospheric exposure. Further investigations were therefore undertaken to understand and control the mechanisms modifying PV operation processes to improve performance.

3.5.2 Atmospheric Treatments

To determine the cause of the s-shaped IV curve elimination, a comparison was made between Ptn-QD devices treated with either ambient air (Ptn-Air) or N_2 (Ptn-N2). Devices were kept in the dark during the treatment process and oxygen-free dry N_2 (99.998% minimum N_2, BOC) was used at slightly above atmospheric pressure. After 24 hours, the ambient air treatment produces markedly higher performing devices than the N_2 treatment process.

The difference in *PCE* primarily stems from the *FF* values (Table 3-2), which for Ptn-N2 devices are still restricted by space-charge effects [81]. The evolution of the Ptn-Air IV curves clearly shows the origin of the performance improvement (Figure 3-11). The s-shape decreases with longer treatment times and eventually the characteristic PV rectifying shape is achieved. The s-shape strength can be quantified by the open circuit resistance (R_{oc}), which is the reciprocal of the IV curve gradient at the s-shape inflection point. Comparing the R_{oc} values for Ptn-N2 and Ptn-Air devices (Table 3-2) demonstrates the significant reduction in s-shape strength conferred by the air treatment process.

24 hr	*PCE* (%)	J_{sc} (mA/cm^2)	V_{oc} (V)	*FF*	R_{oc} (ohm/cm^2)
Ptn-N2	2.1 ± 0.2	14.0 ± 0.5	0.49 ± 0.01	0.30 ± 0.02	101 ± 30
Ptn-Air	2.9 ± 0.4	12.9 ± 0.9	0.50 ± 0.01	0.45 ± 0.08	20 ± 7

Table 3-2: The average PV parameters from IV testing of devices with a Ptn HTL after 24 hours of treatment with either N_2 (Ptn-N2) or ambient air (Ptn-Air).

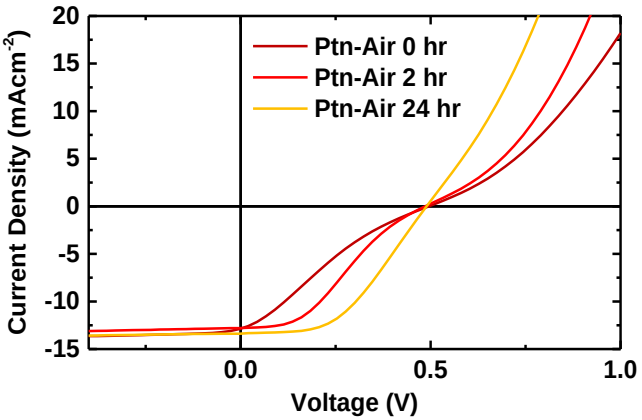


Figure 3-11: Representative IV curves of devices with a Ptn HTL after 0, 2 or 24 hours of treatment with ambient air.

Kelvin probe measurements taken over the same 24 hour period (Figure 3-12), reveal changes in the energetic properties of the Ptn layer. Ptn is known to oxidise under ambient conditions, which causes p-type doping and an associated deepening of the Fermi level [253]. The Ptn Fermi level changes by nearly 0.1 eV, moving progressively deeper with longer treatment times indicating an oxidative p-doping process. The QD Fermi level, however, remains approximately constant over the duration of the air treatment. The Fermi level of the Ptn therefore approaches that of the QD, to a point where they are within measurement error of each other. This alignment may reduce energy barrier formation and so improve interface charge transport [254] [255].

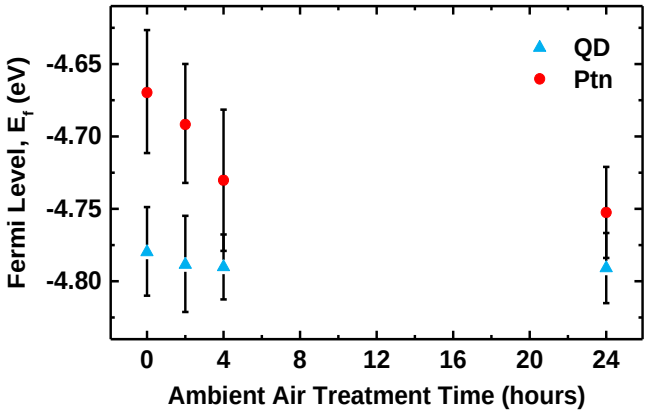


Figure 3-12: The average Fermi level positions of Ptn and QD layers in devices treated with ambient air.

The PV operation processes may be improving through an energy level alignment mechanism, given that s-shaped IV curve elimination is measured alongside coincident Fermi level values. Schottky-Mott interface formation theory can be used to predict energetic alignments based on relative Fermi level positions (Section 1.2.1) [237] [67] [68]. Before oxidation (Figure 3-13), a Ptn Fermi level shallower than the QD Fermi level would form a Schottky barrier at the interface. This hinders hole extraction from the Ptn layer, causing holes instead to accumulate at the interface. A space-charge field opposing carrier collection is therefore produced, resulting in s-shaped IV curves as explained previously (Section 3.1.3). After oxidation (Figure 3-14), a Ptn Fermi level the same or deeper than the QD Fermi level would form an Ohmic junction. Holes can be extracted to the anode unimpeded by energetic barriers, therefore no space-charge field is created as holes do not accumulate.

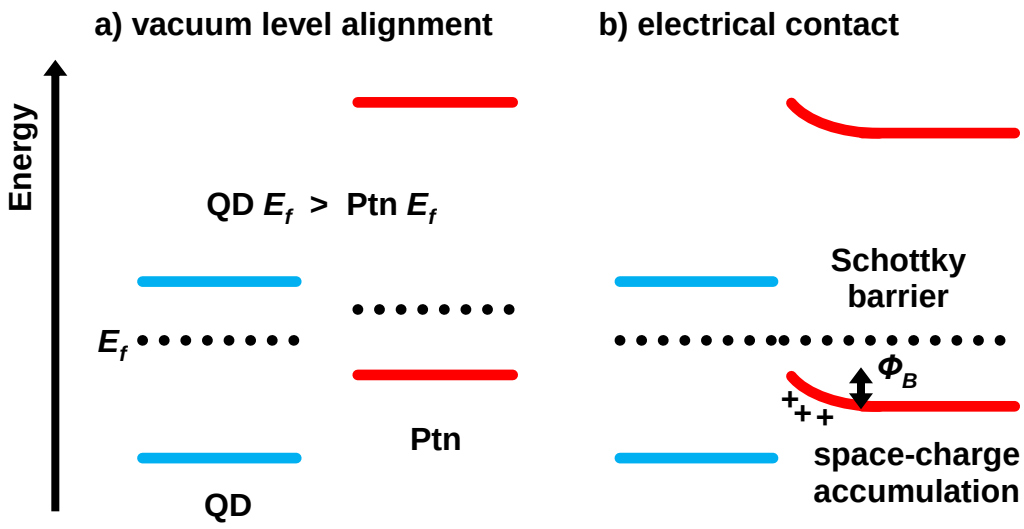


Figure 3-13: An energy level schematic illustrating the mechanism of Schottky barrier (Φ_B) formation and space-charge accumulation at the QD-Ptn interface before oxidation.

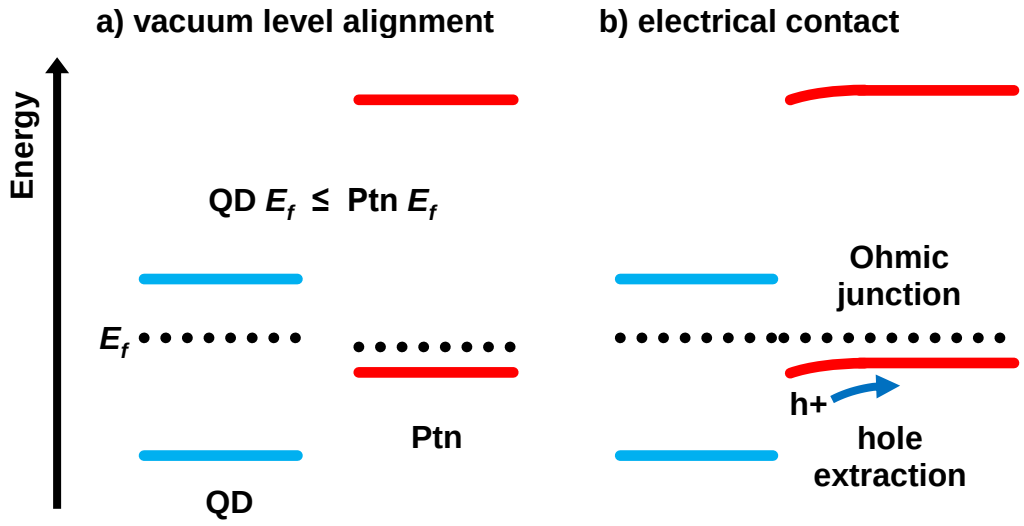


Figure 3-14: An energy level schematic illustrating the mechanism of ohmic junction formation enabling hole extraction at the QD-Ptn interface after oxidation.

After 24 hours of air treatment, aligned Fermi level values and rectifying IV characteristics are observed. This suggests that a Ptn Fermi level equivalent to that of the QD is already deep enough to prevent barrier formation and a limiting space-charge accumulating [81] [255]. The Ptn-Air device was tested again 4 days after fabrication to determine whether further oxidation effects occur. However, the *PCE* is unaltered and specifically, the *FF* is the same within error between day 1 (0.45 ±0.08) and day 4 (0.47 ± 0.04). No further s-shape changes are observed, as R_{oc} is essentially constant from day 1 (20 ±7) to day 4 (19 ±3), which is supported by the

same Fermi level values being measured on day 4. This test provides evidence that longer air treatments, do not confer additional performance improvements.

The possibility that the barrier limiting extraction could originate from the Ptn-Au interface is now considered. Applying Schottky-Mott interface formation theory, using the Fermi level value measured at 0 hours for Ptn (-4.67 eV), predicts upward band bending in Ptn at the interface, thus enabling hole extraction to Au (-5.1 eV) [256]. After 24 hours of air treatment, the measured Fermi level of Ptn (-4.75 eV) is still shallower than that of Au, so no change in bending direction and associated extraction ability is predicted to occur. Therefore, the energy level alignment between Ptn and Au cannot explain the significant change in IV characteristics observed.

Ultraviolet photoelectron spectroscopy (UPS) studies of interface energetics provide evidence that barrier-free hole collection from Ptn to Au can be expected. The Ptn HOMO is measured to be deeper than the Au WF and upward band bending of the HOMO toward the metal interface is observed [250] [257] [258]. Energy level offsets calculated from transport studies, of single layer Ptn devices with top and bottom Au contacts, corroborate these findings [259]. Additionally, because Au is a non-reactive metal, Fermi level pinning and the associated barriers to extraction are not anticipated [106] [260]. However, depositing Au on Ptn can produce complex interface effects if metal migration into the underlying organic occurs [261], possibly causing a small amount of state creation near the Ptn HOMO [262]. Overall, the Kelvin Probe measurements and literature reports support the hypothesis that the primary barrier modifying extraction occurs at the QD-Ptn interface, although the Ptn-Au interface may contribute some additional collection losses.

In combination with energetic effects, associated carrier transport changes have the potential to influence the s-shaped IV curve elimination mechanism. Literature reports demonstrate that transport processes also contribute to space-charge accumulation effects [238] [239]. In the Ptn-Air devices here, the measured Fermi level changes indicate an energetic modification mechanism occurs. Accompanying transport improvements may make additional contributions though, as p-doping from oxidation also improves the conductivity of Ptn [253].

The R_s of Ptn-Air and Ptn-N2 devices was measured over the course of the treatment process (Figure 3-15), to determine the influence of transport properties on the s-shaped IV curve elimination. From 0 to 4 hours, there is no clear change in R_s, despite reductions in s-shape occurring on this timescale, as observed in improving *FF* and R_{oc} values. After 24 hours, however, the R_s of the Ptn-Air device improves, becoming better than that of the Ptn-N2 device whose R_s remains unchanged. These trends suggest that overall device transport remains limited until the energy barrier is removed. The 24-hour R_s values are congruent with the Ptn-Air device s-shape elimination and the Ptn-N2 device s-shape persistence, suggesting that the concurrent R_s enhancement with air treatment may play a role in reducing the space-charge accumulation. Overall therefore, transport modifications with oxidation may also contribute to reducing space-charge accumulation effects, but corresponding energy level alignment alterations may dominate.

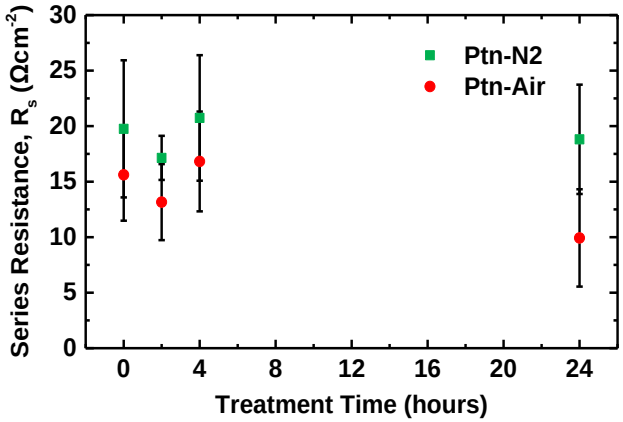


Figure 3-15: The average R_s values of devices with a Ptn HTL treated with either N_2 (Ptn-N2) or ambient air (Ptn-Air).

The results presented in this section therefore suggest that Ptn oxidation primarily causes the alignment of the Ptn and QD Fermi levels, removing an interface barrier and associated space-charge previously hindering hole collection. Performance improvements of a similar nature were observed by Neo et al. in QD devices with a P3HT HTL [227]. Compared to the P3HT layer, the Ptn layer studied here has a shallower initial Fermi level which shifts by a larger amount during the air treatment process. This further demonstrates the capacity of the oxidation mechanism to affect significant electronic structure changes in a variety of organic materials. Correspondingly, the Ptn-QD devices display initial IV curves with much stronger s-shapes than those observed for P3HT devices. The fact that rectifying characteristics are still achieved after only 24 hours of Ptn air treatment, emphasises the ability of the procedure to rapidly eliminate substantial space-charge accumulations. Together, these studies highlight the generality and effectiveness of post-fabrication air treatments to overcome unfavourable energy level alignments and improve device performances.

3.5.3 Photonic Treatments

Having identified the cause of performance improvements, treatments were sought to accelerate and control the energy level alignment transition. UV light exposure is a quick and effective

method of doping Ptn [263] because Ptn is oxidised by reactive singlet-oxygen and ozone species produced at wavelengths below 242 nm [263] [264]. Oxygen physically and chemically incorporates into Ptn thin films, increasing their conductivities [253]. Exposing Ptn-Au contacts to UV irradiation in the presence of oxygen has shown various benefits. Oxidative Ptn doping improves hole conduction [265] and Ptn electronic structure modifications improve energy level alignments, reducing the contact resistance [253].

It was therefore hypothesised that additional UV light treatments could rapidly induce PV performance improvements. A 150 W xenon lamp provided illumination, with an emission spectrum extending to 200 nm. Samples were positioned 30 cm from the lamp with Ptn layers facing the incident beam. Ptn-QD devices were treated in ambient conditions with UV irradiation (Ptn-UV) from the unfiltered lamp beam for 0 to 120 minutes. Samples were otherwise kept under dark ambient conditions.

The post-treatment IV characteristics (Figure 3-16 and Figure 3-17) clearly show high-intensity UV exposure degrades device performance. Just one minute of irradiation reduces the average *PCE* and 120 minutes eliminates any rectifying features, giving very low *PCEs*. This is consistent with observations of oxidation-induced Ptn decomposition occurring rapidly in the first 10 minutes of UV exposure, then continuing more slowly over several hours [264]. In high energy UV environments, oxidation-induced defects can reduce Ptn thin film mobilities [266]. Therefore, the deleterious effects of intense UV irradiation may outweigh any underlying benefits from Ptn oxidation.

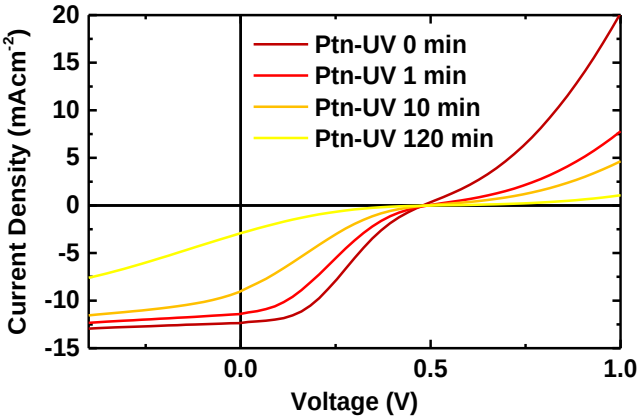


Figure 3-16: Representative IV curves of devices with a Ptn HTL after 0, 1, 10 or 120 minutes of treatment with high-intensity UV irradiation.

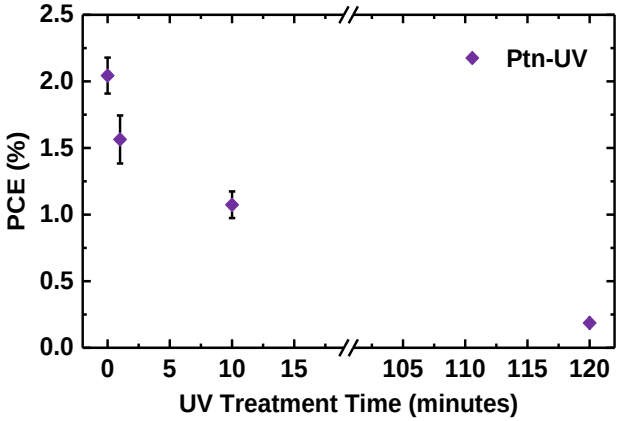


Figure 3-17: The average *PCE* values of devices with a Ptn HTL treated with high-intensity UV irradiation for different durations of time.

Further testing of lower intensity treatments was undertaken to explore whether UV-induced oxidation could improve performances. A neutral-density filter was fitted to reduce transmission across the spectrum to below 0.1 %. In 10 minute increments, the Ptn-QD devices were treated with either UV exposure (Ptn-UV) or dark storage (Ptn-Dark), both under ambient conditions.

Whilst *PCEs* improve with UV exposure (Figure 3-18), no significant differences are observed compared to dark controls. Kelvin Probe measurements confirm comparable oxidation across all samples (Figure 3-19) [253]. Therefore, UV exposure is not accelerating a limiting step in

the oxidation-induced energy level alignment process. Samples may still be equilibrating with the ambient environment where conditions conducive to Ptn oxidation are already present [267] [268]. It is concluded, therefore, that low-intensity UV exposure does not enhance Ptn oxidation to improve PV performance. Photonic treatments were not investigated further, as high UV intensities degrade performance and effective atmospheric treatments have already been demonstrated.

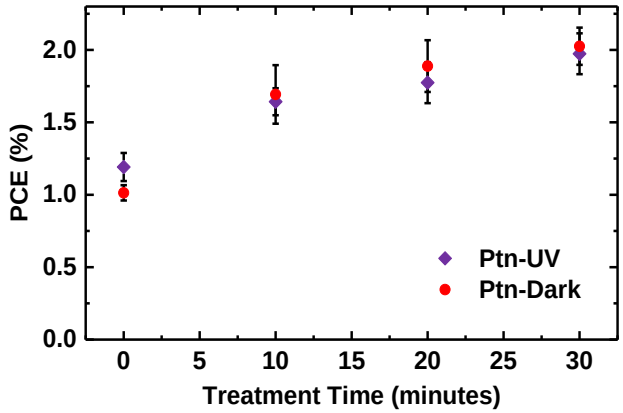


Figure 3-18: The average *PCE* values of devices with a Ptn HTL treated with low-intensity UV irradiation (Ptn-UV) or stored in the dark (Ptn-Dark). (Note that experimental procedures extend atmospheric exposure times to a few hours or more.)

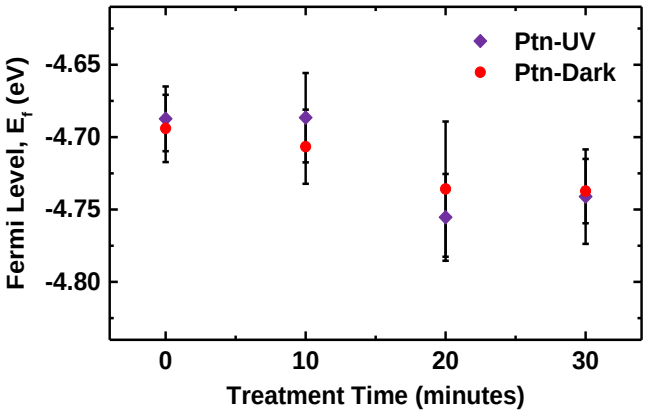


Figure 3-19: The average Fermi level positions of Ptn layers in devices treated with low-intensity UV irradiation (Ptn-UV) or stored in the dark (Ptn-Dark). (Note that experimental procedures extend atmospheric exposure times to a few hours or more.)

3.6 Hole Extracting Role

3.6.1 Pentacene Thickness Effects

The influence of Ptn layer thickness on device *PCE* was investigated, with the intent of optimising performance post energy level alignment. In an analogous device structure, Neo et al. varied the P3HT HTL thickness from 50 to 140 nm [227]. The J_{sc} improved with thickness because the organic over-layer reduced shunt pathways to the rough QD surface. At high thicknesses, however, performances were limited by *FF* degradation due to the increasing series resistance of the HTL. An optimum *PCE* was observed at 105 nm, demonstrating that for QD devices a thick HTL is desirable to form a smooth uniform electrode contact.

Based on this precedent, Ptn layer thicknesses of 50, 75 and 100 nm are tested. The *PCE* is measured on day 1 (Figure 3-20) for performance comparisons after energy level alignment is anticipated to be achieved (Section 3.5.2). Whilst 50 nm of Ptn confers benefits over the 0 nm control device, a 75 nm HTL already causes performance deteriorations. The same hindering transport mechanism found by Neo et al. is observed, however, the effects initiate at a lower HTL thickness. This might suggest that Ptn has a larger resistance than P3HT, although this is unexpected given the high mobility of Ptn [229]. More probable, is that the resistance increases more rapidly with thickness for Ptn than for P3HT [245] [246] [269], as discussed subsequently.

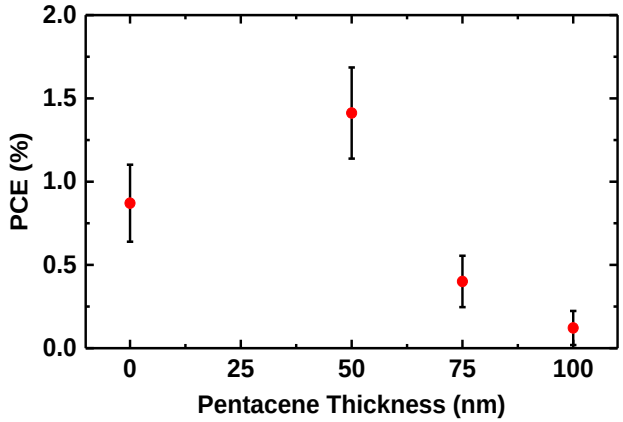


Figure 3-20: The average *PCE* values of devices with various thicknesses of Ptn HTL after one day of ambient air treatment.

Before analysing the Ptn thickness trends of the IV curves measured on day 1 (Figure 3-21), the unexpected s-shape in the 50 nm sample will be discussed. Previous air treatment testing (Section 3.5.2) indicates that 24 hours is sufficient time to produce fully aligned energy levels for 50 nm Ptn-QD devices. However, the 50 nm sample in this batch still displays a slightly s-shaped IV curve on day 1. Despite this s-shape, above 0.4 V the IV curves are similar in shape to the 0 nm controls, indicating a considerable degree of energy level alignment has been achieved. The s-shape persisted when IV measurements were conducted again on day 2. This suggests no further alignment is achieved with extended air treatment, which is consistent with the previous results. The unexpected slight s-shape on day 1 may therefore be due to a persistent energy level misalignment. This effect is anticipated to be relatively small and to be consistent across all Ptn-QD devices. Additionally, the 0 nm control itself displays a worse performance than controls from other sample batches (compare QD-only in Figure 3-21 and Figure 3-23). Poor underlying QD characteristics may therefore also contribute to an increased s-shape for all samples in this batch. Overall, whilst the persistent s-shape may be a small confounding factor for this sample batch, it does not prevent conclusions being drawn about the effect of Ptn thickness on device transport.

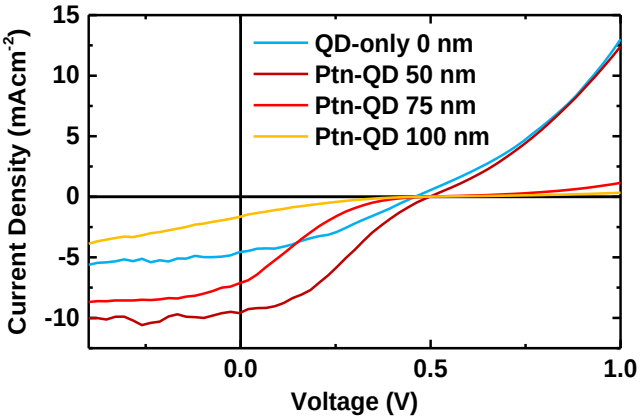


Figure 3-21: Representative IV curves of devices with various thicknesses of Ptn HTL after one day of ambient air treatment.

The IV curves elucidate the origins of the performance differences with Ptn thickness (Figure 3-21). The 75 and 100 nm curves show a persistent s-shape and low currents at high forward biases. Although energy level limitations have predominantly been lifted, transport limits clearly remain and cause strongly s-shaped IV curves. The layer thickness causes inefficient hole extraction, so more hole accumulation produces a larger space-charge giving a stronger s-shape with increasing thickness [239]. For 100 nm devices, the thickness related transport limits are significant, substantially reducing the J_{sc} in addition to the *FF*. The 50 nm curve with reduced s-shape, on the other hand, shows a large current at high forward bias similar to that of the QD-only 0 nm controls. Therefore, 50 nm of Ptn is thin enough to extract holes efficiently and does not impose substantial thickness-induced space-charge effects [239]. As such, once energy alignment limits are lifted, no additional thickness related transport limitations are expected to persist.

The device R_s is strongly affected by the Ptn thickness (Figure 3-22, note log scale), showing the cause of the rapid fourth quadrant photoresponse degradation The non-linear relationship could be due to the thickness dependent crystal structure of Ptn [246]. At higher thicknesses, a bulk phase grows which has worse transport properties than the thin film phase prevalent at lower thicknesses [245]. Substrate temperatures of 55 °C measured during device fabrication

could cause bulk phase nucleation in 75 or 100 nm thick layers [246]. The higher R_s clearly hinders hole extraction, so thinner Ptn layers should be used for better device performance. These results demonstrate the importance of Ptn transport to device operation, so the most efficient 50 nm device is now used to investigate extraction mechanisms further.

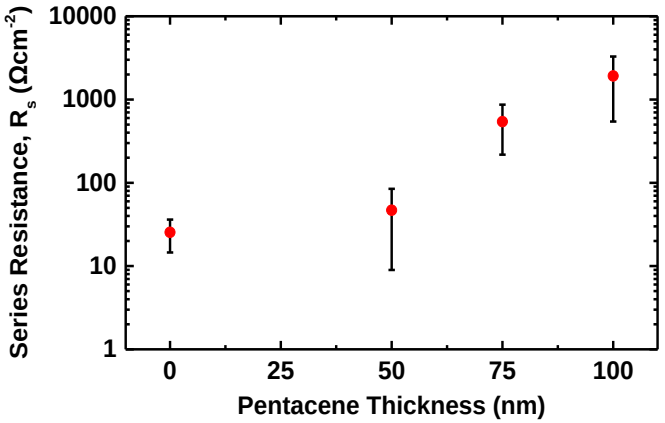


Figure 3-22: The average R_s values of devices with various thicknesses of Ptn HTL after one day of ambient air treatment.

3.6.2 Extraction Mechanisms

After energy level alignment has been achieved, the Ptn-QD device outperforms the QD-only device (Figure 3-23). The J_{sc} and V_{oc} gains (Table 3-3) demonstrate that a 50 nm Ptn layer improves carrier extraction overall. The Ptn electron blocking mechanism is anticipated to still be active, as the difference in J_0 values remains similar to that measured on day 0 (Table 3-3 and Table 3-1).

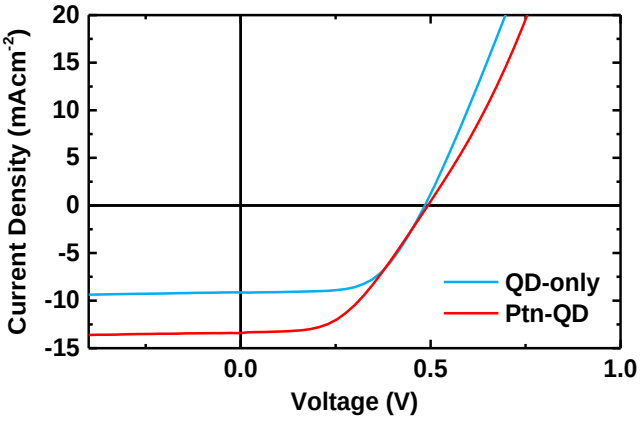


Figure 3-23: Representative IV curves of devices without (QD-only) or with (Ptn-QD) a Ptn HTL after one day of ambient air treatment.

day 1	***PCE*** **(%)**	J_{sc} **(mA/cm^2)**	V_{oc} **(V)**	***FF***	J_0 **(mA/cm^2)**
QD-only	2.4 ± 0.6	9.2 ± 0.5	0.47 ± 0.02	0.55 ± 0.10	$1.3 \times 10^{-3} \pm 0.5 \times 10^{-3}$
Ptn-QD	2.9 ± 0.4	12.9 ± 0.9	0.50 ± 0.01	0.45 ± 0.08	$1.6 \times 10^{-5} \pm 0.4 \times 10^{-5}$

Table 3-3: The average PV parameters from IV testing of devices without (QD-only) or with (Ptn-QD) a Ptn HTL after one day of ambient air treatment.

In parallel, now the energy levels are aligned, the Ptn may also play a role actively extracting holes from the QD to the Au anode. This would be an additional mechanism contributing to the higher J_{sc} and V_{oc} values observed. The R_s is higher for the Ptn-QD device (11 ±7 ohm/cm^2) than the QD-only device (7 ±3 ohm/cm^2). This slightly worse charge transport results in a lower *FF* for the Ptn-QD device. Despite lowering the carrier collection efficiency, the Ptn layer still produces a higher J_{sc}. A specific charge extraction improvement would help to explain these parameter trends. Now the limiting space-charge is gone, carrier collection dynamics can be tested to investigate the Ptn hole extraction hypothesis.

To measure whether charge accumulation in the device is altered, alpha values were calculated from J_{sc}-intensity plots (Figure 3-24). The alpha value nearer to 1 for the Ptn-QD device, indicates that charge extraction is more balanced with the Ptn layer present [270]. The Ptn can mirror the ZnO electron transport role, so Ptn reduces excess hole build-up in the device that

would otherwise lead to space-charge formation and associated recombination [227] [219]. Additionally, the Ptn provides a volume for hole transport without the simultaneous presence of photoelectrons, which should also reduce recombination [109]. The calculated alpha values therefore support the hypothesis that the Ptn layer improves hole extraction which contributes to the increased J_{sc}.

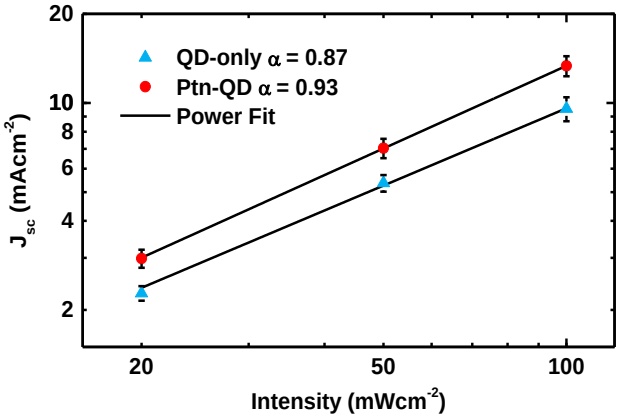


Figure 3-24: J_{sc} values measured at various intensities for devices without (QD-only) or with (Ptn-QD) a Ptn HTL after ambient air treatment. A power law fit is used to extract the space-charge recombination parameter alpha [192].

An additional mechanism improving the electron and hole extraction balance could be better hole extraction from the QD interface layers. Literature reports describe J_{sc} and V_{oc} losses in devices due to Fermi level pinning at the PbS-Au interface [237] [271]. The slightly increased V_{oc} of the Ptn-QD device could suggest that the Ptn layer relieves Fermi level pinning at the QD-Au interface to improve extraction, which would also increase the device J_{sc} [227] [272]. This explanation is supported by higher beta values for the QD-only device indicating more trap-induced recombination (Figure 3-25), possibly in the interface states causing pinning [272] [179].

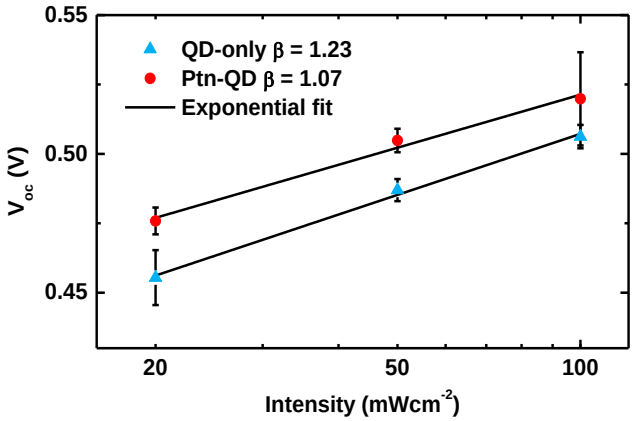


Figure 3-25: V_{oc} values measured at various intensities for devices without (QD-only) or with (Ptn-QD) a Ptn HTL after ambient air treatment. An exponential fit is used to extract the trapping recombination parameter beta [192].

The additional Ptn layer has mixed effects on the underlying QD device. On one hand, the carrier collection efficiency is degraded due to transport through an organic semiconductor. On the other hand, a 50 nm Ptn layer can improve hole extraction from the QD layer. It would be interesting to study whether a thinner Ptn layer could improve device transport, in addition to enhancing extraction. The electron blocking and hole extracting roles probably require a continuous Ptn layer to operate optimally. A smoothing layer function, however, may necessitate a thicker Ptn layer to effectively prevent shunting losses. A balance will need to be struck between conferring these benefits successfully, without R_s increases significantly limiting collection.

3.7 Conclusions

In this chapter, studies were undertaken to understand the effects of a Ptn HTL on QD device performance. PV operation processes were improved by the Ptn layer via two mechanisms and a post-fabrication treatment was employed to achieve energy level alignment in devices.

The Ptn layer deposition conditions were found to be critical in controlling the crystal structure. An appropriate evaporation rate and substrate temperature were identified to produce the thin

film phase desired for device applications. The morphology of the Ptn layer was not investigated but might provide information on any role Ptn plays as a smoothing layer.

The Ptn layer was first observed to play an electron blocking role, emphasising the importance of selective contacts. The energy level offset between the Ptn LUMO and QD conduction band creates a barrier to electron transport. This reduces recombination with holes at the Au anode and so enhances carrier collection. Tests probing carrier lifetime could be used to further elucidate changes in recombination dynamics.

The Ptn-QD device performance was initially significantly limited by s-shaped IV curves. This feature indicates that poor energetic and transport properties are causing carrier accumulation to create a space-charge field hindering extraction. Fermi level measurements suggested a Schottky barrier at the QD-Ptn interface was primarily responsible, highlighting the importance of energy level alignment to effective PV operation.

An atmospheric air treatment was found to be an effective method of alleviating the s-shaped IV curves. Oxidation deepened the Fermi level of the Ptn, aligning it with that of the QD. This removed the space-charge limiting collection, by eliminating the QD-Ptn interface barrier and causing associated transport improvements. Various UV photonic treatments were tested to control the oxidation process, but none were found to be effective and intense irradiation deteriorated device performances. Literature reports indicate UV exposure does accelerate Ptn oxidation, however, so a different range of intensities and durations could be investigated in future. Alternative treatments to modify the QD-Ptn energy level alignment could also be studied, for example, an oxygen plasma treatment or an oxygen purge before anode deposition.

The Ptn layer was subsequently found to perform a hole extracting role, once energy level alignment had been achieved. The Ptn then mirrored the ZnO ETL, balancing hole and electron transport in the device to reduce space-charge recombination. Hole extraction was also improved as the Ptn layer relieved Fermi level pinning previously causing losses at the QD-Au interface. As thicker Ptn layers increased device resistances and strongly degraded PV performance, it was concluded that charge transport is a crucial function of the Ptn HTL. Mobility measurements could give a more detailed understanding of changes in carrier dynamics.

Future studies to optimise device performance could focus on varying the Ptn layer thickness. Thinner layers, below 50 nm, might improve hole transport and enable even higher efficiencies after energy level alignment. It would also be interesting to use EQE measurements to investigate whether the Ptn layer induces any generation changes. In addition to potentially contributing photocarriers through direct Ptn absorption, optical spacer effects could alter the generation profile in the QD active layer.

Chapter 4: Metal Nanoparticles in Organic Charge Transport Layers

4.1 Introduction

Chapter 3 demonstrated that CTL electronic properties can be modified by post-fabrication treatments of the full device structure to improve CTL performance. Chapter 4 seeks to control the CTL properties directly during the fabrication process, through the incorporation of metal NPs. Chapter 5 then employs the composite CTLs in a full PV device to improve efficiencies. This introduction begins by presenting the unique optoelectronic properties of metallic NPs and explaining their fabrication process. It then explores the literature on metal-organic interactions for bulk interfaces and atomic doping embodiments. The purpose is to provide a precedent for NP-CTL interactions which may occur in the composite layer. It subsequently draws lessons from the field of organic non-volatile memory (ONVM), which investigates devices analogous to those tested in this chapter. The aim is to elucidate electrical changes metal NPs may induce and to provide mechanistic frameworks to interpret these modifications.

4.1.1 Metal Nanoparticles

Effects associated with the small size of NPs can cause unique physical and chemical properties, which differ significantly from those observed in bulk materials. Metal NPs exhibit enhanced reactivity due to both geometric and electronic effects [273]. Undercoordinated atoms on the NP surface act as chemically active sites due to ‘dangling bonds’ [274]. The cluster size and shape controls the number of surface atoms and the nature of bonding is determined by the crystallographic structure [275], which itself is size dependent [276]. Nanoclusters of metal atoms are also subject to quantum size effects which govern their electronic band structure. Initially they exhibit insulating behaviour due to the existence of discrete energy levels, which broaden as the particle size increases, eventually becoming continuous and allowing bulk

metallic conduction [277]. The critical cluster size at which this insulator-metal transition occurs varies from metal to metal [278].

Metal NPs also display distinct optical properties. For particles much smaller than the wavelength of incident light, the electromagnetic field is uniformly distributed over the volume. Localised surface plasmon resonance (LSPR) excitations can then be induced by light at a frequency resonant with that of the metal free electrons [279]. The interaction with the electromagnetic field causes the collective oscillation of electrons confined within the NP structure [280]. The particle polarizability, which controls resonance interactions, depends on the geometric size and shape, as well as the permittivity of the metal and surrounding medium [279]. The LSPR causes increased absorption at the plasmonic wavelength and a strong local field enhancement [281], both of which can increase photogeneration [282] [283].

Well-controlled fabrication processes are therefore important to achieve the NP properties desired. Thermally evaporated noble metal films follow the Volmer-Weber growth mechanism, whereby a continuous layer is eventually formed through the growth and coalescence of islands initially nucleated on the substrate (Figure 4-1 a) [284]. At low coverages therefore, discrete NP structures can be realised, where the NP dimensions are controlled by the nominal thickness of metal deposited (Figure 4-1 b) [285] [286] [287]. Low deposition rates are generally used [288], allowing fine nominal thickness control to tune the NP properties [289]. The wetting behaviour of the metal islands is altered by the substrate material [290] [282] and any annealing treatments [291], which provide additional methods to manipulate the NP shape.

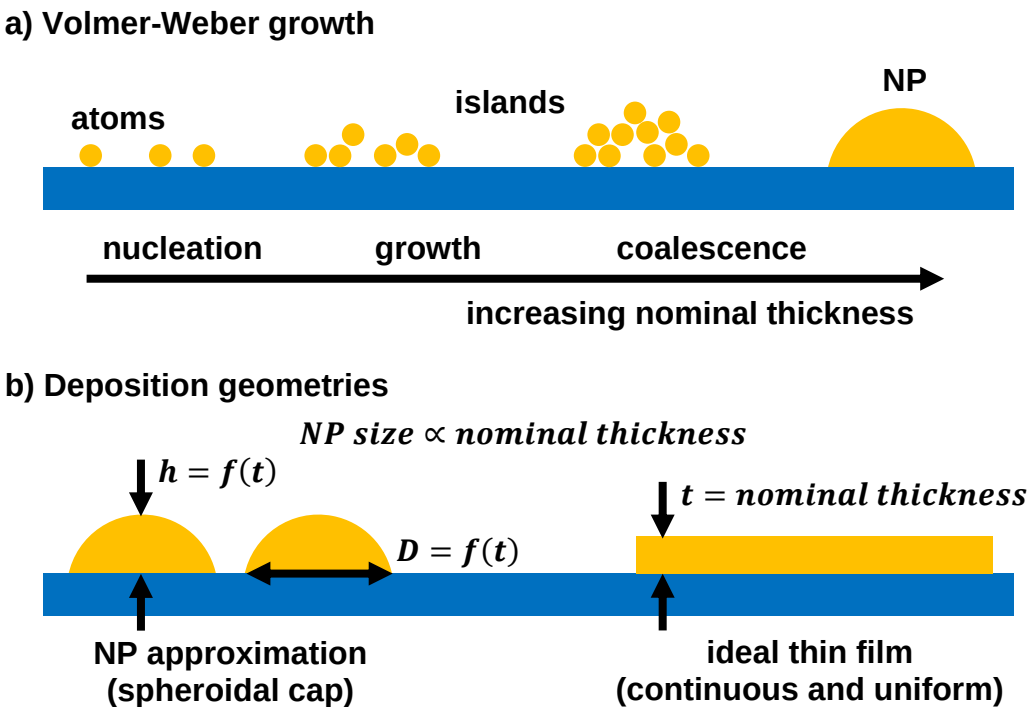


Figure 4-1: An illustrative schematic of a) the formation of NPs by metal thermal evaporation [284] and b) the correspondence of NP and thin film geometries [287].

Alternatively, NP structures can be formed by colloidal chemistry, through a process of precipitation and stabilisation [292]. Composite films can then be produced from mixed solutions with soluble polymers [293]. Whilst solution synthesis enables complex NP geometries to be created more easily [294], thermal evaporation enables more accurate NP location control, through independent deposition with fine thickness control [288].

Metal NPs are employed in the CTL of OPV devices to overcome various performance limitations using the unique characteristics of NPs [115] [113]. PV operation can be enhanced by NPs modifying both the optical [290] [282] and electronic [183] [295] properties of devices, as detailed in the following chapter (Section 5.1.1). Therefore, to realise the full potential of metal NPs in OPVs, it is important to understand the nature of the NP-organic interaction. The theory of NP optics is well developed, with models able to describe both dielectric medium and NP geometry effects [280]. In contrast, a framework with which to interpret NP electrical

effects is less clear [288]. Metal-organic electronic interactions are complex [105] [106], especially when additional NP reactivity effects are considered [184].

4.1.2 Metal-Organic Interactions

Metal-organic interactions are primarily studied in two embodiments: metal-organic interfaces and metal-doped organic layers. Findings from these investigations are now outlined, to introduce phenomena relevant to organic layers with embedded metal NPs.

• Metal-Organic Interfaces

At metal-organic interfaces, interactions create organic gap states and cause charge transfer. The metal wavefunction extends into the organic, shifting and broadening the discrete energy levels to create electronic states in the bandgap [296]. Bandgap states may originate from interactions with either the HOMO or LUMO [105] [296]. Chemical reactions can also occur, producing new organometallic species with altered molecular orbitals, which generates chemistry-induced states in the bandgap [297] [298]. Metal to organic charge transfer takes place and more donation to gap states occurs from shallower WF metals [105] [299] [300].

Metal-organic interfaces are classified as strongly or weakly interacting, depending on the dominance of chemistry effects which increase state generation and charge transfer [74]. Reactive, shallow WF metals include Ca, In, Al, Sn and sometimes Ag [105] [299] [260]. More inert, deeper WF metals include Ag, Au and Cu [105] [299]. Interfaces between Al and Alq3 cause strong chemical interactions [297], whereas Au and Ag exhibit limited reactions at Alq3 interfaces [301] [302].

Predicting interface characteristics is a complex task, but is easier for weaker interactions dominated by electronics with fewer chemical effects (Figure 4-2). For weakly interacting interfaces, the extent of gap state generation determines the analysis approach required. If the interaction produces few gap states, then Schottky-Mott theory applies directly. The barrier height is found to depend on the metal WF, relative to the organic Fermi level [105]. With more significant gap state generation, first, the organic charge neutrality level must be identified, by calculating the induced density of states using density functional theory [303]. Then, the offset between the organic charge neutrality level and metal WF can be used to determine the interface charge transfer [74] [75].

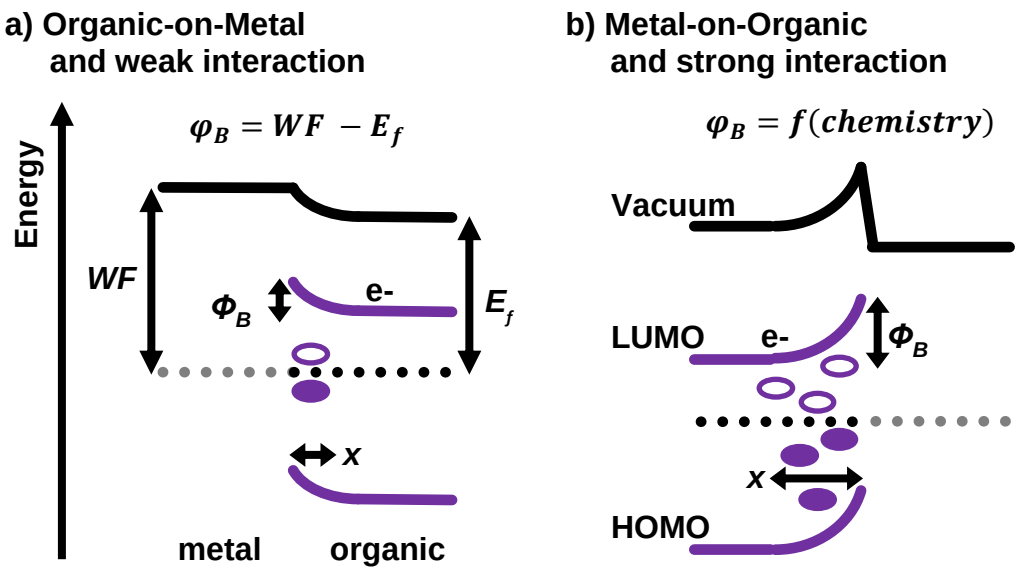


Figure 4-2: Schematic illustrations of metal-organic interfaces with different deposition geometries and interaction strengths.

For strongly interacting interfaces prediction is harder, because the electron occupation of the organic cannot be explained simply from the metal WF and charge transfer [298]. Chemically generated states dominate the organic energetics [69], so the density of states is influenced by chemical bonding and molecular orientation [74] [75]. Each interface must be investigated individually because the reactions are specific to the materials combination, meaning

conclusions cannot be extrapolated for a generalised understanding of reactive interfaces [106] [74].

The nature of the interface changes depending on the deposition order of organic and metal (Figure 4-2). For metal-on-organic structures, the penetration of metal into the underlying organic causes extended strongly reacted regions, compared to the abrupt interfaces formed for organic-on-metal structures [297]. Both organic and metal material properties control the degree of intermixing. For organics, more structural defects and grain boundaries increase the damage depth and gap state generation [153]. For reactive metal deposition, the penetration was found to increase for shallower WF values [260]. Despite clear structural differences between the two cases, however, devices may not exhibit strong carrier injection differences because of similar chemically-induced energetic properties dominating interface processes [297] [304].

In a full PV device structure, these phenomena can manifest as beneficial cathode migration into the CTL. During cathode deposition, the metal can diffuse into the underlying organic, inducing gap states in the CTL [305]. These gap states can facilitate carrier transport, giving ohmic interface conduction and improving device performances [260] [306]. Various strategies have been employed to maximise these effects in PV devices. Thin CTLs ensured through-thickness metal diffusion enabling collection from the active layer [307] and roughening underlayers were used to enhance metal penetration into the CTL [308].

• Metal-doped Organic Layers

Metal doping of organic layers is achieved by co-evaporating metal during the thin film deposition process. Deliberate intermixing appears to be the logical next step having observed the benefits of cathode migration. The approach is advantageous as the metal concentration can be controlled via the relative deposition rates [309]. Co-evaporation studies uncover similar

characteristic features as observed in interface investigations, and measure the resultant changes in transport properties.

The metal to organic charge transfer process now causes bulk electrical doping, which increases the conductivity of the co-evaporated layers [310]. As before, metal-organic complex formation and associated gap state creation are observed [311]. The generation of gap states, often around the Fermi level energy [105] [241] with an increasing proximity of the Fermi and LUMO level positions [311] [312], facilitates carrier transfer between adjacent states improving the charge transport through the layer [105]. When located at an interface with a barrier, these gap states can provide a transport channel circumventing the previous collection limitation (Figure 4-3 a) [241]. Barriers can also be changed directly because orbital interactions shift the HOMO and LUMO level positions [312] [313] which can improve the energy level alignment with adjacent layers and so increase carrier injection [311] [313] [151].

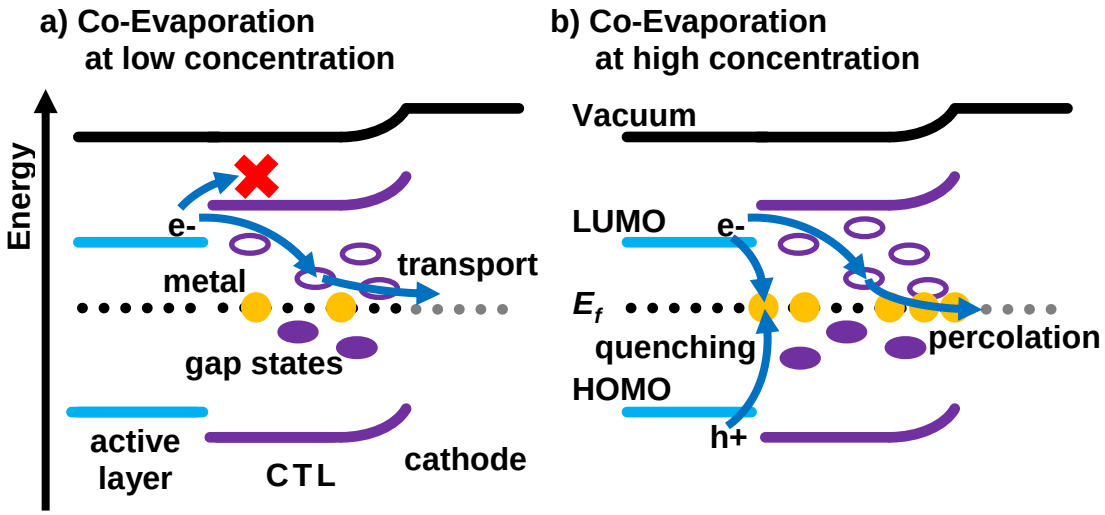


Figure 4-3: Schematic illustrations of the device processes which can occur in co-evaporated CTLs at with a) low and b) high metal concentrations.

Whilst chemistry clearly plays a role in some of the interactions, the effects observed are often explained by electronic considerations. The mechanism for charge transfer to the organic is dependent on the metal WF, with shallower WF metals observed to donate more to gap states

[105] and a WF shallower than the organic electron affinity recommended for efficient doping [310]. Analogously to metal and semiconductor band structures, it is suggested that partially filled gap state levels enable carrier transport whilst fully filled levels are prohibitive [105]. Observed conductivity increases with metal concentration and eventual decreases for some metals, are therefore explained by the changing gap state occupation level [105]. A chemical reaction was not observed for Alq3 co-evaporated with Au, but device performances still improved due to the Au shifting the HOMO level to reduce an interface barrier [313].

The metal concentration can also affect device operation through other mechanisms (Figure 4-3 b). At high doping concentrations, metallic cluster formation has been observed [309]. When present at an interface with an organic absorber layer, these clusters cause exciton quenching [309]. Similar recombination increases are observed when metal NPs contact the active layer in OPV devices [295]. At very high concentrations, the metal additives can form a percolating network, resulting in high conductivities which are independent of the metal WF value [310].

• NP-organic Composite Conclusions

Having discussed the interactions of organic layers with metal atoms and interfaces, it is conceivable that metal NPs may induce similar effects. At low nominal thicknesses, NPs likely resemble localised co-evaporation. At electrode interfaces, metal migration into the underlying organic may form NP structures [308]. Some studies provide evidence of the interaction similarities and differences for metal atoms, interfaces and NPs. Interfaces between Au and Alq3 were observed to be minimally reactive, but Au NPs created gap states and redistributed charge because NP size effects increase reactivity [184] [314]. When deposited on Ptn, NPs of Au produced more gap states at a shallower energy than atomic doping, for which the mobile atoms migrated deep into the film [262] [315]. The NP-induced gap states were found to occur at energies approximately corresponding to the metal WF [262]. These observations caveat the

direct application of property trends from co-evaporation and interface studies to NPs, despite similar interaction phenomena operating.

It is apparent that the properties associated with metal NPs differ to those for individual atoms or bulk interfaces, therefore, studies specifically focusing on NP structures are desired to inform further understanding. Additionally, the metal-organic investigations discussed above often do not test the implications of the interaction effects in device structures.

4.1.3 Organic Non-Volatile Memory

Therefore, we now turn to the field of ONVM, which investigates devices exhibiting distinct high and low conductivity states which are controlled by the bias voltage applied [316]. The field aims to develop next-generation information storage technologies by understanding then exploiting this bistable resistive switching effect.

ONVM devices are relevant to the studies in this chapter because many embodiments are an organic matrix containing a metal additive that has a NP structure formed by thermal evaporation [288] [317]. Crucially, electrical testing is conducted on single layer devices where metal NPs are key to the transport mechanism [318] [319]. There are, however, several key differences between ONVMs and OPVs which should be considered (Table 4-1). These observations should be taken as caveats to the direct application of specific ONVM conclusions, especially given we do not actually measure two co-existing resistance regimes. However, the ONVM operation mechanisms may provide frameworks to interpret NP electronic effects and the electrical characterisation techniques can be applied to single layer devices.

	ONVM	OPV
Voltage range	High voltages probed ‣ induce resistive switching	Low voltages probed
Testing environment	Dark conditions	Light conditions ‣ photoexcitation for generation ‣ metal NP plasmonics
Mechanism explanations	Simple energetics ‣ vacuum level alignment	Complex energetics ‣ band bending ‣ gap states

Table 4-1: A summary of key characterisation and analysis differences between the fields of ONVM and OPVs.

There is a great deal of debate in the ONVM field as to the origin of the resistive switching behaviour. Whilst no universal mechanism explaining the observations exists, two main theories are proposed based on either charge trapping [320] or conductive pathways [321] (Figure 4-4). The devices reported all exhibit very similar electrical switching characteristics [288], despite a range of different embodiments existing [317]. A variety of material combinations are employed, both in terms of the organic and metal used. Device structures also vary, as solution processing gives fully blended organic-NP layers. It is worth noting that a particular challenge in the field is poor reproducibility of precise electrical properties, both between laboratories [288] and on a device-to-device level [322].

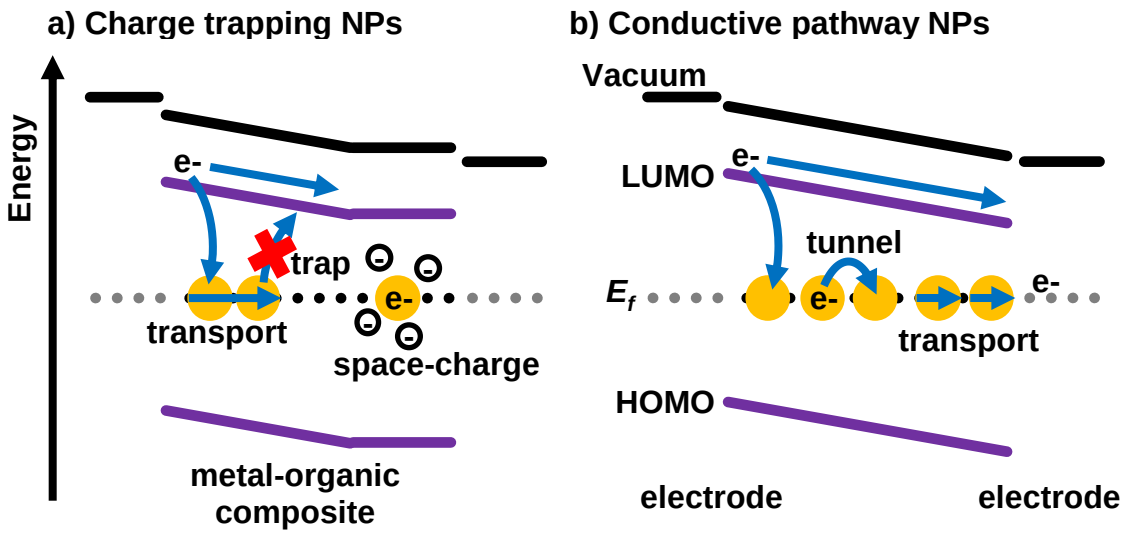


Figure 4-4: Schematic illustrations of the processes which can occur in ONVM devices, based on the NP a) charge trapping and b) conductive pathway mechanisms proposed.

The charge trapping switching mechanism has various associated theories aiming to explain the bistability observed. However, there exists a deviation of opinion in the literature as to whether a fully trapped configuration produces the high or low resistance state [288]. There does though seem to be agreement on the energy level structure required for carrier trapping to occur: the WF of the NP trap states should be between the HOMO and LUMO levels of the organic matrix [288] [323]. Charge transfer to the NP depends on the resultant energy barrier for the majority carrier type [324] and may be restricted by the presence of a NP surface oxide layer [320]. These barriers are then overcome by the applied bias, allowing trapping and de-trapping processes to operate [317] [325]. Poor control and reproducibility of device characteristics, however, has sometimes hindered the observation of systematic trends with the variation of NP or electrode WF [322].

The trapping effects are suggested to alter carrier dynamics in various ways (Figure 4-4 a). Transport may occur through trap states directly and so depends on their filling distribution and energy level [288] [318] [326]. Resultant space-charges may also alter currents depending on the NP trapping characteristics and device carrier type [318] [323]. Most of the mechanisms describe trap limited currents which therefore restrict collection to some degree [288]. Knock-

on effects to the collection of other carriers occur concurrently, but which dominates collection depends on the specifics of the system under study [327]. The generation of a space-charge hinders carrier collection [317] [323] and creating a full trap level makes transport worse [288] [326], in contrast, trapping emptying another transport level improves collection by doping [328].

The mechanistic principles of charge trapping have been applied to a device not exhibiting bistable resistive switching, despite being based on evaporated Au NPs in a small molecule organic matrix [323]. It was demonstrated that charge trapping on NPs reduced the device current due to the associated space-charge hindering drift. This was evidenced by optically-induced de-trapping causing the current to increase again [314]. The occurrence of trapping in ONVMs is also measured using AC impedance, where a change in the capacitive characteristics is caused by NPs charging and discharging [329] [330]. Larger NPs may have a stronger trapping effect, increasing the charge stored [322] [331]. Additionally, it may be possible to identify different trap distribution functions by fitting IV characteristics with theoretical models of space-charge-limited conduction processes [323] [332] [333]. Based on the charge trapping mechanisms outlined above, therefore, NPs may increase trapping which hinders carrier extraction and manifests as a changing capacitance.

The conductive pathways switching mechanism operates by reducing the amount of semiconducting organic material which has to be traversed between the two electrodes (Figure 4-4 b) [329]. A key feature is a highly localised conductivity improvement [334] [335], and the switching feature stems from the formation and rupture of this low resistance filament with applied bias.

Metal NPs are deliberately introduced into the organic structure to increase the conduction in ONVM devices [329]. The current in both the high and low resistance states is observed to be greater for increasing NP nominal thicknesses [322] [336]. This is because the NPs may function as conduction sites, in addition to acting as traps, in a semiconductor matrix [322] [326]. Charge transport can occur via direct tunnelling between the localised NP sites [337] [338]. The presence of metal NPs also promotes the growth of conducting filaments the between electrodes, so switching is observed on the first voltage sweep without any pre-conditioning [329] [339].

In addition to NP incorporation, or as an alternative, conductive metallic filaments can be formed by mobile atoms from the metal electrodes [288] [329] [340]. A conditioning process, where the applied bias is swept to high voltages, is required to drive metal atom migration from the electrode and produce metal clusters in the organic [323] [329] [339]. The advantage of deliberate NP incorporation now becomes clear, as it enables the size and location of NPs to be carefully controlled for uniformity and reproducibility [341].

The operation of a conductive pathway type mechanism can be identified from AC impedance measurements, which exhibit changing ohmic characteristics alongside minimal capacitance variations [329] [330]. Additionally, specific device property characteristics should result from the localised and metallic nature of filamentary transport. The current is expected to be broadly invariant with changes in device area [317] [322] and the conductivity is likely to be relatively temperature independent [339]. Recently, it became possible to directly image metallic filament formation, although it is technically challenging [339] [342].

In ONVM devices localised non-uniformities give uneven current distribution across device area [341]. It is also possible for conduction processes to occur via both the organic and NP

components [322]. Different transport mechanisms may be taking place simultaneously at various locations throughout a device, thus operating as parallel collection pathways [288]. Therefore, based on the above descriptions of this mechanism, NPs may improve carrier transport through various pathways and exhibit changing ohmic characteristics.

4.1.4 Approach

The literature reviewed above presents a variety of phenomena which may be encountered in metal-organic composites. It demonstrates that metal NPs can alter the optoelectronic properties of organics, leading to changes in device operation (Table 4-2). It also highlights the complexity of the interactions and thus the challenges in predicting resulting device characteristics for a given materials combination. Therefore, this chapter will investigate composite layers to understand how metal NP additions to CTLs may affect device operation processes.

	Organic layer properties	**PV device characteristics**
Metal NP Additions	• Optical field distribution [343] • Carrier concentration [184] • Density of states [262]	• Conductivity [105] [322] • Energetic barriers [241] [151] • Space-charge formation [323] • Photocarrier generation [282] • Charge trapping [318] [322] • Charge recombination [309]

Table 4-2: A summary of the possible effects of metal NP additions to organic devices.

This chapter investigates single layer devices where sequential thermal evaporation is used to form NPs in an organic matrix. Ag and Au NPs are employed, as their plasmonic resonances occur in the visible region and they are resistant to oxidation. The NPs are embedded in Alq3, which is known to be suitable for NP formation [314] [344] and to function as an effective CTL in OPV devices [153].

It is hypothesised that the NPs will alter the carrier dynamics and interface energetics, as well as modifying the optical response of the device. To probe the mechanism of interaction, Au and Ag NPs are tested across a nominal thickness range of 1 to 5 nm. This explores the influences of metal WF, plasmonic wavelength and NP size. Both the electronic and optical properties of single layer composite devices are measured. However, the absence of an absorber layer means optical effects may be different in a full PV device structure. This study extends the existing literature, as CTLs with metal NPs are rarely studied separately before OPV device integration and ONVM devices are predominantly studied in the absence of illumination.

To confirm NP formation, the morphology is measured using AFM and the absorption spectrums are analysed. Kelvin probe is used to examine the NP electronic properties and elucidate the NP-organic interaction in composite films. The device optoelectronics are then characterised. Transport properties are measured using IV and AC impedance techniques, to calculate changes in resistance, mobility and capacitance. In order to probe interface effects and investigate NP transport, the primary Al cathode is compared against a Au cathode. To determine which composite components are photoactive, carrier collection under both full and wavelength-filtered illumination is measured. Radiative loss routes operating in the composite are also explored using photoluminescence (PL) testing.

4.2 Experimental

The Equipment and Methods chapter (Section 2.2) describes fabrication procedures common to all embodiments. For this chapter, device fabrication was completed using a deposition system designed and built for this research project (Section 2.1.2). The deposition sequence was: Alq3 50 nm at 0.2 Å/sec (99.995%, Sigma-Aldrich); Au (99.99%, Testbourne) or Ag (99.99%, K. J. Lesker) 0 to 5 nm at 0.1 Å/sec; Alq3 50 nm at 0.2 Å/sec; Al (99.999%, K. J. Lesker) or Au 30 nm at 0.1-0.5 Å/sec.

The Equipment and Methods chapter (Section 2.3) also describes all characterisation methods used. The composite device active area is 0.025 cm^2 and throughout the chapter, error values represent the standard deviation across 3 pixels on each substrate. The composite layer absorption was determined from UV-VIS-NIR transmission measurements. For AFM analysis, three randomly selected areas of 250 by 250 nm were scanned on each sample, to provide average values for calculated parameters. One representative scan was selected as a topography image. For Kelvin probe analysis, 25 measurements were taken at each of 3 different scanning positions on each sample. For PL analysis, the samples were placed on a blackout tape background and excited at 405 nm. For IV characterisation, the voltage was swept between -2 V and +2 V with a step size of 0.1 V and delay time of 100 ms. Wavelength filtered IV measurements were conducted by placing long pass filters above the sample holder in the illuminating beam's path. For AC Impedance characterisation, impedance-frequency measurements were taken under 100 mW/cm^2 illumination, at biases of 0 V and +2 V across a frequency range of 100 Hz to 2 MHz.

4.3 NP Characterisation

4.3.1 Optics

The composite films consist of two 50 nm Alq3 layers, between which Au or Ag was deposited with a nominal thickness of 1 to 5 nm forming NPs (Figure 4-1). During metal NP deposition the lateral dimension grows faster than the height, producing increasingly oblate NPs [287]. NP plasmonic resonance wavelengths are understood to redshift with such increasing NP aspect ratios [345] [346]. The NP absorption strength also increases with nominal thickness, due to higher material volumes and greater coverages [282]. The Au composite absorption spectrum (Figure 4-5) exhibits a new plasmonic absorption peak, which redshifts and strengthens with

increasing nominal thickness as predicted. These characteristic features provide evidence for the controlled formation of discrete NP structures [280]. Beyond the plasmonic peak, longer wavelengths are dominated by Drude band absorption from bulk free electrons [347]. Longer wavelength absorption increases with nominal thickness suggest NPs may begin to form localised percolating networks.

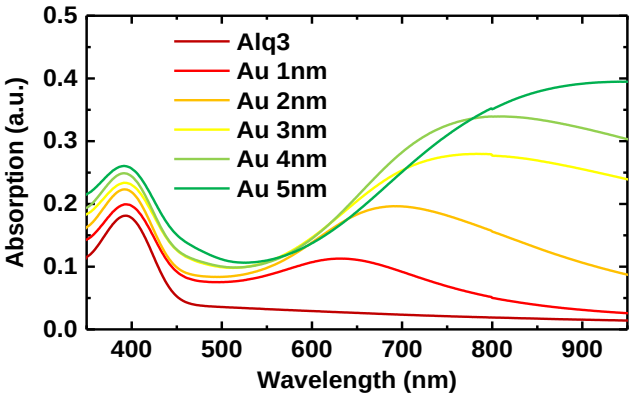


Figure 4-5: The absorption spectrums of Alq3-Au composite layers with various nominal thicknesses of Au NPs, showing large plasmonic NP absorption increases above 500 nm.

Both Au and Ag NPs exhibit visible region plasmonic resonances, so optical changes can be observed by eye (Figure 4-6). Dielectric function differences, however, mean Ag has a higher Fröhlich frequency than Au, so plasmonic absorption occurs at shorter wavelengths [281]. The Ag composite absorption spectrum (Figure 4-7) confirms this theory and shows nominal thickness trends similar to Au NPs.

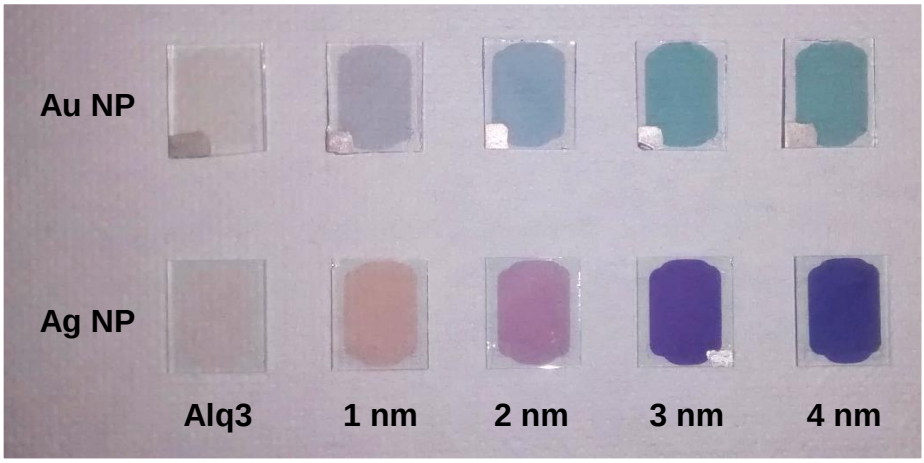


Figure 4-6: The Alq3-Au and Alq3-Ag composite layer samples, showing colour changes with NP material and nominal thickness.

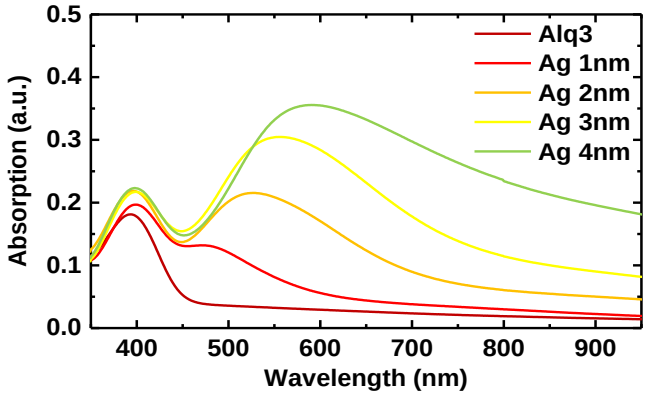


Figure 4-7: The absorption spectrums of Alq3-Ag composite layers with various nominal thicknesses of Ag NPs, showing large plasmonic NP absorption increases above 450 nm.

Both composite absorption spectrums exhibit small increases in the 350 to 450 nm Alq3 wavelength range. NP near-field effects can enhance organic absorption if the resonance and absorption wavelengths are concurrent [282]. However, the overlap between NP resonances and Alq3 absorption is limited (Figure 4-5 Figure 4-7), meaning the increases are unlikely to originate from NP-induced Alq3 enhancements. Alternatively, the small increases may simply originate from underlying NP absorption. The NP-only absorption spectrums (Figure 4-8) show Au interband [289] and Ag plasmonic tail absorptions clearly extending into the Alq3 wavelength range. Therefore, the small absorption increases are more likely to originate from NPs directly.

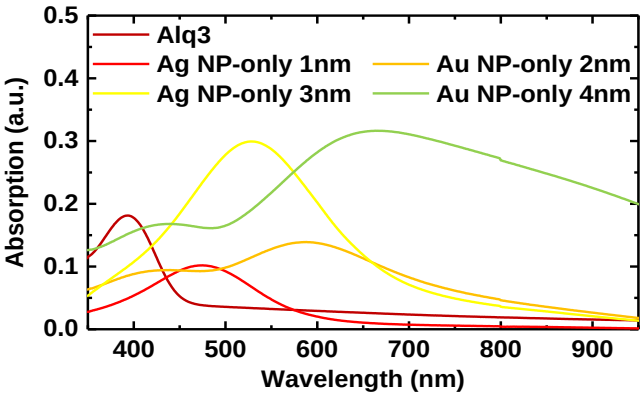


Figure 4-8: The absorption spectrum of the Alq3 layer alongside those of various nominal thicknesses of Au and Ag NPs not embedded in Alq3, demonstrating the absorption range overlap from 350 to 450 nm.

4.3.2 Morphology

• AFM measurements

To investigate the physical features of the NPs, AFM imaging was undertaken. Sample structures with exposed NPs were created by not depositing the final Alq3 layer. The topography images were analysed using a segmentation algorithm to identify individual NPs, allowing their height and diameter to be calculated [348]. Images of as-fabricated samples show cap shape features possibly indicative of NPs (Figure 4-9 a). However, the NP size parameters (Figure 4-10 and Figure 4-11) do not increase with nominal thickness as expected. The NPs may be partially embedded in the underlying Alq3, preventing them being fully imaged.

A UV-ozone plasma treatment, commonly used to eliminate organic contaminants, was employed to reveal the NPs by removing the surrounding Alq3. Absorption spectra (Figure 4-12) were measured before and after an 8-minute treatment and show that the Alq3 absorption is eliminated. NP absorption changes possibly indicate small material losses [282] and slightly increased aggregation [347]. The peak resonance wavelengths and nominal thickness trends, however, are not altered significantly. Therefore, AFM analysis should be undertaken with the

slight caveat that the plasma may have altered the NP structures, but in similar ways for 1 nm and 3 nm samples.

After the plasma treatment, discrete NPs are clearly resolved (Figure 4-9). As expected, fewer but larger NPs are observed at higher nominal thicknesses. The NP diameter and height analysis confirms this quantitatively (Figure 4-10 and Figure 4-11), showing the aspect ratio increases from 0.24 for 1 nm to 0.32 for 3 nm NPs, supporting the optical redshifts observed. The measurements are limited by tip convolution effects, however, because feature sizes are comparable to tip diameters (Figure 4-11 dashed lines). The small NP size causes tip convolution in the x-y plane and the z resolution is limited by close NP proximities [285]. Therefore, the NP shape is not fully resolved, and the size measurements are distorted, with overestimated diameters and underestimated heights.

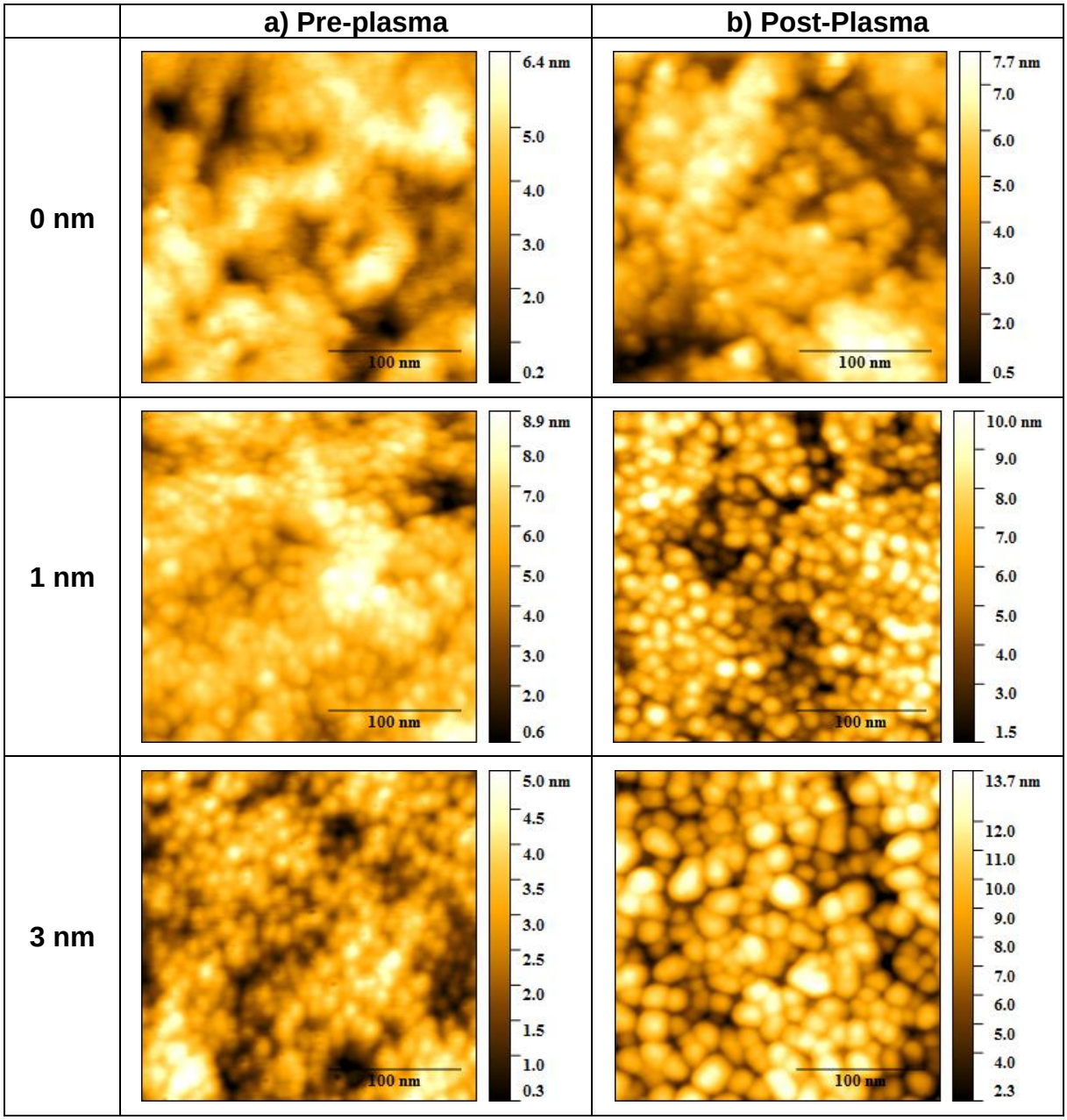


Figure 4-9: Representative topographic AFM images of Alq3-Au composite layers various nominal thicknesses of Au NPs a) before and b) after plasma treatment. NP shaped features in the 1 and 3 nm images become more defined after plasma treatment.

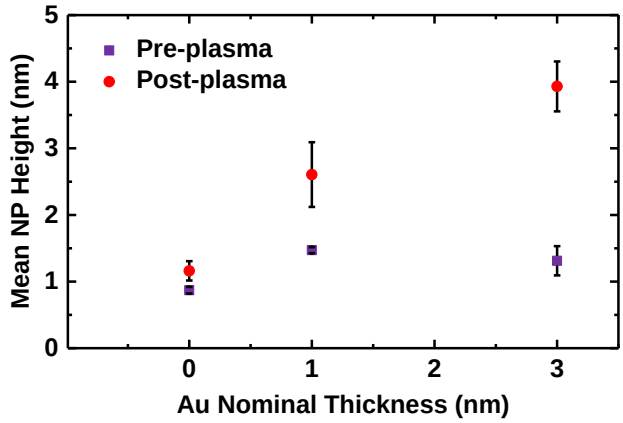


Figure 4-10: The mean NP height derived from AFM topography images before (Pre-plasma) and after (Post-plasma) plasma treatment, the error bars represent the standard deviation across three locations imaged.

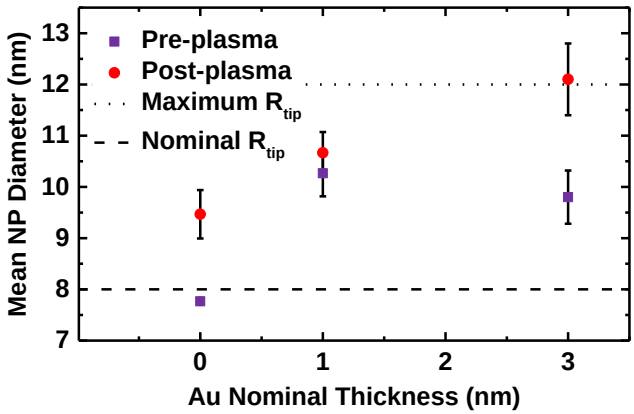


Figure 4-11: The mean NP diameter derived from AFM topography images before (Pre-plasma) and after (Post-plasma) plasma treatment, the error bars represent the standard deviation across three locations imaged. The dashed horizontal lines depict the nominal and maximum radius of the probe tip, providing a rough guide to the resolution limitations.

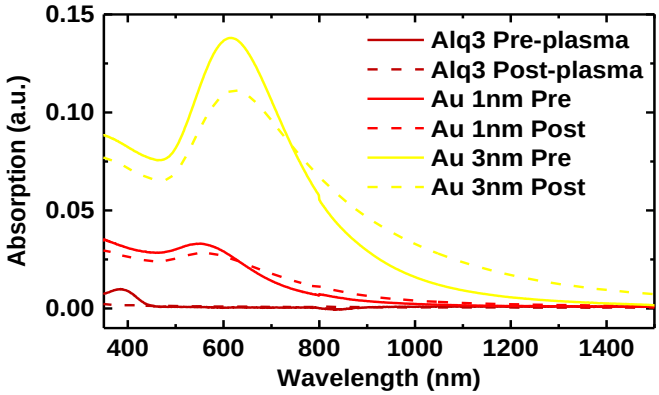


Figure 4-12: The absorption spectrums of Alq3-Au composite layers with various nominal thicknesses of NPs before (Pre) and after (Post) plasma treatment. The Alq3 peak is eliminated and the plasmonic peak is reduced for 3 nm NPs.

• Semi-Empirical Predictions

Given the imaging limitations, comparisons with NP sizes from the literature were undertaken. By fitting equations for a spherical cap geometry to empirical Au NP measurements from the literature, Axelevitch et. al. developed a model which predicts the diameter and height of Au NPs from the nominal thickness [287]. The sizes predicted for 1 and 3 nm of Au (Table 4-3) indicate NP imaging may be limited by tip convolution. The Au NP sizes measured by AFM (Figure 4-10 and Figure 4-11) are similar in magnitude to the predicted values and agree better for 3 nm Au, where convolution may be less significant.

Nominal Thickness	**Predicted Diameter (nm)**		**Predicted Height (nm)**	
	Au NP	**Ag NP**	**Au NP**	**Ag NP**
1 nm	4.2	11.5	1.5	1.5
3 nm	13.7	11.5	3.6	2.3

Table 4-3: The NP diameter and height values predicted from the nominal thickness using semi-empirical models [287].

Data was gathered to additionally apply this predictive model to Ag NPs. The Ag NP dataset is less robust, however, as there is a reduced balance between electron microscopy and AFM measurements [290] [349] [286] [350]. Comparing the Au and Ag NPs datasets revealed similar diameters and heights below approximately 5 nm, however, at higher nominal thicknesses the Ag NP dataset showed both smaller heights and diameters. This finding is unphysical and may indicate that different fabrication conditions and measurement techniques are influencing the results. The sizes predicted for 1 and 3 nm Ag (Table 4-3) suggest that height, but not diameter, differences might be measured with increasing nominal thickness, given that the diameters are identical and comparable to the tip size range.

Overall, this comparison demonstrates that the AFM measurements are consistent with NP sizes reported in the literature. As the datasets suggest similar sizes for low nominal thickness Au

and Ag NPs and the measurement accuracy is tip convolution limited, the Ag NP samples were not studied by AFM.

4.3.3 Electronics

Metallic nanoclusters exhibit a size-induced insulator-metal transition, which is reported to occur at a particle size of approximately 4 nm for Ag [278] and 1 nm for Au [273] [276] [351]. The morphology analysis (Section 4.3.2) for 1 nm Au NPs suggests a height and diameter in the range 1-3 nm and 4-12 nm respectively. Therefore, the particles are anticipated to be above the transition size, which is supported by literature reports of small metallic Au NPs on Alq3 [314]. Additionally, the observation of plasmonic free electron oscillation is evidence of bulk-like electronic properties in the discrete NPs [276]. Therefore, it is hypothesised that the NPs are metallic and would exhibit the same electronic structure as the respective bulk materials.

The Fermi levels measured by Kelvin probe (Figure 4-13), however, do not support this hypothesis. The 0.5 to 5 nm NPs of Au and Ag have Fermi levels which vary outside the error range of the respective bulk values. The Fermi levels are similar and become shallower with nominal thickness for both Au and Ag. This could be a NP size geometry effect because the band structure of NPs is influenced by undercoordinated surface atoms [273]. NP Fermi level measurements were not possible on glass substrates, providing evidence that the NPs are not electrically percolating. The necessity of utilising conducting ITO indicates that the substrate influences the measurement, which could explain the similarity of the NP values given the low material coverages [352].

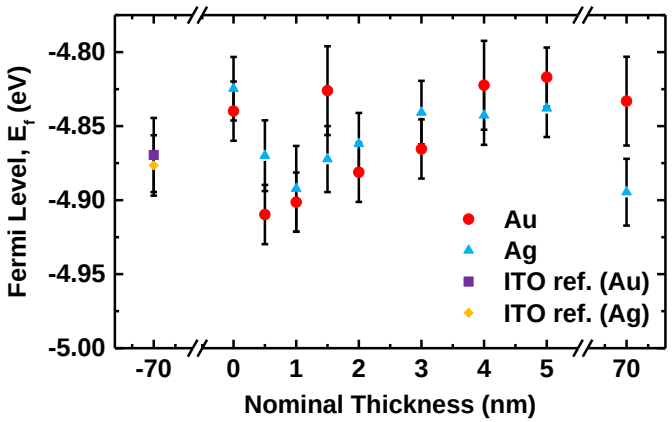


Figure 4-13: The average Fermi level positions of Au and Ag NPs (1 to 5 nm) and bulk films (70 nm) measured on ITO substrates (0 nm) by Kelvin probe. At -70 nm the ITO references facing the chamber walls are shown for comparison to the ITO substrate facing the evaporation sources at 0 nm.

It is noted that the Fermi levels of the continuous films are somewhat unexpected; Au is shallower than Ag and both lie outside the literature WF ranges [256]. This could be due to different interactions with surface Alq3 contaminants [353]. Absorbed species can modify the Fermi level of a surface by up to 2 eV [354] and the Fermi levels for ITO substrates facing the evaporation sources and chamber walls are different (Figure 4-13, 0 nm and -70 nm). Au and Ag are expected to interact differently with any Alq3 contamination because composite layers show different Fermi levels as reported subsequently (Figure 4-22).

Overall, the Kelvin probe results suggest that NP geometry and ITO substrate effects may dominate the measured NP Fermi level more than the bulk electronic properties. The Fermi level of the NPs might be expected to shift shallower with increasing nominal thickness, however, this could depend on the underlying substrate.

4.4 Device Electronics

4.4.1 Device Architecture

To explore the effect of NPs on Alq3 optoelectronic properties, devices based on a single composite layer were fabricated (Figure 4-14). Between two 50 nm Alq3 layers, NPs were formed by evaporating Ag or Au with a nominal thickness of 1 to 5 nm. Devices were primarily fabricated with Al cathodes, although Au was used for specific studies as indicated. The 100 nm Alq3 thickness was chosen through testing which proved it was thin enough to produce measurable effects with 1 nm NPs whilst also being thick enough to avoid 5 nm NPs simply shorting the device.

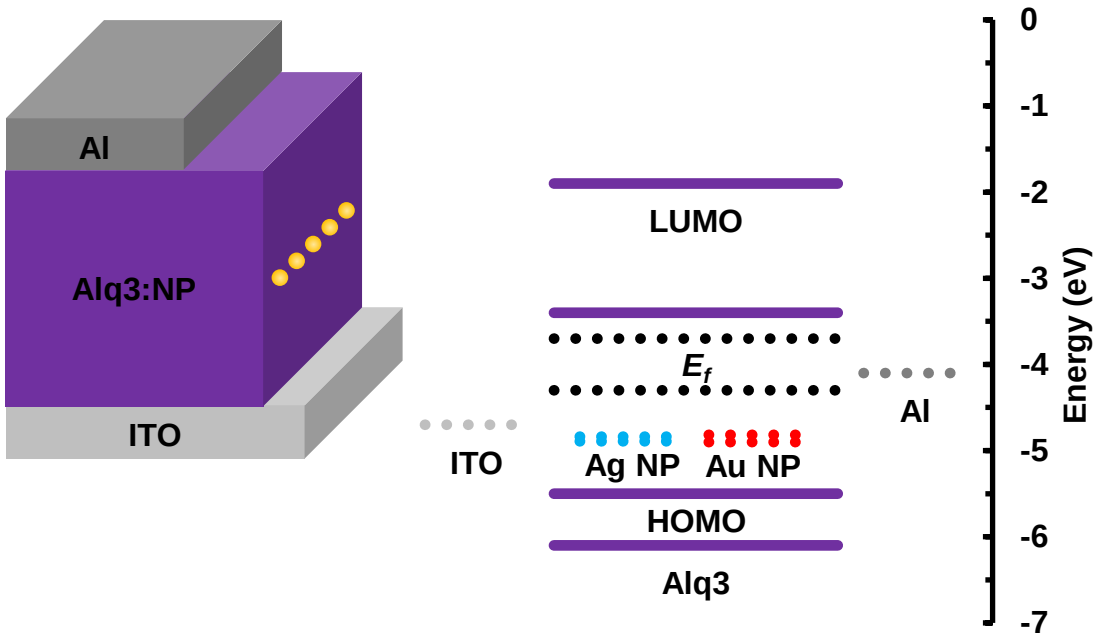


Figure 4-14: A schematic of the device architecture (left) and the energy level positions under vacuum level alignment (right), where an upper and lower bound are shown for the HOMO, LUMO and E_f to reflect the range of values reported in the literature.

The 100 nm Alq3 thickness used in this chapter is larger than would generally be employed for a CTL in a PV device, where thicknesses of under 10 nm are more common [153]. At this stage, however, the purpose of the study is to probe the interaction mechanisms between the NPs and Alq3 which control the device property changes. Additionally, when employed as an optical

spacer, doped organic CTLs of up to 80 nm can be used [355], demonstrating thick layers are still relevant to device embodiments. In these cases, the ability to improve the properties of thick layers would be valuable.

When testing various Alq3 thicknesses, unusual features were sometimes observed in the IV curves. These features were identified as characteristic of bi-stability properties, which are exploited in ONVM devices [322] and often reported for Alq3 samples [329]. However, these features were found to be highly variable and the literature reports that such inconsistencies are a general phenomenon [288]. Investigations into this bi-stability property were not pursued, because the features occurred at voltages beyond the PV operating range and no systematic data trends were observed.

4.4.2 Transport Modification by NPs

The IV characteristics tested under illumination reveal significant changes caused by NP additions. The absolute current density plotted on a log scale (Figure 4-15) shows that NPs can increase the device current by over an order of magnitude across a wide range of voltages as the nominal thickness increases. The vertex shifting towards lower biases indicates a barrier is reducing with increasing nominal thickness, as discussed subsequently (Section 4.4.3). The average resistance extracted from the illuminated (light) IV curves ($R_{iv}(L)$) is shown for both Ag and Au NPs (Figure 4-16). For both metals, the resistance initially increases, before eventually reducing at higher nominal thicknesses. The resistance improvements occur sooner for Au NPs and are also on average larger for a given nominal thickness.

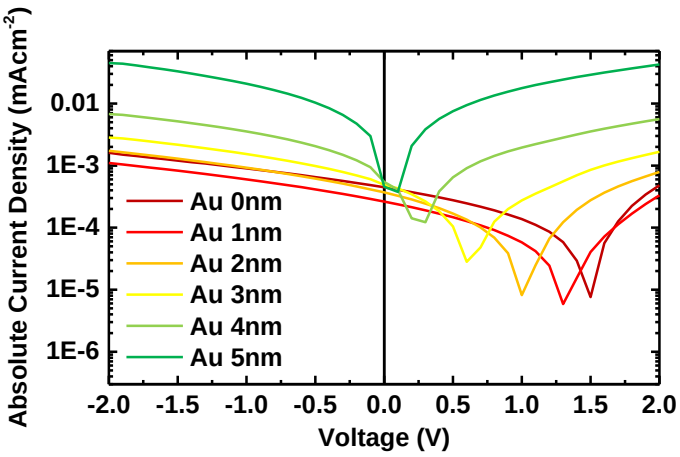


Figure 4-15: Representative illuminated IV curves of Alq3-Au composite devices with various nominal thicknesses of NPs, plotted as absolute current on a log scale. The device structure is ITO-Alq3-NP(x)-Alq3-Al.

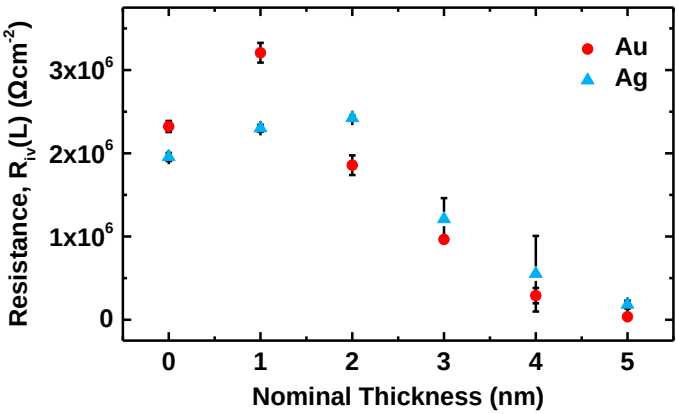


Figure 4-16: The average resistance values from illuminated IV curves of Alq3-Au (Au) and Alq3-Ag (Ag) composite devices with various nominal thicknesses of NPs.

NPs may affect carrier transport through a variety of mechanisms. They may hinder extraction by trapping carriers and possibly creating a space-charge build-up within the device [323]. Conversely, they may enhance collection by providing a network of conductive pathways [105] [322]. The strength of each effect may also change with nominal thickness, which could alter which behaviour prevails eventually [322]. For example, at higher nominal thicknesses percolation to the cathode may reduce the impact of trapping despite a larger NP volume existing to trap on [356].

The AC impedance response was measured to determine the mechanisms causing resistance changes and explore whether transport dynamics improved with increasing NP nominal thickness. The impedance data was fit using an ECM of a resistor (R) in series with a parallel resistor-constant phase element (R-CPE) combination (Figure 4-17). A CPE is commonly employed in place of a capacitor (C) element to improve the fit accuracy, as it represents a non-ideal capacitor [357]. The full fitting results are presented in the appendix (Section A.1). This transport analysis was undertaken at a bias of +2 V because in a PV device transport processes are dominated by the series resistance in this voltage range. Additionally, this ensures the transport in the single layer devices is not limited by a barrier, as the vertex in the IV curves occurs below +2 V for all samples (Figure 4-15).

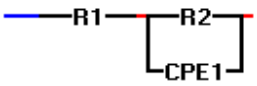


Figure 4-17: The ECM used to fit the AC impedance measurements of composite devices.

Mobility values can be extracted from fitting to a parallel R-CPE combination. Multiplying the *R* and *C* values generated produces a characteristic transport time (τ_t) [358]:

$$\tau_t = R\,C \qquad \text{Equation 4-1}$$

The carrier mobility (μ) is then calculated from the Nernst–Einstein relationship:

$$\mu = \frac{e\,L^2}{\tau_t\,k_B\,T} \qquad \text{Equation 4-2}$$

where *e* is the elementary charge, *L* is the diffusion length (organic layer thickness 100 nm), k_B is the Boltzmann constant and *T* is the temperature [358].

The mobility values extracted (Figure 4-18) show an initial reduction for both NPs, suggesting transport may be affected by some hindering NP effects discussed above. Subsequently, the

mobility increases with nominal thickness, demonstrating the ability of NPs to improve carrier transport dynamics. The mobility is consistently higher for Au NPs and the transition to improvement occurs sooner, suggesting that Au NPs provide better carrier transport than Ag NPs.

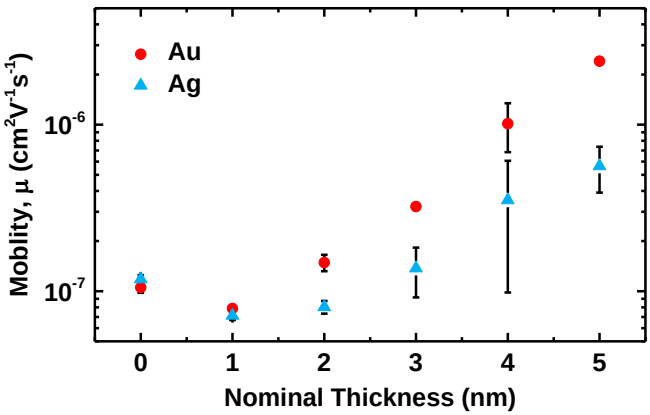


Figure 4-18: The average mobility values, from fitting impedance measurements at +2 V, for Alq3-Au (Au) and Alq3-Ag (Ag) composite devices with various nominal thicknesses of NPs.

The field of ONVM provides a theoretical framework suggesting two distinct origins for NP-induced transport changes. New paths may be created which manifest as changes in the ohmic impedance characteristics (R elements) or charge trapping effects occur as identified by changes in the capacitive impedance characteristics (C elements) [329]. An ECM with a parallel resistor-capacitor (R-C) combination can be used to represent the formation of a conductive pathway, where carriers take the lowest impedance route determined by any changes in the resistance (R_p) or capacitance (C) [330]. The observed initial increase in $R_{iv}(L)$ for both NPs could be due to an increase in C before the R_p route becomes low enough impedance to dominate transport characteristics. To investigate this hypothesis and determine whether the mechanism of transport changes is capacitive or ohmic in nature, the AC impedance response at 0 V was fitted to an ECM with a parallel R_p-CPE combination in series with an additional R element accounting for high-frequency transmission line effects. The full AC impedance fitting results

are presented in the appendix (Section A.1). The 0 V bias was chosen to maximise the potential capacitive response as there is no external bias to induce de-trapping effects [359].

The fitted capacitance values (Figure 4-19) show a general increase with the introduction and increasing nominal thickness of NPs. The origin of this increase could be charge trapping, which may occur either on the NPs which increase in volume or in NP-induced trap states [105] [184] [322]. The trends are broadly similar between Au and Ag NPs, given the offsets of the nominally identical 0 nm samples. This could suggest a mechanism more dependent on similar volumes of material, than one heavily reliant on differences in electronic or chemical properties. The primary effect of the increased capacitance is anticipated to be reduced extraction as the carriers are trapped [288]. However, there may be secondary effects such as the formation of a space-charge which may further hinder collection [323] or conversely carrier accumulation may dope the composite improving collection [328]. Intensity-J_{sc} measurements were undertaken to further investigate space-charge effects, however, the small photoresponses of CTL-only devices produced unphysical alpha values. The observed capacitance increase and suggested extraction hindering mechanism mean charge trapping effects could be a contributing factor to the observed initial increase in $R_{iv}(L)$.

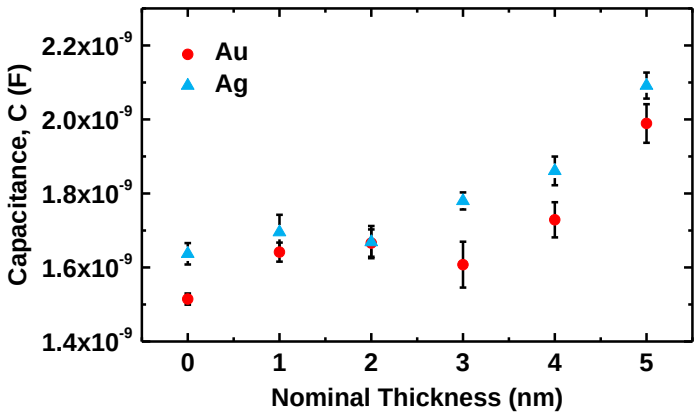


Figure 4-19: The average capacitance, *C*, values, from fitting impedance measurements at 0 V, for Alq3-Au (Au) and Alq3-Ag (Ag) composite devices with various nominal thicknesses of NPs.

The R_p values (Figure 4-20), however, still show an initial increase despite the capacitive effects having been accounted for separately in the parallel element. This implies an additional mechanism operates which increases the resistance directly (the details are discussed imminently). The eventual reduction in R_p with increasing nominal thickness suggests the NPs are creating low resistance ohmic transport pathways [329] [330]. These could again stem from transport on the NPs themselves which may become more percolating or could occur via NP-induced gap states [105] [184] [322] [329]. The reduction of a barrier could also contribute resistance improvements, as discussed subsequently (Section 4.4.3). The Au NPs produce a lower R_p at higher nominal thicknesses and initiate the transition sooner, demonstrating that the improved transport observed for Au NPs relies on ohmic effects. The distinct R_p trends of Au and Ag suggest differences in the electronics and chemistry of the two metal NPs may affect the mechanism.

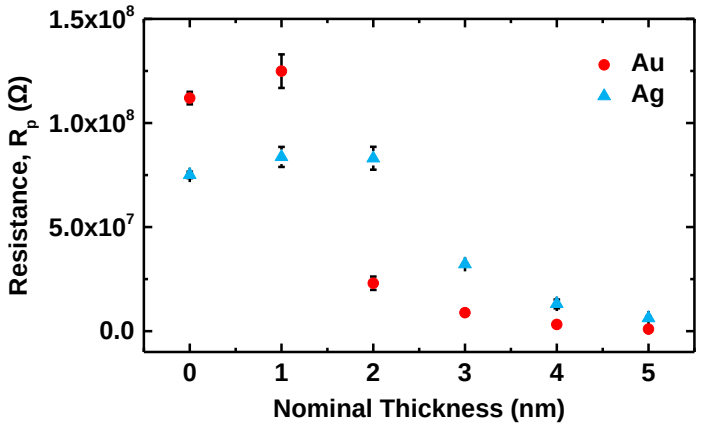


Figure 4-20: The average parallel resistance, R_p, values, from fitting impedance measurements at 0 V, for Alq3-Au (Au) and Alq3-Ag (Ag) composite devices with various nominal thicknesses of NPs.

In the applied transport model with capacitive and ohmic elements, changes were observed in both parameters, although the relative magnitude of the change was larger for R_p. The R_p reduction is anticipated to improve transport, whilst the C increase may hinder transport. The

trends in $R_{iv}(L)$ follow those of R_p suggesting this is the lowest impedance route limiting transport. However, the *C* route also extracts carriers, despite increasing trapping, as $R_{iv}(L)$ is not equal to R_p. This demonstrates the existence of both ohmic and capacitive contributions to the transport mechanism, although ohmic factors dominate transport behaviour improvements. This is manifest as the development of a lower resistance pathway which prevents trapping increases hindering transport overall. The impedance analysis has therefore demonstrated: that the initial $R_{iv}(L)$ increase is resistive in origin and not just a trapping effect, and that transport improvements are larger for Au NPs and ohmic in nature.

The initial increase in $R_{iv}(L)$ now requires an alternative explanation, having disproved the hypothesis that it originates solely from capacitive effects. Resistance increases could originate from reductions in Alq3 photodoping [360], as the introduction of 1 nm NPs is observed to strongly quench Alq3 excitons, as discussed subsequently (Section 4.5.4). To test this hypothesis, the R_{iv} values from light and dark ($R_{iv}(D)$) measurements are compared (Figure 4-21). The $R_{iv}(L)$ values are found to be lower than $R_{iv}(D)$, especially at low nominal thicknesses, suggesting Alq3 photodoping operates. In the light, the resistance increase with 1 nm NPs corresponds to the observed quenching. In the dark, however, the resistance never increases, as there are no photodoping gains to lose, so transport changes are governed by the formation of new pathways. The $R_{iv}(D)$ trends also confirm the underlying transport differences between the metals; Au shows a rapid improvement in resistance whilst Ag shows a slower transition. These results suggest the $R_{iv}(L)$ increases initially because: NP quenching reduces Alq3 photodoping before NP transport enhancements become significant enough to compensate the losses.

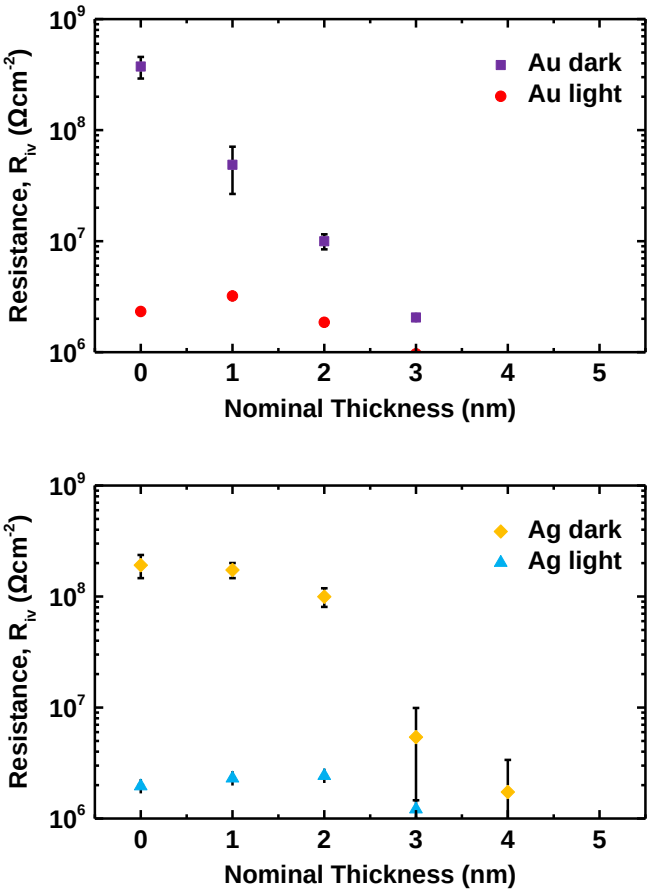


Figure 4-21: The average resistance values from dark and illuminated IV curves of Alq3-NP composite devices with various nominal thicknesses of NPs, for Au NPs (top) and Ag NPs (bottom).

• New Transport Pathways

The possible origins of these new pathways, namely a modified organic route and a new NP route, will now be investigated. Their formation and operation mechanisms will be used to explain the measured device parameters trends.

In OPV devices, metal-organic interactions in various embodiments produce changes in the transport properties of CTLs. Cathode deposition on organic layers generates metal-induced gap states which provide a carrier extraction pathway [260] [308]. Metals are co-evaporated during CTL deposition for atomic doping to improve the conductivity [105] [310]. Sitting in-between an interface and full intermixing, NPs may behave as some combination of the two.

There is evidence that Au NPs induce changes in the electronic structure of Alq3 [314], causing state generation and charge transfer as chemical reactions produce new organometallic complexes [184]. It is therefore hypothesised that the NPs will alter the electronic structure of the organic, creating new transport pathways. These effects might be weaker with Au NPs, as Au has a deeper WF and is less reactive than Ag. In this work, however, a shallower Fermi level was measured for a continuous Au film compared to Ag (Section 4.3.3). The modification is predicted to be stronger at larger nominal thicknesses, as the NP loading proportion is higher and the interface area for metal-organic interaction is increased.

To test these hypotheses the Fermi levels of the composite layers were measured using Kelvin probe microscopy. For both Ag and Au, the NP additions produce a shallower composite Fermi level (Figure 4-22), indicating that the electronics of the pristine Alq3 has been modified. The NPs and the continuous metal films (Figure 4-13) have measured Fermi levels deeper than that of the pristine Alq3, however, indicating that a traditional charge transfer to electronic equilibrium mechanism is not operating. This suggests the cause is due to a chemical interaction, namely that new electronic gap states are generated and their associated charge transfer to Alq3 shifts the Fermi level shallower. New state generation and charge transfer from Au NPs to Alq3 has been measured using X-ray photoemission spectroscopy (XPS) and UPS [184] [314]. The Kelvin Probe results presented here suggest Ag NPs might have similar but weaker effects on Alq3. The shift shallower suggests particular interaction characteristics: some of the states created have a donor character so charge transfer increases the electron density of Alq3 and more states may be created nearer the LUMO leading to a higher average electron occupation level.

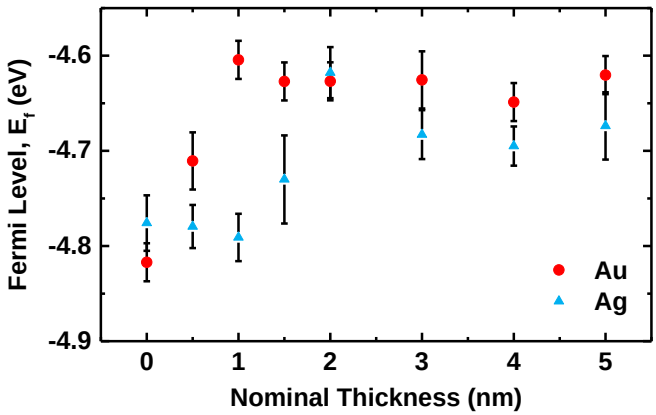


Figure 4-22: The average Fermi level positions of Alq3-Au (Au) and Alq3-Ag (Ag) composite layers with various nominal thicknesses of NPs.

Au NPs initiate the Fermi level change at a lower nominal thickness than Ag NPs and produce a shallower final value, demonstrating that Au NPs cause more doping and gap state generation. This challenges the understanding that bulk Au is more inert than Ag, suggesting that NP reactivity effects may be important and Au NPs appear to have a stronger electrochemical interaction with Alq3. Although the NP Fermi levels were similar for Au and Ag, the continuous Au film was shallower so electronic effects and the influence of WF are possibly confirmed, with the caveats that for bulk values reported in the literature Au is consistently deeper than Ag [256] and that the NP and continuous film Fermi levels measurements may have been influenced by contamination and substrate effects.

The composite Fermi level initially increases with nominal thickness before plateauing, which only somewhat supports the hypothesis that NP loading or interface area effects would cause a nominal thickness dependence. Fermi level measurements only indicate changes in the filling level of existing states; whilst some states distribution characteristics can be inferred, the number or energy of the states is not measured directly. The initial increase could be due to the new state occupation level reaching an equilibrium with the pristine Alq3 and any pre-existing defect states therein (Figure 4-23a). As the NP structure is below the continuous film limit, with a higher nominal thickness more interaction would be expected and therefore more state

generation. The plateau may possibly be due to more states being created with a similar energy distribution, but because of a large number of existing states to fill, the newest donor states are less likely to cause continued occupational shifts (Figure 4-23b). In addition, the number of states generated with each nm increment might be expected to curtail at higher nominal thicknesses where the NP surface to volume ratio decreases and coalescence effects could reduce interaction area increases. The distribution of filled and unfilled states could be measured directly using UPS and inverse photoemission spectroscopy (IPES) techniques.

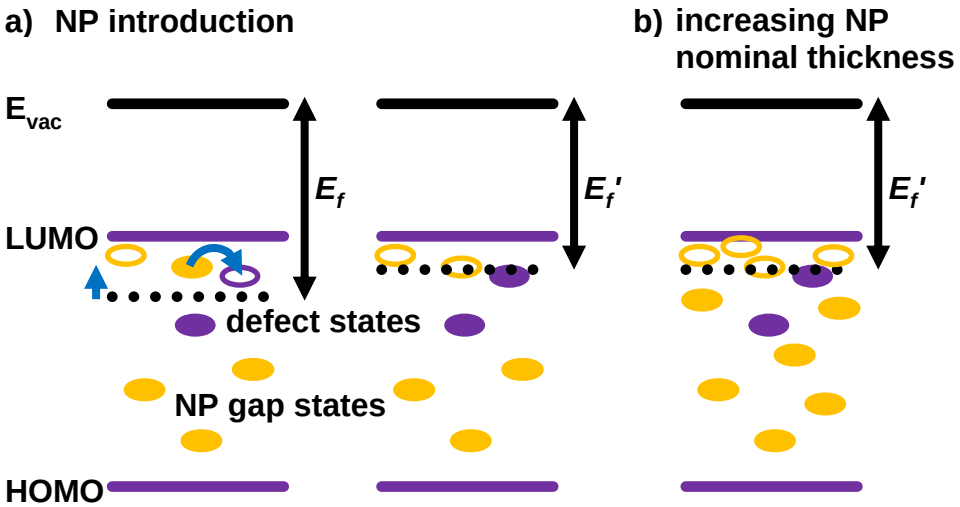


Figure 4-23: An illustrative schematic of the proposed gap state creation and charge redistribution with the introduction and increasing nominal thickness of NPs, showing the effect on the Fermi level position.

These interactions would alter the transport pathways in the organic. The conductivity would improve through doping as deep traps would be filled and band transport increased [361] and the additional gap states with nominal thickness would provide a parallel hopping route increasing transport at lower energies [241]. There is a correspondence between the stronger interaction of Au NPs with Alq3 and their greater transport enhancement, because of the increased amount of state creation and filling with Au NPs. The Fermi level shift at lower nominal thickness mirrors the more rapid resistance reduction, as the shallower Fermi level means higher doping levels and states nearer the LUMO so the mobility is improved [105]. The

transition nominal thicknesses do not match exactly, however, which is possibly due to the initial influence of photodoping losses on transport behaviour. No transport improvements are observed until after the Fermi level shift for both Au and Ag which suggests doping may critically contribute to initiating a change from intrinsic properties. Transport improvements are observed in the Fermi level plateau region, however, suggesting the presence of unoccupied states is important to the transport mechanism.

The modified organic transport route is therefore generally anticipated to be: higher energy so allowing photo-collection through a distribution of shallow gap states, and higher resistance due to the semiconductor band structure and possible gap state trapping, but with improving resistance as doping occurs and additional parallel hopping sites are generated with increasing nominal thickness.

An additional cause of continued transport improvements with increasing nominal thickness could be a route directly via the NPs themselves [322]. Organics have a higher resistance than metals, due to their semiconductor band structure and intermolecular hopping transport. The resistance of Alq3 increases non-linearly with thickness (Figure 4-24), possibly due to Alq3 bulk trapping restricting transport [362]. Therefore, substituting Alq3 transport with NP transport is expected to reduce the resistance by shortening the Alq3 path length [329]. If the NP route is non-continuous, collection to the cathode would be achieved by transferring back to the Alq3 before extraction.

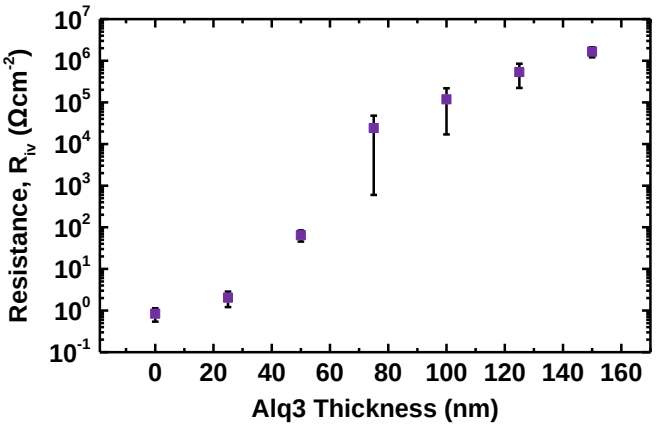


Figure 4-24: The average resistance value of Alq3-only devices with different Alq3 layer thicknesses (note log scale), the device structure is ITO-Alq3(x)-Al.

The NP route's contribution to collection could be tested by removing the Alq3 and depositing only NPs, however, all samples would simply have shorted ITO and Al electrodes. An alternative test was therefore conducted, which compared Al and Au cathodes. The hypothesis being that a deeper WF cathode is better able to collect carriers from the deep NP Fermi levels measured (Figure 4-13) [336]. However, several confounding effects must be considered when drawing conclusions. The deeper Au WF might produce lower device currents, as the smaller ITO WF offset lessens the driving force for carrier collection. Conversely, the Au cathode may increase Alq3 carrier collection, as Au is expected to have a lower extraction barrier than Al, as discussed subsequently (Section 4.4.3). The NP Fermi level changing with nominal thickness is unlikely to influence this study significantly, as Fermi levels becoming slightly shallower should not hinder collection.

The IV characteristics of devices with Au NPs and either an Al or Au cathode were measured for comparative analysis. The IV curves of devices with 4 nm NPs (Figure 4-25) show that whilst the overall current is increased with a Au cathode, the fourth quadrant photoresponse is reduced. Less photo-collection might be expected as the lower barrier for the Au cathode also reduces the depletion region collection driving force, as discussed subsequently (Section 4.4.3). The practical result is a smaller contribution to transport by excited Alq3, suggesting the route

is more likely to be via direct NP transport. This conclusion is reinforced by the lack of an initial resistance increase for a Au cathode (Figure 4-26), indicating that Alq3 photodoping is less relevant to the transport mechanism.

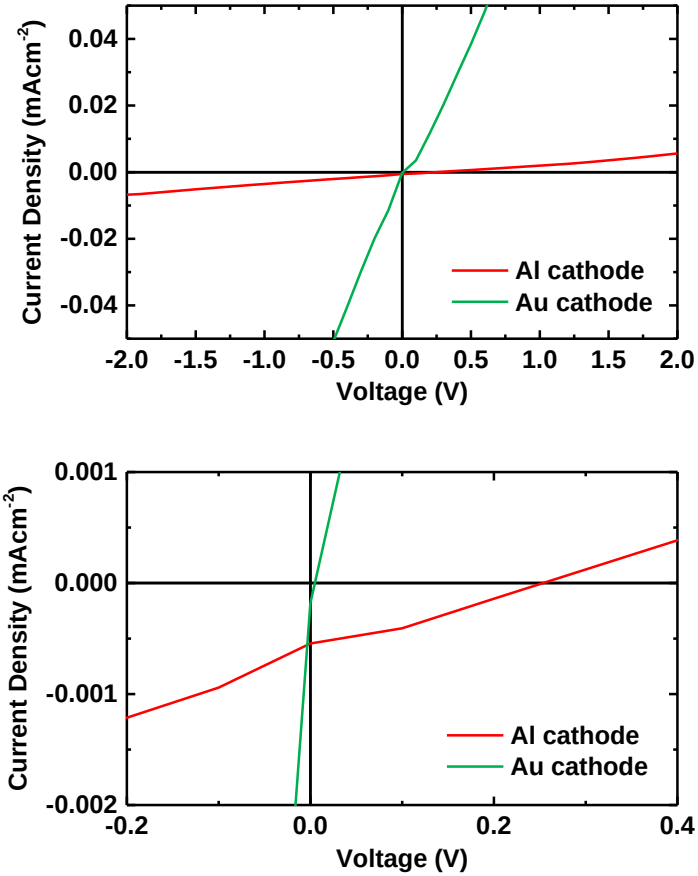


Figure 4-25: Representative illuminated IV curves of 4 nm Au NP devices with an Al or Au cathode, showing the Au cathode produces a larger current (top) but smaller photoresponse (bottom).

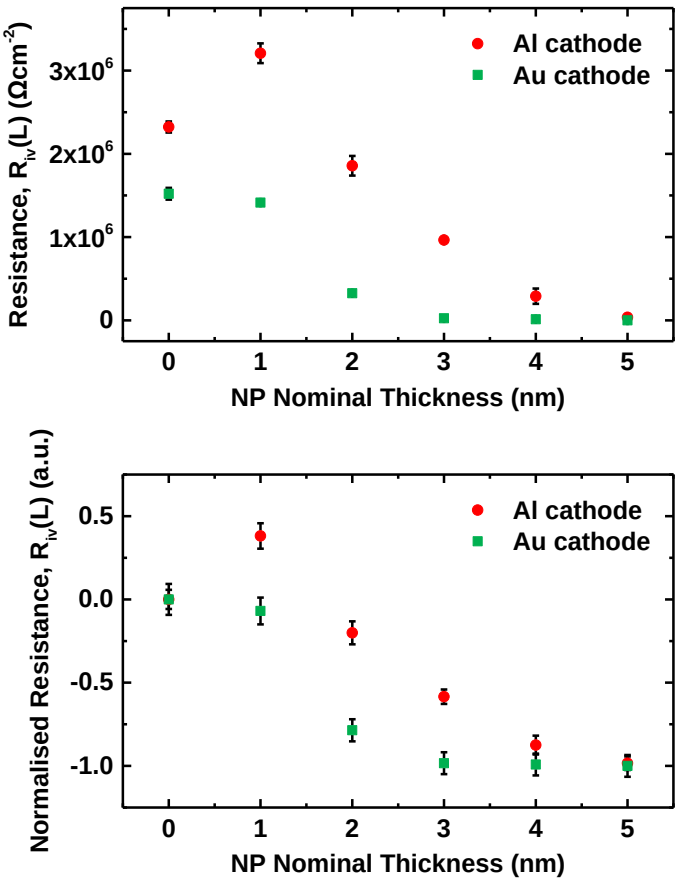


Figure 4-26: The average resistance values from illuminated IV curves of Au NP devices with an Al or Au cathode and various nominal thicknesses of NPs. Both absolute (top) and normalised to 0 nm (bottom) resistance values are shown for trend comparisons.

The Au cathode was consistently found to produce lower resistances than the Al cathode and displayed a similar reducing trend with nominal thickness (Figure 4-26). The reduction in $R_{iv}(L)$ with the Au cathode suggests that direct NP collection is possible with a deep WF cathode and the quantity increases with more NP volume present for metallic transport. However, the increased current may just be a result of the reduced barrier as mentioned above. To account for barrier differences therefore, the resistances were normalised to the 0 nm value and compared (Figure 4-26). The transport is still observed to improve faster and more significantly with the Au cathode, supporting the suggestion that direct NP collection is active.

Transport through a direct NP route is likely to be limited by the continuity of the pathway, necessitating transport via the Alq3 HOMO or deep gap states for collection. The reduction in

resistance with nominal thickness may therefore also stem from increased NP percolation, which could potentially eventually short the two electrodes at high enough nominal thicknesses. The predicted height of a 5 nm NP is under 6 nm for Au and Ag (Section 4.3.2), making shorting appear unlikely with a 100 nm Alq3 layer, although, the ITO surface roughness and any cathode penetration increase this likelihood. Cross-sectional TEM analysis could be used to directly image the composite components, however, this technique is challenging [339] [342].

These observations suggest some non-organic route partially contributes to the current collected in composite devices [322]. The results show more collection with a deep cathode WF better aligned to the NP Fermi level, despite this providing less collection from Alq3 excitation. As the route is limited by the volume and percolation of the NPs, the transport is improved more at higher nominal thicknesses. The test conducted does not provide conclusive proof, however, as it is hard to isolate NP transport. Collection from deep gap states is probably necessarily occurring, which may also increase with nominal thickness. Additionally, the extraction barrier reduction with a Au cathode confounds results, as this would also be expected to increase the overall device current measured. To further elucidate different routes contributing to transport, the temperature dependence of the conductivity could be investigated, as organic carrier transport increases with temperature in contrast to metallic conduction.

The new direct NP transport route is therefore generally anticipated to be: lower energy as the cathode WF is deeper, and lower resistance as the transport is metallic, but ultimately the route is continuity limited. The current contribution of the NP direct route is expected to be smaller for the Al cathode as the shallow WF will reduce collection. If this route is contributing, it will be strongest at high nominal thicknesses.

4.4.3 Interface Modification by NPs

Simple Schottky-Mott theory predicts metal-semiconductor interface formation characteristics based on energy level offsets and associated semiconductor band bending (Section 1.2.1) [67] [68]. Based on Fermi level values measured by Kelvin Probe, barrier-free hole and electron collection is predicted for the ITO-Alq3 and Alq3-Al interfaces respectively (Figure 4-27). Therefore, barrier-free carrier collection is anticipated for the single layer device. The device IV characteristics (Figure 4-28), however, contradict the Schottky-Mott theory predictions. The observed rectifying shape shows the presence of a junction limiting current collection until the barrier is overcome at a high positive bias [336]. These findings are consistent with reports that Schottky-Mott theory often fails to predict experimentally measured barrier heights for metal-organic semiconductor junctions [72] [73].

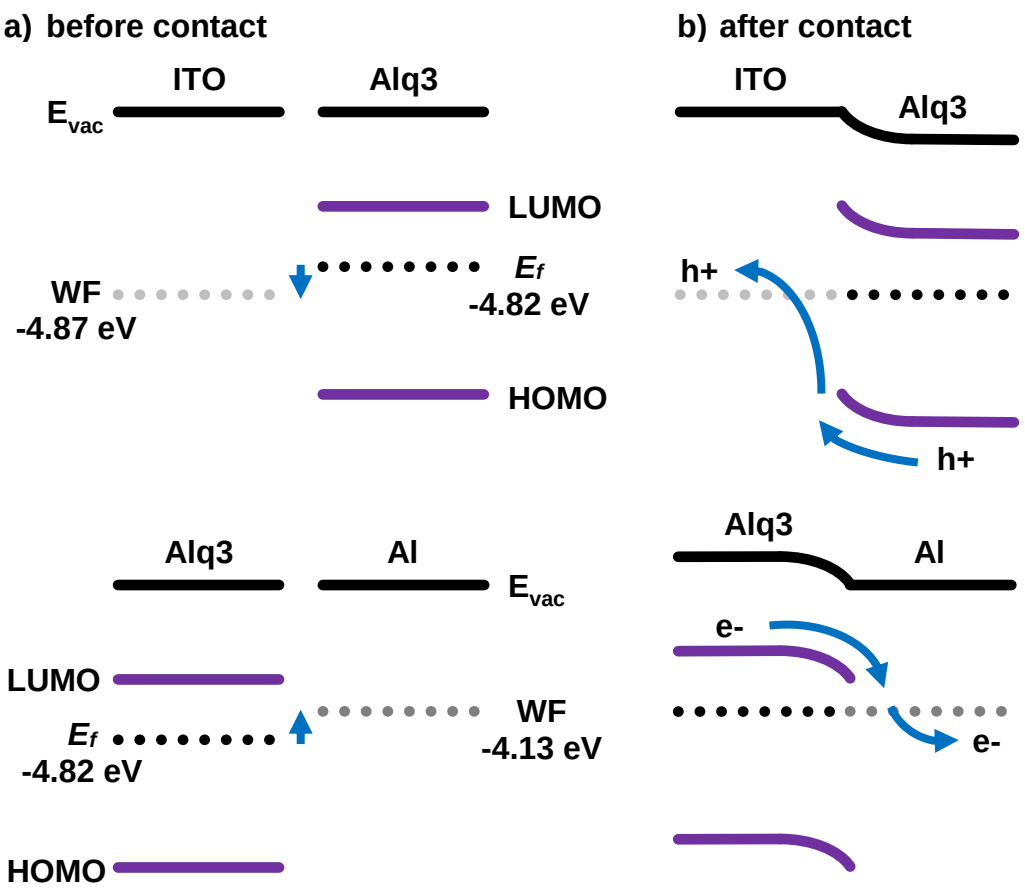


Figure 4-27: An illustrative schematic of Schottky-Mott interface formation for the ITO-Alq3 (top) and Alq3-Al (bottom) device interfaces. The Fermi level-WF offset and associated band bending produce barrier-free extraction in both cases.

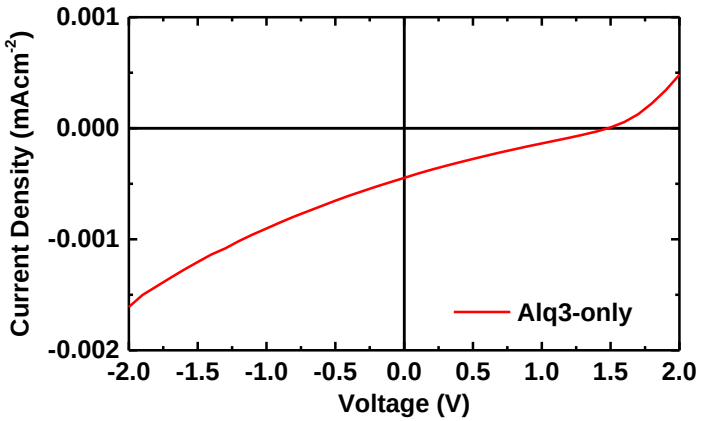


Figure 4-28: A representative illuminated IV curve of an Alq3-only device with an Al cathode, displaying rectifying characteristics.

To reproduce experimental results, the phenomenon of Fermi level pinning often needs to be considered [69] [363] [364]. When an n-type organic forms an interface with a metal, acceptor surface states are created in the bandgap (Figure 4-29 a) [365] [70]. Electron transfer, from higher energy levels into these surface states, shifts and pins the Fermi level deeper [365] [71]. The resulting electron depletion therefore produces upward band bending at the organic surface (Figure 4-29 b), due to the electric field created by the metal-induced Fermi level pinning [365] [70] [71]. The barriers to extraction caused by Fermi level pinning have contributions both from: energy barriers due to the band bending, and transport restrictions due to the surface state carrier dynamics [109]. Al is considered to be a reactive metal and so is expected to produce a large number of mid-gap states penetrating deep into the organic [260]. It has been demonstrated that Al has this effect on Alq3 [297], therefore, Fermi level pinning at the cathode interface provides an explanation for the presence of an extraction barrier.

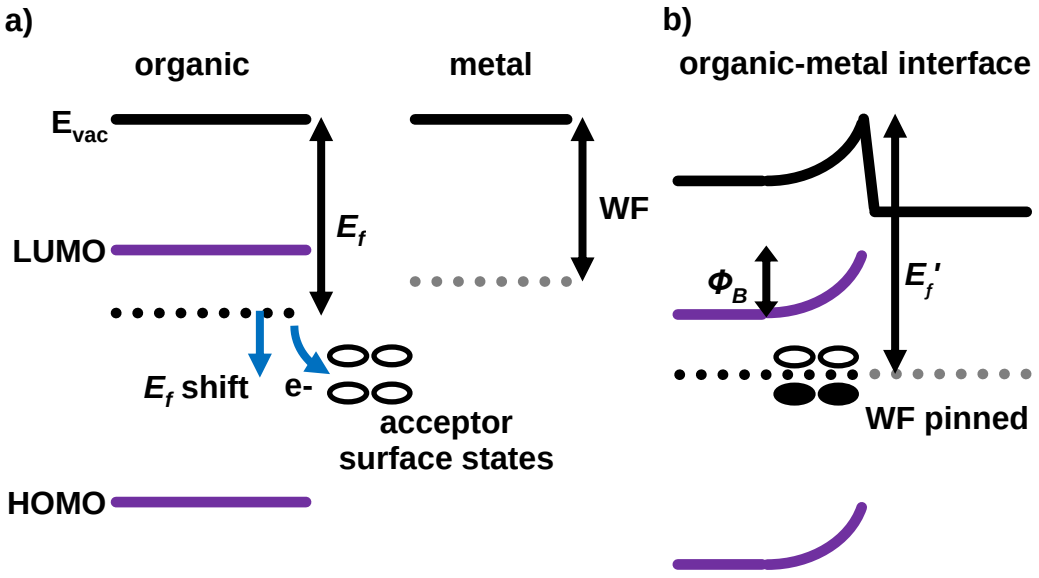


Figure 4-29: An illustrative schematic of the Fermi level pinning process showing a) the effect of surface acceptor states on the E_f and b) the resultant energy barrier (Φ_B) formed due to the band bending.

To test this hypothesis, a device structure with a Au cathode was employed. This reveals the location of the interface that is limiting collection: if no changes occur with the cathode swap,

the extraction barrier is likely to be at the ITO interface. Additionally, it provides a further test of Schottky-Mott or Fermi level pinning interface theory as the two cathode metals have different WFs and reactivities.

Comparing the IV characteristics (Figure 4-30) and extracted parameters (Table 4-4), the Au cathode configuration displays reduced extraction barrier effects. A rectification ratio (*RR*) is calculated from the ratio of the current at +2 V and -2 V, with a value of 1 indicating an ohmic contact allowing identical forward and reverse conduction [336]. The photovoltage (V_{ph}) is identified as the intersection of the IV curve with the x-axis, which indicates the bias at which the energy barrier is overcome. The Au cathode shows an increased forward bias current, leading to a higher *RR*, which demonstrates that the Al cathode interface was limiting carrier extraction. The reduced V_{ph} value shows the extraction limitation was overcome at a lower bias, indicating that the barrier is smaller for a Au than an Al cathode.

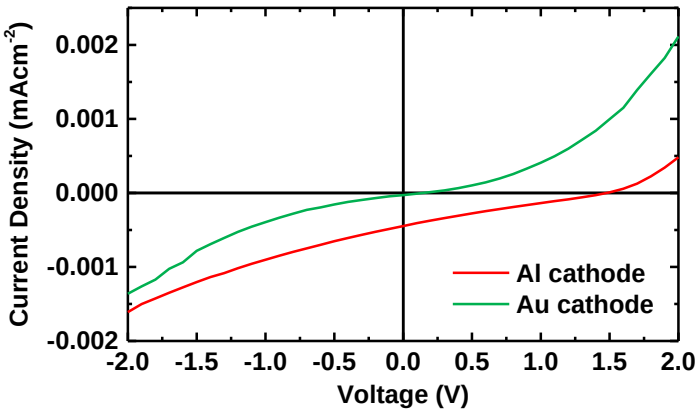


Figure 4-30: Representative illuminated IV curves of Alq3-only devices with an Al or Au cathode, showing different rectifying characteristics.

	Rectification Ratio, *RR* (a.u.)	**Photovoltage, V_{ph} (V)**
Al cathode	0.29 ± 0.02	1.52 ± 0.04
Au cathode	1.48 ± 0.14	0.15 ± 0.01

Table 4-4: The average *RR* and V_{ph} values from illuminated IV curves of Alq3-only devices with an Al or Au cathode.

The measured Fermi level values for Alq3 and Au were almost identical, at -4.82eV and -4.83 eV respectively. Thus, the Schottky-Mott rule predicts minimal band bending and barrier-free electron extraction would be expected. However, based on literature values for the Au WF and Alq3 Fermi level, a barrier would be predicted. From a Fermi level pinning perspective, a reduced barrier to extraction is expected with Au because fewer gap states would be generated [299] [260]. Often reports suggest Fermi level pinning is completely absent for interfaces with Au [105]. These results show that a barrier does exist with a Au cathode, but that it is smaller than the barrier for an Al cathode. Therefore, it is possible that for reactive Al, Fermi level pinning effects need to be considered, but for inert Au, the Schottky-Mott rule may be appropriate.

Differences in the IV characteristics of the two cathodes (Figure 4-30) can be understood by considering depletion region effects (Figure 4-31). An increasing forward bias causes the depletion region to be eliminated and the barrier overcome through electron injection into the Alq3 as the cathode is biased shallower than the LUMO level. Because the Au cathode has a smaller barrier and so depletion region, a lower voltage is required to balance the charge and overcome the barrier. An increasing reverse bias causes electron depletion from the Alq3 as the cathode is biased deeper, this results in a wider depletion region with a higher field and an increased barrier height. Stronger Fermi level pinning with the Al cathode creates a higher field and increases gap states, so more photo-collection produces larger currents [366]. The current is always small, however, because the barrier limits carrier extraction and Alq3 is a weak absorber.

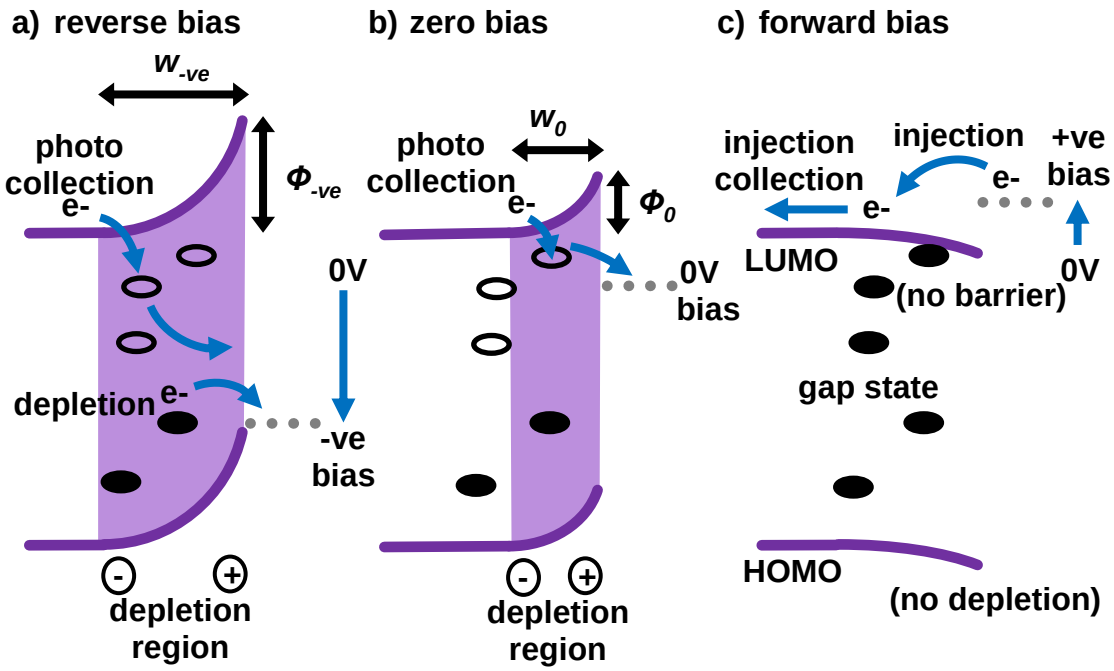


Figure 4-31: An illustrative schematic of carrier collection processes and band bending at a) reverse bias, b) zero bias and c) forward bias. The energy barrier (Φ) and depletion width (w) are labelled.

The shape of the IV curves (Figure 4-32) demonstrates junction improvements with increasing nominal thickness. At higher nominal thicknesses, the linearity and higher currents suggest that ohmic conduction has been activated by the NPs. For Ag NPs, however, the 5 nm curve is not quite fully linear, and the current magnitude is lower than the Au NP equivalent. The *RR* values (Figure 4-33) generally increase and approach 1 at higher nominal thickness, demonstrating the transition to an ohmic contact. For Au NPs, the transition starts at 1 nm and reaches a *RR* of 1 within error at 4 nm. For Ag NPs, however, the *RR* is initially reduced due to photo-doping losses and does not reach 1 which is likely a result of the less favourable transport properties. The V_{ph} (Figure 4-34) is reduced significantly with nominal thickness, demonstrating a reduction in barrier height. Again, the Ag NPs are slower to effect change, as the V_{ph} is constant until 2 nm, and their V_{ph} generally remains higher than that of Au NPs. These *RR* and V_{ph} features suggest that NPs incrementally reduce the junction limiting collection with increasing nominal thickness and that Au NPs are more effective than Ag NPs.

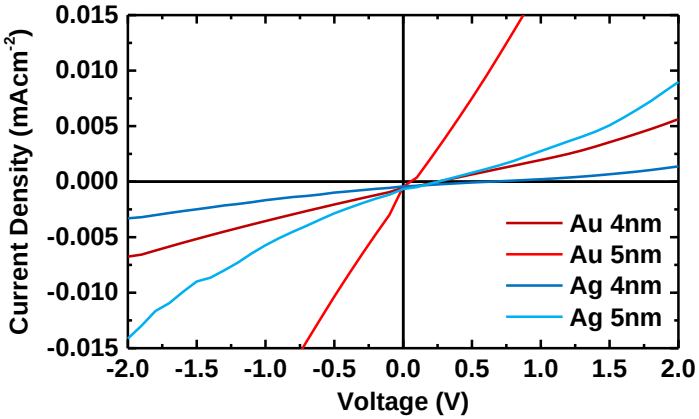


Figure 4-32: Representative illuminated IV curves of Alq3-Au and Alq3-Ag composite devices with 4 or 5 nm NPs and an Al cathode, showing increasingly linear current characteristics.

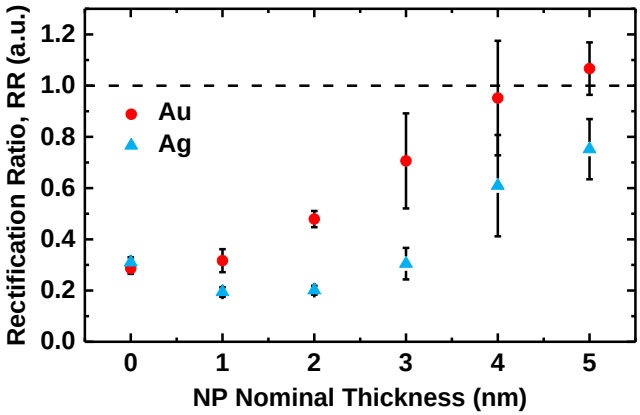


Figure 4-33: The average *RR* values from illuminated IV curves of Alq3-Au (Au) and Alq3-Ag (Ag) composite devices with various nominal thicknesses of NPs. The dashed line at *RR* = 1 indicates the condition for ohmic contact.

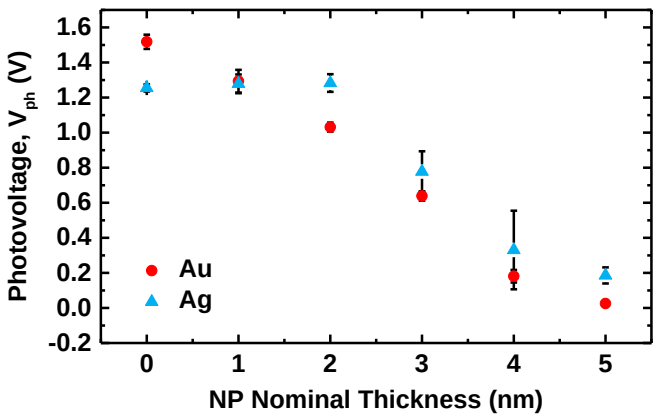


Figure 4-34: The average V_{ph} values from illuminated IV curves of Alq3-Au (Au) and Alq3-Ag (Ag) composite devices with various nominal thicknesses of NPs.

The interface transition observed could be explained by the mechanisms causing the energetic changes measured by Kelvin probe. The Au NPs altering the barrier to extraction sooner could stem from more gap states and doping as observed in the Fermi level shifting shallower sooner (Figure 4-22). In the Fermi level pinning theory, charge transfer doping in shallower states would reduce the width of the depletion region and the barrier height [367]. However, the nominal thickness trends don't match, as the Fermi level is not increased continually whilst the *RR* changes gradually. This could suggest that charge transfer may help initiate change but is not the limiting factor. Schottky-Mott interface formation theory cannot explain the barrier changes observed: the measured composite Fermi levels (Figure 4-22) shift closer to the shallow Al WF, reducing band bending but continuing to allow barrier-free electron collection. The generation of new gap states would allow a parallel transport pathway to circumvent the extraction barrier [241]. This could explain the barrier related nominal thickness trends as continued state creation would allow the route to accommodate more carriers. Additionally, at high nominal thicknesses, a direct NP transport route could allow increased parallel carrier collection avoiding barrier limitations.

To test the theories for extraction barrier elimination with NP additions, the junction changes with a Au cathode were investigated. Ohmic contact without barrier limitations was found to occur sooner: the *RR* was 1 within error for 1 nm (Figure 4-35) and the V_{ph} was negligible (Figure 4-36). However, it is hard to isolate only barrier changes as the NP direct transport route contributes more current for a Au cathode. Schottky-Mott interface formation theory contradicts the barrier changes observed: the measured composite Fermi levels (Figure 4-22) shift further from the deep Au WF, increasing the barrier to electron extraction. For Fermi level pinning, the Au cathode is anticipated to have a reduced barrier to extraction and so it would be overcome more easily by state creation or charge transfer. Differences in Fermi level pinning can therefore explain the changes observed for both Au and Al cathodes.

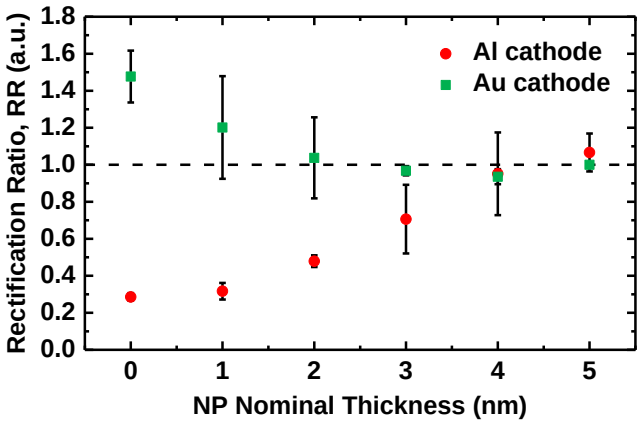


Figure 4-35: The average *RR* values from illuminated IV curves of Au NP devices with an Al or Au cathode and various nominal thicknesses of NPs. The dashed line at *RR* = 1 indicates the condition for ohmic contact.

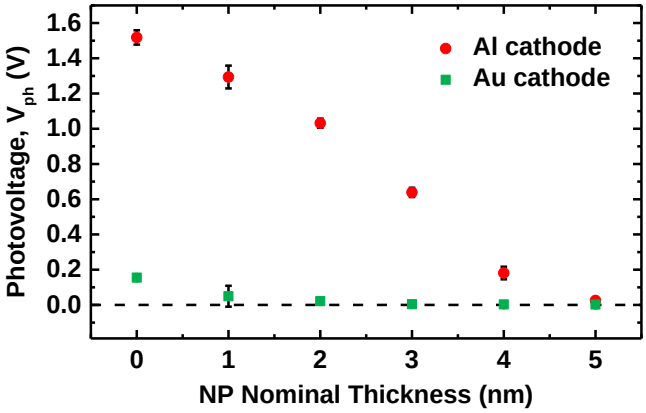


Figure 4-36: The average V_{ph} values from illuminated IV curves of Au NP devices with an Al or Au cathode and various nominal thicknesses of NPs. The dashed line shows V_{ph} = 0 to guide the eye.

Overall, the results suggest a Fermi level pinning induced barrier to extraction is probably circumvented by gap state creation and direct NP transport, although it may possibly initially be reduced by change transfer altering the interface band bending energetics.

4.5 Device Optoelectronics

4.5.1 Photoresponse

Examining the fourth quadrant of the IV curves (Figure 4-37) the NPs are observed to change the photoresponse characteristics. As Alq3 is a weak absorber, device generation is limited so the photoresponse is very small. The photocurrent from illuminated (light) IV curves ($J_{ph}(L)$) (Figure 4-38) displays complex trends with nominal thickness and NP material. This indicates various influencing factors, both positive and negative, which may affect generation, collection and recombination.

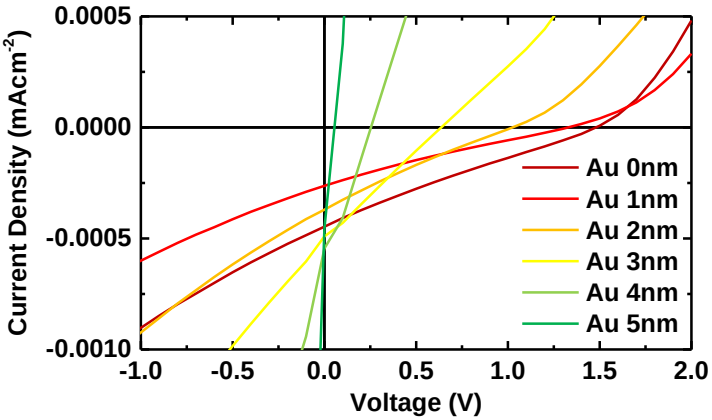


Figure 4-37: Representative illuminated IV curves of Alq3-Au composite devices with various nominal thicknesses of NPs, showing a changing photoresponse.

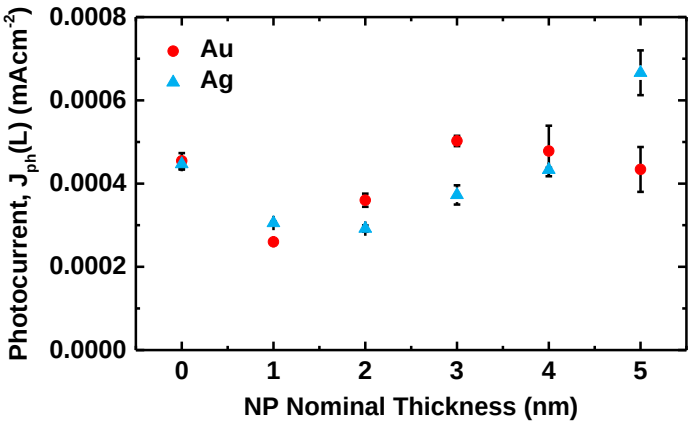


Figure 4-38: The average $J_{ph}(L)$ values from illuminated IV curves of Alq3-Au (Au) and Alq3-Ag (Ag) composite devices with various nominal thicknesses of NPs.

4.5.2 Collection Changes with NPs

The photoresponse (Figure 4-38) depends, in part, on carrier collection processes which are altered by NP additions. The initial $J_{ph}(L)$ decrease observed may originate from exciton quenching, as discussed subsequently (Section 4.5.4). Transport properties improving (Section 4.4.2) is a possible origin of the lower nominal thickness increase in $J_{ph}(L)$ which is larger and faster for Au NPs as expected. The lessening influence of an extraction barrier (Section 4.4.3) may similarly improve $J_{ph}(L)$ with nominal thickness and NP metal. However, if the barrier is eliminated then the depletion region is reduced, and so photo-collection may decrease despite junction improvements [366]. This is a possible origin of the higher nominal thickness $J_{ph}(L)$ decrease seen for Au NPs which had a *RR* of approximately 1 for 4 nm and 5 nm NPs.

Carrier collection was enhanced so significantly by NPs that a 'photocurrent' could eventually be measured in the dark. The dark IV curves were therefore analysed to extract $J_{ph}(D)$, thus probing any underlying pure collection changes contributing to photocurrent trends. The $J_{ph}(D)$ trends (Figure 4-39) show a small positive value for 5 nm of NPs. This is larger for Au NPs which might be expected given they produced better transport and lessened extraction barrier limitations. The $J_{ph}(D)$ emergence at high nominal thickness could suggest the current originates from a direct NP route or that extraction was previously barrier limited. These findings demonstrate that a direct change in dark transport needs to be accounted for.

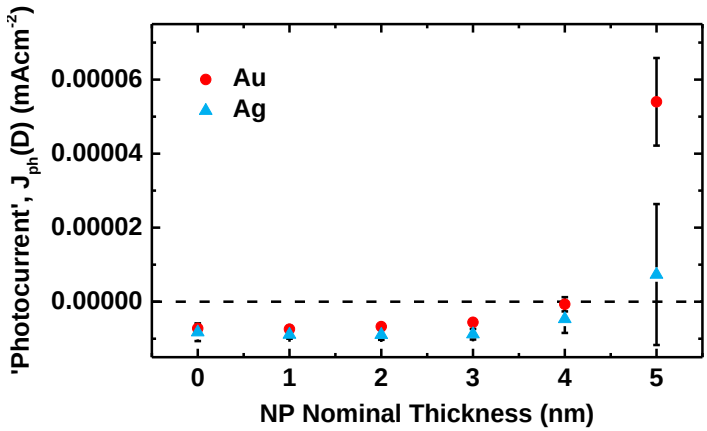


Figure 4-39: The average $J_{ph}(D)$ values from dark IV curves of Alq3-Au (Au) and Alq3-Ag (Ag) composite devices with various nominal thicknesses of NPs. At high nominal thicknesses, positive values are observed, the dashed line shows $J_{ph}(D) = 0$ to guide the eye.

4.5.3 Generation Changes with NPs

The photoresponse originates from carrier generation, which will now be investigated for the individual composite components. Overall generation changes are compared through the $J_{ph}(L\text{-}D)$ parameter (Figure 4-40), where underlying dark transport changes have been subtracted. The 0 nm $J_{ph}(L\text{-}D)$ values show a baseline Alq3 generation contribution exists. The Alq3 absorption characteristics are unlikely to explain the observed $J_{ph}(L\text{-}D)$ trends, however, as small increases in the Alq3 range are probably due to underlying NP absorption, as discussed previously (Section 4.3.1). The observed $J_{ph}(L\text{-}D)$ trends may instead be dominated by photo-collection effects or NP generation.

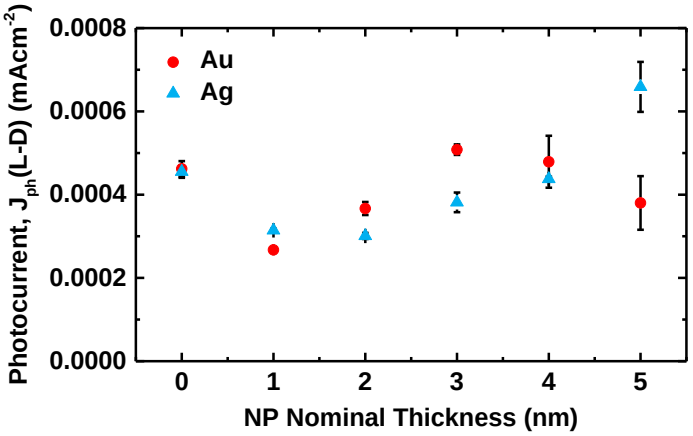


Figure 4-40: The average $J_{ph}(L\text{-}D)$ values calculated by subtracting $J_{ph}(D)$ from $J_{ph}(L)$ for Alq3-Au (Au) and Alq3-Ag (Ag) composite devices with various nominal thicknesses of NPs.

NP absorption increases significantly with nominal thickness, so could be a source of generation improvements. For Au NPs (Figure 4-5), the absorption increases begin to plateau at higher nominal thicknesses. For Ag NPs (Figure 4-7), the absorption increases continue to be large as the nominal thickness increases. Additionally, the plasmonic absorption of Ag NPs is always higher energy than that of Au NPs, which may aid collection through shallow organic states. The NP absorption differences could therefore potentially contribute to the increasing $J_{ph}(L\text{-}D)$ trends at higher nominal thicknesses and may explain some of the decrease observed for Au NPs.

Generally, therefore, generation increases with nominal thickness are primarily expected from NP absorption increases, rather than Alq3. This could possibly contribute to the $J_{ph}(L\text{-}D)$ increase observed after the initial loss but may be modulated by collection effects as the absorption and $J_{ph}(L\text{-}D)$ trends with nominal thickness do not match directly.

Testing was undertaken to determine whether NP plasmonic generation was being collected and so contributing to the photoresponse. The photoresponse was too small for detection at individual wavelengths by EQE equipment, so long pass filters were used to isolate the NP wavelength ranges and measure a filtered photocurrent $J_{ph}(F)$. For Au NPs a 500 nm filter was

used to ensure no Alq3 excitation occurred, which was confirmed by the 0 nm $J_{ph}(F\text{-}D)$ value being zero. For Ag NPs the plasmonic range extends to shorter wavelengths, however, so a 455 nm filter was used to maximise the NP plasmonic contribution despite a small amount of Alq3 excitation giving a non-zero value for $J_{ph}(F\text{-}D)$ at 0 nm. These filtering differences prevent direct magnitude comparisons, but mechanistic insights are still possible.

Both Ag and Au NPs showed a positive $J_{ph}(F\text{-}D)$ at various nominal thicknesses (Figure 4-41), providing evidence for the contribution of plasmonic NP generation to the photoresponse. It is possible that the generation is excitation into modified Alq3 gap states or direct NP plasmonic absorption [368] [283]. The $J_{ph}(F\text{-}D)$ of Au NPs was observed to decrease at high nominal thicknesses despite absorption generally increasing, so collection effects may be limiting the photoresponse here. The cause appears to be a non-negligible $J_{ph}(D)$ which is approximately equal to the $J_{ph}(F)$ resulting in a $J_{ph}(F\text{-}D)$ of zero for 5 nm NPs. It should also be noted, however, that the $Jph(F\text{-}D)$ would be higher for Au NPs if a 455 nm filter was used.

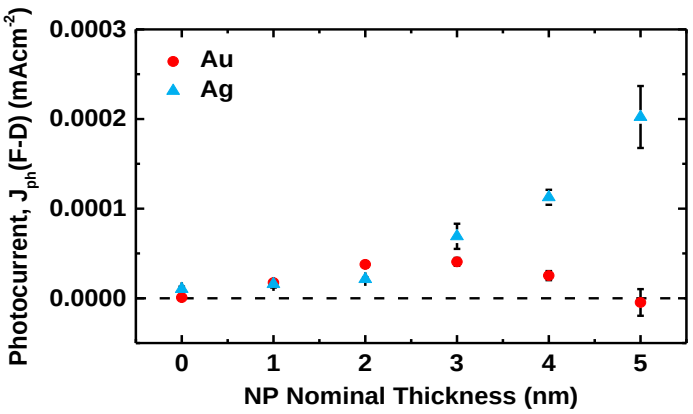


Figure 4-41: The average $J_{ph}(F\text{-}D)$ values from filtered IV curves with $J_{ph}(D)$ then subtracted for Alq3-Au (Au) and Alq3-Ag (Ag) composite devices with various nominal thicknesses of NPs. The dashed line shows $J_{ph}(F\text{-}D) = 0$ to guide the eye.

Some of the decrease could be explained by the slightly reduced absorption between 550 and 750 nm for 5 nm Au NPs. Additionally, the stronger transport and junction improvements gained with Au NPs may come at the expense of filtered generation collection. The *RR* was

approximately 1 for 4 nm and 5 nm Au NPs, so reduced depletion region effects could be limiting collection and increasing recombination [366]. The larger Fermi level change with Au NPs could be due to the creation of more shallow gap states which would increase trap-assisted recombination [179]. These postulated loss mechanisms could not be proved, however, due to measurement and analysis challenges. The dark IV curves did not display a region of constant positive gradient, so fitting the diode equation to extract n and J_0 values was inappropriate, as confirmed by variable n values sometimes over 100 [85] [86] [369]. Intensity-V_{oc} measurements were undertaken to further investigate trap-assisted recombination, however, the small photoresponses of CTL-only devices produced unphysical beta values.

The *Jph(F-D)* results therefore provide evidence that the high nominal thickness trends in *Jph(L-D)* originate from NP generation effects. They also suggest that collection changes modulate generation differently for Au and Ag at high nominal thickness.

4.5.4 NP Related Losses

The initial $J_{ph}(L)$ reduction (Figure 4-38) may originate from an Alq3 generation related mechanism, as the feature is absent from $J_{ph}(D)$ and $J_{ph}(F\text{-}D)$ trends. NPs embedded in an absorbing organic medium can cause exciton quenching [370]. The excitons couple to the NPs, where additional radiative and non-radiative decay processes accelerate recombination [343]. PL testing was undertaken to probe changes in Alq3 radiative recombination rates with NP incorporation. Alq3 was excited at a wavelength of 405 nm and the PL emission peak was monitored at 525 nm. The coupling of the Alq3 excitation to the metal NP reduces the magnitude of the Alq3 emission, a process described as quenching.

The PL spectrum of Alq3 (Figure 4-42) shows a strong reduction in emission immediately upon the introduction of 1 nm NPs, which correlates with the drop in $J_{ph}(L\text{-}D)$ at 1 nm. As the nominal

thickness is then increased further, the continued emission reduction is smaller in magnitude. Quenching increases may therefore be outweighed by generation and collection enhancements at higher nominal thicknesses, allowing $J_{ph}(L\text{-}D)$ to increase again. The peak emission magnitudes are broadly similar between Ag and Au NPs (Figure 4-43), which supports quenching as the origin of the comparable initial drops in $J_{ph}(L\text{-}D)$. The quenching of Alq3 PL is reported to be atomic in nature and metal WF independent [371], which explains the immediate and similar quenching observed with Au and Ag.

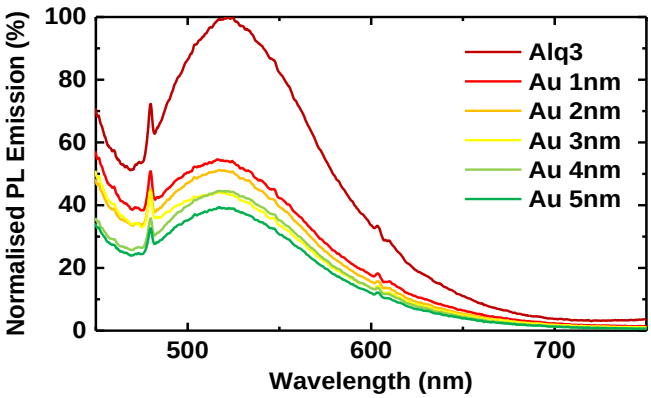


Figure 4-42: The PL emission spectrums of Alq3-Au composite layers with various nominal thicknesses of NPs, showing a reduction in Alq3 emission at 525 nm.

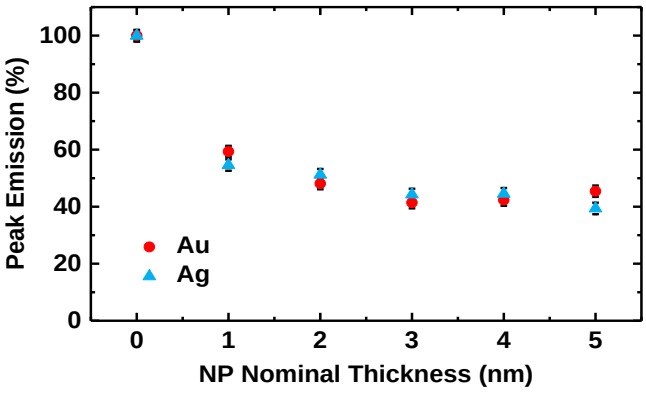


Figure 4-43: The peak emission magnitudes calculated from the PL emission spectrums of Alq3-Au (Au) and Alq3-Ag (Ag) composite layers with various nominal thicknesses of NPs.

These results provide evidence that at low nominal thicknesses moderate Alq3 recombination via NPs can outweigh any small transport or generation increases to explain the initial reduction

in $J_{ph}(L\text{-}D)$. Furthermore, quenching recombination could provide another mechanism causing V_{ph} to decrease in addition to barrier height reductions [295] [84].

The overall photoresponse trends can now be understood by comparing the different dark, filtered and light contributions to current (Figure 4-44). Initially, the light component is reduced for both due to quenching. At lower nominal thicknesses the Au NPs give a higher photoresponse because the transport and interface properties are better sooner, imparting faster collection benefits. At higher nominal thicknesses the Ag NPs then provide a larger photoresponse due to increases in filtered generation without losses to collection effects, allowing the filtered generation benefits to be retained.

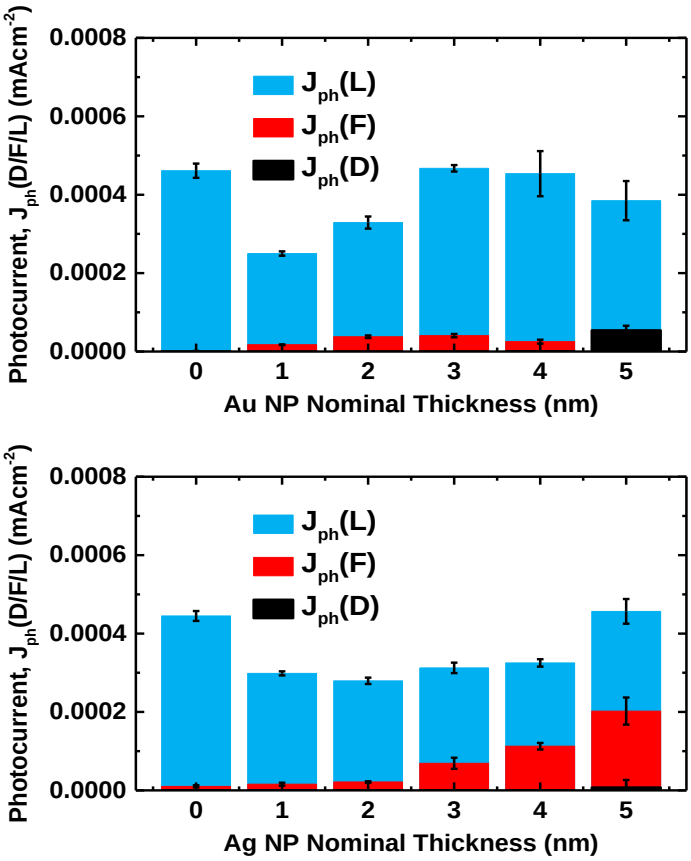


Figure 4-44: The overall average photocurrent divided into $J_{ph}(L)$, $J_{ph}(F)$ and $J_{ph}(D)$ contributions, for Alq3-Au (top) and Alq3-Ag (bottom) composite devices with various nominal thicknesses of NPs.

4.6 Conclusions

NPs were created in an Alq3 organic matrix by the evaporation of thin non-continuous layers of noble metals Ag and Au. The formation of NPs was confirmed by the presence of the characteristic plasmonic resonance in the absorption spectrum. The nominal thickness was varied between 1 and 5 nm to control the NP size, as demonstrated by AFM imaging of discrete NP structures which increased in diameter and height. High-resolution SEM could be used to resolve the NP dimensions in the x-y plane more accurately, although issues with the surrounding organic obscuring the NP structure may complicate the measurement, as encountered with AFM.

The NPs were observed to modify the optics of the composite layer, most notably through a strong plasmonic absorption which increased and redshifted for higher nominal thicknesses. Ag and Au NPs exhibited optical differences, with Ag absorbing more strongly at shorter wavelengths whilst Au absorbed more strongly at longer wavelengths. The Ag NP plasmonic wavelength range could possibly induce near-field absorption increases in Alq3, especially at low nominal thicknesses. However, testing the optical response of NP-only samples indicated that absorption increases in the Alq3 wavelength range predominantly originate from the NPs themselves.

The electronics of Alq3 were also modified by the introduction of NPs, as the reactive NPs cause a chemical interaction which alters the electronic structure of Alq3. States are generated within the organic bandgap, especially at shallower energies, and charge redistribution occurs from the NPs to Alq3, both causing the Fermi level to shift shallower. Au NPs were observed to interact more strongly with Alq3 than Ag NPs, possibly due to a shallower measured bulk Fermi level which indicates more reactivity. Although NP reactivity properties may cause chemical effects to dominate, suggesting Au NPs and Alq3 have a unique chemical interaction.

To measure additional aspects of the changes induced in the Alq3, XPS could identify the emergence of new chemical species and UPS alongside IPES could elucidate associated modifications of the electronic band structure.

The optoelectronic effects induced by the NPs manifested as changes in measured device properties. After a small initial increase, the resistance of devices is reduced significantly by NP additions of increasing nominal thickness. The photocurrent is also affected: when first introduced the NPs reduce the photoresponse, but improvement is subsequently observed at higher nominal thicknesses.

The trends in photocurrent and resistance can be explained by mechanisms which elucidate the role of NPs in carrier generation. NPs were observed to quench Alq3 excitons, which lowers the number of excited carriers decreasing the photoresponse and reduces photodoping effects increasing the resistance. PL measurements showed this effect was strong from the first introduction of NPs and was similar in magnitude for Ag and Au. Conversely, NPs were found to generate photocarriers from plasmonic absorption, although this contribution to the photocurrent was small in magnitude. The photoresponse from the plasmonic spectral range increased with nominal thickness for Ag NPs. For Au NPs, however, collection effects causing photocarrier losses eventually dominated, resulting in a reduced contribution at higher nominal thicknesses. The different absorption ranges of the Au and Ag NPs led to different filters being used for plasmonic photoresponse testing. To directly compare the plasmonic generated photocurrents over a specified wavelength range, filters with identical cut-on wavelengths could be used to test both Au and Ag NPs.

The role of NPs in altering carrier collection mechanisms also contributes to the observed changes in photoresponse and resistance. Results suggest that the NPs create lower resistance

pathways, which outweigh increased trapping effects and thus improve carrier transport. A modified organic route may contribute, as gap states function as new hopping transport pathways and charge transfer results in doping which improves conductivities. Whilst capacitance increases with nominal thickness, (interpreted as trapping), were similar for both NPs, the mobility increases occurred sooner and were larger for Au NPs, possibly because the Au NP interaction with Alq3 was stronger. A new NP-direct route may also contribute, although confounding variables prevent definitive proof. This pathway shows increasing metallic transport with nominal thickness but is always continuity limited by the percolation of the NPs. This pathway is less relevant for the Al cathode architecture as the shallow Al WF doesn't collect as effectively from the deeper NP Fermi level. To probe the contributions of the two pathways further, temperature dependent conductivity measurements could be undertaken. Transport in the modified organic route should be influenced by temperature, whereas the NP-direct metallic transport is expected to be temperature independent.

The NPs also modify collection by diminishing the Fermi level pinning barriers to extraction at the Al cathode interface. The NP to Alq3 charge transfer may slightly reduce depletion region effects, but gap state transport circumventing the barrier is probably a larger factor. The rectification ratios indicate that extraction limitations improve more rapidly for Au NPs, possibly due to the stronger interaction with Alq3.

In a full PV device architecture, a CTL is primarily employed to enhance collection. Direct generation contributions are not generally sought, although indirect improvements are achieved by modifying the active layer's optical profile. When anticipating the application of these composite layers in a PV device, some key differences in the operation mechanism need to be considered. The active layers will now generate carriers, this produces higher photocarrier concentrations and so more photodoping. Also, the donor-acceptor HJ provides exciton

dissociation, meaning the cathode depletion region is relied on less for photocollection. Additionally, the absorption range of the active layer may overlap that of the CTL components. This could reduce Alq3 excitation due to its position at the back of the device and also has implications for plasmonic NP effects which could give near-field enhancements or parasitic absorption losses. These differences mean the translation of single layer effects into PV operation modifications may not be straightforward.

Various PV processes could be affected, both positively and negatively, by the NP roles observed. Fermi level pinning at metal cathodes is a known problem in OPVs, so NP interface effects could be valuable to overcome barriers to extraction. Improved transport with the incorporation of NPs should help increase carrier collection, unless the new routes degrade the CTL's ability to block minority carriers, which could be the case for the NP-direct route with a deeper Fermi level. Additionally, the increased photodoping should be considered as this may improve Alq3 transport anyway, meaning NP-induced gains are less important. NPs could generate additional photocarriers, however, this contribution is probably small compared to the active layer generation, which the NP may also enhance or degrade as discussed in the previous paragraph. The NP quenching effects are possibly a concern as carrier losses are incurred. This effect, however, may be less relevant if Alq3 is not excited as much in the full PV architecture. Additionally, the NPs are physically isolated from the active layer so direct contact with excitons is reduced.

When deciding what embodiment might be most beneficial in a PV architecture, both the NP material and size should be considered. Given CTL generation is less important with the presence of an active layer, the eventual benefits of Ag plasmonic generation are less necessary. As the primary CTL role is collection related, transport and interface effects are more important, so the larger improvements observed sooner with Au NPs may be beneficial. For the

conventional architecture PV device, the use of an Al cathode with a shallow WF means the organic route is expected to dominate; Au NPs are therefore preferred as they interact more strongly with Alq3 than Ag NPs. In terms of losses, both NPs showed comparable effects for mechanism parameters measurable in the single layer configuration. Although the eventual photocurrent decrease for Au NPs is potentially negative from a performance perspective, if mechanistic insight is the investigation's aim then Au NPs appear to provide a wider range of phenomena for exploration. Overall therefore, Au NPs seem to be a more appropriate choice for application in a PV architecture to further understand the effects of NPs on device operation.

Actually achieving PV performance improvements may be a case of balancing gains against losses with Au NPs. Whilst resistances continued to improve with nominal thickness increases, photocurrents were eventually degraded, suggesting an optimum nominal thickness may exist. The value may differ from a single layer device depending on whether transport routes and losses affect minority and majority carriers from the active layer differently to excitons in the Alq3. It is also worth considering that the CTL will be thinner in the PV device, so NP loading is effectively higher which may result in NPs influencing properties more strongly at lower nominal thicknesses.

Chapter 5: Hybrid Charge Transport Layers in Organic Photovoltaic Devices

5.1 Introduction

Chapter 4 demonstrated the ability of metal NPs to modify the optoelectronic properties of single layer organic devices. Chapter 5 explores whether these composite layers can be employed in a full PV structure to enhance device operation. This introduction initially outlines the general principles associated with incorporating metal NPs into OPVs. Without restricting the scope to a particular embodiment, it aims to demonstrate the range of effects which can be conferred on device performance. Subsequently, the discussion focuses specifically on evaporated metal NPs in organic CTLs. This enables a detailed exploration of the operation mechanisms relevant to the experimental work presented in this thesis.

5.1.1 Metal NPs in Organic Photovoltaics

Whilst organic materials have strong absorption coefficients [372], they generally exhibit poor exciton diffusion and low carrier mobilities [373]. These transport limitations impose a thickness constraint on OPV devices, which curtails the amount of incident light it is possible to collect [113]. Additionally, most organic molecules tend to exhibit weaker absorption extending into the IR region which limits broadband generation possibilities [374]. Given the unique optical properties of metal NPs described in the previous chapter (Section 4.1.1), they have been identified as a route to improved light harvesting in OPVs without increasing the active layer thickness [114].

Metal NPs in OPVs have been demonstrated to improve absorption through the LSPR near-field enhancement coupling to the absorber layer and through reflection and scattering increasing the optical path length in the device [115]. The NPs position, as well as size,

generally determines the relative contributions from each of these effects. As well as determining the plasmonic resonance frequency, the NP size dictates the ratio of scatting to absorption efficiency [375]. For larger NPs, approximately over 70 nm in diameter, scattering dominates, whilst absorption prevails for smaller 5 – 20 nm diameter NPs and so associated LSPR enhancements are dominant [376] [377]. As a near-field effect, LSPR enhancements are more significant for NPs located in the active layer [378] [379]. Therefore, LSPR contributions from NPs in CTLs may be more limited [380] but are possible depending on the relative sizes of the CTL and NP [381]. The interface is the obvious limiting case for these two locations and so NPs here may exhibit both enhancement mechanisms [382] [383]. The production of these optical phenomena may be accompanied by concurrent electrical effects which are not yet as well understood [115].

In OPV devices, transport to collection energy level offsets [384] and Fermi level pinning at the metal cathode interface [109] can create barriers to carrier collection. Often CTLs are employed to perform a variety of important roles: from forming ohmic contacts to electrodes [148] and blocking minority carriers [251] to protecting active layers from metal deposition damage [109] and modifying the optical field distribution [79]. However, their transport properties and interface energetics can limit performance improvements [385][307], especially for thicker layers [147] [239]. There are various reports of metal NPs being used within OPVs to improve electronic properties of this variety.

NPs have been used to increase the conductivity of both CTLs [386] and active layers [387], through changes in doping [388] and morphology [380]. When added to active layers, high concentrations may eventually degrade carrier mobilities [387] and NPs are also found to function as exciton quenching sites [370]. Therefore, various coatings are sometimes applied to the NPs to passivate quenching [389] [390] and whilst the contributing factors are not fully

understood an optimum NP concentration is sought [115]. Extraction barriers in OPV devices have also been reduced with the incorporation of metal NPs, through mechanisms of charge transfer [391] and energy level modification [392]. Despite a lack of consensus in the literature about the influence of metal NPs on charge transport [393], there are pieces of evidence to suggest improved device electronics could be achieved.

The broad survey of literature undertaken above showed that metal NPs are most commonly embedded in or adjacent to the active layer to offer optical enhancements in OPV devices. Whilst metal NPs have the capacity to improve conductivities and reduce extraction barriers, reports of these abilities are more unusual. Adding NPs to the CTL may be beneficial as exciton quenching is avoided and the active layer morphology is minimally disrupted, however, the scope for LSPR enhancement may potentially be more limited. In line with the OPV field as a whole, many of the devices reported employ a BHJ architecture where the nanoscale structure significantly influences photovoltaic operation [394]. Therefore, morphology changes conferred with NP additions are a central concern, however, for the PHJs studied herein morphology may be a less critical consideration. The NPs themselves can be created by a variety of fabrication techniques, from colloidal chemistry [395] to electron-beam evaporation [396]. Most reports employ solution synthesised NPs and much of the future outlook appears to rely on associated complex engineering of the NP material, shape and coating [115], which may be less applicable to NPs formed by vacuum deposition.

The surface of NPs synthesised from solution will be covered in a layer of surfactants. Subsequently, passivating ligands are often added or insulating shells grown around the metallic core. Compared to physical preparation methods, this fabrication process and surface modification leads to significant differences in the NPs interaction with the surrounding materials, both during NP formation and device operation [397]. Therefore, to keep this review

relevant to the experimental work presented, the mechanistic details of NP effects on OPV function will be examined for evaporated metal NPs in organic CTLs.

5.1.2 Evaporated NPs in Transport Layers

Examples of evaporated NPs in organic CTLs are more unusual, but the structure has benefits as active layer NP-induced recombination is reduced by keeping the NPs contained to the CTL (Figure 5-1) [370]. When they are reported, the NPs are often located at the front of the optical stack, which causes more parasitic absorption losses than if the NPs were positioned adjacent to the metal cathode (Figure 5-1) [396]. Again, generally for this embodiment optical effects tend to be the main focus, with similar LSPR and scattering mechanisms as the bulk of the literature [282]. Reports investigating electrical effects are rarer, but conductivity changes and interface modifications have been demonstrated, both relying on a metal-induced gap states mechanism to explain the improvements (Figure 5-1) [295] [183]. Therefore, evaporated metal NPs within an organic ETL before the cathode is a novel system for investigation with promising initial demonstrations of optical, transport and interface modifications.

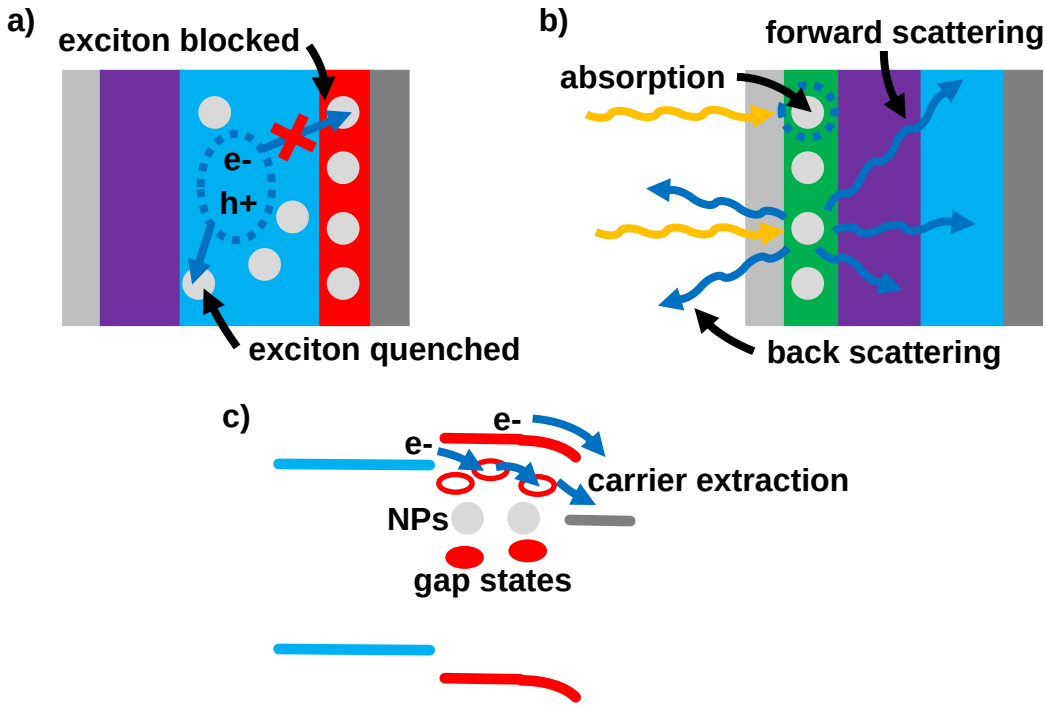


Figure 5-1: Examples of operation mechanisms for CTLs with metal NPs: a) avoidance of active layer exciton quenching, b) optical effects of NPs at the front of the device stack, and c) electrical gap state effects modifying the interface energetics and charge transport.

The first method of optical enhancement by NPs results from reflection and scattering. EQE improvements at short wavelengths have been identified as originating from a selective mirror effect, whereby NP reflection and scattering increases the light intensity in the absorber layers [282]. Stronger reflection can be achieved by increasing the quantity of NPs [282], however, if positioned at the front contact a thin NP layer may be necessary as smaller NPs are required for preferential forward scattering [398]. From Mie theory, as the NP size increases, the scattering cross section increases more rapidly than the absorption cross section, therefore, larger NPs are generally favoured for scattering effects [375]. Simulations of Ag NPs in zinc phthalocyanine (ZnPc) showed that, from a range of 10 - 80 nm, diameters above 40 nm gave a scattering efficiency greater than the absorption efficiency [290]. This understanding was used to increase the ZnPc absorption in a device, where Ag NP size was manipulated through annealing treatments and altered substrate wetting, in addition to the deposition nominal thickness [290].

The second method of optical enhancement by NPs relates to the NPs LSPR. EQE improvements at longer wavelengths in the plasmonic range may be due to optical near-field effects, as the electric field of the LSPR concentrates at the NP-semiconductor interface and optical absorption scales with the square of the field enhancement factor [115]. To achieve increased generation in the active layer, therefore, the NP size must be tuned so the plasmonic wavelengths overlap the absorption range of the adjacent donor or acceptor layer [282]. This has also been successfully demonstrated for Ag NPs and ZnPc, where the effect was found to be strongly proximity dependent, enhancements tailed off as the NPs were positioned deeper in the CTL further from the active layer [282]. Beyond 8 nm of separation, no LSPR improvements could be observed, highlighting the near-field nature of the mechanism [282]. LSPR effects may also be limited for NPs in CTLs because the simulated electric field has been shown to distribute laterally in the plane of the CTL, which suggests that the LSPR would only penetrate the active layer if the NPs were placed directly within it [399].

A modification of the optical response can impact the device electronics at a very basic level, if absorption is increased then the organic layers can be thinned, without loss of generation, to improve transport [282]. More direct and specific electronic effects from NP additions to the CTL have also been demonstrated, however. To improve the series resistance of an OPV device Ag NPs were added to a BCP buffer layer before the metal cathode [295]. The BCP conductivity was increased by the NPs due to the generation of mid-gap states in the organic which served as electron transport channels [295]. Electronic effects have also been demonstrated for Ag NPs in BCP on ITO, where NPs were employed to modify the interface properties [183]. Again, the conductivity of the BCP layer was observed to improve, due to dopant states induced by the NPs [183]. Electron extraction at the cathode was improved by NPs altering the charge distribution at the BCP-ITO interface causing an energy shift of the mid-gap states [183]. These

reports demonstrate the possibility of modifying carrier transport and interface energetics with the addition of evaporated NPs to organic CTLs.

Whilst evaporated NPs clearly have the potential to enhance various aspects of device operation, they can also have a deleterious impact on performance. A common problem is parasitic plasmonic absorption by NPs, this is particularly acute for NPs at the front of the optical stack were backscattering can dominate forward scattering [399]. This effect can be minimised by reducing the NP coverage by depositing thinner nominal thicknesses [290] [400], however, the NP size also controls the absorption range so should be tuned to avoid overlap with the active layer, minimising parasitic potential [398] [282]. However, even when NP plasmonics cause clear photogeneration enhancements, the carrier collection properties can be deteriorated by the presence of metal NPs. Recombination can be increased in devices with NPs due to exciton quenching, which depends on the degree of contact between the metal NP and the active layer [295]. Incorporation in an organic CTL is an ideal way to mitigate these losses, as just a few nm of buffer layer covering the NPs has been shown to suppress quenching, for larger NPs thicker CTLs may therefore be required to prevent penetration into the active layer [183].

The V_{oc} of OPV devices has been observed to be degraded by metal NP additions, even when the J_{sc} and FF are improved [282], and higher nominal thicknesses have been found to give larger V_{oc} reductions [400]. It was suggested that these losses originate from differences between the electrode WF and the NP Fermi level [400]: a NP Fermi level that is shallower (or deeper) than the anode (or cathode) WF will reduce the V_{oc} [290]. To avoid these effects it may be advisable to choose the NP location based on the electrodes relative WFs [295]. It has also been suggested that passivating the metal NP with an insulating layer or deeper (or shallower) WF layer may be a route to limit losses [290].

There are various embodiments reported where the NP gains do not offset the overall losses. This can be the case when small optical improvements are accompanied by worse electronics [290]. It is also often found for larger nominal thicknesses of NPs, where parasitic absorption becomes significant and more penetration causes exciton quenching [183]. Careful optimisation can produce net gains however, for example, a peak performance was achieved when the buffer layer was thick enough to prevent quenching but thin enough to allow LSPR enhancements [295]. The performance trade-offs discussed above emphasise the importance of considering the electrical properties of the metal NPs in the CTL alongside their optical properties.

5.1.3 Hypotheses and Approach

In Chapter 4, NPs were investigated in single layer organic devices and observed to alter the organic's electronic properties, as well as modifying the absorption spectrum, and so induced changes in device operation. If similar effects prevail in a full PV device, NP additions are expected to result in increases to carrier generation and collection, as well as possibly recombination. Measured changes in the rectification characteristics predict that interface formation in the device will be altered by NPs (Section 4.4.3), possibly eliminating an extraction barrier at the cathode contact. Changes to carrier transport may increase current magnitudes (Section 4.4.2), through new routes created by the NP additions, however, there may also be associated photocarrier losses (Section 4.5.1). Optical effects increasing NP plasmonic generation (Section 4.5.3), are expected to be outweighed initially by losses due to NPs quenching Alq3 excitons (Section 4.5.4). However, as the CTL no longer performs the primary absorber role, these generation and recombination changes may have a less significant impact on overall device operation.

In Chapter 5, the NPs are added to the CTL of a full OPV device structure in order to explore performance enhancement possibilities. To probe the mechanism of modification with NP incorporation, the nominal thickness of the deposited NPs will be varied, elucidating the effect of NP size on various device functions. To reveal the role of the Alq3 and its interaction with the Au NPs, and to discover the direct impacts of the Au NPs themselves, devices without the Alq3 ETL will be fabricated for comparison.

5.2 Experimental

The Equipment and Methods chapter (Section 2.2) describes fabrication procedures common to all embodiments. For this chapter, device fabrication was completed using a deposition system designed and built for this research project (Section 2.1.2). The deposition sequence was: MoO_3 1 nm at 0.1 Å/sec (99.97%, Sigma-Aldrich); 6T (alpha-sexithiophene) 60 nm at 0.2 Å/sec (sublimed, Tokyo Chemical Industry UK); SubPc (boron subphthalocyanine chloride) 15 nm at 0.2 Å/sec (85%, Sigma-Aldrich); Alq3 0 or 5 nm at 0.2 Å/sec (99.995%, Sigma-Aldrich); Au 0 to 5 nm at 0.1 Å/sec (99.99%, Testbourne); Alq3 0 or 5 nm at 0.2 Å/sec; Al 30 nm at 0.1 Å/sec (99.999%, K. J. Lesker).

The Equipment and Methods chapter (Section 2.3) also describes all characterisation methods used. The OPV device active area is 0.02 cm^2 and throughout the chapter, error values represent the standard deviation across 3 pixels on each substrate. For IV characterisation, the voltage was swept between -2 V and +2 V with a step size of 0.1 V and delay time of 100 ms. For EQE characterisation, the illumination spot size was controlled to be smaller than the device active area. For AC Impedance characterisation, impedance-frequency measurements were taken under 100 mW/cm^2 illumination, at biases of -2 V, 0 V and +2 V across a frequency range of 100 Hz to 2 MHz. Impedance-voltage measurements were taken in the dark at a frequency of 200 Hz, the bias was swept from -2 V to +3 V with a step size of 0.1 V. For device absorption

determination, the reflectance-based method of Verreet et. al. was employed [191]. For Kelvin probe analysis, 25 measurements were taken at each of 3 different scanning positions on each sample.

5.3 Device Architecture

The PV architecture (Figure 5-2) was designed based on the understanding of materials interactions gained in the previous chapter. Au NPs were selected over Ag NPs, because they showed a larger change in composite Fermi level initiated at a smaller nominal thickness (Figure 4-22), indicating a stronger interaction with Alq3. This may improve performance, as the gap state route is important for collection to shallow WF cathodes, and may produce larger, easier to measure, device operation changes. Differences in photocurrent trends were also considered: Au NPs displayed a wider variety of features than Ag NPs (Figure 4-38), enabling a greater range of mechanistic phenomena to be explored in PV devices. Additionally, Au NPs produced larger transport improvements which may be key to enhancing CTL operation, whilst the comparatively larger Ag NP generation gains may now be less relevant due to stronger active layer absorption in a full PV architecture.

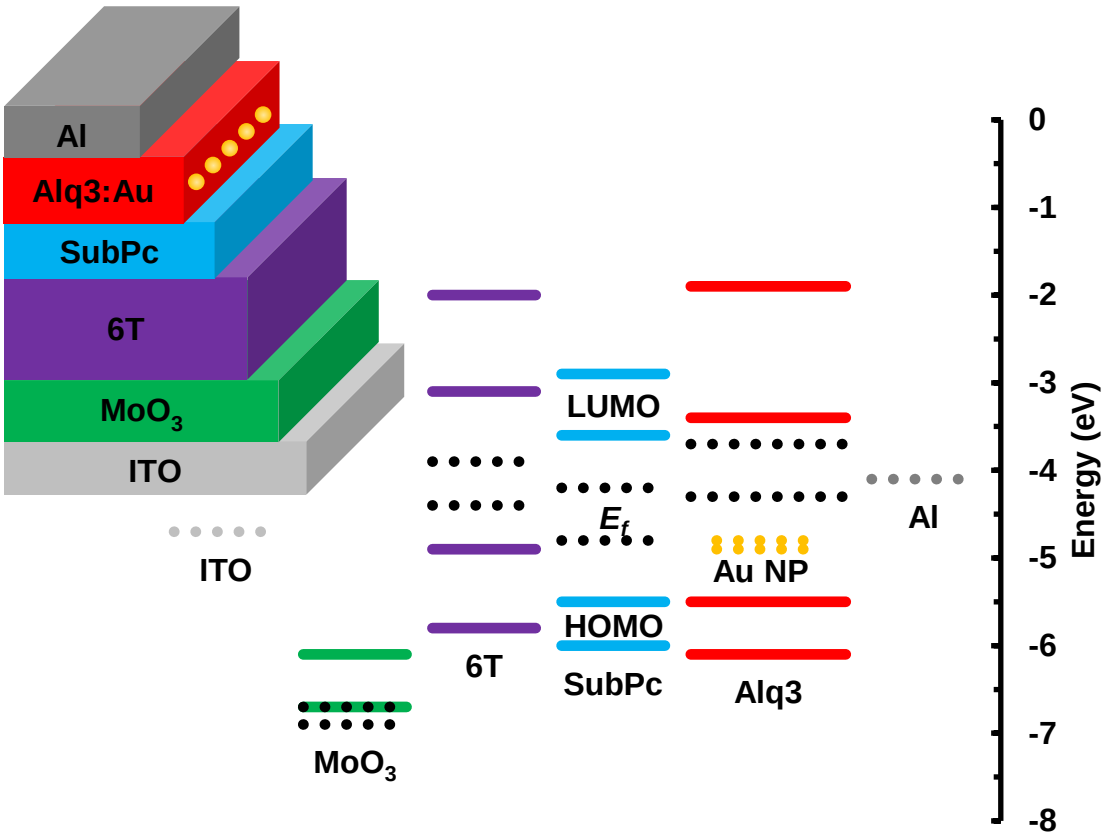


Figure 5-2: A schematic of the device architecture (left) and the energy level positions under vacuum level alignment (right), where an upper and lower bound are shown for the HOMO, LUMO and E_f to reflect the range of values reported in the literature.

A shallow WF Al cathode will be used, to provide a high driving force for collection in the conventional architecture. Although Chapter 4 observed Fermi level pinning at the Al cathode interface, this may not occur with different underlayers and the NPs effectively alleviated the associated extraction limits. The active layer materials were chosen to give a high V_{oc}, because in Chapter 4 NPs were observed to reduce the V_{ph} (Figure 4-34), suggesting the new routes have transport states deeper in energy and may degrade the PV device V_{oc}. Large V_{oc} values of over 1 V have been reported for the 6T-SubPc combination, due to the deep 6T HOMO and shallow SubPc LUMO giving a large donor-acceptor energy offset [401] [47].

5.4 Device Operation

5.4.1 Collection Limited Controls

To understand baseline performances, control devices without (SubPc-Al) and with (Alq3-Al) Alq3 ETLs were characterised. Both devices show s-shaped IV curves (Figure 5-3), which significantly restricts the fourth quadrant photoresponse. This feature indicates that extraction limitations, due to transport restrictions or energy barriers [238] [240] [236] [237], are causing space-charge accumulation within the devices [81], as discussed previously (Section 3.1.3). The correspondingly low *FFs*, of 0.25 for SubPc-Al and 0.19 for Alq3-Al, indicate collection-limited device operation. This is supported by the moderate absorption but limited *EQE* response of SubPc-Al devices (Figure 5-4), showing photocarriers are being generated but not extracted. These collection limits are reflected in high R_s values of 4.7 x 10^4 and 28.1 x 10^4 Ohms/cm^2 for SubPc-Al and Alq3-Al devices respectively. These poor performances are unexpected given the variety of functioning 6T-SubPc architectures reported in the literature [175] [402] [403].

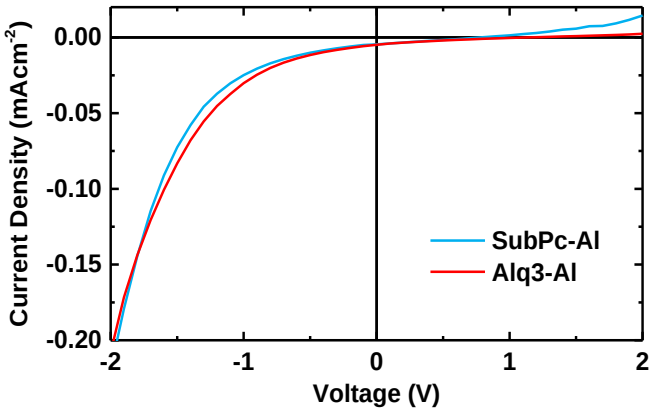


Figure 5-3: Representative IV curves of control devices without (SubPc-Al) or with (Alq3-Al) an Alq3 ETL. The device structure is ITO-MoO_3-6T-SubPc-(Alq3)-Al.

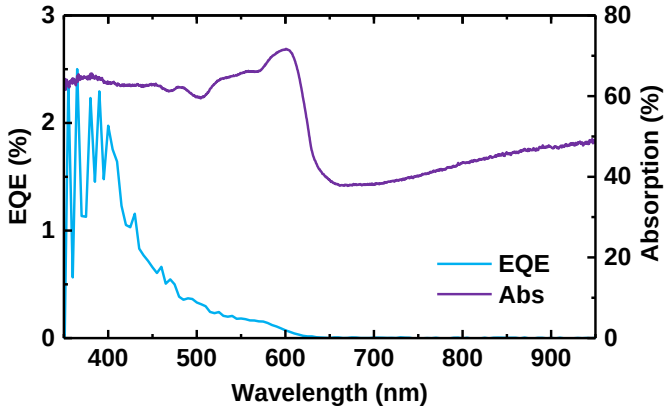


Figure 5-4: The *EQE* (blue line, left axis) and absorption (purple line, right axis) spectrums of the control device without an Alq3 ETL (SubPc-Al).

Alq3 may be an unsuitable ETL for SubPc and Al, as this materials combination has not been presented in the literature. Given the energy level ranges reported, the band diagram (Figure 5-2) indicates that the Alq3 LUMO may possibly be too shallow for effective electron extraction from SubPc. However, SubPc is used successfully with BCP [47] and BPhen [175] ETLs, which have comparable LUMO energies to Alq3 [153]. Whilst there are slight performance differences, BCP, BPhen and Alq3 are similar and operate effectively in various PV architectures [153] [166] [404]. Alq3 can improve ohmic contact to Al cathodes [404] and demonstrates lower R_s values than BCP and BPhen [153]. These reports provide evidence that Alq3 could be an effective ETL for SubPc and Al.

The performance limits observed could be due to Fermi level pinning, discussed previously (Section 4.4.3). Depositing shallow WF cathodes on organic layers can induce Fermi level pinning, causing extraction limits in OPVs [109]. This results in: energy barriers due to interface band bending and transport restrictions due to surface state carrier dynamics. Under these circumstances, the V_{oc} is determined predominantly by the organic energetics and is almost independent of the cathode WF [365]. Al can induce gap states in Alq3 [297], this could create Fermi level pinning extraction limits at the cathode interface. Different fabrication conditions can significantly alter the organic density of states [405], affecting interface formation

processes. This could explain the performance limits observed here despite literature reports of effective Alq3-Al interfaces [404].

Electrical characterisation was undertaken to test the Fermi level pinning hypothesis. Whilst the V_{oc} has complex influences, it originates from the donor-acceptor HOMO-LUMO offset and is determined by the relative electrode WFs for non-ohmic contacts [406]. Despite having the same HOMO-LUMO offset and cathode WF, the Alq3-Al device shows larger V_{oc} values (Table 5-2). This V_{oc} dependence on the organic-metal interface is characteristic of Fermi level pinning [365] [109]. Kelvin probe measurements give Fermi levels deeper than literature values (Table 5-1), especially for Alq3. This could indicate Fermi levels shifted towards deep Al-induced acceptor states [297], which would produce upwards interface band bending, forming energetic barriers. Whilst the literature discrepancies may originate from different measurement techniques [352] or sample structures [407], these effects are unlikely to fully account for the deepening observed [408]. These results indicate stronger extraction limits may exist for the Alq3-Al interface.

	E_f Literature Range (eV)	**E_f Kelvin Probe (eV)**	**Minimum Difference (eV)**
SubPc	-4.2 to -4.9 [409] and [410]	-5.167 ± 0.003	0.3
Alq3	-3.7 to -4.3 [411] and [412]	-5.032 ± 0.006	0.7

Table 5-1: A comparison of the Fermi level values reported in the literature and those measured by Kelvin probe. The final column is the calculated minimum difference between the measured and reported values.

The apparent built-in voltage (V_{ms}) and apparent dopant density (N_{ms}) are extracted from Mott-Schottky (M-S) plots (Figure 5-5). In the ideal case of flat bands (Figure 5-6 a), the V_{ms} and V_{oc} coincide. The voltage giving flat bands in the bulk (V_{ms}) also gives no net field at the contacts, and so equals the voltage with no charge extraction (V_{oc}). Experimentally, however, the V_{ms} is often offset from the V_{oc} due to band bending at the contacts [413]. The bending causes a

residual field in the bulk when the net field at the contacts is zero (Figure 5-6 b), and hence results in a bias difference between the V_{oc} and V_{ms} conditions. The V_{ms} is significantly larger than the V_{oc} for both devices (Table 5-2), this would result from band bending in a direction hindering extraction (Figure 5-6 b). The V_{ms} offset is slightly larger for Alq3-Al devices, possibly indicating a larger energetic barrier. The N_{ms} represents the majority (assumed p-type) carrier density resulting from both doping and charge injection [414] [193]. The higher N_{ms} for Alq3-Al devices (Table 5-2) could indicate: increased hole doping, supporting the larger Fermi level difference from literature values, or reduced electron injection, suggesting a larger interface extraction barrier.

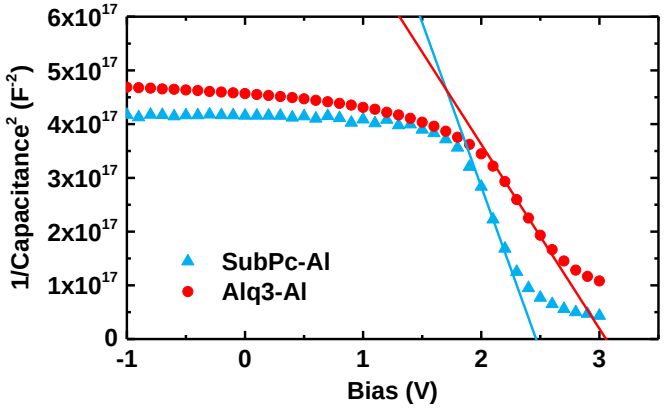


Figure 5-5: Representative M-S plots of control devices without (SubPc-Al) or with (Alq3-Al) an Alq3 ETL. The linear fits used to extract N_{ms} and V_{ms} are shown.

	N_{ms} (cm^{-3})	V_{ms} (V)	V_{oc} (V)	V_{ms} V_{oc} Difference (V)
SubPc-Al	21 x 10^{16} ± 2 x 10^{16}	2.6 ± 0.1	0.8 ± 0.2	1.8
Alq3-Al	33 x 10^{16} ± 2 x 10^{16}	3.0 ± 0.1	1.1 ± 0.1	1.9

Table 5-2: The average N_{ms} and V_{ms} values from fitting M-S plots of control devices without (SubPc-Al) or with (Alq3-Al) an Alq3 ETL. For comparison, the V_{oc} values from IV testing and their difference from the V_{ms} values.

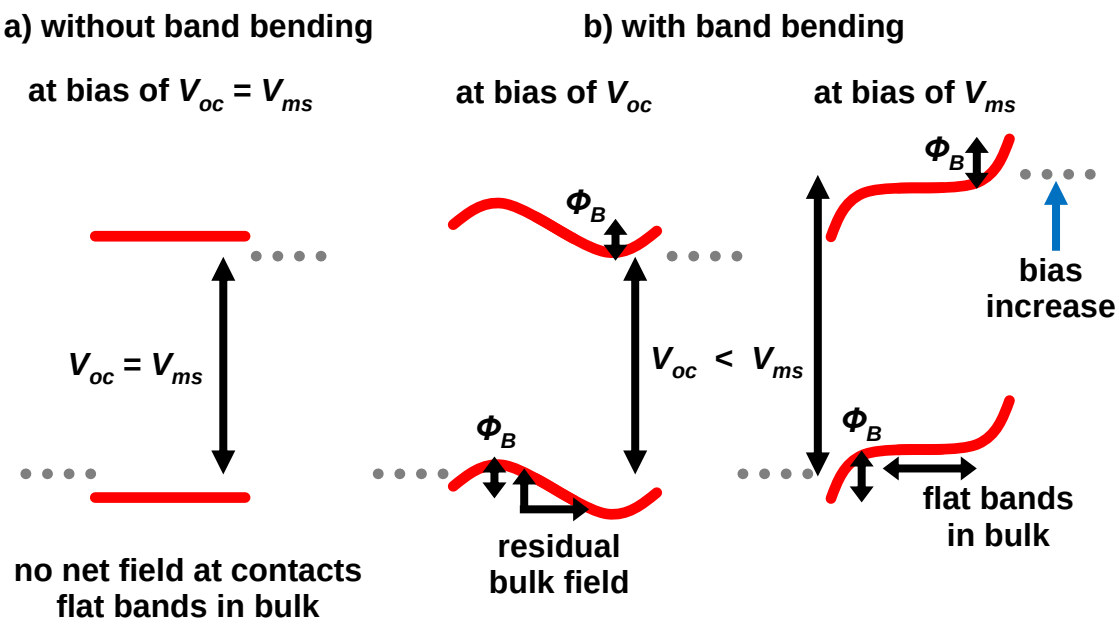


Figure 5-6: A schematic illustrating that band bending at the contacts, which gives energetic barriers (Φ_B) causes a residual field in the bulk which increases the voltage offset required to achieve bulk flat band conditions, resulting in V_{ms} values larger than V_{oc}.

Whilst adding Alq3 ETLs exacerbates extraction limits, improvements to leakage recombination losses are conferred. Fitting dark IV curves (Figure 5-7) reveals lower J_0 values for Alq3-Al devices, alongside improved R_{sh} values (Table 5-3). This suggests Alq3 reduces recombination through inhibiting leakage currents [86] [415], possibly by performing various buffer layer roles, as discussed subsequently (Section 5.6). Therefore, Alq3 may be beneficial to PV operation if NP additions can improve the interface energetics and transport properties currently limiting extraction due to Fermi level pinning.

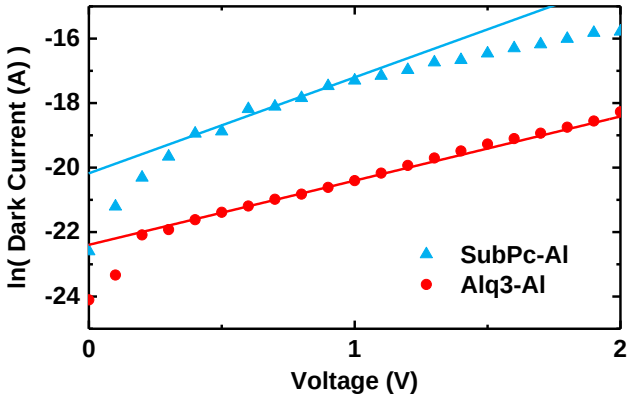


Figure 5-7: Representative dark IV data of control devices without (SubPc-Al) or with (Alq3-Al) an Alq3 ETL. Linear fits used to extract J_0 are shown.

	R_{sh} (Ω/cm^2)	J_0 (mA/cm^2)
SubPc-Al	1.9 x 10^6 ± 2.7 x 10^6	47 x 10^{-6} ± 42 x 10^{-6}
Alq3-Al	4.9 x 10^6 ± 0.7 x 10^6	7 x 10^{-6} ± 3 x 10^{-6}

Table 5-3: The average R_{sh} and J_0 values of control devices without (SubPc-Al) or with (Alq3-Al) an Alq3 ETL.

5.4.2 NP Performance Enhancements

After the control devices had been characterised and understood, a composite ETL of NPs and Alq3 was employed, with the intention of improving performance. The IV curves of devices with composite ETLs reveal substantially larger fourth quadrant photoresponses than those of the control device (Figure 5-8). With increasing nominal thickness, the IV curves transition from s-shaped to fully rectifying characteristics. This demonstrates that the NPs eventually completely alleviate the extraction limitations, due to transport restrictions and energy barriers, previously causing a space-charge accumulation to dominate the IV response [81]. The 0.5 nm device still shows s-shaped IV features, but the larger current magnitudes and more positive voltage position of the kink both suggest the accumulated space-charge is reducing [81]. The extraction limitations remaining for the 0.5 nm device may be caused more by transport dynamics than by energetic barriers, as discussed subsequently (Sections 5.5.1 and 5.5.2). The NP additions clearly relieve the photocollection limitations observed in the control devices. The

device parameters (Figure 5-9), however, show a trade-off between extraction current and voltage. More carriers are collected, as J_{sc} increases, but each is at a lower energy, as V_{oc} decreases.

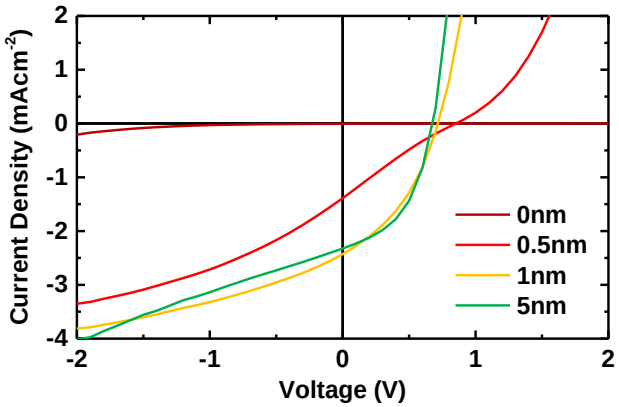


Figure 5-8: Representative IV curves of devices with an Alq3 ETL and various nominal thicknesses of NPs. The device structure is ITO-MoO_3-6T-SubPc-Alq3-NP(x)-Alq3-Al.

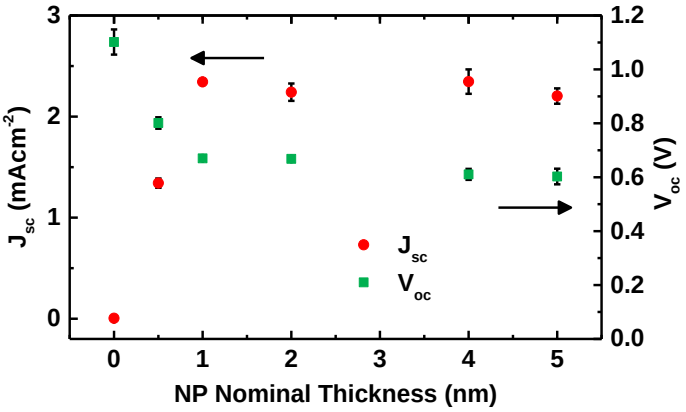


Figure 5-9: The average J_{sc} (left axis, dark red circles) and V_{oc} (right axis, green squares) values of devices with an Alq3 ETL and various nominal thicknesses of NPs.

The observed changes could be explained by the metal NPs inducing mid-gap state creation in the organic (Section 4.1.2) [306] [105]. Alq3 has been shown to interact strongly with Au NPs: chemical reactions modified the Alq3 electronic structure and charge transfer to Alq3 created new organometallic species [184]. These characteristics suggest that the incorporated Au NPs could create and fill new electronic states in the Alq3 ETL.

The effects of these new states can include changes to carrier dynamics and interface energetics in PV devices. Gap states near the Fermi level can act as alternative transportation channels [241] and below the LUMO can provide appropriate energy levels for electron extraction [416]. Therefore, this mechanism could result in more states at a mid-gap energy to transport through, giving additional collection via lower energy routes. This would be expected to increase the photocurrent whilst reducing the photovoltage, as observed in the J_{sc} and V_{oc} trends (Figure 5-9).

To test the hypothesis of mid-gap state creation and filling, measurements of electron occupation energy and charge density were conducted. The Fermi level position (Figure 5-10) becomes shallower with the introduction and increasing nominal thickness of NPs. This indicates new generation of shallow gap states or an increased filling of existing states [184] [417]. Given the Fermi level is probably pinned initially, an increase in filling is likely necessary to effect a significant change in position. The N_{ms} values (Figure 5-11) show a reduction in the carrier density of holes following the incorporation of NPs. This could be caused by n-doping of new donor states or from electron injection due to interface barrier reduction [414]. Fitting of dark IV curves returns n values greater than two for all nominal thicknesses, indicating defect-rich devices [418].

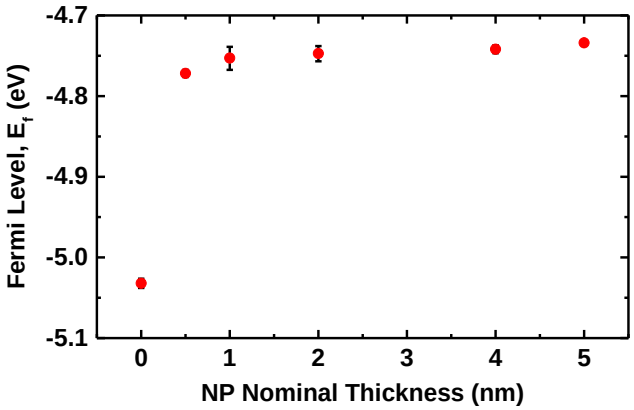


Figure 5-10: The average Fermi level position of the composite layer for devices with an Alq3 ETL and various nominal thicknesses of NPs.

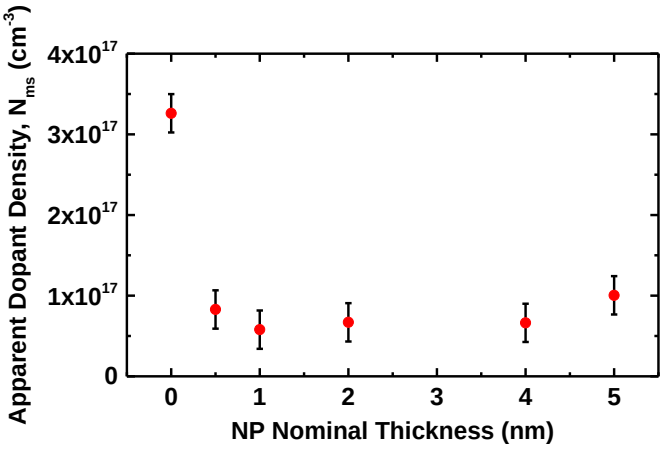


Figure 5-11: The average N_{ms} value from fitting M-S plots of devices with an Alq3 ETL and various nominal thicknesses of NPs.

The IV, Fermi level and N_{ms} trends observed suggest a mechanism of state creation and filling with specific characteristic features. The introduction of NPs may induce the creation of states within the organic bandgap, some of which have donor character (Figure 5-12 a) [184]. Filling of mid-gap states, or just creation of shallow states, would move the Fermi level closer to the LUMO, which is supported by the Fermi level shifting shallower (Figure 5-10). Donor states would reduce the hole density in the device, as is observed in the reduction of N_{ms} (Figure 5-11). Additionally, filling of surface states and creation of transporting gap states would reduce the effects of interface extraction limits, leading to the observed evolution of rectifying IV characteristics (Figure 5-8).

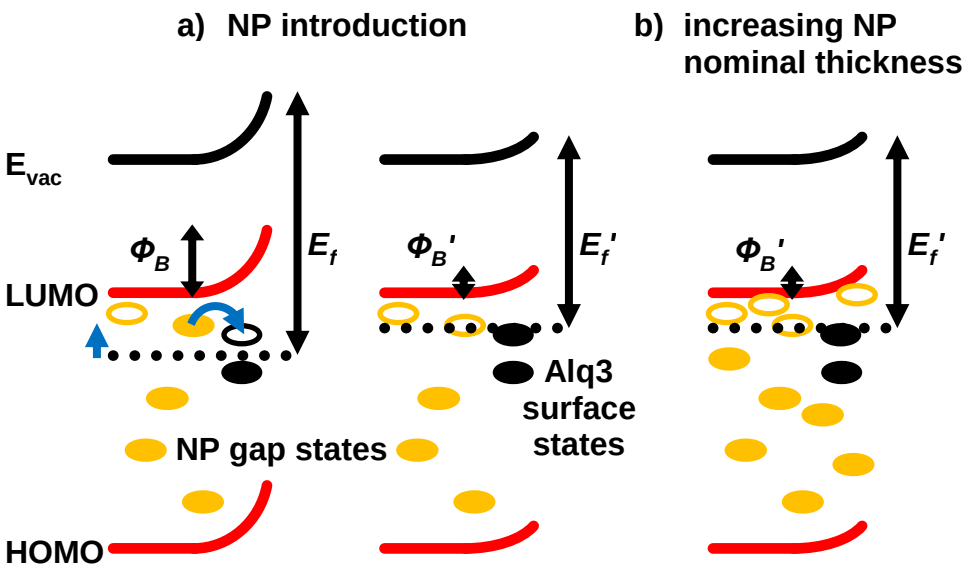


Figure 5-12: A schematic of the proposed mid-gap state creation and filling with the introduction and increasing nominal thickness of NPs, showing the effect on the Fermi level position and energetic barrier (Φ_B).

It is intuitive that with increasing nominal thickness of NPs, the process of state creation and filling will continue, as the saturation condition of continuous film formation is not met. As the nominal thickness increases NPs will grow in size and coalesce, both of which reduce the surface area to volume ratio and therefore may reduce the rate of state creation. A curtailment of change, or indeed a plateau, is observed in each of the parameters, which is consistent with a reducing generation rate. The plateauing behaviour observed for Fermi level and N_{ms} values could indicate minimal changes in gap state distribution or character. However, it may be that a high density of existing states masks any subtler changes with increasing nominal thickness. Overall, it is possible that the creation of states persists at a reduced rate and with an approximately similar energy distribution and character as the nominal thickness increases (Figure 5-12 b). For more direct characterisation, UPS and IPES measurements could be used to probe the presence of gap states in organic thin films.

5.5 Role of NPs

5.5.1 Performance Limit Lifted

A mechanism through which NPs could increase collection is the removal of extraction limits that were created by Fermi level pinning in Alq3 surface states at the Al cathode interface. To investigate the potential presence of interface extraction limits, AC impedance measurements were analysed using ECMs, where model elements represent specific features of device operation. The full AC impedance fitting results are presented in the appendix (Section B.1). The IV properties are dominated by the extraction limitations at 0 V, where no applied bias assists the built-in voltage to overcome the space-charge field restricting photocollection. Therefore, the impedance data used for fitting interface extraction models was measured at this voltage.

For the analysis of PV devices, it is common to employ a simple model of a resistor in series with a parallel R-CPE combination [357]. The CPE models non-ideal capacitor behaviour, including resistive features and processes occurring over a range of timescales. We will call this equivalent circuit, -R-[R-CPE]-, the ‘PV-conventional’ model. The PV-conventional model was able to appropriately describe the impedance features of 1-5 nm devices. The correspondence between the fitting line and measured data points for the 1 nm device is a representative example (Figure 5-13 c). However, the PV-conventional model was clearly unsuitable for devices without NPs (Figure 5-13 a) and for the 0.5 nm devices. The fitting line deviates from the measured data points, suggesting additional circuit elements are required.

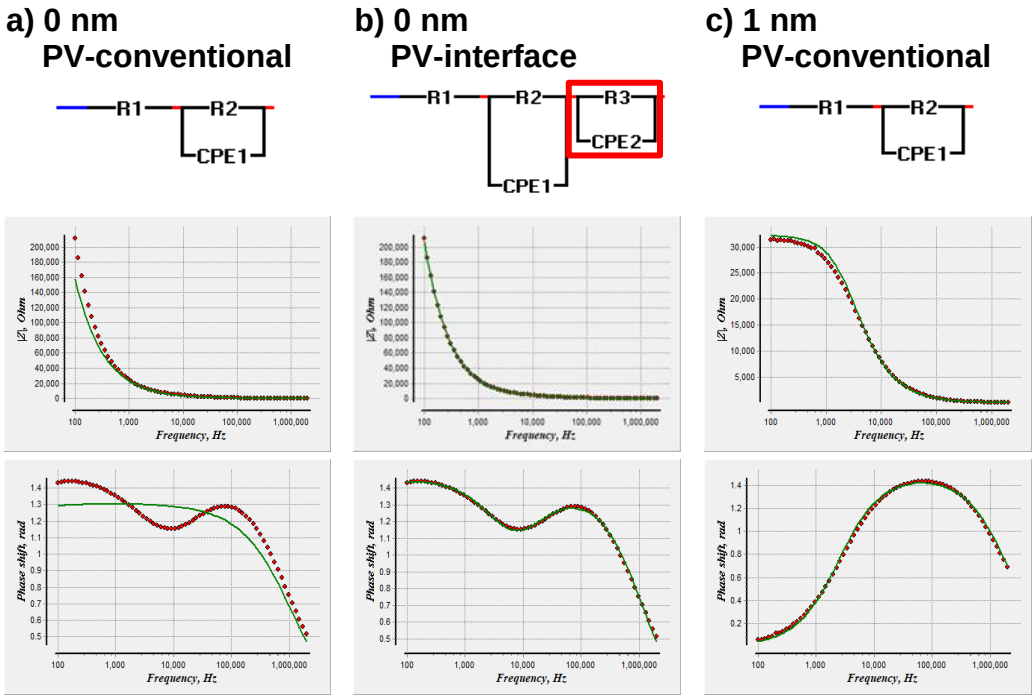


Figure 5-13: ECMs and representative Bode plots showing a comparison of the fitting results (green line) to the measured data points (red circles) of devices with an Alq3 ETL for: a) a 0 nm device with a PV-conventional model, b) a 0 nm device with a PV-interface model, and c) a 1 nm device with a PV-conventional model.

General interface recombination processes, related to carrier energetics or dynamics, can be represented by a parallel R-CPE combination fitting the low-frequency region [419] [420]. Adding this element in series with a standard PV model has specifically been used to model interface extraction limits caused by Fermi level pinning in surface states [109]. We will call this equivalent circuit, -R-[R-CPE]-[R-CPE]-, the 'PV-interface' model. The fit for devices without NPs is significantly improved with the PV-interface model (Figure 5-13 b), suggesting the additional low-frequency feature is due to interface extraction related recombination. The 0.5 nm devices also required the PV-interface model to fit the impedance data accurately, as expected given the persistent s-shaped IV characteristics (Figure 5-8).

For consistency, and in an attempt to improve our understanding of device operation, the PV-interface model was applied to all nominal thicknesses of NPs. A more detailed discussion and the results of the universal PV-interface model fitting can be found in the appendix (Section

B.2). Overall, the universal fitting test provided evidence that: it is appropriate to use the PV-interface model for 0-0.5 nm devices but the PV-conventional model for 1-5 nm devices, and that fitting the PV-interface model at all nominal thicknesses cannot reasonably provide any further mechanistic insights. Therefore, the results from fitting only the 0 and 0.5 nm devices with the PV-interface model will be discussed.

R and *C* values were extracted from the additional model elements used for the 0 nm and 0.5 nm devices (Table 5-4). The *R3* interface resistance value decreases, effectively shorting the capacitor more, which is interpreted as the activation of charge transport previously prohibited by interface extraction limits [330]. The 0.5 nm device *R3* value is still relatively high, suggesting that interface transport dynamics still contribute to the extraction limits causing s-shaped IV curves (Figure 5-8). The *C2* interface capacitance value increase with the introduction of NPs. *C2* values, combined with the device area, can be used to calculate the density of surface states [109] [421] [422] [423]. This is found to increase from 3.0×10^{12} to 3.6×10^{12} $eV^{-1}cm^{-2}$ for 0 nm to 0.5 nm devices, supporting the hypothesis of mid-gap state creation with the addition of NPs (Section 5.4.2). These results are consistent with measurements from Chapter 4 (Section 4.4.2), which showed that although NPs increase the capacitance through carrier trapping effects, resistance decreases dominate to give performance improvements.

	R3 **(Ω)**	***C2*** **(F)**
0 nm	$8.1 \times 10^{6} \pm 1.5 \times 10^{6}$	$9.7 \times 10^{-9} \pm 0.7 \times 10^{-9}$
0.5 nm	$4.2 \times 10^{4} \pm 0.3 \times 10^{4}$	$1.2 \times 10^{-8} \pm 0.6 \times 10^{-9}$

Table 5-4: The average *R3* and *C2* interface parameters from the additional R-CPE element necessary to fit the 0 nm and 0.5 nm devices with an Alq3 ETL using the PV-interface ECM.

Overall, the necessity of the additional R-CPE element to fit the no NP and low nominal thickness devices and the change in the resulting fit parameters provide evidence to support the

hypothesis of initial interface extraction limitations which are eliminated with increasing NP nominal thickness.

Extraction limitations may be mitigated by parallel transport in mid-gap states, which increases carrier collection and can circumvent energetic barriers [241] [416]. Whilst the V_{oc} has many influencing factors, it depends on the difference in quasi-Fermi level for electrons and holes, offering a rough guide to their transport energy level difference [84]. Transporting electrons in mid-gap states below the LUMO therefore reduces the V_{oc} [424], making it lower than the HOMO-LUMO offset energy that would result from band-state transport [239]. Between 6T and SubPc, the HOMO-LUMO offset is a minimum of 1.3 V and from 6T to the Alq3 LUMO would be even higher (Figure 5-2). However, the device V_{oc} is 0.67 V with 1 nm NPs. This substantially lower potential difference indicates a degree of mid-gap state transport is likely to be occurring and enhancing extraction [239].

Additionally, energetic barriers can be reduced if the Fermi level is pinned in newly created shallower donor states [70] (Figure 5-12). Comparing the V_{ms} and V_{oc} values (Figure 5-14), for devices without NPs the V_{ms} is far larger than the V_{oc}, but for 1-5 nm of NPs, the V_{ms} is consistently smaller than the V_{oc}. This transition indicates a reduction and reversal of the residual field in the bulk and hence of the band bending at the contacts [413]. This provides evidence for the direct reduction of an energetic barrier to extraction at the contact with the addition of sufficient NPs. The 0.5 nm device shows coincident V_{oc} and V_{ms} values, which suggests that, although no downward bending driving collection is yet present, the upward bending causing an energetic barrier is now gone. Therefore, direct energetic effects are anticipated to contribute less substantially to the extraction limits causing the s-shaped IV curves (Figure 5-8). Extraction limitations may also remain in the 0.5 nm device due to transport restrictions as a high interface resistance persists, as discussed subsequently (Section 5.5.2).

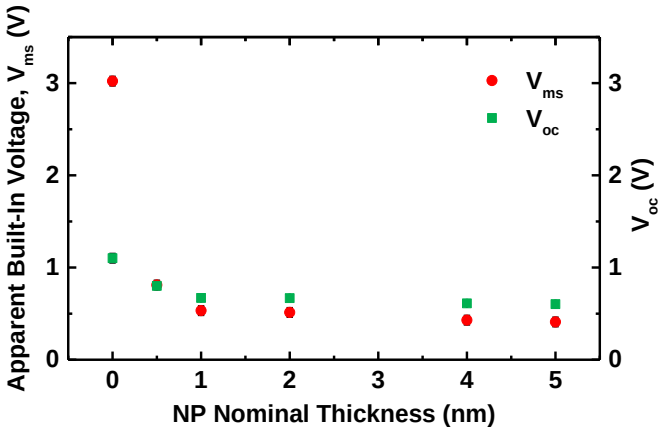


Figure 5-14: The average V_{ms} value (red circles, left axis) from fitting M-S plots compared to the average V_{oc} value (green squares, right axis) from IV testing of devices with an Alq3 ETL and various nominal thicknesses of NPs.

These carrier transport and energy level observations support the hypothesis put forward in Chapter 4 that NPs could reduce barriers to extraction at the cathode interface. The specific mechanisms previously suggested are supported by the V_{oc} results, indicating parallel transport in a modified organic route, and the V_{ms} and N_{ms} trends, demonstrating a direct reduction in the energetic barrier possibly caused by increased doping.

To probe whether the elimination of extraction limits originates from a NP-Alq3 interaction or directly from NPs alone, NP-only devices without an Alq3 layer were fabricated. The operation differences are evident in the IV curves of 4 nm NP devices with and without Alq3 ETLs (Figure 5-15). The NP-only device displays s-shaped IV characteristics, indicating that extraction limitations, from transport restrictions or energy barriers, still exist despite the large NP size [81]. This is evidence against the suggestion in Chapter 4 that at high nominal thicknesses a mechanism contributing to lifting extraction limits could be an alternative pathway via a direct NP route.

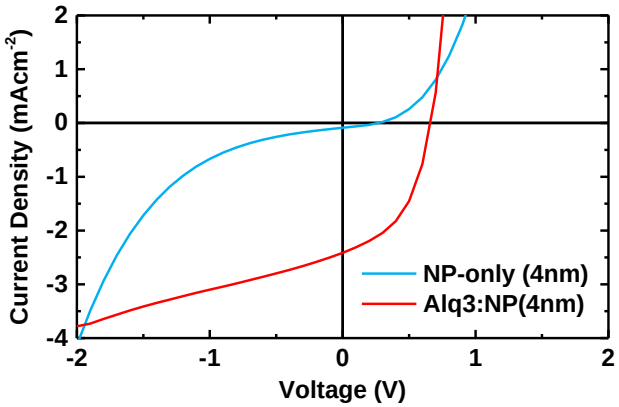


Figure 5-15: Representative IV curves of 4 nm NP devices without (NP-only) and with (Alq3:NP) Alq3 ETLs. The device structure is ITO-MoO_3-6T-SubPc-(Alq3)-NP-(Alq3)-Al.

The moderate current magnitudes achieved once the space-charge field is overcome, suggest transport improvements with NPs alone could contribute somewhat to reducing extraction limitations [238], as discussed subsequently (Section 5.5.2). However, the negative voltage position of the kink suggests that the accumulated space-charge field remains large [81]. Comparing the V_{ms} and V_{oc} values for NP-only devices (Figure 5-16), the V_{ms} over-estimate clearly persists, although it does reduce with increasing nominal thickness. This indicates the bending reduction with NPs alone is not enough to eliminate the energetic barrier limiting extraction [413]. These results indicate the NPs are not simply providing an alternative direct NP route which shorts the Alq3 circumventing the extraction limits, but that the two components must work in synergy to eliminate energetic barriers.

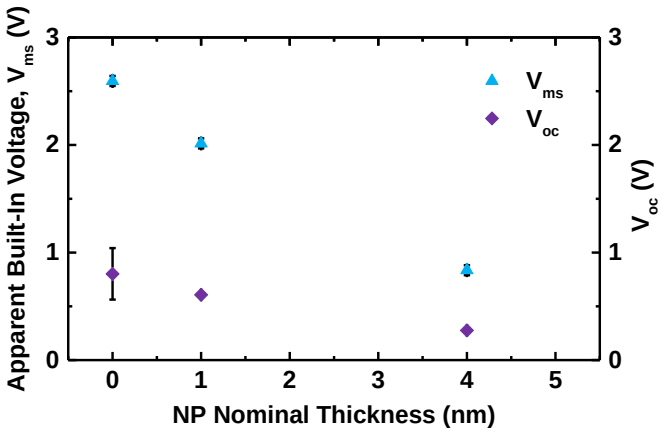


Figure 5-16: The average V_{ms} value (blue triangles, left axis) from fitting M-S plots compared to the average V_{oc} value (purple diamonds, right axis) from IV testing of NP-only devices without an Alq3 ETL and various nominal thicknesses of NPs.

Additional measurements of the NP-only and Alq3 ETL devices were used to compare the NP-Alq3 and NP-SubPc interactions and the state distributions they might generate. Upon the inclusion of 4 nm of NPs, the change in both Fermi level and N_{ms} (Table 5-5) is larger for devices with an Alq3 ETL. This suggests the states from NP-Alq3 interactions could have more donor character or be located nearer the LUMO than those from NP-SubPc interactions. This could be due to differences in the energetic band structure [296] of SubPc and Alq3 or through different interface chemical compositions and molecular orientations [75]. Additionally, the SubPc layer is 15 nm thick whereas the Alq3 layer is only 10 nm, therefore the higher NP:organic ratio may increase the influence of state generation on bulk properties. Fitting of intensity-V_{oc} measurements (Figure 5-17), produced higher beta values for devices with 4 nm NPs and an Alq3 ETL, possibly indicating more gap states were created by the NP-Alq3 interaction and so trapping recombination was increased [179]. The higher number of states created could be due to the NPs being fully embedded in Alq3 for the Alq3-NP-Alq3 sandwich structure, increasing the interface area for interaction. Whereas, when deposited only on top of the SubPc layer, some of the NP interface may be contacting the cathode, reducing the degree of NP-organic interaction possible.

	E_f **difference (eV)**	N_{ms} **difference (cm^{-3})**
Alq3:NP	+ 0.29	- 2.6 x 10^{17}
NP-only	+ 0.23	- 9.2 x 10^{16}

Table 5-5: The change in Fermi level position and N_{ms} value upon the addition of 4 nm NPs for devices without (NP-only) and with (Alq3:NP) Alq3 ETLs.

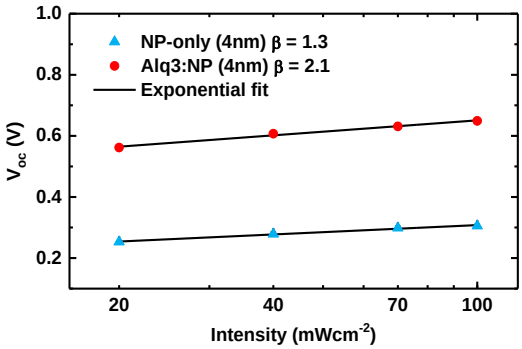


Figure 5-17: V_{oc} values measured at various intensities for 4 nm NP devices without (NP-only) and with (Alq3:NP) Alq3 ETLs. An exponential fit is used to extract the trapping recombination parameter beta [192].

The layer structure may also explain the effects of the NP-organic interaction on device operation. The cathode deposition is expected to produce gap states deep into the organic layer due to the reactivity of Al [260]. The Au NPs, however, are expected to generate less penetrating gap states, hence the location of the NPs determines more specifically where gap state modification occurs [260]. As the NPs are on the surface of the SubPc, they cannot counteract any effects of deep Al penetration, so the extraction limitations may remain. The Alq3 layer, however, has the NPs centrally embedded and so state creation throughout the Alq3 thickness may enable the Al effects to be countered and the extraction limits removed. A different or stronger interaction for the NP-Alq3 structure therefore appears to have a critical role in eliminating extraction limitations. Given that Au NPs produced a larger change in Fermi level than Ag NPs in single layer devices (Figure 4-22), Au NPs may be expected to relieve extraction limits more effectively than Ag NPs when incorporated into the ELT of PV devices.

5.5.2 Transport Improves Performance

Device characterisation was undertaken to understand the effect of NP additions on carrier transport and collection. A low initial alpha value (Figure 5-18) increases with the addition of 0.5 nm NPs which improve interface extraction, as discussed previously (Section 5.5.1). In Chapter 4, it was hypothesised that carrier trapping by NPs might increase the space-charge in the device, hindering transport (Section 4.4.2), but intensity-J_{sc} measurements to prove this were not practical. The improving alpha values of the full PV device, however, suggest that the alleviation of extraction limits dominates any modifications to the device space-charge due to NP trapping.

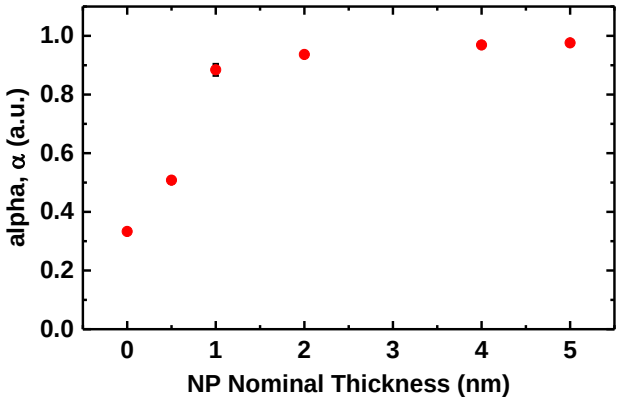


Figure 5-18: The average alpha value from fitting intensity-J_{sc} plots of devices with an Alq3 ETL and various nominal thicknesses of NPs.

A reduction in space-charge recombination increasing alpha could be caused by the increase in electron extraction when an energetic barrier is relieved [425], as was observed with NP additions (Figure 5-14). Whilst less electron pile-up is anticipated in the 0.5 nm devices with the absence of an energetic barrier, the persistently low alpha value shows the current is still fully space-charge limited [270].

A reduction in space-charge recombination could also originate from carrier transport improvements to extraction limitations. With higher nominal thickness, the alpha values (Figure

5-18) continue to increase and approach 1, which indicates balanced electron and hole extraction [270]. The R_s decreases significantly with 0.5 nm NPs and continues to reduce substantially with increasing nominal thickness (Figure 5-19). This indicates carrier transport through the ETL is improving and could explain why 0.5 nm devices still have a space-charge-limited current. The space-charge in the device may be reducing with increasing nominal thickness as the electron mobility is enhanced to match that of holes and so provides balanced collection without extraction limitations [270]. An ongoing creation of gap states with nominal thickness could explain these improvements as a modified organic transport route. Around the Fermi level more states increase the capacity of a parallel transport pathway [241] and pinning the Fermi level nearer the LUMO increases the transport level occupation probability. Transport increases relieving extraction limits to improve device operation suggest that Au NPs are a better choice than Ag NPs for the ETL, as they were observed to give larger transport improvements for a given nominal thickness in single layer devices (Section 4.4.2).

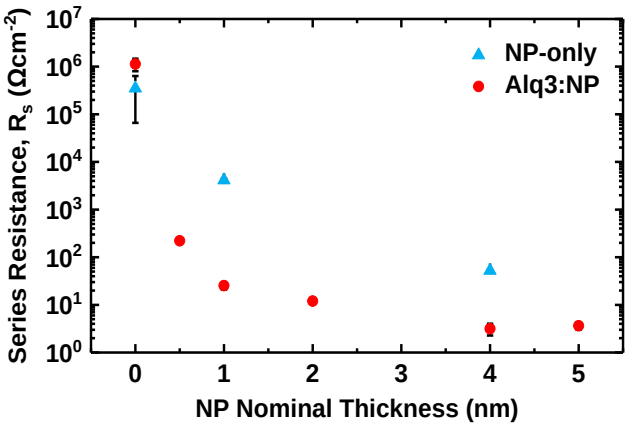


Figure 5-19: The average R_s values of devices without (NP-only) and with (Alq3:NP) Alq3 ETLs.

Chapter 4 suggested transport improvements might stem from a new direct NP route in addition to a modified organic route (Section 4.4.2). Comparing the R_s values of NP-only and Alq3 ETL devices allows some limited inferences to be drawn about the impacts of direct NP transport on PV device operation. The NP-only devices show transport improvements as R_s decreases with

nominal thickness (Figure 5-19). Some of the R_s reduction will be due to the energetic barrier decreasing, as band bending is reduced in NP-only devices (Figure 5-16). However, some portion of the R_s reduction probably originates from additional transport improvements, as the NP-only 4 nm device with bending still present has a lower R_s than the Alq3:NP 0.5 nm device which shows flat bands.

Without Alq3 all the NPs provide a direct connection between the active layer and the cathode, so a direct NP route probably contributes to improved transport processes. However, some transport in the NP-only device might also be occurring via NP-induced gap states in the SubPc, as discussed previously (Section 5.5.1). This confounding factor, which cannot be excluded, prevents definitive identification of the contributions to transport improvements. Overall therefore, it is possible that a direct NP route might also play a role improving transport in devices with an Alq3 ETL, especially at higher nominal thicknesses given the now thin CTL. However, it is not as critical to transport performance as the NP-Alq3 interaction which removes the extraction limitations giving lower R_s values.

AC impedance measurements were taken to further investigate changes in charge transport dynamics. The full AC impedance fitting results are presented in the appendix (Section B.1). At +2 V the IV properties are dominated by the series resistance, therefore to measure a transport resistance, devices were probed at a DC bias of +2 V. The characteristic features of the impedance traces measured can be understood by examining the behaviour of a parallel R-C combination circuit (Figure 5-20) [426]. At low frequencies the behaviour is purely resistive: the impedance (Z) is frequency independent with a gradient of zero and its value is equal to the impedance of a resistor (Z_R):

$$Z_R = R \qquad \text{Equation 5-1}$$

where R is the resistance of a resistor. At high frequencies the behaviour is purely capacitive: the impedance is linearly dependent on frequency with a gradient of -1 (on a log-log plot) and its magnitude is the impedance of a capacitor (Z_C):

$$Z_C = \frac{1}{j\,\omega\,C} \qquad \text{Equation 5-2}$$

where j is the imaginary number equal to $\sqrt{(-1)}$, ω is the frequency in radians and C is the capacitance of a capacitor. The regimes transition at the R-C corner frequency (ω_0), where the impedance magnitudes are equal giving:

$$R = \frac{1}{\omega_0\,C} \qquad \text{Equation 5-3}$$

Therefore, ω_0 is proportional to $(R\,C)^{-1}$ and is shifted to lower frequencies as the resistance or capacitance increases. If ω_0 is shifted beyond the frequency measurement range, the transition may appear absent.

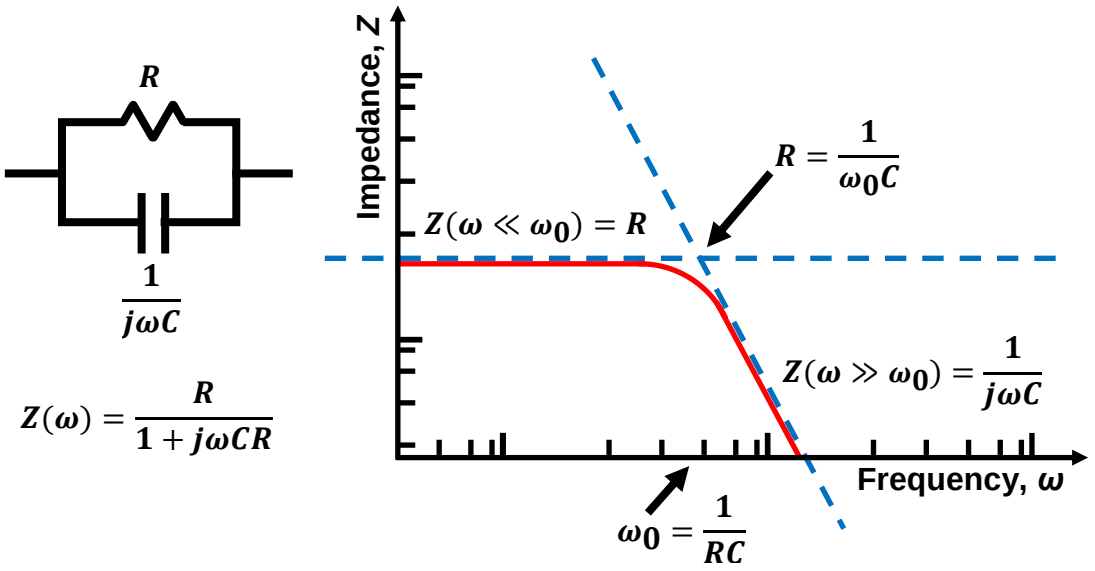


Figure 5-20: A schematic of a parallel resistor-capacitor (R-C) combination circuit with associated equations (left) and the corresponding impedance-frequency characteristics and limiting behaviour (right), adapted from reference [426].

Divergent impedance behaviour emerging over different frequency ranges is often interpreted by a physical model where interface layer processes dominate the lower frequency response and bulk behaviour becomes evident at higher frequencies [427]. This makes intuitive sense: a

low-frequency signal allows carriers to travel further and probe an interface before the field is reversed, conversely, a high-frequency signal only allows carriers to probe their immediate vicinity which is bulk material for the majority. The regime transition frequency depends on the carrier velocity which defines the distance travelled in a given time, i.e. the feature size probed at a given frequency.

The device impedance behaviour was examined to determine whether changes in interface conduction might contribute to increasing alpha values. In the low-frequency range, the impedance traces (Figure 5-21) show the appearance of predominantly resistive transport behaviour for 0.5 nm NPs and above. The impedance becomes almost frequency independent (note log scale) and the resistive impedance decreases, shifting ω_0 to higher frequencies. This transition at low frequencies, from capacitance influenced to resistance dominated behaviour, has been interpreted as the physical process of overcoming transport limitations at a collecting electrode [330]. Frequency independence in this range suggests the creation of an ohmic contact [428] [329].

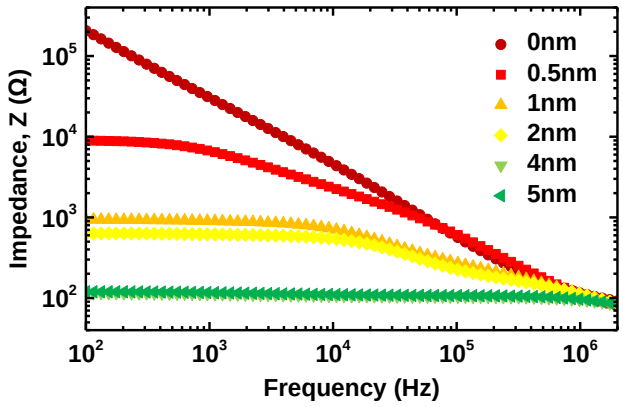


Figure 5-21: Representative impedance traces at a DC bias of +2 V for devices with an Alq3 ETL and various nominal thicknesses of NPs.

Low-frequency device impedance changes are often interpreted as originating from CTL interfaces [420]. At a +2 V bias, the impedance traces exhibit a distinct lower frequency feature

for all nominal thicknesses of NPs (Figure 5-21). This allows an R-CPE combination to be fitted, for a consistent comparison of changes to the interface resistance, *R3*. The fitted *R3* values show a significant initial decrease at 0.5 nm, followed by a substantial continued reduction to become very low at high nominal thicknesses (Figure 5-22). The moderate *R3* value for 0.5 nm devices, suggests interface transport effects may still contribute to the extraction limits causing s-shaped IV curves (Figure 5-8), especially given energetic effects may be less significant (Section 5.5.1). These impedance traces and fitting results therefore suggest that interface transport improvements begin to reduce the extraction limits from 0.5 nm and a low resistance contact is achieved with increasing nominal thickness.

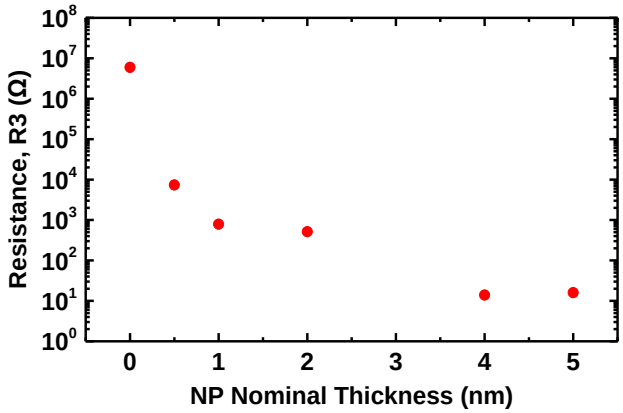


Figure 5-22: The average *R3* interface resistance parameter, from fitting the lower frequency region of impedance measurements taken at +2 V, for devices with an Alq3 ETL and various nominal thicknesses of NPs.

The transient impedance properties were examined to determine whether additional transport improvements could also increase alpha. In the high-frequency range, the impedance traces (Figure 5-21) show a strong frequency dependence with a non-unity gradient, so mixed resistive and capacitive transport is occurring. High-frequency R-C type behaviour in OPV devices is commonly assumed to originate from bulk transport and capacitance characteristics [357]. The higher frequency range was therefore fitted with an R-CPE combination, which was interpreted as corresponding to device charge accumulation and transport.

Having fit the high-frequency range to extract *R* and *C* parameters, a characteristic transport time (τ_t) can be calculated from the R-C product [358]:

$$\tau_t = R\ C \qquad \text{Equation 5-4}$$

This allows the carrier mobility (μ) to be derived from the Nernst–Einstein relationship:

$$\mu = \frac{e\ L^2}{\tau_t\ k_B\ T} \qquad \text{Equation 5-5}$$

where *e* is the elementary charge, *L* is the diffusion length (here organic layer thickness 85 nm), k_B is the Boltzmann constant and *T* is the temperature [358]. The calculated mobility increases with nominal thickness (Figure 5-23), so bulk carrier transport is also improved by CTL modifications. This is consistent with eventual mobility increases observed in Chapter 4 (Figure 4-18); active layer generation increasing carrier concentrations may explain why initial photodoping losses are absent for full PV devices. Mobility enhancements with nominal thickness are expected to improve the electron and hole extraction balance and so contribute to increasing alpha values [270].

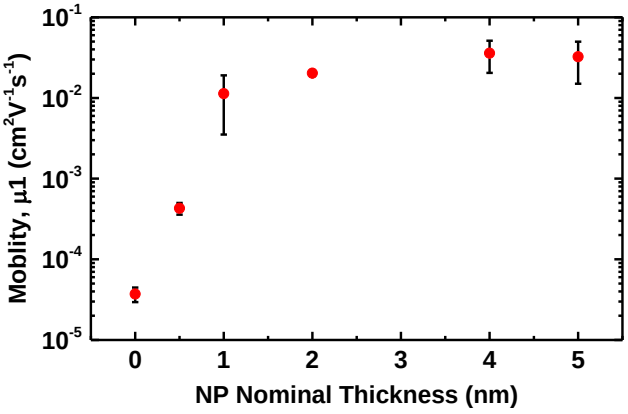


Figure 5-23: The average *μ1* bulk mobility parameter, from fitting the higher frequency region of impedance measurements taken at +2 V, for devices with an Alq3 ETL and various nominal thicknesses of NPs.

5.5.3 Generation Improves Performance

Metallic NPs are frequently incorporated in OPV CTLs to increase absorption, through scattering or near-field effects [115], and so enhance generation for a given active layer

thickness [376]. The net change in device absorption with NP additions (Figure 5-24) shows enhancements at various wavelengths which could increase generation. Comparing the profile shape of the net change (Figure 5-24, 4 nm trace) to the constituent elements spectrum (Figure 5-25, PV-only trace): the broad 6T absorption appears to be reproduced, whereas the sharp SubPc peak is not, and the NP plasmonic absorption feature (Figure 5-25, CTL-NP trace) is only reproduced above 600 nm (Figure 5-24, 4 nm trace).

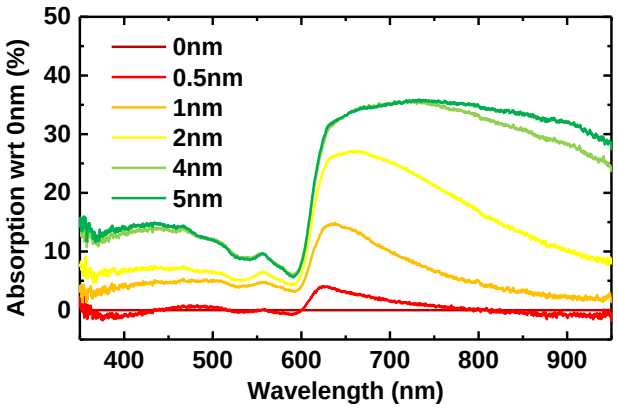


Figure 5-24: The net change in the device absorption spectrum with the addition of various nominal thicknesses of NPs, calculated by subtracting the spectrum of the device with an Alq3 ETL only.

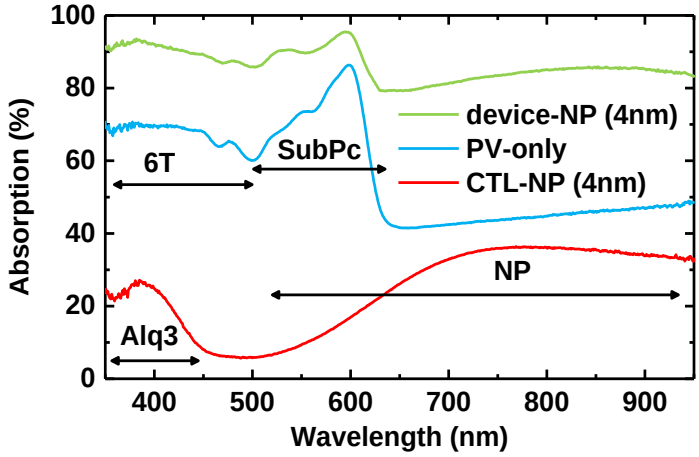


Figure 5-25: The absorption spectrums of the constituent elements of the device, vertically offset for clarity. The device-NP structure is glass-ITO-MoO_3-6T-SubPc-Alq3-NP(4 nm)-Alq3-Al. The PV-only structure is glass-ITO-MoO_3-6T-SubPc. The CTL-NP structure is glass-Alq3-NP(4 nm)-Alq3.

The anticipated contributions to the absorption spectrum changes are direct NP plasmonic absorption and NP-induced enhancement of active layer absorption. Direct NP plasmonic absorption is observed at long wavelengths, except for a sharp reduction at 600 nm where an inverted SubPc shaped profile suggests SubPc absorption nearer the front of the device dominates. The moderate absorption increases with nominal thickness in the 6T range (Figure 5-24) could be explained by NP scattering, which increases with NP size [282]. The smaller increases in the SubPc range could be because: the plasmonic and SubPc absorption ranges overlap (Figure 5-25) and parasitic NP absorption can dominate scatting effects for smaller NPs, which AFM measurements suggest these are (Section 4.3.2) [282]. Au NP near-field enhancement might occur for SubPc, as the plasmonic and organic absorption ranges overlap and the components are in close proximity [282]. However, the small absorption increases in the plasmonic overlap region around 600 nm (Figure 5-24) suggest any effects are not substantial. To conclusively prove near-field effects, the absorption spectrum could be measured for NPs positioned in the CTL at increasing distances from the active layer.

The optical features discussed above suggest that NP absorption increases are significant and that whilst 6T generation may be increasing through scattering enhancements, this is likely to be less significant for SubPc where neither scattering nor near-field effects facilitate large gains.

In OPV devices an optical field profile exists, due to thin film interference effects after light reflection at the back cathode, and more absorption occurs at locations where the field strength is higher [429]. An optical spacer layer at the cathode in planar HJ devices can: increase absorption in long wavelength acceptor layers and move the generation maximum nearer to the donor-acceptor interface (Figure 5-26) [191].

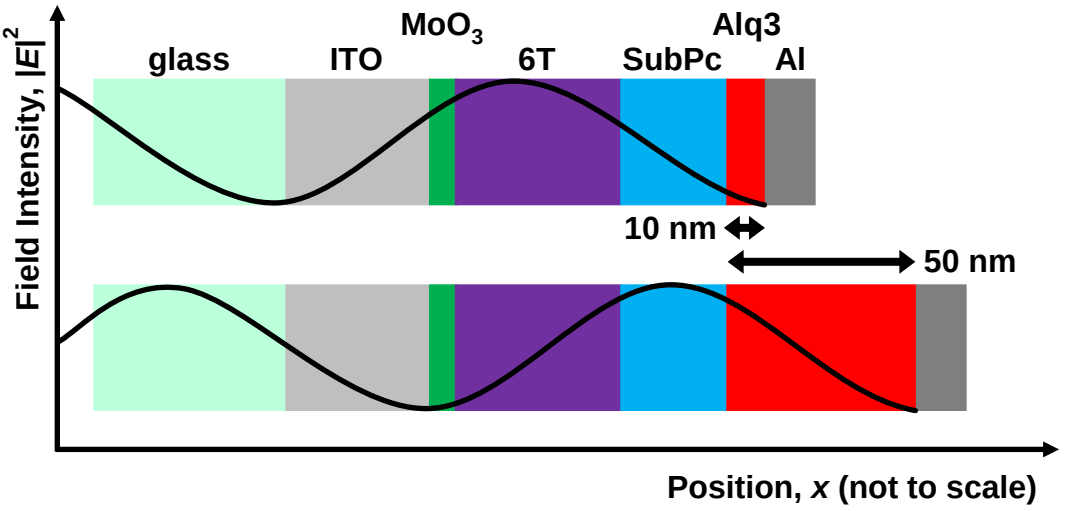


Figure 5-26: An illustrative schematic of the optical field profile in a device with a thin and thick optical spacer layer in front of the reflective back cathode. Adapted from reference [79].

Alq3 may be able to perform this role as characteristic absorption changes are observed with increasing Alq3 thickness (Figure 5-27). The optical field strength is zero at the back electrode reflection point, hence absorption in any adjacent layers is low unless a spacer is used [429]. This mechanism explains the SubPc absorption increase with an adjacent 50 nm Alq3 layer. However, a spacer also shifts the position of the field maximum, which initially depends on the thickness and refractive indices of the individual layers, and hence may reduce absorption in layers further from the back electrode [429]. This could be the cause of generally reduced absorption in the 6T range, with the exception of an increase around 400 nm due to direct Alq3 absorption.

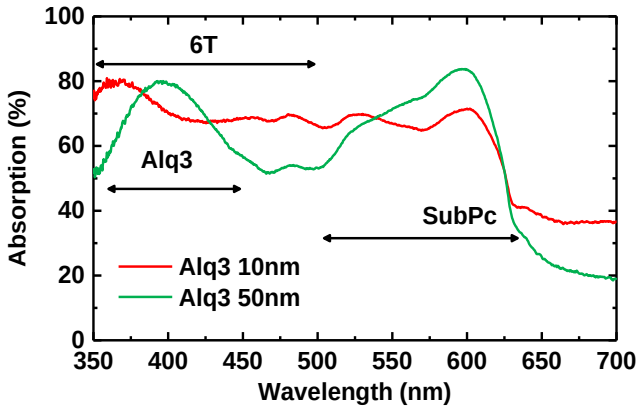


Figure 5-27: The absorption spectrums of devices with a 10 nm or 50 nm thick Alq3 ETL.

However, this modified generation does not translate to the *EQE* spectrums (Figure 5-28) because the devices are collection limited. The 10 nm Alq3 device has a high R_s of 3.2 x 10^6 Ohm/cm^2, which further increases to 4.1 x 10^7 Ohm/cm^2 for 50 nm of Alq3. Any optical gains from thicker Alq3 are clearly outweighed by electrical losses from transport.

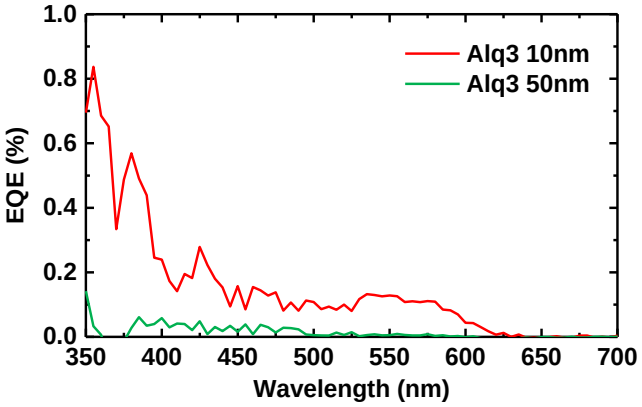


Figure 5-28: The *EQE* spectrums of devices with a 10 nm or 50 nm thick Alq3 ETL.

Even for thin 10 nm Alq3 layers, the generation enhancements observed with NP inclusion are not generally reflected in the *EQE* trends. The largest discrepancy between the absorption (Figure 5-29) and *EQE* (Figure 5-30) spectrums is at long wavelengths, where the *EQE* measures negligible currents associated with the NP plasmonic absorption. In Chapter 4, plasmonic NP generation was observed to contribute photocurrent in filtered IV testing (Section 4.5.3). Comparing the photocurrents with 4 nm Au NPs: the Chapter 4 single layer device filtered J_{sc} was 0.000025 mA/cm^2 and the full PV device J_{sc} was 2.3 mA/cm^2, there is a 5 orders of magnitude difference. This suggests, given active layer absorption, any plasmonic contributions would not significantly impact device operation. Therefore, in a full PV device, Au NPs are unlikely to give a worse performance than Ag NPs, despite Au NPs contributing smaller plasmonic generation gains in single layer devices (Figure 4-41).

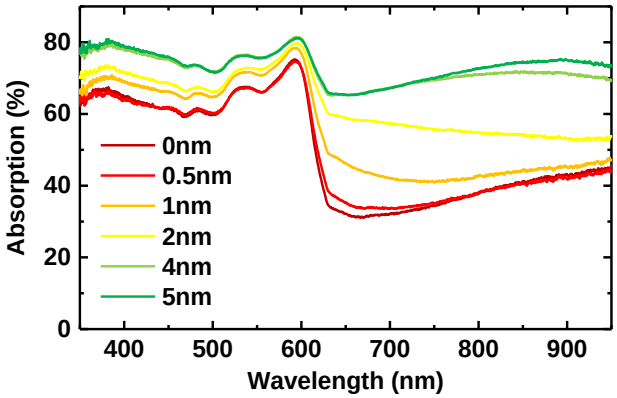


Figure 5-29: The absorption spectrums of devices with an Alq3 ETL and various nominal thicknesses of NPs. The NP plasmonic absorption causes large increases above 600 nm.

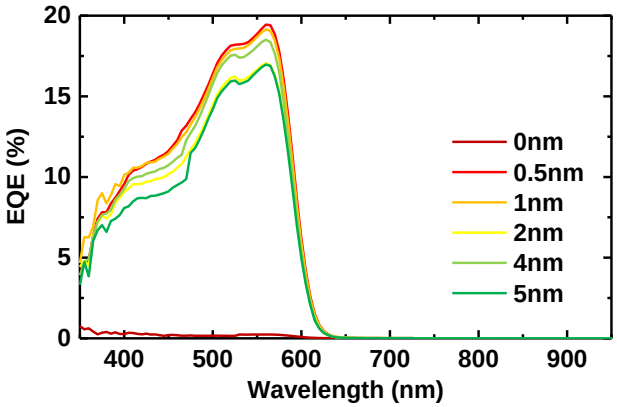


Figure 5-30: The *EQE* spectrums of devices with an Alq3 ETL and various nominal thicknesses of NPs. The increase in NP plasmonic absorption observed in Figure 5-29 is not translated into device current, as charges generated above 600 nm are not extracted.

The *EQE* measurements can be understood by considering carrier collection, in addition to generation effects. The sample without NPs clearly absorbs (Figure 5-29) but *EQE* values are below 1 % (Figure 5-30). The lack of collection is due to Alq3-cathode interface extraction limits, as discussed previously (Section 5.4.1). With the introduction of NPs and lifting of extraction limits, a broad-spectrum step-change to higher collection occurs in the *EQE* spectrums. This is in contrast to the small and wavelength dependent incremental increases observed in the absorption spectrums. Whilst the absorption continues increasing with nominal thickness the *EQE* does not, suggesting collection limitations may still dominate device operation, even after initial extraction limits are removed.

5.5.4 Recombination Impairs Performance

Collection trends can be understood by examining the *FF* of the IV curves. Increasing *FF* values (Figure 5-31) show that collection improves with nominal thickness, however, the rate of improvement reduces at higher nominal thicknesses and possibly inverts for 5 nm devices. This tail-off in collection enhancement could be due to the effects of an improving process plateauing or an impairing process increasing. In the mobility (Figure 5-23) and R_s (Figure 5-19) trends, a degree of plateau behaviour is indeed observed. However, the reducing V_{oc} values (Figure 5-9) suggest that increasing degradation mechanisms do also play a role in reducing collection enhancements. In particular, V_{oc} is known to reduce with increasing recombination [84], suggesting that NP additions may negatively affect recombination dynamics in the device.

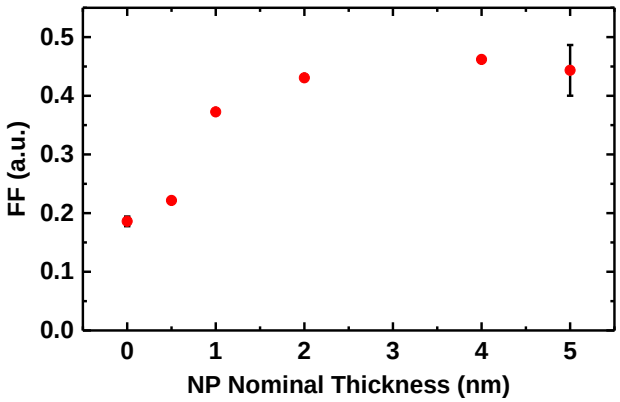


Figure 5-31: The average *FF* value of devices with an Alq3 ETL and various nominal thicknesses of NPs.

ECM analysis of AC impedance measurements was undertaken to investigate changes in charge recombination dynamics. The full AC impedance fitting results are presented in the appendix (Section B.1). At -2 V the IV properties are dominated by the shunt resistance which is related to recombination, therefore devices were probed at a DC bias of -2 V. The PV-interface and PV-conventional models were used to fit the 0-0.5 nm and 1-5 nm devices respectively, as discussed previously (Section 5.5.1). The parallel R-C combination fitting the high-frequency

response for all nominal thicknesses is conventionally interpreted as giving the recombination resistance (R_r) of the device [430]. Similarly to R_{sh}, higher values of R_r mean more carriers can be collected by the external circuit. The effective carrier lifetime (τ_r), which is controlled by recombination events, can therefore be determined from the R-C product [358]:

$$\tau_r = R_r\, C \qquad \text{Equation 5-6}$$

The trends in effective carrier lifetime with nominal thickness (Figure 5-32) show that with the initial introduction of NPs lifetimes increase, but at higher nominal thicknesses lifetimes begin to shorten once more. This indicates that the recombination processes occurring in the device change in nature and magnitude with the inclusion and increasing nominal thickness of NPs [358]. The *n* values, calculated from fitting dark IV data, could support this suggestion. Without NPs, *n* values are above 15, but for 0.5 to 5 nm NPs, *n* values are below 5. This magnitude difference broadly indicates a change in dominant recombination mechanism [85]. A trade-off between two mechanisms may be occurring with nominal thickness, namely a space-charge reduction followed by increasing trapping and leakage. Various parameters were therefore tested to probe changes in specific recombination mechanisms.

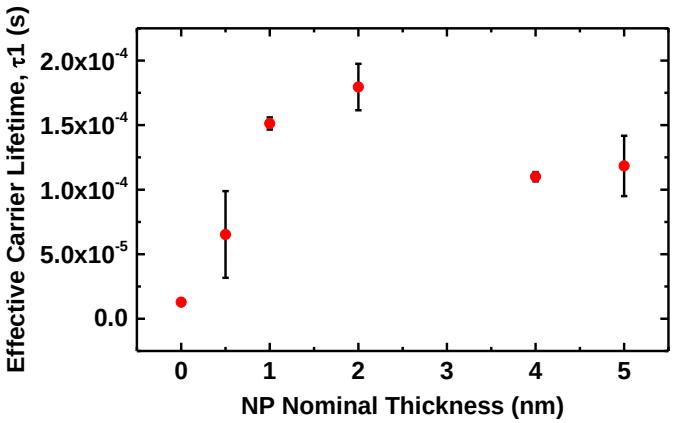


Figure 5-32: The average effective carrier lifetime value, from fitting impedance measurements taken at -2 V, for devices with an Alq3 ETL and various nominal thicknesses of NPs.

As discussed above, the trend in alpha (Figure 5-18) shows less space-charge recombination with nominal thickness, possibly due to extraction limits being lifted through both energy level and transport improvements. On the other hand, larger beta values (Figure 5-33) show more trap-assisted recombination losses with increasing nominal thickness [424]. This could be caused by the continued creation of more mid-gap states with nominal thickness, providing increasing numbers of trap sites for recombination [179]. In Chapter 4, it was hypothesised that NPs generate trap states which might cause recombination increases (Section 4.5.3), but intensity-V_{oc} measurements to prove this were not practical. The beta values from full PV devices now suggest this mechanism is a reasonable explanation.

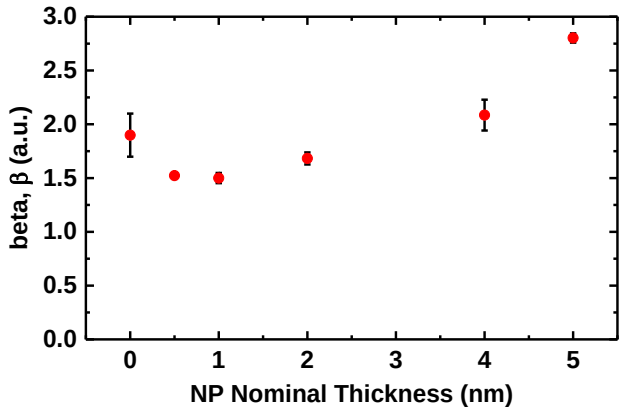


Figure 5-33: The average beta value extracted from fitting intensity-V_{oc} plots of devices with an Alq3 ETL and various nominal thicknesses of NPs.

The high beta value for 0 nm devices may result from trapping in the Alq3 surface states induced during cathode deposition [431]. The introduction of NPs, whilst creating new mid-gap states, might also fill the Alq3 surface states present, as discussed previously (Section 5.4.2). Therefore, the initial reduction in beta may originate from filling the gap states at the Alq3-cathode interface [432]. Once these surface states are filled, further NP additions would create additional mid-gap states without concurrently filling surface states and hence beta would be increased, as observed [179].

Dark IV measurements were undertaken to explore changes in recombination-related parameters. The fitted J_0 values (Figure 5-34) increase by orders of magnitude, indicating significant recombination increases with nominal thickness [86]. Under dark conditions, the device current flows via the recombination of electrons and holes, which would be facilitated by an increase in the presence of mid-gap states [433]. The R_{sh} values (Figure 5-35) correspondingly indicate higher photocurrent losses through leakage currents which can be increased by transport via defect states in the CTL [386] [429]. These recombination increases will contribute to the V_{oc} reduction observed with increasing nominal thickness (Figure 5-9) [84] [239].

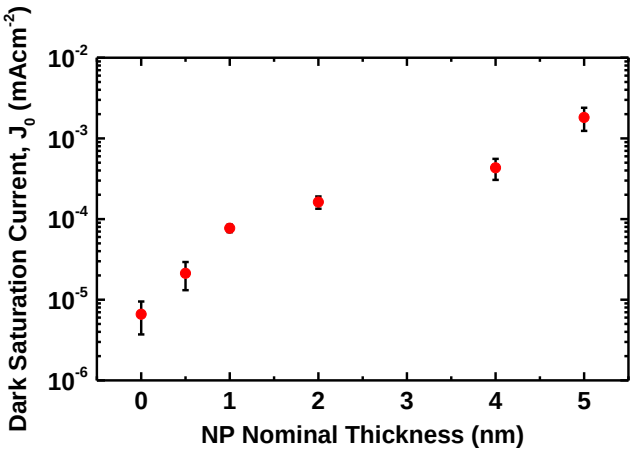


Figure 5-34: The average J_0 value of devices with an Alq3 ETL and various nominal thicknesses of NPs.

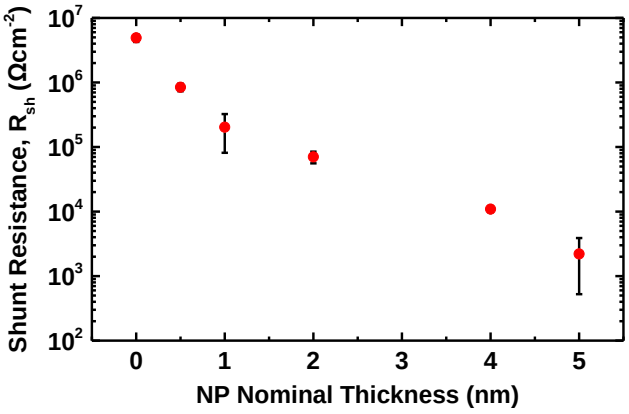


Figure 5-35: The average R_{sh} value of devices with an Alq3 ETL and various nominal thicknesses of NPs.

Recombination parameters which could not be extracted for CTL-only devices in Chapter 4 (Section 4.5.3) have now been explored. The mechanisms revealed suggest that in a full PV device Ag NPs may have similar recombination effects to Au NPs, but at higher nominal thicknesses. Ag NPs were previously observed to relieve extraction barrier effects later than Au NPs (Section 4.4.3), so the associated large recombination reduction will occur at higher nominal thicknesses. Additionally, Ag NPs were found to produce smaller Fermi level shifts and suggested to induce fewer gap states with nominal thickness (Section 4.4.2), so leakage and trapping effects may moderately increase recombination later than for Au NPs.

As well as originating from NP-induced gap states in the organic, recombination could be caused by NPs directly. Any NPs in physical contact with the active layer could act as significant recombination centres due to quenching of generated excitons [370] [343]. The strong Alq3 exciton quenching effects discussed in Chapter 4 (Section 4.5.4) are now expected to be a less significant source of recombination, as photocarriers are generated at the active layer HJ. Alq3 exciton generation is likely to be reduced because the layer is thinner and positioned after 6T which absorbs in the same spectral region. As predicted, the strong photocurrent reductions due to quenching in single layer devices are not observed in the full PV device J_{sc} values (Figure 5-9).

Metal NPs fully embedded in the ETL, isolated from both the active layer and the cathode, could also act as charge carrier recombination centres [179]. If electrons moving through the Alq3 encounter a NP and transfer to the metal, they become trapped because there is no direct contact to the cathode. The electron must be re-excited to Alq3 transport levels for collection or it will encounter a hole with which it will recombine [356]. For NPs which do directly contact the cathode, a collection route with increased photocurrent losses may operate. The effective cathode penetration depth is increased by NPs so collection may occur sooner [386], however,

the deeper WF of the Au NP reduces the collection field compared to the Al cathode [434]. The electron may transfer to the cathode due to the direct metallic electrical contact, however, the concurrent lower shunt resistance causes power dissipation reducing collection overall [429].

Therefore, the changes in recombination parameters described above could also originate from NPs directly. An increase in the isolated NP surface area and volume with nominal thickness could increase the magnitude of recombination current able to flow [356] and so will increase J_0. Larger NPs are more likely to penetrate the active layer and so beta may increase through more trapping and quenching of generated carriers [183]. The R_{sh} values decrease can now be understood as a physical shorting route, with higher nominal thicknesses acting as larger defects creating a continuous path from active layer to cathode contact [386].

Comparing devices with Au or Al cathodes in Chapter 4 (Section 4.4.2) suggested that the shallow Al WF might limit the collection from a direct NP transport route, although there were confounding interface barrier effects. In a full PV device therefore, the NP route might predominantly be expected to result in carrier losses. The direct NP mechanisms outlined above for the recombination related data support the expectation from Chapter 4 that this route might cause losses. The subsequent investigation of Alq3 buffer properties adds further weight (Section 5.6), as devices with more direct NP transport opportunities and fewer gap states show increased recombination and leakage.

5.5.5 Net Performance Balance

Overall there is a trade-off of initial improvements with later losses, resulting in an optimum nominal thickness between 2 nm and 4 nm. The *PCE* of devices (Figure 5-36) increases rapidly at low nominal thicknesses but begins to reduce at higher nominal thicknesses. This suggests that after the extraction limitations creating a space-charge are removed, recombination effects

increasingly dominate despite improvements in transport and generation. This chapter suggests various roles for mid-gap states in device operation, which both enhance and hinder performance. The direct NP effects discussed often act to degrade performance and were unable to relieve the extraction limits in the NP-only devices. This is reflected in the significantly lower *PCE* values (Figure 5-36, note axis scale) for devices with only NPs and no Alq3 ETL.

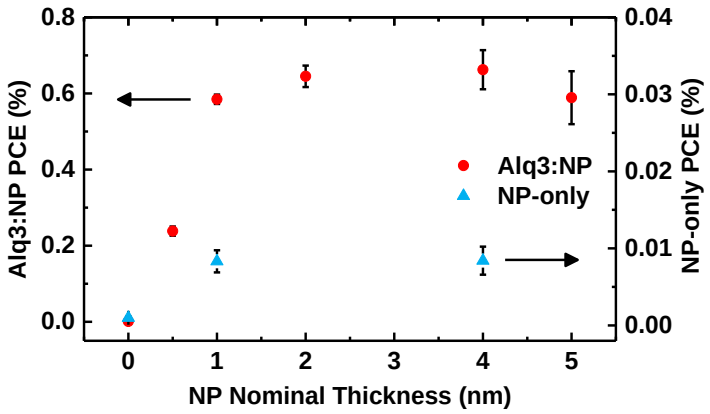


Figure 5-36: The average *PCE* value of devices without (NP-only, right axis) and with (Alq3:NP, left axis) an Alq3 ETL. Note the left and right vertical axes have different maximum values.

5.6 Role of Alq3

It has been demonstrated that Alq3 interacting with NPs is critical to removing extraction limits (Section 5.5.1) and that Alq3 can produce optical spacer effects (Section 5.5.3). Alq3 may also perform other roles in the device. Metallic NPs can be passivated by buffer layers, which prevent direct contact between the metal and the organic absorber, reducing exciton quenching [295]. Buffer layers at the collecting electrode can additionally: block minority carrier transport [251] and protect active layers from cathode deposition damage [109].

Devices were characterised with and without ETLs, but with NPs still present, to explore the role of Alq3. The J_0 value (Figure 5-37) is lower with Alq3 for a given nominal thickness, indicating the device recombination current is reduced with Alq3. The recombination with

minority carriers may be reduced by the deep HOMO of Alq3 blocking hole transport to the cathode [435], which may particularly occur directly via the NPs as they provide an intermediate Fermi level energy. Recombination currents through damage-induced defect states may be reduced by the Alq3 over-layer protecting the SubPc during NP and cathode deposition. Organic material damage by direct metal deposition modifies the density of states around the bandgap [260] and hence a lower optical absorption is observed in damaged layers [266] [436]. The device absorption spectrum (Figure 5-38) shows a broader and lower SubPc peak around 600 nm without Alq3, suggesting increased metal deposition damage without Alq3 protection.

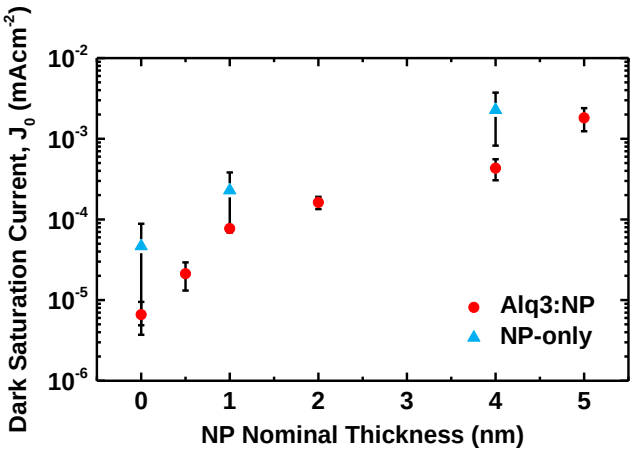


Figure 5-37: The average J_0 value of devices without (NP-only) and with (Alq3:NP) Alq3 ETLs.

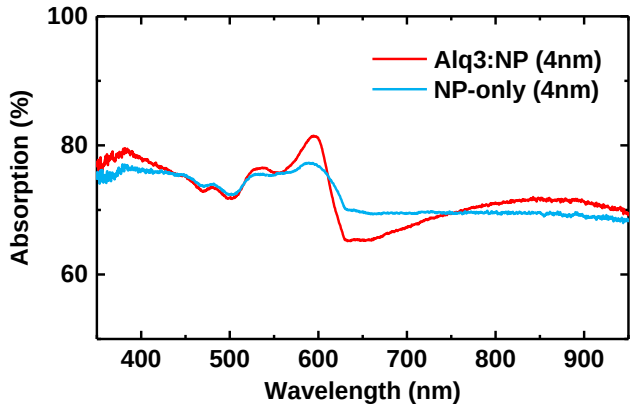


Figure 5-38: The absorption spectrums of 4 nm NP devices without (NP-only) and with (Alq3:NP) Alq3 ETLs.

The higher R_{sh} values (Figure 5-39) produced with the presence of Alq3, suggest that the buffer layer reduces leakage currents. Less physical shorting is expected because without Alq3 layers every NP provides a direct metallic electronic contact between the active layer and cathode. Recombination may also be reduced by suppressed exciton quenching as the buffer inhibits contact between the active layer and the NPs [295]. The spectral overlap between SubPc emission [437] and Au NP plasmonic absorption (Figure 4-5), however, makes this mechanism hard to prove decisively with PL measurements.

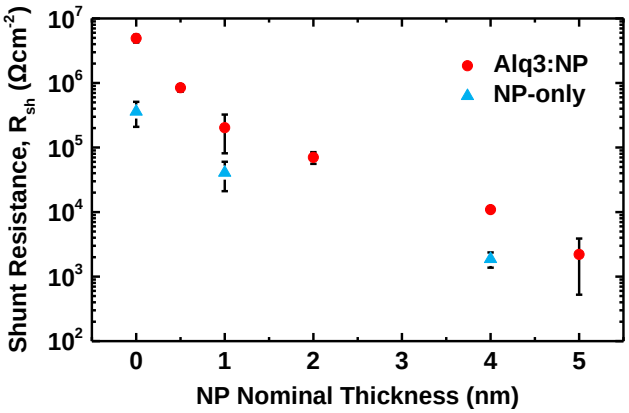


Figure 5-39: The average R_{sh} value of devices without (NP-only) and with (Alq3:NP) Alq3 ETLs.

These results demonstrate that Alq3 buffer properties assist in mitigating losses, particularly those associated with the incorporation of NPs. Future testing could explore the effects of Alq3 thickness and NP position to optimise the buffer effect for different NP nominal thicknesses [295].

5.7 Conclusions

Having shown in Chapter 4 that metal NPs can modify the optoelectronic properties of an organic layer, this chapter reported the effect of using an ETL with embedded NPs in an OPV device structure. In particular, the nominal thickness of Au NPs was varied to investigate the role of NPs in device operation. The contribution of the Alq3 ETL was also explored through

comparisons to NP-only device structures. The IV characteristics of the devices were understood through further testing of the optical generation spectrum, electronic device structure, carrier transport properties and charge recombination mechanisms.

The findings presented in this chapter demonstrate the utility of NPs in PV devices, but also identify accompanying drawbacks. Two key theories are employed to explain the observed results. Initially, with no embedded NPs, interface extraction is limited by Fermi level pinning at the cathode. This creates energy barriers and transport restrictions in devices both with and without an Alq3 ETL. Subsequently, with the addition of NPs, mid-gap states are induced in the organic layer, which alter the carrier dynamics and energetics, in addition to the direct effects of the NPs themselves. Further testing to measure details of the gap state distribution could employ UPS and IPES techniques.

The NP additions produced improved interface carrier dynamics and energy level alignment through metal-organic interactions. This enabled the benefits of the Alq3 ETL to be accessed in a PV device, after the Fermi level pinning related extraction limitations were lifted. The interface improvements were found to be materials combination and layer structure dependent. For devices with an Alq3 ETL and fully embedded NPs, the NP-Alq3 interaction alleviated the extraction limits curtailing PV performances. Here, improving interface transport processes and a transition to favourable band bending were observed. Without the Alq3 ETL, however, the extraction limits persisted, possibly due to differences related to the NP position or NP-SubPc interaction. In this case, transport improvements were also observed, but band bending was not modified enough to remove energetic barriers.

The NP additions also improved both bulk and interface transport processes with increasing nominal thicknesses. This appears to be achieved primarily through gap state generation and

filling modifying the transport in the organic, although NP-only device testing revealed that direct NP transport may also contribute, especially at high nominal thicknesses. The direct NP route, however, is not as important to transport overall as the removal of an energetic barrier. Despite the interface extraction and transport improvements, persistent collection limitations restricted any generation benefits being conferred by NPs. Whilst device absorption increases correlated with NP nominal thickness, associated photocarrier collection improvements could not be identified.

Alongside transport enhancements, the NP additions caused increased recombination at higher nominal thicknesses. Whilst initially recombination was improved, as the space-charge effects reduced when the extraction limitations were alleviated, eventually increases in carrier trapping and leakage currents caused performance degradations. A number of loss mechanisms occur via the NPs directly, although the modified organic also contributes carrier losses due to gap states. Some of the NP associated losses were mitigated by the presence of the Alq3 ETL. This diminishes active layer to cathode shorting routes, reducing leakage currents, and is anticipated to inhibit exciton quenching. The Alq3 also performed more conventional buffer roles by blocking hole transport and providing protection from electrode deposition damage. Further experiments could vary the Alq3 layer thickness to explore minimising device resistance increases whilst maintaining beneficial buffer effects, although the optimum Alq3 thickness is likely to differ depending on the NP size.

Testing metal NPs in the CTL of a full PV device structure enabled new understanding to be gained that could not previously be uncovered by testing the single layer devices in Chapter 4. The presence of the absorbing active layer permitted the optical interactions with the NPs and their effects on carrier generation to be explored. The Alq3 now performing a CTL role for the carriers dissociated at the 6T-SubPc HJ, allowed its beneficial effects as a buffer layer to be

observed. The full operation of PV processes also enabled additional measurements and data analysis to be undertaken for the PV devices. Dark IV analysis and intensity dependent photoresponse testing enabled changes in device recombination to be attributed to specific loss mechanisms. This allowed losses at high nominal thicknesses to be confirmed as originating from trap states, whilst identifying space-charge improvements to be occurring initially. It also elucidated the role of direct NP transport in leakage currents, especially through comparisons with NP-only devices. Frequency-dependent impedance analysis and fitting of M-S plots enabled different origins of interface extraction effects to be identified. This revealed that both interface transport resistance improvements and energy level bending changes contribute to eliminating the extraction limits.

The deeper mechanistic understanding gained in this chapter allows the potential differences between the application of Au and Ag NPs in a full PV device to be considered. Plasmonic generation from NPs was negligible in the full PV structure, but removing extraction limits hinged on a strong NP-organic interaction. From these perspectives, Au NPs are favoured over Ag NPs as CTL additions. This is because the Au NPs reduced plasmonic effects (leading to smaller filtered photocurrents) are less important, but their increased organic interaction (producing a larger composite Fermi level shift) is more critical. In terms of changes to transport and recombination dynamics, Ag NPs may produce similar phenomena to Au NPs with the effects just occurring at higher nominal thicknesses, as observed for related parameter trends in Chapter 4. To confirm these hypotheses, further tests of Ag NPs in a full PV device could be undertaken. This would also allow the optical effects of a different plasmonic wavelength range to be investigated.

Additionally, given that a key NP role is removing extraction limits and considering the loss mechanisms observed, Au NPs may be able to maximise performance improvements

achievable. Because Au was observed to reduce barriers to extraction faster than Ag in Chapter 4, the desired effects should be achieved in a full PV device at a lower nominal thickness. This should reduce the likelihood of recombination losses dominating transport gains, which occurred at higher nominal thicknesses. It could also help keep the Alq3 contribution to device resistance low because smaller NPs could be fully covered (to prevent losses) by a thinner Alq3 layer.

The observations made in this chapter suggest some further guidelines for the application of metal NPs to organic CTLs. For any metal, selecting a smaller nominal thickness of NP should avoid eventual recombination effects becoming dominant over transport improvements. Additionally, locating the NPs fully within the CTL, not at the surface, would be beneficial by maximising the organic interaction volume and depth to effectively counter the effects of deeper penetrating reactive cathode materials. It should also be possible to choose the thickness of the encapsulating organic CTL to optimise its various contributions to performance. A minimum thickness will be required to perform buffer layer functions, (thicker layers could produce optical spacer effects), but high thicknesses will mitigate any enhancements due to large transport resistance losses.

Overall, metal NPs have been found to impact specific areas of OPV device performance to different degrees. On one hand, they have not been observed to enhance the optics of the device, as is often suggested in the literature. This could be due to a non-optimised device structure causing collection limits to dominate PV operation. On the other hand, they can be used as a method of improving interface extraction and transport properties. In particular, metal NP and organic CTL interactions can effectively relieve Fermi level pinning effects at metal cathode contacts. In addition to these two aspects, however, the concurrent increases in loss processes with the incorporation of NPs should also be considered.

Chapter 6: Conclusions and Future Work

6.1 Conclusions

• QD PVs with Organic CTLs

QDs have the potential to provide high performance PV technologies. However, inefficient extraction can limit the *PCE*s achieved, so CTLs are often incorporated to improve device operation. To explore this possibility, a Ptn HTL was employed in a QD PV device and an atmospheric treatment was applied post-fabrication to modify the Ptn properties. The Ptn layer was then found to improve the J_{sc} from 9.2 to 12.9 mA/cm^2.

These studies showed that the Ptn-QD interface energy alignment was critical to performance. Initially s-shaped IV curves were improved by atmospheric treatments, which altered the Ptn energetic structure, lifting extraction limits. Ptn transport effects also contributed to extraction limitations, as oxidative doping may improve conductivities and thicker layers were found to substantially curtail performances. The studies also elucidated two specific performance enhancing roles played by the Ptn. As an electron blocking layer Ptn minimised rear contact recombination, and by improving hole extraction Ptn balanced carrier collection in the device.

S-shaped IV curves are a commonly encountered problem when characterising novel PV architectures. These results demonstrate a simple post-fabrication treatment which can be applied to improve PV operation. This research extends the work of Neo et. al. [227] showing the findings are applicable to a new material with superior properties and demonstrating the effectiveness of the approach as the initial s-shape was stronger. Additionally, this research identifies that space-charge effects can originate from transport restrictions, as well as the energy barriers discussed in their work. Our results demonstrate that whilst doping transport

improvements are less significant than energy level alignment for eliminating s-shaped IV curves, the transport limitations of high nominal thickness CTLs cause substantial and persistent space-charge effects. The inclusion of a P3HT HTL in their work improved the *PCE* of a control device from 3.1 % to 5.2 %. The Ptn HTL herein showed more modest results, only improving controls from 2.4 % to 2.9 % *PCE*. This is possibly due to the non-optimised Ptn layer thickness increasing the device resistance.

• Organic Layers with Metal NPs

To directly control the CTL properties during fabrication, metal NPs were added, as this is a known method to enhance OPV device performance. A simple device architecture was used to understand the operation mechanisms, as it is rare to study the CTL separately before full PV device integration. For these studies, NPs were formed in single layer Alq3 organic devices by thermal evaporation. The NP material and size effects were explored by varying the nominal thickness of Au and Ag deposited from 1 to 5 nm. The Al cathode was also swapped for Au to test the extraction mechanisms operating.

The optoelectronic interactions of the NP and organic materials were studied. The Alq3 electronic structure was modified by gap state generation and charge transfer. This interaction was stronger for Au NPs, which shifted the composite Fermi level by 0.2 eV, compared to a 0.1 eV shift for Ag NPs. In terms of optics, the Alq3 absorption appears not to be enhanced by near-field effects of the plasmonic NPs.

Device operation was altered by the NPs in various different respects. Generation was increased as a small photocurrent originated from direct plasmonic NP absorption, however, Alq3 exciton quenching by NPs substantially reduced photocurrents. A significant effect of the NP incorporation was the creation of lower resistance transport routes. A modified organic route

was suggested to operate via gap state hopping transport and charge transfer doping effects. A NP-direct route was suggested to have metallic transport and be collection limited by the NP continuity and cathode WF. These effects enabled Fermi level pinning related interface extraction limits to be lifted with increasing NP nominal thickness. The routes also substantially improved the transport properties, outweighing concurrent but small increases in trapping.

The differences between Au and Ag NPs were explored. Whilst Au NPs had a stronger interaction with Alq3, the Ag NP plasmonic generation was possibly larger. Quenching effects were similar for both metals, but photocollection losses were eventually larger for Au NPs.

This research draws together and extends the related but distinct fields of metal-organic interactions and ONVM devices, considering both direct NP effects and NP-induced organic changes. Observations of NP plasmonic photocurrents are significant as illumination effects in ONVM devices are often not explored. The interactions of NPs and organics are not well understood, so extending the range of materials tested and characterisation methods used is valuable.

• OPVs with Composite CTLs

The NP-organic composite was utilised as a CTL to improve the PV device efficiency and explore the operation mechanisms in a full PV architecture. Adding metal NPs to OPVs can be a method of overcoming the absorption-diffusion trade-off or enhancing the device electronic properties. Studies were conducted on a 6T-SubPc active layer OPV device, with a composite CTL of Alq3 and Au NPs whose nominal thicknesses varied from 0.5 to 5 nm. Comparisons to NP-only devices, without an Alq3 layer, were used to explore: direct NP effects, the Alq3 buffer role and the nature of NP-Alq3 interactions.

In a full PV structure, the removal of extraction limitations was found to be a key NP role, whilst optical effects were negligible. The strong active layer absorption and collection restrictions meant NP plasmonic contributions to the photocurrent were insignificant. Initially, Fermi level pinning effects caused severely space-charge limited extraction, producing control device *PCE*s of only 0.001 %. In NP-only devices, transport properties improved but energy barriers remained; the direct NP effects were not enough to fully lift the extraction limits. For devices with NPs and Alq3, however, the materials combination and layer structure gave favourable band bending in addition to interface transport improvements. The strong interaction modifying the organic Fermi level position appears important in lifting extraction limitations.

The NPs conferred both bulk and interface transport improvements, but these were outweighed by recombination losses with increasing nominal thickness. Whilst both transport routes contribute to each process, it is suggested that generally gap states facilitate more transport and that the NP-direct effects induce more losses. The recombination characteristics varied with nominal thickness: initially the space-charge limiting extraction was reduced but eventually trapping and leakage effects increased. This led to an optimum *PCE* of 0.66 % being achieved with 4 nm NPs. The Alq3 ETL performed buffer layer roles and mitigated NP losses, thus reducing recombination in the device. However, the most significant benefit of Alq3 inclusion is extraction limit lifting, as the NP-only devices still had severely limited *PCE*s of only 0.008% with 4 nm NPs.

The literature reporting metal NPs in OPV devices generally focuses on optical modifications. Electrical investigations are rarer and there is a lack of consensus on NP transport effects. This work therefore contributes to the field by emphasising the electronic aspects and studying the transport and recombination dynamics in detail. There are also relatively few reports of

evaporated NPs located in CTLs, so this study presents a new materials combination and device structure and associated mechanisms to add to the existing knowledge base.

6.2 Future Work

• Electronic structure characteristics

It would be desirable to measure changes in the organic energy levels and gap states with treatments or NP additions. Testing could directly probe details of gap state distributions and explore any shifts in the HOMO and LUMO levels. UPS and IPES could be used to measure the electronic structure of both filled and unfilled states. This would be complemented by XPS measurements of the chemical bonding, elucidating any new species generation or charge transfer occurring.

• Physical structure characteristics

For the NP-organic composite, it would be valuable to determine structural details of the NP layer, especially continuity features. This could be achieved by TEM imaging of cross-sectional samples, however, this is technically complex as sample preparation by ion-milling may cause material mixing issues. The size and shape of the metal NPs could be measured more accurately in the x-y plane by high-resolution SEM, but the surrounding organic material may limit this approach. When modified with treatments or NP additions, the organic CTLs may undergo changes in crystal structure or domain size, which could be measured by TEM and XRD analysis. However, evaporated Alq3 is expected to be amorphous and oxidation is not anticipated to alter the Ptn crystal structure.

• Device operation mechanisms

To isolate and understand the effects of individual components on device operation, a wider variety of metal and organic materials could be tested. Studies undertaken demonstrated that some insights into operation mechanisms can be gained by comparing different metals as the NP and electrode materials. Whilst intrinsically the NPs cannot be separated from the gap states they induce, the sources of the effect can be varied individually by changing either the NP or organic materials. Chapter 4 showed the electrochemical interactions are metal dependent, by testing Au and Ag NPs. In a similar fashion, the organic could be varied, e.g. n-type and p-type, to see if interaction characteristics differ. Whilst the direct NP properties remain unchanged in this scenario, knock-on modifications to overall device operation must be considered.

Another mechanism exploration approach is varying the position of the NPs within the CTL, from the active layer interface to the cathode interface. This would elucidate the impact of different direct continuity routes, in addition to exploring changes in quenching or near-field effects with active layer proximity.

• Device performance optimisation

This thesis emphasised experimentation for mechanistic understanding over device engineering for performance. Given baseline samples had strong extraction limits, any optimisation would need to be conducted on QD devices post-treatment or organic devices with NP additives. To identify an optimum architecture, the thicknesses of the active and transport layers could be varied in an iterative manner. In particular, the Ptn and Alq3 layer thicknesses could be varied to balance enhancement roles and resistance losses. The peak performance possible with the Ptn or NP enhancements could then be ascertained. As examples, this work identified that a

thinner Ptn layer could reduce the R_s to improve performances and that NP-induced optical enhancements might be possible if the full device architecture was optimised.

• Materials and structural innovation

Specific NP-organic material combinations and architectures produced different interactions and device effects. Alternative embodiments may allow some tuning of the positive and negative gap state influences to control performance enhancements. Having varied the NP nominal thickness, it would be interesting to compare samples with the same nominal thickness but with single- or multi-layer NP distributions. This could be a method of accessing low nominal thickness transport gains whilst avoiding high nominal thickness recombination losses. Additionally, alternative approaches to NP size and shape control could be explored, such as thermal annealing or wetting layers.

To probe optical enhancement possibilities further, the CTL, active layer or NP materials could be varied to increase the absorption range overlap. Additionally, the NPs could be located closer to the active layer and a device structure with fewer collection restrictions would be desirable. For QD devices, EQE and absorption testing could explore whether the Ptn acts as an optical spacer layer. Although, given the transport limits for thicker layers, the scope of this feature may be limited.

It would be desirable to have control PV devices without extraction limitations, to make stringent performance comparisons when enhancing features are added. This could be achieved by employing alternative materials or architectures. A different HTL material than Ptn may not be extraction limited initially, potentially enabling larger performance gains. It would be interesting to see if metal NPs can enhance a fully functioning optimised device.

• Alternative applications

The NP-organic composite layer could be used in tandem PVs to connect the sub-cells, functioning as a recombination layer [438]. A higher NP nominal thickness may be desirable to increase recombination and the metal WF could be chosen to provide appropriate extraction fields. A highly adjustable optical spacer layer could be constructed using multi-layer NP structures. Transport improvements could be gained from low nominal thickness NPs distributed throughout the layer. This would enable a wider range of layer thicknesses to be used to modulate the optical field distribution [295]

The air treatments applied to Ptn-QD devices could provide a method of achieving environmentally stable PVs. In this situation, the oxidation is key to activating high performance, rather than causing degradation, because the operation is initially inhibited. The treatment approach could also be used to circumvent issues around materials selection, by modifying the original properties and so making them less critical. Selecting appropriate material combinations is challenging given the range of energy level values and transport properties reported in the literature.

References

[1] International Energy Agency, “World Energy Outlook 2017,” 2017.

[2] Intergovernmental Panel on Climate Change, “Climate change 2013: The physical science basis,” 2013.

[3] J. Hansen *et al.*, “Assessing ‘Dangerous Climate Change’: Required Reduction of Carbon Emissions to Protect Young People, Future Generations and Nature,” *PLoS One*, vol. 8, no. 12, p. e81648, Dec. 2013.

[4] NASA, “Carbon Dioxide,” *Climate Change: Vital Signs of the Planet*, 2018. [Online]. Available: https://climate.nasa.gov/vital-signs/carbon-dioxide/. [Accessed: 29-Aug-2018].

[5] NASA, “Global Temperature,” *Climate Change: Vital Signs of the Planet*, 2018. [Online]. Available: https://climate.nasa.gov/vital-signs/global-temperature/. [Accessed: 29-Aug-2018].

[6] Q. Schiermeier, “Droughts, heatwaves and floods: How to tell when climate change is to blame,” *Nature*, vol. 560, no. 7716, pp. 20–22, Aug. 2018.

[7] Intergovernmental Panel on Climate Change, “Climate Change 2014: Impacts, Adaptation, and Vulnerability,” 2014.

[8] ActionAid, “Hotter Planet, Humanitarian Crisis,” 2016.

[9] European Comission, “Paris Agreement,” *Climate Action*, 2015. [Online]. Available: https://ec.europa.eu/clima/policies/international/negotiations/paris_en. [Accessed: 29-Aug-2018].

[10] Joydeep Gupta, “Climate change, El Nino combined to create possibly the largest drought across the world,” *Scroll.in*, 23-Nov-2016.

[11] International Energy Agency, “Renewables Information 2017: Overview,” 2017.

[12] Intergovernmental Panel on Climate Change, “Climate change 2014: Mitigation of climate change,” 2014.

[13] International Renewable Energy Agency, “Renewable Energy Source, Statistics Time Series,” *Data and Statistics*. [Online]. Available: http://resourceirena.irena.org/gateway/dashboard/. [Accessed: 29-Aug-2018].

[14] R. Perez, “A Way to the Most Abundant Energy,” *Scientific American*, 2013. [Online]. Available: http://www.scientificamerican.com/article/a-way-to-the-most-abundant-energy/. [Accessed: 10-Aug-2014].

[15] J. Rowlatt, “Silicon: After the chip, another revolution?,” *BBC News Magazine*, 2014. [Online]. Available: http://www.bbc.co.uk/news/magazine-28600802. [Accessed: 10-

Aug-2014].

[16] R. M. Swanson, “A vision for crystalline silicon photovoltaics,” *Prog. Photovoltaics Res. Appl.*, vol. 14, no. 5, pp. 443–453, Aug. 2006.

[17] J. D. Farmer and F. Lafond, “How predictable is technological progress?,” *Res. Policy*, vol. 45, no. 3, pp. 647–665, Apr. 2016.

[18] Origin Energy, “5 largest solar farms in the world,” *Blog*, 27-Jul-2018. [Online]. Available: https://www.originenergy.com.au/blog/lifestyle/5-largest-solar-farms-in-the-world.html. [Accessed: 29-Aug-2018].

[19] ACWA POWER, “ACWA Power wins the first ever Utility Scale Renewable Energy project in Saudi Arabia,” *Press Releases*, 2018. [Online]. Available: http://www.acwapower.com/en/newsroom/press-releases/latest-news/acwa-power-wins-the-first-ever-utility-scale-renewable-energy-project-in-saudi-arabia/. [Accessed: 29-Aug-2018].

[20] H. Ritchie and M. Roser, “Renewables,” *Our World in Data*, 2018. [Online]. Available: https://ourworldindata.org/renewables. [Accessed: 29-Aug-2018].

[21] NREL: National Center for Photovoltaics, “Best Research-Cell Efficiencies,” *Research Cell Record Efficiency Chart*, 2018. [Online]. Available: https://www.nrel.gov/pv/. [Accessed: 24-Aug-2018].

[22] C. J. Mulligan, C. Bilen, X. Zhou, W. J. Belcher, and P. C. Dastoor, “Levelised cost of electricity for organic photovoltaics,” *Sol. Energy Mater. Sol. Cells*, vol. 133, pp. 26–31, Feb. 2015.

[23] J. Perlin, “The Silicon Solar Cell Turns Fifty,” 2004.

[24] C. Battaglia, A. Cuevas, and S. De Wolf, “High-efficiency crystalline silicon solar cells: status and perspectives,” *Energy Environ. Sci.*, vol. 9, no. 5, pp. 1552–1576, May 2016.

[25] H. Yang, W. He, H. Wang, J. Huang, and J. Zhang, “Assessing power degradation and reliability of crystalline silicon solar modules with snail trails,” *Sol. Energy Mater. Sol. Cells*, vol. 187, pp. 61–68, Dec. 2018.

[26] S. R. Wenham *et al.*, “Advanced hydrogenation of silicon solar cells,” PCT/AU2013/000528, 29-Nov-2013.

[27] G. Hou *et al.*, “Life cycle assessment of grid-connected photovoltaic power generation from crystalline silicon solar modules in China,” *Appl. Energy*, vol. 164, pp. 882–890, Feb. 2016.

[28] E. J. Juarez-Perez *et al.*, “Photoinduced Giant Dielectric Constant in Lead Halide Perovskite Solar Cells,” *J. Phys. Chem. Lett.*, vol. 5, no. 13, pp. 2390–2394, Jul. 2014.

[29] K. T. Cho *et al.*, “Highly efficient perovskite solar cells with a compositionally engineered perovskite/hole transporting material interface,” *Energy Environ. Sci.*, vol. 10, no. 2, pp. 621–627, Feb. 2017.

[30] H. J. Snaith, “Perovskites: The Emergence of a New Era for Low-Cost, High-Efficiency Solar Cells,” *J. Phys. Chem. Lett.*, vol. 4, no. 21, pp. 3623–3630, Nov. 2013.

[31] M. Abd Mutalib *et al.*, “Progress towards highly stable and lead-free perovskite solar cells,” *Mater. Renew. Sustain. Energy*, vol. 7, no. 2, p. 7, May 2018.

[32] E. M. Sanehira *et al.*, “Enhanced mobility CsPbI3 quantum dot arrays for record-efficiency, high-voltage photovoltaic cells,” *Sci. Adv.*, vol. 3, no. 10, p. eaao4204, Oct. 2017.

[33] A. R. Kirmani *et al.*, “Overcoming the Ambient Manufacturability-Scalability-Performance Bottleneck in Colloidal Quantum Dot Photovoltaics,” *Adv. Mater.*, p. 1801661, Jul. 2018.

[34] M. A. Green, Y. Hishikawa, E. D. Dunlop, D. H. Levi, J. Hohl-Ebinger, and A. W. Y. Ho-Baillie, “Solar cell efficiency tables (version 52),” *Prog. Photovoltaics Res. Appl.*, vol. 26, no. 7, pp. 427–436, Jul. 2018.

[35] M. Jørgensen *et al.*, “The state of organic solar cells - a meta analysis,” *Sol. Energy Mater. Sol. Cells*, vol. 119, pp. 84–93, Dec. 2013.

[36] R. R. Søndergaard, M. Hösel, and F. C. Krebs, “Roll-to-Roll fabrication of large area functional organic materials,” *J. Polym. Sci. Part B Polym. Phys.*, vol. 51, no. 1, pp. 16–34, Jan. 2013.

[37] S. R. Forrest, “The path to ubiquitous and low-cost organic electronic appliances on plastic,” *Nature*, vol. 428, no. 6986, pp. 911–918, Apr. 2004.

[38] H. Sirringhaus, “25th Anniversary Article: Organic Field-Effect Transistors: The Path Beyond Amorphous Silicon,” *Adv. Mater.*, vol. 26, no. 9, pp. 1319–1335, Mar. 2014.

[39] J.-F. Tremblay, “The rise of OLED displays,” *Chem. Eng. News*, vol. 94, no. 28, pp. 30–34, 2016.

[40] B. P. Rand, J. Genoe, P. Heremans, and J. Poortmans, “Solar cells utilizing small molecular weight organic semiconductors,” *Prog. Photovoltaics Res. Appl.*, vol. 15, no. 8, pp. 659–676, Dec. 2007.

[41] A. Mishra and P. Bäuerle, “Small molecule organic semiconductors on the move: promises for future solar energy technology,” *Angew. Chemie Int. Ed.*, vol. 51, no. 9, pp. 2020–2067, Feb. 2012.

[42] V. I. Madogni, B. Kounouhéwa, A. Akpo, M. Agbomahéna, S. A. Hounkpatin, and C. N. Awanou, “Comparison of degradation mechanisms in organic photovoltaic devices

upon exposure to a temperate and a subequatorial climate," *Chem. Phys. Lett.*, vol. 640, pp. 201–214, Nov. 2015.

[43] M. Hermenau, M. Riede, K. Leo, S. A. Gevorgyan, and K. Norrman, "Water and oxygen induced degradation of small molecule organic solar cells," *Sol. Energy Mater. Sol. Cells*, vol. 95, no. 5, pp. 1268–1277, May 2011.

[44] Y. Zhang, I. D. W. Samuel, T. Wang, and D. G. Lidzey, "Current Status of Outdoor Lifetime Testing of Organic Photovoltaics," *Adv. Sci.*, vol. 5, no. 8, p. 1800434, Aug. 2018.

[45] W. Zhao *et al.*, "Molecular Optimization Enables over 13% Efficiency in Organic Solar Cells," *J. Am. Chem. Soc.*, vol. 139, no. 21, pp. 7148–7151, May 2017.

[46] Y. Huang, E. J. Kramer, A. J. Heeger, and G. C. Bazan, "Bulk Heterojunction Solar Cells: Morphology and Performance Relationships," *Chem. Rev.*, vol. 114, no. 14, pp. 7006–7043, Jul. 2014.

[47] K. Cnops, B. P. Rand, D. Cheyns, B. Verreet, M. A. Empl, and P. Heremans, "8.4% efficient fullerene-free organic solar cells exploiting long-range exciton energy transfer," *Nat. Commun.*, vol. 5, pp. 3406–3412, Jan. 2014.

[48] O. L. Griffith and S. R. Forrest, "Exciton management in organic photovoltaic multidonor energy cascades," *Nano Lett.*, vol. 14, no. 5, pp. 2353–2358, May 2014.

[49] H.-S. Shim *et al.*, "Efficient Vacuum-Deposited Ternary Organic Solar Cells with Broad Absorption, Energy Transfer, and Enhanced Hole Mobility," *ACS Appl. Mater. Interfaces*, vol. 8, no. 2, pp. 1214–1219, Jan. 2016.

[50] H.-S. Shim *et al.*, "Efficient Vacuum-Deposited Tandem Organic Solar Cells with Fill Factors Higher Than Single-Junction Subcells," *Adv. Energy Mater.*, vol. 5, no. 13, p. 1500228, Jul. 2015.

[51] T.-H. Han, M.-R. Choi, C.-W. Jeon, Y.-H. Kim, S.-K. Kwon, and T.-W. Lee, "Ultrahigh-efficiency solution-processed simplified small-molecule organic light-emitting diodes using universal host materials," *Sci. Adv.*, vol. 2, no. 10, pp. e1601428–e1601428, Oct. 2016.

[52] M. Riede, T. Mueller, W. Tress, R. Schueppel, and K. Leo, "Small-molecule solar cells - status and perspectives," *Nanotechnology*, vol. 19, no. 42, pp. 424001–424012, Oct. 2008.

[53] A. M. Gaikwad, Y. Khan, A. E. Ostfeld, S. Pandya, S. Abraham, and A. C. Arias, "Identifying orthogonal solvents for solution processed organic transistors," *Org. Electron.*, vol. 30, pp. 18–29, Mar. 2016.

[54] X. Che, X. Xiao, J. D. Zimmerman, D. Fan, and S. R. Forrest, "High-Efficiency,

Vacuum-Deposited, Small-Molecule Organic Tandem and Triple-Junction Photovoltaic Cells," *Adv. Energy Mater.*, vol. 4, no. 18, p. 1400568, Dec. 2014.

[55] L. Meng *et al.*, "Organic and solution-processed tandem solar cells with 17.3% efficiency.," *Science*, vol. 361, no. 6407, pp. 1094–1098, Sep. 2018.

[56] Y. Cui *et al.*, "Fine-Tuned Photoactive and Interconnection Layers for Achieving over 13% Efficiency in a Fullerene-Free Tandem Organic Solar Cell," *J. Am. Chem. Soc.*, vol. 139, no. 21, pp. 7302–7309, May 2017.

[57] Heliatek, "Heliatek sets new Organic Photovoltaic world record efficiency of 13.2%," *Press Release*, 2016. [Online]. Available: https://www.heliatek.com/en/press/press-releases/details/heliatek-sets-new-organic-photovoltaic-world-record-efficiency-of-13-2. [Accessed: 16-Sep-2018].

[58] Heliatek, "Heliatek – The future is light." [Online]. Available: https://www.heliatek.com/en/. [Accessed: 28-Aug-2018].

[59] C. Brabec, U. Scherf, and V. Dyakonov, Eds., *Organic photovoltaics: materials, device physics, and manufacturing technologies*, Second Edi. Weinheim, Germany: Wiley-VCH, 2014.

[60] J. Clayden, N. Greeves, and S. G. Warren, *Organic chemistry*, Second Edi. Oxford University Press, 2012.

[61] W. Tress, *Organic Solar Cells Theory, Experiment, and Device Simulation*. Springer International Publishing, 2014.

[62] C. Deibel and V. Dyakonov, "Polymer–fullerene bulk heterojunction solar cells," *Reports Prog. Phys.*, vol. 73, no. 9, p. 096401, Sep. 2010.

[63] J. A. Carr and S. Chaudhary, "The identification, characterization and mitigation of defect states in organic photovoltaic devices: a review and outlook," *Energy Environ. Sci.*, vol. 6, no. 12, pp. 3414–3438, Nov. 2013.

[64] S. E. Gledhill, B. Scott, and B. A. Gregg, "Organic and nano-structured composite photovoltaics: An overview," *J. Mater. Res.*, vol. 20, no. 12, pp. 3167–3179, Mar. 2005.

[65] B. A. Gregg, S.-G. Chen, and R. A. Cormier, "Coulomb Forces and Doping in Organic Semiconductors," *Chem. Mater.*, vol. 16, no. 23, pp. 4586–4599, Nov. 2004.

[66] H. Bässler, "Charge Transport in Disordered Organic Photoconductors a Monte Carlo Simulation Study," *Phys. status solidi*, vol. 175, no. 1, pp. 15–56, Jan. 1993.

[67] W. Schottky, "Abweichungen vom ohmschen gesetz in halbleitern," *Phys. Zeitschr*, vol. 41, no. 570, 1940.

[68] N. F. Mott, "Note on the contact between a metal and an insulator or semi-conductor,"

Math. Proc. Cambridge Philos. Soc., vol. 34, no. 04, p. 568, Oct. 1938.

[69] L. J. Brillson, "The structure and properties of metal-semiconductor interfaces," *Surf. Sci. Rep.*, vol. 2, no. 2, pp. 123–326, 1982.

[70] H. Vázquez, F. Flores, R. Oszwaldoski, J. Ortega, R. Pérez, and A. Kahn, "Barrier formation at metal–organic interfaces: dipole formation and the charge neutrality level," *Appl. Surf. Sci.*, vol. 234, no. 1–4, pp. 107–112, 2004.

[71] K. Akaike, N. Koch, and M. Oehzelt, "Fermi level pinning induced electrostatic fields and band bending at organic heterojunctions," *Appl. Phys. Lett.*, vol. 105, no. 22, p. 223303, Dec. 2014.

[72] I. G. Hill, A. Rajagopal, A. Kahn, and Y. Hu, "Molecular level alignment at organic semiconductor-metal interfaces," *Appl. Phys. Lett.*, vol. 73, no. 5, p. 662, Jul. 1998.

[73] S. Olthof, W. Tress, R. Meerheim, B. Lüssem, and K. Leo, "Photoelectron spectroscopy study of systematically varied doping concentrations in an organic semiconductor layer using a molecular p-dopant," *J. Appl. Phys.*, vol. 106, no. 10, p. 103711, Nov. 2009.

[74] D. Cahen, A. Kahn, and E. Umbach, "Energetics of molecular interfaces," *Mater. Today*, vol. 8, no. 7, pp. 32–41, Jul. 2005.

[75] N. Koch, "Energy levels at interfaces between metals and conjugated organic molecules," *J. Phys. Condens. Matter*, vol. 20, no. 18, p. 184008, May 2008.

[76] P. Heremans, D. Cheyns, and B. P. Rand, "Strategies for increasing the efficiency of heterojunction organic solar cells: material selection and device architecture," *Acc. Chem. Res.*, vol. 42, no. 11, pp. 1740–1747, Nov. 2009.

[77] W. Shockley and H. J. Queisser, "Detailed Balance Limit of Efficiency of p-n Junction Solar Cells," *J. Appl. Phys.*, vol. 32, no. 3, p. 510, Jun. 1961.

[78] C. H. Henry, "Limiting efficiencies of ideal single and multiple energy gap terrestrial solar cells," *J. Appl. Phys.*, vol. 51, no. 8, p. 4494, Jul. 1980.

[79] J. Y. Kim *et al.*, "New Architecture for High-Efficiency Polymer Photovoltaic Cells Using Solution-Based Titanium Oxide as an Optical Spacer," *Adv. Mater.*, vol. 18, no. 5, pp. 572–576, Mar. 2006.

[80] C. W. Tang, "Two-layer organic photovoltaic cell," *Appl. Phys. Lett.*, vol. 48, no. 2, pp. 183–185, Jan. 1986.

[81] B. Qi and J. Wang, "Fill factor in organic solar cells," *Phys. Chem. Chem. Phys.*, vol. 15, no. 23, p. 8972, 2013.

[82] T. Sakurai, S. Toyoshima, and K. Akimoto, "Role of electrode buffer layers in organic solar cells," in *2013 International Renewable and Sustainable Energy Conference*

(IRSEC), 2013, pp. 46–48.

[83] C. A. Gueymard, D. Myers, and K. Emery, "Proposed reference irradiance spectra for solar energy systems testing," *Sol. Energy*, vol. 73, no. 6, pp. 443–467, Dec. 2002.

[84] N. K. Elumalai and A. Uddin, "Open circuit voltage of organic solar cells: an in-depth review," *Energy Environ. Sci.*, vol. 9, no. 2, pp. 391–410, Feb. 2016.

[85] K. Tvingstedt and C. Deibel, "Temperature Dependence of Ideality Factors in Organic Solar Cells and the Relation to Radiative Efficiency," *Adv. Energy Mater.*, vol. 6, no. 9, p. 1502230, May 2016.

[86] A. Cuevas, "The Recombination Parameter J0," *Energy Procedia*, vol. 55, pp. 53–62, 2014.

[87] D. Pysch, A. Mette, and S. W. Glunz, "A review and comparison of different methods to determine the series resistance of solar cells," *Sol. Energy Mater. Sol. Cells*, vol. 91, no. 18, pp. 1698–1706, Nov. 2007.

[88] J. Bullock *et al.*, "Efficient silicon solar cells with dopant-free asymmetric heterocontacts," *Nat. Energy*, vol. 1, no. 3, p. 15031, Jan. 2016.

[89] X. Zhao and M. Wang, "Organic hole-transporting materials for efficient perovskite solar cells," *Mater. Today Energy*, vol. 7, pp. 208–220, Mar. 2018.

[90] J. E. Houston, S. Richeter, S. Clément, and R. C. Evans, "Molecular design of interfacial layers based on conjugated polythiophenes for polymer and hybrid solar cells," *Polym. Int.*, vol. 66, no. 10, pp. 1333–1348, Oct. 2017.

[91] B. Walker, H. Choi, and J. Y. Kim, "Interfacial engineering for highly efficient organic solar cells," *Curr. Appl. Phys.*, vol. 17, no. 3, pp. 370–391, Mar. 2017.

[92] R. Steim, F. R. Kogler, and C. J. Brabec, "Interface materials for organic solar cells," *J. Mater. Chem.*, vol. 20, no. 13, p. 2499, Mar. 2010.

[93] L. Lu, T. Xu, I. H. Jung, and L. Yu, "Match the Interfacial Energy Levels between Hole Transport Layer and Donor Polymer To Achieve High Solar Cell Performance," *J. Phys. Chem. C*, vol. 118, no. 40, pp. 22834–22839, Oct. 2014.

[94] C. Liu *et al.*, "Decreased Charge Transport Barrier and Recombination of Organic Solar Cells by Constructing Interfacial Nanojunction with Annealing-Free ZnO and Al Layers," *ACS Appl. Mater. Interfaces*, vol. 9, no. 26, pp. 22068–22075, Jul. 2017.

[95] B. Lüssem, M. Riede, and K. Leo, "Doping of organic semiconductors," *Phys. status solidi*, vol. 210, no. 1, pp. 9–43, Jan. 2013.

[96] P. Wei, T. Menke, B. D. Naab, K. Leo, M. Riede, and Z. Bao, "2-(2-Methoxyphenyl)-1,3-dimethyl-1H-benzoimidazol-3-ium Iodide as a New Air-Stable n-Type Dopant for Vacuum-Processed Organic Semiconductor Thin Films," *J. Am. Chem. Soc.*, vol. 134,

no. 9, pp. 3999–4002, Mar. 2012.

[97] Z. Zhao *et al.*, "Improving the Conductivity of PEDOT:PSS Hole Transport Layer in Polymer Solar Cells via Copper(II) Bromide Salt Doping," *ACS Appl. Mater. Interfaces*, vol. 7, no. 3, pp. 1439–1448, Jan. 2015.

[98] L. Caliò *et al.*, "Benzothiadiazole–triphenylamine as an efficient exciton blocking layer in small molecule based organic solar cells," *Sustain. Energy Fuels*, 2018.

[99] A. W. Hains, J. Liu, A. B. F. Martinson, M. D. Irwin, and T. J. Marks, "Anode Interfacial Tuning via Electron-Blocking/Hole-Transport Layers and Indium Tin Oxide Surface Treatment in Bulk-Heterojunction Organic Photovoltaic Cells," *Adv. Funct. Mater.*, vol. 20, no. 4, pp. 595–606, Feb. 2010.

[100] R. Lampande, G. W. Kim, J. Boizot, Y. J. Kim, R. Pode, and J. H. Kwon, "A highly efficient transition metal oxide layer for hole extraction and transport in inverted polymer bulk heterojunction solar cells," *J. Mater. Chem. A*, vol. 1, no. 23, p. 6895, May 2013.

[101] X. Jia *et al.*, "Highly Efficient and Air Stable Inverted Polymer Solar Cells Using LiF-Modified ITO Cathode and MoO3/AgAl Alloy Anode," *ACS Appl. Mater. Interfaces*, vol. 8, no. 6, pp. 3792–3799, Feb. 2016.

[102] Q. Sun *et al.*, "A two-step strategy to clarify the roles of a solution processed PFN interfacial layer in highly efficient polymer solar cells," *J. Mater. Chem. A*, vol. 3, no. 36, pp. 18432–18441, Sep. 2015.

[103] M. O. Reese, M. S. White, G. Rumbles, D. S. Ginley, and S. E. Shaheen, "Optimal negative electrodes for poly(3-hexylthiophene): [6,6]-phenyl C61-butyric acid methyl ester bulk heterojunction photovoltaic devices," *Appl. Phys. Lett.*, vol. 92, no. 5, p. 053307, Feb. 2008.

[104] H. Ju *et al.*, "Interplay between Interfacial Structures and Device Performance in Organic Solar Cells: A Case Study with the Low Work Function Metal, Calcium," *ACS Appl. Mater. Interfaces*, vol. 8, no. 3, pp. 2125–2131, Jan. 2016.

[105] T. Sakurai, S. Toyoshima, H. Kitazume, S. Masuda, H. Kato, and K. Akimoto, "Influence of gap states on electrical properties at interface between bathocuproine and various types of metals," *J. Appl. Phys.*, vol. 107, no. 4, p. 043707, Feb. 2010.

[106] H. Vázquez, F. Flores, and A. Kahn, "Induced Density of States model for weakly-interacting organic semiconductor interfaces," *Org. Electron.*, vol. 8, no. 2–3, pp. 241–248, Apr. 2007.

[107] J. Blochwitz *et al.*, "Interface electronic structure of organic semiconductors with controlled doping levels," *Org. Electron.*, vol. 2, no. 2, pp. 97–104, Sep. 2001.

[108] M. Li, W. Zhang, H. Wang, L. Chen, C. Zheng, and R. Chen, “Effect of organic cathode interfacial layers on efficiency and stability improvement of polymer solar cells,” *RSC Adv.*, vol. 7, no. 50, pp. 31158–31163, Jun. 2017.

[109] B. Qi, Z.-G. Zhang, and J. Wang, “Uncovering the role of cathode buffer layer in organic solar cells,” *Sci. Rep.*, vol. 5, p. 7803, Jan. 2015.

[110] H. Gommans *et al.*, “On the Role of Bathocuproine in Organic Photovoltaic Cells,” *Adv. Funct. Mater.*, vol. 18, no. 22, pp. 3686–3691, Nov. 2008.

[111] M. Gaceur *et al.*, “Ligand-Free Synthesis of Aluminum-Doped Zinc Oxide Nanocrystals and their Use as Optical Spacers in Color-Tuned Highly Efficient Organic Solar Cells,” *Adv. Funct. Mater.*, vol. 26, no. 2, pp. 243–253, Jan. 2016.

[112] S.-H. Lee, J.-W. Seo, and J.-Y. Lee, “Stable inverted small molecular organic solar cells using a p-doped optical spacer,” *Nanoscale*, vol. 7, no. 1, pp. 157–165, Dec. 2015.

[113] S. R. Forrest, “The Limits to Organic Photovoltaic Cell Efficiency,” *MRS Bull.*, vol. 30, no. 01, pp. 28–32, Jan. 2011.

[114] H. A. Atwater and A. Polman, “Plasmonics for improved photovoltaic devices,” *Nat. Mater.*, vol. 9, no. 3, pp. 205–13, Mar. 2010.

[115] S. Ahn, D. Rourke, and W. Park, “Plasmonic nanostructures for organic photovoltaic devices,” *J. Opt.*, vol. 18, no. 3, p. 033001, Mar. 2016.

[116] S. Shao *et al.*, “In situ formation of MoO 3 in PEDOT:PSS matrix: A facile way to produce a smooth and less hygroscopic hole transport layer for highly stable polymer bulk heterojunction solar cells,” *Adv. Energy Mater.*, vol. 3, no. 3, pp. 349–355, Mar. 2013.

[117] H. Choi, H.-B. Kim, S.-J. Ko, J. Y. Kim, and A. J. Heeger, “An Organic Surface Modifier to Produce a High Work Function Transparent Electrode for High Performance Polymer Solar Cells,” *Adv. Mater.*, vol. 27, no. 5, pp. 892–896, Feb. 2015.

[118] K. Suemori, M. Yokoyama, and M. Hiramoto, “Electrical shorting of organic photovoltaic films resulting from metal migration,” *J. Appl. Phys.*, vol. 99, no. 3, p. 036109, Feb. 2006.

[119] Y. Lare *et al.*, “Influence of the exciton blocking layer on the stability of layered organic solar cells,” *J. Phys. Chem. Solids*, vol. 72, no. 2, pp. 97–103, Feb. 2011.

[120] L. Yang, H. Xu, H. Tian, S. Yin, and F. Zhang, “Effect of cathode buffer layer on the stability of polymer bulk heterojunction solar cells,” *Sol. Energy Mater. Sol. Cells*, vol. 94, no. 10, pp. 1831–1834, Oct. 2010.

[121] J. Li *et al.*, “A study of stabilization of P3HT/PCBM organic solar cells by

photochemical active TiOx layer," *Sol. Energy Mater. Sol. Cells*, vol. 95, no. 4, pp. 1123–1130, Apr. 2011.

[122] Y. Cao, G. Yu, C. Zhang, R. Menon, and A. . Heeger, "Polymer light-emitting diodes with polyethylene dioxythiophene–polystyrene sulfonate as the transparent anode," *Synth. Met.*, vol. 87, no. 2, pp. 171–174, Mar. 1997.

[123] S. A. Carter, M. Angelopoulos, S. Karg, P. J. Brock, and J. C. Scott, "Polymeric anodes for improved polymer light-emitting diode performance," *Appl. Phys. Lett.*, vol. 70, no. 16, p. 2067, Jun. 1998.

[124] J. Huang, P. F. Miller, J. S. Wilson, A. J. de Mello, J. C. de Mello, and D. D. C. Bradley, "Investigation of the Effects of Doping and Post-Deposition Treatments on the Conductivity, Morphology, and Work Function of Poly(3,4-ethylenedioxythiophene)/Poly(styrene sulfonate) Films," *Adv. Funct. Mater.*, vol. 15, no. 2, pp. 290–296, Feb. 2005.

[125] Y. Kim, A. M. Ballantyne, J. Nelson, and D. D. C. Bradley, "Effects of thickness and thermal annealing of the PEDOT:PSS layer on the performance of polymer solar cells," *Org. Electron.*, vol. 10, no. 1, pp. 205–209, Feb. 2009.

[126] Y. Xia and J. Ouyang, "PEDOT:PSS films with significantly enhanced conductivities induced by preferential solvation with cosolvents and their application in polymer photovoltaic cells," *J. Mater. Chem.*, vol. 21, no. 13, p. 4927, Mar. 2011.

[127] M. P. de Jong, L. J. van IJzendoorn, and M. J. A. de Voigt, "Stability of the interface between indium-tin-oxide and poly(3,4-ethylenedioxythiophene)/poly(styrenesulfonate) in polymer light-emitting diodes," *Appl. Phys. Lett.*, vol. 77, no. 14, p. 2255, Sep. 2000.

[128] A. K. K. Kyaw, X. W. Sun, C. Y. Jiang, G. Q. Lo, D. W. Zhao, and D. L. Kwong, "An inverted organic solar cell employing a sol-gel derived ZnO electron selective layer and thermal evaporated MoO3 hole selective layer," *Appl. Phys. Lett.*, vol. 93, no. 22, p. 221107, Dec. 2008.

[129] Z. Tan *et al.*, "Efficient and stable polymer solar cells with solution-processed molybdenum oxide interfacial layer," *J. Mater. Chem. A*, vol. 1, no. 3, pp. 657–664, Dec. 2013.

[130] B. Li, H. Ren, H. Yuan, A. Karim, and X. Gong, "Room-Temperature, Solution-Processed MoOx Thin Film as a Hole Extraction Layer to Substitute PEDOT/PSS in Polymer Solar Cells," *ACS Photonics*, vol. 1, no. 2, pp. 87–90, Feb. 2014.

[131] M. J. Tan, S. Zhong, J. Li, Z. Chen, and W. Chen, "Air-Stable Efficient Inverted Polymer Solar Cells Using Solution-Processed Nanocrystalline ZnO Interfacial Layer,"

ACS Appl. Mater. Interfaces, vol. 5, no. 11, pp. 4696–4701, Jun. 2013.

[132] S. Kundu *et al.*, "Device stability of inverted and conventional bulk heterojunction solar cells with MoO3 and ZnO nanoparticles as charge transport layers," *Org. Electron.*, vol. 14, no. 11, pp. 3083–3088, Nov. 2013.

[133] V. Shrotriya, G. Li, Y. Yao, C.-W. Chu, and Y. Yang, "Transition metal oxides as the buffer layer for polymer photovoltaic cells," *Appl. Phys. Lett.*, vol. 88, no. 7, p. 073508, Feb. 2006.

[134] M. Yoosuf Ameen, S. Pradhan, M. Remyth Suresh, and V. S. Reddy, "MoO3 anode buffer layer for efficient and stable small molecular organic solar cells," *Opt. Mater. (Amst).*, vol. 39, pp. 134–139, Jan. 2015.

[135] T. Umeda, T. Shirakawa, A. Fujii, and K. Yoshino, "Improvement of Characteristics of Organic Photovoltaic Devices Composed of Conducting Polymer-Fullerene Systems by Introduction of ZnO Layer," *Jpn. J. Appl. Phys.*, vol. 42, no. Part 2, No. 12A, pp. L1475–L1477, Dec. 2003.

[136] Z. Liang, Q. Zhang, L. Jiang, and G. Cao, "ZnO cathode buffer layers for inverted polymer solar cells," *Energy Environ. Sci.*, vol. 8, no. 12, pp. 3442–3476, Nov. 2015.

[137] S. Woo, W. Hyun Kim, H. Kim, Y. Yi, H.-K. Lyu, and Y. Kim, "8.9% Single-Stack Inverted Polymer Solar Cells with Electron-Rich Polymer Nanolayer-Modified Inorganic Electron-Collecting Buffer Layers," *Adv. Energy Mater.*, vol. 4, no. 7, p. 1301692, May 2014.

[138] B. A. Gregg, "Bilayer molecular solar cells on spin-coated TiO2 substrates," *Chem. Phys. Lett.*, vol. 258, no. 3–4, pp. 376–380, Aug. 1996.

[139] D. Muñoz-Rojas *et al.*, "High-speed atmospheric atomic layer deposition of ultra thin amorphous TiO2 blocking layers at 100 °C for inverted bulk heterojunction solar cells," *Prog. Photovoltaics Res. Appl.*, vol. 21, no. 4, p. n/a-n/a, Apr. 2013.

[140] A. Guerrero, S. Chambon, L. Hirsch, and G. Garcia-Belmonte, "Light-modulated TiOx Interlayer Dipole and Contact Activation in Organic Solar Cell Cathodes," *Adv. Funct. Mater.*, vol. 24, no. 39, pp. 6234–6240, Oct. 2014.

[141] X. Bao, L. Sun, W. Shen, C. Yang, W. Chen, and R. Yang, "Facile preparation of TiOx film as an interface material for efficient inverted polymer solar cells," *J. Mater. Chem. A*, vol. 2, no. 6, pp. 1732–1737, Jan. 2014.

[142] S. Trost *et al.*, "Overcoming the 'Light-Soaking' Issue in Inverted Organic Solar Cells by the Use of Al:ZnO Electron Extraction Layers," *Adv. Energy Mater.*, vol. 3, no. 11, pp. 1437–1444, Nov. 2013.

[143] F. J. Lim, Y. T. Set, A. Krishnamoorthy, J. Ouyang, J. Luther, and G. W. Ho,

"Addressing the light-soaking issue in inverted organic solar cells using chemical bath deposited fluorinated TiOx electron transport layer," *J. Mater. Chem. A*, vol. 3, no. 1, pp. 314–322, Dec. 2015.

[144] J. Liu *et al.*, "Enhancement of inverted polymer solar cells with solution-processed ZnO-TiOx composite as cathode buffer layer," *Appl. Phys. Lett.*, vol. 100, no. 21, p. 213906, May 2012.

[145] A. G. Pattantyus-Abraham *et al.*, "Depleted-Heterojunction Colloidal Quantum Dot Solar Cells," *ACS Nano*, vol. 4, no. 6, pp. 3374–3380, Jun. 2010.

[146] J. M. Luther, J. Gao, M. T. Lloyd, O. E. Semonin, M. C. Beard, and A. J. Nozik, "Stability Assessment on a 3% Bilayer PbS/ZnO Quantum Dot Heterojunction Solar Cell," *Adv. Mater.*, vol. 22, no. 33, pp. 3704–3707, Sep. 2010.

[147] P. Peumans and S. R. Forrest, "Very-high-efficiency double-heterostructure copper phthalocyanine/C60 photovoltaic cells," *Appl. Phys. Lett.*, vol. 79, no. 1, pp. 126–128, Jul. 2001.

[148] M. Vogel, S. Doka, C. Breyer, M. C. Lux-Steiner, and K. Fostiropoulos, "On the function of a bathocuproine buffer layer in organic photovoltaic cells," *Appl. Phys. Lett.*, vol. 89, no. 16, p. 163501, Oct. 2006.

[149] C. K. Chan, W. Zhao, A. Kahn, and I. G. Hill, "Influence of chemical doping on the performance of organic photovoltaic cells," *Appl. Phys. Lett.*, vol. 94, no. 20, p. 203306, May 2009.

[150] I. S. Oh, C. H. Ji, and S. Y. Oh, "Effects of ytterbium on electrical and optical properties of BCP/Ag/WO3 transparent electrode based organic photovoltaic cells," *Electron. Mater. Lett.*, vol. 12, no. 1, pp. 156–162, Jan. 2016.

[151] M. Y. Chan, S. L. Lai, K. M. Lau, C. S. Lee, and S. T. Lee, "Application of metal-doped organic layer both as exciton blocker and optical spacer for organic photovoltaic devices," *Appl. Phys. Lett.*, vol. 89, no. 16, p. 163515, Oct. 2006.

[152] V. Tripathi, D. Datta, G. S. Samal, A. Awasthi, and S. Kumar, "Role of exciton blocking layers in improving efficiency of copper phthalocyanine based organic solar cells," *J. Non. Cryst. Solids*, vol. 354, no. 19–25, pp. 2901–2904, May 2008.

[153] N. Wang, J. Yu, Y. Zang, J. Huang, and Y. Jiang, "Effect of buffer layers on the performance of organic photovoltaic cells based on copper phthalocyanine and C60," *Sol. Energy Mater. Sol. Cells*, vol. 94, no. 2, pp. 263–266, Feb. 2010.

[154] T. Wang, C. Chen, K. Guo, G. Chen, T. Xu, and B. Wei, "Improved performance of polymer solar cells by using inorganic, organic, and doped cathode buffer layers," *Chinese Phys. B*, vol. 25, no. 3, p. 038402, Mar. 2016.

[155] J. Y. Lee, T. Lee, H. J. Park, and L. J. Guo, “Improved solar cell performance by adding ultra-thin Alq3 at the cathode interface,” *Org. Electron.*, vol. 15, no. 11, pp. 2710–2714, Nov. 2014.

[156] J.-H. Kim and J.-G. Park, “Effect of a Co-evaporated Alq3:Liq cathode buffer layer on the performance of a polymer photovoltaic cell,” *J. Korean Phys. Soc.*, vol. 66, no. 12, pp. 1872–1878, Jun. 2015.

[157] J. K. Baral, R. Izquierdo, M. Packirisamy, and V.-V. Truong, “Improved polymer solar cell performance by engineering of cathode interface,” *Eur. Phys. J. Appl. Phys.*, vol. 55, no. 3, p. 30202, Sep. 2011.

[158] D. Y. Luo *et al.*, “A bi-functional structure with tunable electrical and optical properties for organic photovoltaic cells,” *J. Appl. Phys.*, vol. 113, no. 22, p. 224506, Jun. 2013.

[159] G. D. R. Banoukepa, A. Fujii, Y. Shimizu, and M. Ozaki, “1,3,5-Tris(phenyl-2-benzimidazole)-benzene cathode buffer layer thickness dependence in solution-processable organic solar cell based on 1,4,8,11,15,18,22,25-octahexylphthalocyanine,” *Jpn. J. Appl. Phys.*, vol. 54, no. 4S, p. 04DK11, Apr. 2015.

[160] A. Lakhdar Toumi *et al.*, “On the exciton blocking layer at the interface organic/cathode in planar multiheterojunction organic solar cells,” *Solid. State. Electron.*, vol. 104, pp. 1–5, Feb. 2015.

[161] J. Lee *et al.*, “Electron transport mechanism of bathocuproine exciton blocking layer in organic photovoltaics,” *Phys. Chem. Chem. Phys.*, vol. 18, no. 7, pp. 5444–5452, Feb. 2016.

[162] H. Yoshida, “Electron Transport in Bathocuproine Interlayer in Organic Semiconductor Devices,” *J. Phys. Chem. C*, vol. 119, no. 43, pp. 24459–24464, Oct. 2015.

[163] Sigma-Aldrich, “Organic Materials Supplier.” [Online]. Available: https://www.sigmaaldrich.com/united-kingdom.html. [Accessed: 08-Sep-2018].

[164] Y. Oh *et al.*, “Plasmonic Periodic Nanodot Arrays via Laser Interference Lithography for Organic Photovoltaic Cells with >10% Efficiency,” *ACS Nano*, vol. 10, no. 11, pp. 10143–10151, Nov. 2016.

[165] D. Kozanoglu, D. H. Apaydin, A. Cirpan, and E. N. Esenturk, “Power conversion efficiency enhancement of organic solar cells by addition of gold nanostars, nanorods, and nanospheres,” *Org. Electron.*, vol. 14, no. 7, pp. 1720–1727, Jul. 2013.

[166] A. Singh, A. Dey, D. Das, and P. K. Iyer, “Effect of Dual Cathode Buffer Layer on the Charge Carrier Dynamics of rrP3HT:PCBM Based Bulk Heterojunction Solar Cell,” *ACS Appl. Mater. Interfaces*, vol. 8, no. 17, pp. 10904–10910, May 2016.

[167] J. Farinhas, A. M. Ferraria, A. M. B. do Rego, J. Morgado, and A. Charas, "Understanding the Role of Phenanthroline as Interlayer in Bulk Heterojunction Organic Photovoltaic Cells," *ChemistrySelect*, vol. 1, no. 18, pp. 5638–5646, Nov. 2016.

[168] T. Taima, J. Tanaka, T. Kuwabara, and K. Takahashi, "Insertion effects of interlayers for efficient polymer-based organic solar cells," *Jpn. J. Appl. Phys.*, vol. 54, no. 8S1, p. 08KF05, Aug. 2015.

[169] F. Jin *et al.*, "Improvement in power conversion efficiency and long-term lifetime of organic photovoltaic cells by using bathophenanthroline/molybdenum oxide as compound cathode buffer layer," *Sol. Energy Mater. Sol. Cells*, vol. 117, pp. 189–193, Oct. 2013.

[170] S.-W. Liu *et al.*, "Improving Performance and Lifetime of Small-Molecule Organic Photovoltaic Devices by Using Bathocuproine–Fullerene Cathodic Layer," *ACS Appl. Mater. Interfaces*, vol. 7, no. 17, pp. 9262–9273, May 2015.

[171] Q. Burlingame *et al.*, "Reliability of Small Molecule Organic Photovoltaics with Electron-Filtering Compound Buffer Layers," *Adv. Energy Mater.*, vol. 6, no. 21, p. 1601094, Nov. 2016.

[172] Z. Huai *et al.*, "High-Efficiency and Stable Organic Solar Cells Enabled by Dual Cathode Buffer Layers," *ACS Appl. Mater. Interfaces*, vol. 10, no. 6, pp. 5682–5692, Feb. 2018.

[173] W. Tress, K. Leo, and M. Riede, "Influence of Hole-Transport Layers and Donor Materials on Open-Circuit Voltage and Shape of I-V Curves of Organic Solar Cells," *Adv. Funct. Mater.*, vol. 21, no. 11, pp. 2140–2149, Jun. 2011.

[174] S. Pfuetzner *et al.*, "Characterisation of different hole transport materials as used in organic p-i-n solar cells," in *Proceedings of SPIE - The International Society for Optical Engineering*, 2008, vol. 6999, p. 69991M–69991M–9.

[175] F. Jin *et al.*, "Interface Engineering of Organic Schottky Barrier Solar Cells and Its Application in Enhancing Performances of Planar Heterojunction Solar Cells," *Sci. Rep.*, vol. 6, no. 1, p. 26262, Sep. 2016.

[176] P. Li *et al.*, "Improved charge transport ability of polymer solar cells by using NPB/MoO3 as anode buffer layer," *Sol. Energy*, vol. 170, pp. 212–216, Aug. 2018.

[177] X. Yan *et al.*, "The improvement in organic photovoltaic response by inserting an interlayer between MoO3 and mixed layer of C60:5 wt% TAPC," *Org. Electron.*, vol. 23, pp. 5–10, Aug. 2015.

[178] J. Golder, C.-W. Lin, H.-W. Chen, Y.-B. Lan, C.-T. Chen, and J.-K. Wang,

"Unconventional anode interlayer universally improving solar cell efficiency," *J. Phys. D. Appl. Phys.*, vol. 51, no. 31, p. 314002, Aug. 2018.

[179] B. Wu *et al.*, "Uncovering loss mechanisms in silver nanoparticle-blended plasmonic organic solar cells," *Nat. Commun.*, vol. 4, p. 2004, Jun. 2013.

[180] M. Yao *et al.*, "Performance Improvement of Polymer Solar Cells by Surface-Energy-Induced Dual Plasmon Resonance," *ACS Appl. Mater. Interfaces*, vol. 8, no. 9, pp. 6183–6189, Mar. 2016.

[181] G. Kakavelakis *et al.*, "Plasmonic Backscattering Effect in High-Efficient Organic Photovoltaic Devices," *Adv. Energy Mater.*, vol. 6, no. 2, p. 1501640, Jan. 2016.

[182] S.-W. Baek *et al.*, "Au@Ag Core–Shell Nanocubes for Efficient Plasmonic Light Scattering Effect in Low Bandgap Organic Solar Cells," *ACS Nano*, vol. 8, no. 4, pp. 3302–3312, Apr. 2014.

[183] F. Jin, B. Chu, W. Li, Z. Su, H. Zhao, and C. S. Lee, "Enhanced performances in inverted small molecule solar cells by Ag nanoparticles," *Opt. Express*, vol. 22, no. 107, pp. A1669-79, Dec. 2014.

[184] G. Ligorio, M. V. Nardi, C. Christodoulou, and N. Koch, "Organic Semiconductor/Gold Interface Interactions: From Physisorption on Planar Surfaces to Chemical Reactions with Metal Nanoparticles," *ChemPhysChem*, vol. 16, no. 12, pp. 2602–2608, Aug. 2015.

[185] A. Singh, A. Dey, and P. K. Iyer, "Collective effect of hybrid Au-Ag nanoparticles and organic-inorganic cathode interfacial layers for high performance polymer solar cell," *Sol. Energy*, vol. 173, pp. 429–436, Oct. 2018.

[186] Y. Omoto and K. Harafuji, "Stability in organic solar cells with Ag/pentacene anode buffer under repetitive illumination," *Thin Solid Films*, vol. 615, pp. 374–384, Sep. 2016.

[187] Harrison Research Group, "UHV Tutorial," *University of Virginia Website*, 2006. [Online]. Available: http://faculty.virginia.edu/harrison/STM/tutorials/UHV.html. [Accessed: 03-Aug-2018].

[188] R. M. Tiggelaar, J. W. Berenschot, M. C. Elwenspoek, J. G. E. Gardeniers, R. Dorsman, and C. R. Kleijn, "Spreading of thin-film metal patterns deposited on nonplanar surfaces using a shadow mask micromachined in Si (110)," *J. Vac. Sci. Technol. B Microelectron. Nanom. Struct.*, vol. 25, no. 4, p. 1207, Jun. 2007.

[189] M. Ohring, *Materials science of thin films: deposition and structure*. Academic Press, 2002.

[190] D. R. Hofstadter, *Godel, Escher, Bach: An Eternal Golden Braid*, 20th anniv. Penguin,

1999.

[191] B. Verreet *et al.*, “A 4% Efficient Organic Solar Cell Using a Fluorinated Fused Subphthalocyanine Dimer as an Electron Acceptor,” *Adv. Energy Mater.*, vol. 1, no. 4, pp. 565–568, Jul. 2011.

[192] A. K. K. Kyaw *et al.*, “Intensity dependence of current-voltage characteristics and recombination in high-efficiency solution-processed small-molecule solar cells.,” *ACS Nano*, vol. 7, no. 5, pp. 4569–77, May 2013.

[193] T. Kirchartz *et al.*, “Sensitivity of the Mott–Schottky Analysis in Organic Solar Cells,” *J. Phys. Chem. C*, vol. 116, no. 14, pp. 7672–7680, Apr. 2012.

[194] J. Y. Kim, O. Voznyy, D. Zhitomirsky, and E. H. Sargent, “25th anniversary article: Colloidal quantum dot materials and devices: a quarter-century of advances.,” *Adv. Mater.*, vol. 25, no. 36, pp. 4986–5010, Sep. 2013.

[195] C. B. Murray, D. J. Norris, and M. G. Bawendi, “Synthesis and characterization of nearly monodisperse CdE (E = sulfur, selenium, tellurium) semiconductor nanocrystallites,” *J. Am. Chem. Soc.*, vol. 115, no. 19, pp. 8706–8715, Sep. 1993.

[196] J. Albero, J. N. Clifford, and E. Palomares, “Quantum dot based molecular solar cells,” *Coord. Chem. Rev.*, vol. 263–264, pp. 53–64, Mar. 2014.

[197] E. J. D. Klem, C. W. Gregory, G. B. Cunningham, S. Hall, D. S. Temple, and J. S. Lewis, “Planar PbS quantum dot/C60 heterojunction photovoltaic devices with 5.2% power conversion efficiency,” *Appl. Phys. Lett.*, vol. 100, no. 17, p. 173109, Apr. 2012.

[198] B. Ehrler *et al.*, “In situ measurement of exciton energy in hybrid singlet-fission solar cells,” *Nat. Commun.*, vol. 3, p. 1019, Jan. 2012.

[199] D. V Talapin and C. B. Murray, “PbSe nanocrystal solids for n- and p-channel thin film field-effect transistors.,” *Science*, vol. 310, no. 5745, pp. 86–9, Oct. 2005.

[200] J. Cox, “A quantum paintbox,” *Chemistry World*, pp. 1–8, 2003.

[201] J. Du *et al.*, “Zn–Cu–In–Se quantum dot solar cells with a certified power conversion efficiency of 11.6%,” *J. Am. Chem. Soc.*, vol. 138, no. 12, pp. 4201–4209, 2016.

[202] P. K. Santra and P. V. Kamat, “Tandem-Layered Quantum Dot Solar Cells: Tuning the Photovoltaic Response with Luminescent Ternary Cadmium Chalcogenides,” *J. Am. Chem. Soc.*, vol. 135, no. 2, pp. 877–885, Jan. 2013.

[203] J. Jasieniak, M. Califano, and S. E. Watkins, “Size-dependent valence and conduction band-edge energies of semiconductor nanocrystals.,” *ACS Nano*, vol. 5, no. 7, pp. 5888–902, Jul. 2011.

[204] E. Tekin, P. J. Smith, and U. S. Schubert, “Inkjet printing as a deposition and patterning tool for polymers and inorganic particles,” *Soft Matter*, vol. 4, no. 4, p. 703,

Mar. 2008.

[205] H. Wei, D. Li, X. Zheng, and Q. Meng, “Recent progress of colloidal quantum dot based solar cells,” *Chinese Phys. B*, vol. 27, no. 1, p. 018808, Jan. 2018.

[206] K. S. Leschkies, T. J. Beatty, M. S. Kang, D. J. Norris, and E. S. Aydil, “Solar Cells Based on Junctions between Colloidal PbSe Nanocrystals and Thin ZnO Films,” *ACS Nano*, vol. 3, no. 11, pp. 3638–3648, Nov. 2009.

[207] J. J. Choi *et al.*, “PbSe Nanocrystal Excitonic Solar Cells,” *Nano Lett.*, vol. 9, no. 11, pp. 3749–3755, Nov. 2009.

[208] H. Liu *et al.*, “Systematic optimization of quantum junction colloidal quantum dot solar cells,” *Appl. Phys. Lett.*, vol. 101, no. 15, p. 151112, Oct. 2012.

[209] C. R. Kagan and C. B. Murray, “Charge transport in strongly coupled quantum dot solids,” *Nat. Nanotechnol.*, vol. 10, pp. 1013–1026, Nov. 2015.

[210] J. Tang *et al.*, “Colloidal-quantum-dot photovoltaics using atomic-ligand passivation,” *Nat. Mater.*, vol. 10, pp. 765–771, Sep. 2011.

[211] A. H. Ip *et al.*, “Hybrid passivated colloidal quantum dot solids.,” *Nat. Nanotechnol.*, vol. 7, no. 9, pp. 577–82, Sep. 2012.

[212] C.-H. M. Chuang, P. R. Brown, V. Bulović, and M. G. Bawendi, “Improved performance and stability in quantum dot solar cells through band alignment engineering.,” *Nat. Mater.*, vol. 13, no. 8, pp. 796–801, Aug. 2014.

[213] Z. Ning *et al.*, “Air-stable n-type colloidal quantum dot solids,” *Nat. Mater.*, vol. 13, pp. 822–828, Jun. 2014.

[214] A. J. Labelle *et al.*, “Colloidal Quantum Dot Solar Cells Exploiting Hierarchical Structuring,” *Nano Lett.*, vol. 15, no. 2, pp. 1101–1108, Feb. 2015.

[215] X. Lan, S. Masala, and E. H. Sargent, “Charge-extraction strategies for colloidal quantum dot photovoltaics,” *Nat. Mater.*, vol. 13, pp. 233–240, Feb. 2014.

[216] B.-R. Hyun, J. J. Choi, K. L. Seyler, T. Hanrath, and F. W. Wise, “Heterojunction PbS Nanocrystal Solar Cells with Oxide Charge-Transport Layers,” 2013.

[217] M. Nam, T. Lee, S. Kim, S. Kim, S.-W. Kim, and K.-K. Lee, “Two strategies to enhance efficiency of PbS quantum dot solar cells: Removing surface organic ligands and configuring a bilayer heterojunction with a new conjugated polymer,” *Org. Electron.*, vol. 15, no. 2, pp. 391–398, 2014.

[218] X. Zhang *et al.*, “Slow recombination in quantum dot solid solar cell using p–i–n architecture with organic p-type hole transport material,” *J. Mater. Chem. A*, vol. 3, no. 41, pp. 20579–20585, 2015.

[219] I. Mora-Sero *et al.*, “Selective contacts drive charge extraction in quantum dot solids

via asymmetry in carrier transfer kinetics," *Nat. Commun.*, vol. 4, no. 1, p. 2272, Dec. 2013.

[220] H. Liu *et al.*, "Electron Acceptor Materials Engineering in Colloidal Quantum Dot Solar Cells," *Adv. Mater.*, vol. 23, no. 33, p. n/a-n/a, Jul. 2011.

[221] M. Liu *et al.*, "Double-Sided Junctions Enable High-Performance Colloidal-Quantum-Dot Photovoltaics," *Adv. Mater.*, vol. 28, no. 21, pp. 4142–4148, Jun. 2016.

[222] X. Lan *et al.*, "10.6% certified colloidal quantum dot solar cells via solvent-polarity-engineered halide passivation," *Nano Lett.*, vol. 16, no. 7, pp. 4630–4634, Jul. 2016.

[223] J. Gao *et al.*, "n-Type Transition Metal Oxide as a Hole Extraction Layer in PbS Quantum Dot Solar Cells," *Nano Lett.*, vol. 11, no. 8, pp. 3263–3266, Aug. 2011.

[224] P. R. Brown *et al.*, "Improved Current Extraction from ZnO/PbS Quantum Dot Heterojunction Photovoltaics Using a MoO3 Interfacial Layer," *Nano Lett.*, vol. 11, no. 7, pp. 2955–2961, Jul. 2011.

[225] Y. J. Jeong, J. H. Song, S. Jeong, and S. J. Baik, "PbS Colloidal Quantum Dot Solar Cells With Organic Hole Transport Layers for Enhanced Carrier Separation and Ambient Stability," *IEEE J. Photovoltaics*, vol. 8, no. 2, pp. 493–498, Mar. 2018.

[226] L. Zhu, B. J. Richardson, and Q. Yu, "Inverted hybrid CdSe–polymer solar cells adopting PEDOT:PSS/MoO3 as dual hole transport layers," *Phys. Chem. Chem. Phys.*, vol. 18, no. 5, pp. 3463–3471, 2016.

[227] D. C. J. Neo *et al.*, "Poly(3-hexylthiophene-2,5-diyl) as a hole transport layer for colloidal quantum dot solar cells," *Appl. Mater. Interfaces*, vol. 8, no. 19, pp. 12101–12108, 2016.

[228] F. J. Zhang, A. Vollmer, J. Zhang, Z. Xu, J. P. Rabe, and N. Koch, "Energy level alignment and morphology of interfaces between molecular and polymeric organic semiconductors," *Org. Electron.*, vol. 8, no. 5, pp. 606–614, 2007.

[229] C.-T. Lee and C.-H. Lee, "Conversion efficiency improvement mechanisms of polymer solar cells by balance electron–hole mobility using blended P3HT:PCBM:pentacene active layer," *Org. Electron.*, vol. 14, no. 8, pp. 2046–2050, 2013.

[230] A. Castelli *et al.*, "High-Efficiency All-Solution-Processed Light-Emitting Diodes Based on Anisotropic Colloidal Heterostructures with Polar Polymer Injecting Layers," *Nano Lett.*, vol. 15, no. 8, pp. 5455–5464, Aug. 2015.

[231] A. A. Günther, J. Widmer, D. Kasemann, and K. Leo, "Hole mobility in thermally evaporated pentacene: Morphological and directional dependence," *Appl. Phys. Lett.*, vol. 106, no. 23, p. 233301, Jun. 2015.

[232] D. Kajiya, S. Ozawa, T. Koganezawa, and K. Saitow, "Enhancement of Out-of-plane

Mobility in P3HT Film by Rubbing: Aggregation and Planarity Enhanced with Low Regioregularity," *J. Phys. Chem. C*, vol. 119, no. 15, pp. 7987–7995, Apr. 2015.

[233] R. W. Crisp *et al.*, "Metal halide solid-state surface treatment for high efficiency PbS and PbSe QD solar cells," *Sci. Rep.*, vol. 5, p. 9945, Apr. 2015.

[234] E. L. Unger *et al.*, "Hysteresis and transient behavior in current–voltage measurements of hybrid-perovskite absorber solar cells," *Energy Environ. Sci.*, vol. 7, no. 11, pp. 3690–3698, Aug. 2014.

[235] A. Sundqvist, O. J. Sandberg, M. Nyman, J.-H. Smått, and R. Österbacka, "Origin of the s-shaped JV curve and the light-soaking issue in inverted organic solar cells," *Adv. Energy Mater.*, vol. 6, no. 6, p. 1502265, Mar. 2016.

[236] A. Wagenpfahl, D. Rauh, M. Binder, C. Deibel, and V. Dyakonov, "S-shaped current-voltage characteristics of organic solar devices," *Phys. Rev. B*, vol. 82, no. 11, p. 115306, Sep. 2010.

[237] J. Gao, J. M. Luther, O. E. Semonin, R. J. Ellingson, A. J. Nozik, and M. C. Beard, "Quantum dot size dependent J−V characteristics in heterojunction ZnO/PbS quantum dot solar cells," *Nano Lett.*, vol. 11, no. 3, pp. 1002–1008, 2011.

[238] L. Hu, A. Mandelis, X. Lan, A. Melnikov, S. Hoogland, and E. H. Sargent, "Imbalanced charge carrier mobility and Schottky junction induced anomalous current-voltage characteristics of excitonic PbS colloidal quantum dot solar cells," *Sol. Energy Mater. Sol. Cells*, vol. 155, pp. 155–165, 2016.

[239] M. Zhang, H. Wang, and C. W. Tang, "Hole-transport limited S-shaped I-V curves in planar heterojunction organic photovoltaic cells," *Appl. Phys. Lett.*, vol. 99, no. 21, p. 213506, Nov. 2011.

[240] W. Tress and O. Inganäs, "Simple experimental test to distinguish extraction and injection barriers at the electrodes of (organic) solar cells with S-shaped current–voltage characteristics," *Sol. Energy Mater. Sol. Cells*, vol. 117, pp. 599–603, Oct. 2013.

[241] X. Hao, S. Wang, W. Fu, T. Sakurai, S. Masuda, and K. Akimoto, "Novel cathode buffer layer of Ag-doped bathocuproine for small molecule organic solar cell with inverted structure," *Org. Electron.*, vol. 15, no. 8, pp. 1773–1779, Aug. 2014.

[242] C. D. Dimitrakopoulos and P. R. L. Malenfant, "Organic Thin Film Transistors for Large Area Electronics," *Adv. Mater.*, vol. 14, no. 2, pp. 99–117, Jan. 2002.

[243] J. Lee *et al.*, "Singlet exciton fission photovoltaics.," *Acc. Chem. Res.*, vol. 46, no. 6, pp. 1300–11, Jun. 2013.

[244] G. Witte and C. Wöll, "Growth of aromatic molecules on solid substrates for

applications in organic electronics," *J. Mater. Res.*, vol. 19, no. 07, pp. 1889–1916, Mar. 2004.

[245] R. Ruiz *et al.*, "Pentacene thin film growth," *Chem. Mater.*, vol. 16, no. 23, pp. 4497–4508, Nov. 2004.

[246] I. P. M. Bouchoms, W. A. Schoonveld, J. Vrijmoeth, and T. M. Klapwijk, "Morphology identification of the thin film phases of vacuum evaporated pentacene on SiO2 substrates," *Synth. Met.*, vol. 104, no. 3, pp. 175–178, Jul. 1999.

[247] B. Park, K. Whitham, K. Bian, Y.-F. Lim, and T. Hanrath, "Probing surface states in PbS nanocrystal films using pentacene field effect transistors: Controlling carrier concentration and charge transport in pentacene," *Phys. Chem. Chem. Phys.*, vol. 16, no. 47, pp. 25729–25733, Nov. 2014.

[248] N. J. Hestand *et al.*, "Polarized Absorption in Crystalline Pentacene: Theory vs Experiment," *J. Phys. Chem. C*, vol. 119, no. 38, pp. 22137–22147, Sep. 2015.

[249] S. M. Willis, C. Cheng, H. E. Assender, and A. A. R. Watt, "The Transitional Heterojunction Behavior of PbS/ZnO Colloidal Quantum Dot Solar Cells," *Nano Lett.*, vol. 12, no. 3, pp. 1522–1526, Mar. 2012.

[250] F. Amy, C. Chan, and A. Kahn, "Polarization at the gold/pentacene interface," *Org. Electron.*, vol. 6, no. 2, pp. 85–91, 2005.

[251] O. Malinkiewicz *et al.*, "Perovskite solar cells employing organic charge-transport layers," *Nat. Photonics*, vol. 8, pp. 128–132, Dec. 2014.

[252] C. Ding *et al.*, "Recombination suppression in PbS quantum dot heterojunction solar cells by energy-level alignment in the quantum dot active layers," *ACS Appl. Mater. Interfaces*, vol. Article AS, Sep. 2017.

[253] Y.-J. Lin, F.-M. Yang, W.-Y. Chou, and J. Chang, "Effects of ultraviolet irradiation on conductivity of pentacene and contact resistivity of Au/pentacene," *Jpn. J. Appl. Phys.*, vol. 47, no. 10, pp. 7851–7853, Oct. 2008.

[254] J. T.-W. Wang *et al.*, "Low-temperature processed electron collection layers of graphene/TiO2 nanocomposites in thin film perovskite solar cells," *Nano Lett.*, vol. 14, no. 2, pp. 724–730, Feb. 2014.

[255] H. J. Snaith and M. Grätzel, "The role of a 'Schottky barrier' at an electron-collection electrode in solid-state dye-sensitized solar cells," *Adv. Mater.*, vol. 18, no. 14, pp. 1910–1914, Jul. 2006.

[256] G. N. Derry, M. E. Kern, and E. H. Worth, "Recommended values of clean metal surface work functions," *J. Vac. Sci. Technol. A Vacuum, Surfaces, Film.*, vol. 33, no. 6, p. 060801, Nov. 2015.

[257] K. Hong *et al.*, "Lower hole-injection barrier between pentacene and a 1-hexadecanethiol-modified gold substrate with a lowered work function," *Org. Electron.*, vol. 9, no. 1, pp. 21–29, Feb. 2008.

[258] N. Koch, A. Vollmer, S. Duhm, Y. Sakamoto, and T. Suzuki, "The Effect of Fluorination on Pentacene/Gold Interface Energetics and Charge Reorganization Energy," *Adv. Mater.*, vol. 19, no. 1, pp. 112–116, Jan. 2007.

[259] L. Diao, C. Daniel Frisbie, D. D. Schroepfer, and P. Paul Ruden, "Electrical characterization of metal/pentacene contacts," *J. Appl. Phys.*, vol. 101, no. 1, p. 014510, Jan. 2007.

[260] Y. Hirose, A. Kahn, V. Aristov, P. Soukiassian, V. Bulovic, and S. R. Forrest, "Chemistry and electronic properties of metal-organic semiconductor interfaces: Al, Ti, In, Sn, Ag, and Au on PTCDA," *Phys. Rev. B*, vol. 54, no. 19, pp. 13748–13758, Nov. 1996.

[261] N. J. Watkins, L. Yan, and Y. Gao, "Electronic structure symmetry of interfaces between pentacene and metals," *Appl. Phys. Lett.*, vol. 80, no. 23, pp. 4384–4386, Jun. 2002.

[262] T. Sawabe *et al.*, "Vertical electrical conduction in pentacene polycrystalline thin films mediated by Au-induced gap states at grain boundaries," *Appl. Phys. A*, vol. 95, no. 1, pp. 225–232, Apr. 2009.

[263] A. Vollmer *et al.*, "The effect of oxygen exposure on pentacene electronic structure.," *Eur. Phys. J. E. Soft Matter*, vol. 17, no. 3, pp. 339–43, Jul. 2005.

[264] A. Vollmer, H. Weiss, S. Rentenberger, I. Salzmann, J. P. Rabe, and N. Koch, "The interaction of oxygen and ozone with pentacene," *Surf. Sci.*, vol. 600, no. 18, pp. 4004–4007, Sep. 2006.

[265] Y.-J. Lin, J.-A. Chu, Y.-C. Su, C.-T. Lee, and H.-C. Chang, "Improved ohmic contacts on pentacene based on Au with ultraviolet irradiation treatment," *Thin Solid Films*, vol. 518, no. 10, pp. 2707–2709, Mar. 2010.

[266] J.-M. Choi, D. K. Hwang, J. M. Hwang, J. H. Kim, and S. Im, "Ultraviolet-enhanced device properties in pentacene-based thin-film transistors," *Appl. Phys. Lett.*, vol. 90, no. 11, p. 113515, Mar. 2007.

[267] F. De Angelis, M. Gaspari, A. Procopio, G. Cuda, and E. Di Fabrizio, "Direct mass spectrometry investigation on Pentacene thin film oxidation upon exposure to air," *Chem. Phys. Lett.*, vol. 468, no. 4–6, pp. 193–196, Jan. 2009.

[268] O. D. Jurchescu, J. Baas, and T. T. M. Palstra, "Electronic transport properties of pentacene single crystals upon exposure to air," *Applied Physics Letters*, vol. 87, no. 5.

AIP Publishing, p. 052102, 26-Jul-2005.

[269] S. Joshi *et al.*, "Thickness Dependence of the Crystalline Structure and Hole Mobility in Thin Films of Low Molecular Weight Poly(3-hexylthiophene)," *Macromolecules*, vol. 41, no. 18, pp. 6800–6808, Sep. 2008.

[270] L. J. A. Koster, V. D. Mihailetchi, H. Xie, and P. W. M. Blom, "Origin of the light intensity dependence of the short-circuit current of polymer/fullerene solar cells," *Appl. Phys. Lett.*, vol. 87, no. 20, p. 203502, Nov. 2005.

[271] J. M. Luther *et al.*, "Schottky Solar Cells Based on Colloidal Nanocrystal Films," *Nano Lett.*, vol. 8, no. 10, pp. 3488–3492, Oct. 2008.

[272] M.-J. Choi, J. Oh, J.-K. Yoo, J. Choi, D. M. Sim, and Y. S. Jung, "Tailoring of the PbS/metal interface in colloidal quantum dot solar cells for improvements of performance and air stability," *Energy Environ. Sci.*, vol. 7, no. 9, p. 3052, Jun. 2014.

[273] B. N. Reinecke *et al.*, "Elucidating the electronic structure of supported gold nanoparticles and its relevance to catalysis by means of hard X-ray photoelectron spectroscopy," *Surf. Sci.*, vol. 650, pp. 24–33, 2016.

[274] T. V. W. Janssens *et al.*, "Insights into the reactivity of supported Au nanoparticles: combining theory and experiments," *Top. Catal.*, vol. 44, no. 1–2, pp. 15–26, Jun. 2007.

[275] F. Viñes, J. R. B. Gomes, and F. Illas, "Understanding the reactivity of metallic nanoparticles: beyond the extended surface model for catalysis," *Chem. Soc. Rev.*, vol. 43, no. 14, pp. 4922–4939, Jun. 2014.

[276] Y. Negishi *et al.*, "A Critical Size for Emergence of Nonbulk Electronic and Geometric Structures in Dodecanethiolate-Protected Au Clusters," *J. Am. Chem. Soc.*, vol. 137, no. 3, pp. 1206–1212, Jan. 2015.

[277] R. Kubo, A. Kawabata, and S. Kobayashi, "Electronic Properties of Small Particles," *Annu. Rev. Mater. Sci.*, vol. 14, no. 1, pp. 49–66, Aug. 1984.

[278] L. R. Medrano, C. V. Landauro, and J. Rojas-Tapia, "Implementation of an alternative method to determine the critical cooling rate: Application in silver and copper nanoparticles," *Chem. Phys. Lett.*, vol. 612, pp. 273–279, Sep. 2014.

[279] J. G. Rivas, Y. Zhang, and A. Berrier, "Fundamental aspects of surface plasmon polaritons at terahertz frequencies," in *Handbook of Terahertz Technology for Imaging, Sensing and Communications*, Elsevier, 2013, pp. 62–90.

[280] C. Noguez, "Surface Plasmons on Metal Nanoparticles: The Influence of Shape and Physical Environment," *J. Phys. Chem. C*, vol. 111, no. 10, pp. 3806–3819, 2007.

[281] J. M. Sanz *et al.*, "UV Plasmonic Behavior of Various Metal Nanoparticles in the Near-

and Far-Field Regimes: Geometry and Substrate Effects," *J. Phys. Chem. C*, vol. 117, no. 38, pp. 19606–19615, Sep. 2013.

[282] T. Jägeler-Hoheisel, F. Selzer, M. Riede, and K. Leo, "Direct Electrical Evidence of Plasmonic Near-Field Enhancement in Small Molecule Organic Solar Cells," *J. Phys. Chem. C*, vol. 118, no. 28, pp. 15128–15135, Jul. 2014.

[283] I.-T. Chen, P.-H. Chang, Y.-C. Chang, and T.-F. Guo, "Lighting Up Ultraviolet Fluorescence From Chicken Albumen Through Plasmon Resonance Energy Transfer of Gold Nanoparticles," *Sci. Rep.*, vol. 3, no. 1, p. 1505, Dec. 2013.

[284] G. Abadias, L. Simonot, J. J. Colin, A. Michel, S. Camelio, and D. Babonneau, "Volmer-Weber growth stages of polycrystalline metal films probed by in situ and real-time optical diagnostics," *Appl. Phys. Lett.*, vol. 107, no. 18, p. 183105, Nov. 2015.

[285] I. Doron-Mor, Z. Barkay, N. Filip-Granit, A. Vaskevich, and I. Rubinstein, "Ultrathin Gold Island Films on Silanized Glass. Morphology and Optical Properties," 2004.

[286] L. Li *et al.*, "Characterization of Silver Nanoparticles Thin Films with Various Thicknesses by AFM," *J. Mater. Sci. Chem. Eng.*, vol. 04, no. 01, pp. 34–39, 2016.

[287] A. Axelevitch, B. Apter, and G. Golan, "Simulation and experimental investigation of optical transparency in gold island films," *Opt. Express*, vol. 21, no. 4, p. 4126, Feb. 2013.

[288] T. W. Kim, Y. Yang, F. Li, and W. L. Kwan, "Electrical memory devices based on inorganic/organic nanocomposites," *NPG Asia Mater.*, vol. 4, no. 6, p. e18, Jun. 2012.

[289] R. Gupta, M. J. Dyer, and W. A. Weimer, "Preparation and characterization of surface plasmon resonance tunable gold and silver films," *J. Appl. Phys.*, vol. 92, no. 9, pp. 5264–5271, Nov. 2002.

[290] T. Fleetham *et al.*, "Photocurrent enhancements of organic solar cells by altering dewetting of plasmonic Ag nanoparticles.," *Sci. Rep.*, vol. 5, p. 14250, Jan. 2015.

[291] A. K. Pal and D. Bharathi Mohan, "Structural, morphological and optical properties of Ag–AgO thin films with the effect of increasing film thickness and annealing temperature," *Opt. Mater. (Amst).*, vol. 48, pp. 121–132, Oct. 2015.

[292] D. V. Goia, "Preparation and formation mechanisms of uniform metallic particles in homogeneous solutions," *J. Mater. Chem.*, vol. 14, no. 4, p. 451, Feb. 2004.

[293] P. Y. Lai and J. S. Chen, "Electrical bistability and charge transport behavior in Au nanoparticle/poly(N-vinylcarbazole) hybrid memory devices," *Appl. Phys. Lett.*, vol. 93, no. 15, p. 153305, Oct. 2008.

[294] Y. Sun and Y. Xia, "Shape-Controlled Synthesis of Gold and Silver Nanoparticles," *Science (80-.).*, vol. 298, no. 5601, pp. 2176–2179, 2002.

[295] I. Kim *et al.*, “Enhanced power conversion efficiency of organic solar cells by embedding Ag nanoparticles in exciton blocking layer,” *Org. Electron.*, vol. 15, no. 10, pp. 2414–2419, Oct. 2014.

[296] S. Masuda, “Gap states at organic–metal interfaces: A combined spectroscopic and theoretical study,” *Appl. Surf. Sci.*, vol. 256, no. 13, pp. 4054–4064, Apr. 2010.

[297] C. Shen, A. Kahn, and J. Schwartz, “Chemical and electrical properties of interfaces between magnesium and aluminum and tris-(8-hydroxy quinoline) aluminum,” *J. Appl. Phys.*, vol. 89, no. 1, p. 449, 2001.

[298] A. N. Caruso, D. L. Schulz, and P. A. Dowben, “Metal hybridization and electronic structure of Tris(8-hydroxyquinolato)aluminum (Alq3),” *Chem. Phys. Lett.*, vol. 413, no. 4, pp. 321–325, 2005.

[299] I. G. Hill, J. Schwartz, and A. Kahn, “Metal-dependent charge transfer and chemical interaction at interfaces between 3,4,9,10-perylenetetracarboxylic bisimidazole and gold, silver and magnesium,” *Org. Electron.*, vol. 1, no. 1, pp. 5–13, Dec. 2000.

[300] L. Yan, M. . Mason, C. . Tang, and Y. Gao, “Photoemission study of energy alignment at the metal/Alq3 interfaces,” *Appl. Surf. Sci.*, vol. 175–176, pp. 412–418, May 2001.

[301] A. Turak, D. Grozea, X. D. Feng, Z. H. Lu, H. Aziz, and A. M. Hor, “Metal/AlQ3 interface structures,” *Appl. Phys. Lett.*, vol. 81, no. 4, pp. 766–768, Jul. 2002.

[302] S. Yu *et al.*, “Formation of Al Nanostructures on Alq3: An in Situ Grazing Incidence Small Angle X-ray Scattering Study during Radio Frequency Sputter Deposition,” *J. Phys. Chem. Lett.*, vol. 4, no. 18, pp. 3170–3175, Sep. 2013.

[303] H. Vázquez *et al.*, “Dipole formation at metal/PTCDA interfaces: Role of the Charge Neutrality Level,” *Europhys. Lett.*, vol. 65, no. 6, pp. 802–808, Mar. 2004.

[304] C. Shen and A. Kahn, “The role of interface states in controlling the electronic structure of Alq3/reactive metal contacts,” *Org. Electron.*, vol. 2, no. 2, pp. 89–95, Sep. 2001.

[305] S. T. Lee, Z. Q. Gao, and L. S. Hung, “Metal diffusion from electrodes in organic light-emitting diodes,” *Appl. Phys. Lett.*, vol. 75, no. 10, p. 1404, Sep. 1999.

[306] S. Wang, T. Sakurai, X. Hao, W. Fu, S. Masuda, and K. Akimoto, “Favorable electronic structure for organic solar cells induced by strong interaction at interface,” *J. Appl. Phys.*, vol. 114, no. 18, p. 183707, Nov. 2013.

[307] S. Wang, T. Sakurai, R. Kuroda, and K. Akimoto, “Energy band bending induced charge accumulation at fullerene/bathocuproine heterojunction interface,” *Appl. Phys. Lett.*, vol. 100, no. 24, p. 243301, Jun. 2012.

[308] I. Kim, H. M. Haverinen, J. Li, and G. E. Jabbour, “Enhancement of device

performance of organic solar cells by an interfacial perylene derivative layer," *ACS Appl. Mater. Interfaces*, vol. 2, no. 5, pp. 1390–4, May 2010.

[309] S. Wang, T. Sakurai, K. Komatsu, and K. Akimoto, "Effect of Ag-doped bathocuproine on the recombination properties of exciton in fullerene," *J. Cryst. Growth*, vol. 378, pp. 415–417, Sep. 2013.

[310] A. Mityashin, D. Cheyns, B. P. Rand, and P. Heremans, "Understanding metal doping for organic electron transport layers," *Appl. Phys. Lett.*, vol. 100, no. 5, p. 053305, Feb. 2012.

[311] M. F. Lo *et al.*, "Operation stability enhancement in organic photovoltaic device by a metal doped organic exciton blocking layer," *Appl. Phys. Lett.*, vol. 97, no. 14, p. 143304, Oct. 2010.

[312] K. Kim, K. Hong, S. Kim, and J.-L. Lee, "Doping Mechanism and Electronic Structure of Alkali Metal Doped Tris(8-hydroxyquinoline) Aluminum," *J. Phys. Chem. C*, vol. 116, no. 16, pp. 9158–9165, Apr. 2012.

[313] S. Kwon, S. C. Kim, Y. Kim, J.-G. Lee, S. Kim, and K. Jeong, "Photoemission spectroscopy study of Alq3 and metal mixed interfaces," *Appl. Phys. Lett.*, vol. 79, no. 27, pp. 4595–4597, Dec. 2001.

[314] G. Ligorio *et al.*, "Charging and exciton-mediated decharging of metal nanoparticles in organic semiconductor matrices," *Appl. Phys. Lett.*, vol. 104, no. 16, p. 163302, Apr. 2014.

[315] J.-P. Yang, F. Bussolotti, S. Kera, and N. Ueno, "Origin and role of gap states in organic semiconductor studied by UPS: as the nature of organic molecular crystals," *J. Phys. D. Appl. Phys.*, vol. 50, no. 42, p. 423002, Oct. 2017.

[316] L. Zhou, J. Mao, Y. Ren, S.-T. Han, V. A. L. Roy, and Y. Zhou, "Recent Advances of Flexible Data Storage Devices Based on Organic Nanoscaled Materials," *Small*, vol. 14, no. 10, p. 1703126, Mar. 2018.

[317] T. Lee and Y. Chen, "Organic resistive nonvolatile memory materials," *MRS Bull.*, vol. 37, no. 02, pp. 144–149, Feb. 2012.

[318] L. D. Bozano, B. W. Kean, V. R. Deline, J. R. Salem, and J. C. Scott, "Mechanism for bistability in organic memory elements," *Appl. Phys. Lett.*, vol. 84, no. 4, pp. 607–609, Jan. 2004.

[319] C. Wu, F. Li, T. Guo, B. Qu, Z. Chen, and Q. Gong, "Efficient Nonvolatile Rewritable Memories Based on Three-Dimensionally Confined Au Quantum Dots Embedded in Ultrathin Polyimide Layers," *Jpn. J. Appl. Phys.*, vol. 50, no. 3R, p. 030204, Mar. 2011.

[320] L. Ma, S. Pyo, J. Ouyang, Q. Xu, and Y. Yang, “Nonvolatile electrical bistability of organic/metal-nanocluster/organic system,” *Appl. Phys. Lett.*, vol. 82, no. 9, pp. 1419–1421, Mar. 2003.

[321] D. Tondelier, K. Lmimouni, D. Vuillaume, C. Fery, and G. Haas, “Metal⁄organic⁄metal bistable memory devices,” *Appl. Phys. Lett.*, vol. 85, no. 23, pp. 5763–5765, Dec. 2004.

[322] L. D. Bozano, B. W. Kean, M. Beinhoff, K. R. Carter, P. M. Rice, and J. C. Scott, “Organic Materials and Thin-Film Structures for Cross-Point Memory Cells Based on Trapping in Metallic Nanoparticles,” *Adv. Funct. Mater.*, vol. 15, no. 12, pp. 1933–1939, Dec. 2005.

[323] G. Ligorio *et al.*, “Metal nanoparticle mediated space charge and its optical control in an organic hole-only device,” *Appl. Phys. Lett.*, vol. 108, no. 15, p. 153302, Apr. 2016.

[324] H.-C. Chang, C.-L. Liu, and W.-C. Chen, “Flexible Nonvolatile Transistor Memory Devices Based on One-Dimensional Electrospun P3HT:Au Hybrid Nanofibers,” *Adv. Funct. Mater.*, vol. 23, no. 39, pp. 4960–4968, Oct. 2013.

[325] H. S. Majumdar, A. Bandyopadhyay, A. Bolognesi, and A. J. Pal, “Memory device applications of a conjugated polymer: Role of space charges,” *J. Appl. Phys.*, vol. 91, no. 4, pp. 2433–2437, Feb. 2002.

[326] J. G. Simmons and R. R. Verderber, “New Conduction and Reversible Memory Phenomena in Thin Insulating Films,” *Proc. R. Soc. A Math. Phys. Eng. Sci.*, vol. 301, no. 1464, pp. 77–102, Oct. 1967.

[327] F. Santoni, A. Gagliardi, M. Auf der Maur, and A. Di Carlo, “Charge trapping models of resistance switching in organic bistable devices with embedded nanoparticles,” *Org. Electron.*, vol. 15, no. 11, pp. 2792–2801, Nov. 2014.

[328] J. Ouyang, C.-W. Chu, C. R. Szmanda, L. Ma, and Y. Yang, “Programmable polymer thin film and non-volatile memory device,” *Nat. Mater.*, vol. 3, no. 12, pp. 918–922, Dec. 2004.

[329] S. Nau, S. Sax, and E. J. W. List-Kratochvil, “Unravelling the Nature of Unipolar Resistance Switching in Organic Devices by Utilizing the Photovoltaic Effect,” *Adv. Mater.*, vol. 26, no. 16, pp. 2508–2513, Apr. 2014.

[330] H. L. Gomes *et al.*, “Switching in polymeric resistance random-access memories (RRAMS),” *Org. Electron.*, vol. 9, no. 1, pp. 119–128, 2008.

[331] S.-T. Han, Y. Zhou, Z.-X. Xu, V. A. L. Roy, and T. F. Hung, “Nanoparticle size dependent threshold voltage shifts in organic memory transistors,” *J. Mater. Chem.*, vol. 21, no. 38, p. 14575, Sep. 2011.

[332] D. I. Son *et al.*, “Polymer–ultrathin graphite sheet–polymer composite structured flexible nonvolatile bistable organic memory devices,” *Nanotechnology*, vol. 22, no. 29, p. 295203, Jul. 2011.

[333] S. A. Moiz, I. A. Khan, W. A. Younis, and K. S. Karimov, “Space Charge–Limited Current Model for Polymers,” in *Conducting Polymers*, InTech, 2016.

[334] G. Dearnaley, D. V. Morgan, and A. M. Stoneham, “A model for filament growth and switching in amorphous oxide films,” *J. Non. Cryst. Solids*, vol. 4, pp. 593–612, Apr. 1970.

[335] M. Cölle, M. Büchel, and D. M. de Leeuw, “Switching and filamentary conduction in non-volatile organic memories,” *Org. Electron.*, vol. 7, no. 5, pp. 305–312, Oct. 2006.

[336] V. S. Reddy, S. Karak, S. K. Ray, and A. Dhar, “Carrier transport mechanism in aluminum nanoparticle embedded AlQ3 structures for organic bistable memory devices,” *Org. Electron.*, vol. 10, no. 1, pp. 138–144, 2009.

[337] P. Sheng, B. Abeles, and Y. Arie, “Hopping Conductivity in Granular Metals,” *Phys. Rev. Lett.*, vol. 31, no. 1, pp. 44–47, Jul. 1973.

[338] Y. Busby *et al.*, “Direct observation of conductive filament formation in Alq3 based organic resistive memories,” *J. Appl. Phys.*, vol. 118, no. 7, p. 075501, Aug. 2015.

[339] W. L. Kwan, B. Lei, Y. Shao, S. V. Prikhodko, N. Bodzin, and Y. Yang, “Direct observation of localized conduction pathways in photocross-linkable polymer memory,” *J. Appl. Phys.*, vol. 105, no. 12, p. 124516, Jun. 2009.

[340] Y. T. You *et al.*, “Field-induced evolution of metallic nano-tips in indium tin oxide-tris-(8-hydroxyquinoline) aluminum-aluminum device,” *Appl. Phys. Lett.*, vol. 100, no. 12, p. 123304, Mar. 2012.

[341] B. Lei, W. L. Kwan, Y. Shao, and Y. Yang, “Statistical characterization of the memory effect in polyfluorene based non-volatile resistive memory devices,” *Org. Electron.*, vol. 10, no. 6, pp. 1048–1053, Sep. 2009.

[342] B. Cho, J.-M. Yun, S. Song, Y. Ji, D.-Y. Kim, and T. Lee, “Direct Observation of Ag Filamentary Paths in Organic Resistive Memory Devices,” *Adv. Funct. Mater.*, vol. 21, no. 20, pp. 3976–3981, Oct. 2011.

[343] B. Niesen *et al.*, “Near-Field Interactions between Metal Nanoparticle Surface Plasmons and Molecular Excitons in Thin-Films. Part II: Emission,” *J. Phys. Chem. C*, vol. 116, no. 45, pp. 24215–24223, Nov. 2012.

[344] M. Brinkmann, G. Gadret, M. Muccini, C. Taliani, N. Masciocchi, and A. Sironi, “Correlation between Molecular Packing and Optical Properties in Different Crystalline Polymorphs and Amorphous Thin Films of mer-Tris(8-

hydroxyquinoline)aluminum(III)," *J. Am. Chem. Soc.*, vol. 122, no. 21, pp. 5147–5157, 2000.

[345] K. Lance Kelly, Eduardo Coronado, and Lin Lin Zhao, and G. C. Schatz*, "The Optical Properties of Metal Nanoparticles: The Influence of Size, Shape, and Dielectric Environment," 2002.

[346] W. Gotschy, K. Vonmetz, A. Leitner, and F. R. Aussenegg, "Thin films by regular patterns of metal nanoparticles: Tailoring the optical properties by nanodesign," *Appl. Phys. B Laser Opt.*, vol. 63, no. 4, pp. 381–384, Oct. 1996.

[347] V. Garg *et al.*, "Localized surface plasmon resonance on Au nanoparticles: tuning and exploitation for performance enhancement in ultrathin photovoltaics," *RSC Adv.*, vol. 6, no. 31, pp. 26216–26226, 2016.

[348] E. C. Romani *et al.*, "Gold nanoparticles on the surface of soda-lime glass: morphological, linear and nonlinear optical characterization," *Opt. Express*, vol. 20, no. 5, p. 5429, Feb. 2012.

[349] H. Wei and H. Eilers, "From silver nanoparticles to thin films: Evolution of microstructure and electrical conduction on glass substrates," *J. Phys. Chem. Solids*, vol. 70, no. 2, pp. 459–465, Feb. 2009.

[350] S. D'Addato *et al.*, "Influence of size, shape and core–shell interface on surface plasmon resonance in Ag and Ag@MgO nanoparticle films deposited on Si/SiO $_x$," *Beilstein J. Nanotechnol.*, vol. 6, no. 1, pp. 404–413, Feb. 2015.

[351] H.-S. Kim *et al.*, "Metal-Insulator Transition-Induced Adsorption-Resistant Behavior of Small Au Nanoparticles," *ChemPhysChem*, vol. 10, no. 8, pp. 1270–1273, Jun. 2009.

[352] J. S. Kim *et al.*, "Kelvin probe and ultraviolet photoemission measurements of indium tin oxide work function: a comparison," *Synth. Met.*, vol. 111, pp. 311–314, 2000.

[353] K. Sugiyama, H. Ishii, Y. Ouchi, and K. Seki, "Dependence of indium–tin–oxide work function on surface cleaning method as studied by ultraviolet and x-ray photoemission spectroscopies," *J. Appl. Phys.*, vol. 87, no. 1, p. 295, 2000.

[354] B. Lägel, I. D. Baikie, and U. Petermann, "A novel detection system for defects and chemical contamination in semiconductors based upon the Scanning Kelvin Probe," *Surf. Sci.*, vol. 433–435, pp. 622–626, Aug. 1999.

[355] E. New, T. Howells, P. Sullivan, and T. S. Jones, "Small molecule tandem organic photovoltaic cells incorporating an α-NPD optical spacer layer," *Org. Electron.*, vol. 14, no. 9, pp. 2353–2359, Sep. 2013.

[356] M. Xue *et al.*, "Charge-carrier dynamics in hybrid plasmonic organic solar cells with

Ag nanoparticles," *Appl. Phys. Lett.*, vol. 98, no. 25, p. 253302, Jun. 2011.

[357] B. J. Leever, C. A. Bailey, T. J. Marks, M. C. Hersam, and M. F. Durstock, "In Situ Characterization of Lifetime and Morphology in Operating Bulk Heterojunction Organic Photovoltaic Devices by Impedance Spectroscopy," *Adv. Energy Mater.*, vol. 2, no. 1, pp. 120–128, Jan. 2012.

[358] G. Garcia-Belmonte, A. Munar, E. M. Barea, J. Bisquert, I. Ugarte, and R. Pacios, "Charge carrier mobility and lifetime of organic bulk heterojunctions analyzed by impedance spectroscopy," *Org. Electron.*, vol. 9, no. 5, pp. 847–851, Oct. 2008.

[359] S. Berleb and W. Brütting, "Dispersive Electron Transport in tris(8-Hydroxyquinoline) Aluminum (A l q 3) Probed by Impedance Spectroscopy," *Phys. Rev. Lett.*, vol. 89, no. 28, p. 286601, Dec. 2002.

[360] D. Ray, M. P. Patankar, N. Periasamy, and K. L. Narasimhan, "Photoconduction in Alq3," *J. Appl. Phys.*, vol. 98, no. 12, p. 123704, Dec. 2005.

[361] G. Zuo, Z. Li, O. Andersson, H. Abdalla, E. Wang, and M. Kemerink, "Molecular Doping and Trap Filling in Organic Semiconductor Host–Guest Systems," *J. Phys. Chem. C*, vol. 121, no. 14, pp. 7767–7775, Apr. 2017.

[362] Y. Wang, J. Chen, L. Dong, and D. Ma, "Determination of electron mobility in tris(8-hydroxy-quinolinato) aluminum by admittance spectroscopy," *J. Appl. Phys.*, vol. 114, no. 11, p. 113703, Sep. 2013.

[363] J. Bardeen, "Surface States and Rectification at a Metal Semi-Conductor Contact," *Phys. Rev.*, vol. 71, no. 10, pp. 717–727, May 1947.

[364] V. Heine, "Theory of Surface States," *Phys. Rev.*, vol. 138, no. 6A, pp. A1689–A1696, Jun. 1965.

[365] C. J. Brabec *et al.*, "Origin of the Open Circuit Voltage of Plastic Solar Cells," *Adv. Funct. Mater.*, vol. 11, no. 5, pp. 374–380, Oct. 2001.

[366] G. G. Malliaras, J. R. Salem, P. J. Brock, and J. C. Scott, "Photovoltaic measurement of the built-in potential in organic light emitting diodes and photodiodes," *J. Appl. Phys.*, vol. 84, no. 3, p. 1583, Jul. 1998.

[367] T. Minari, P. Darmawan, C. Liu, Y. Li, Y. Xu, and K. Tsukagoshi, "Highly enhanced charge injection in thienoacene-based organic field-effect transistors with chemically doped contact," *Appl. Phys. Lett.*, vol. 100, no. 9, p. 093303, Feb. 2012.

[368] W. J. D. Beenken *et al.*, "Sub-bandgap absorption in organic solar cells: experiment and theory," *Phys. Chem. Chem. Phys.*, vol. 15, no. 39, p. 16494, Sep. 2013.

[369] Christiana Honsberg and Stuart Bowden, "Measuring Ideality Factor," *PVEducation*, 2018. [Online]. Available:

http://www.pveducation.org/pvcdrom/characterisation/measurement-of-ideality-factor. [Accessed: 27-Apr-2018].

[370] K. Topp *et al.*, "Impact of the Incorporation of Au Nanoparticles into Polymer/Fullerene Solar Cells," *J. Phys. Chem. A*, vol. 114, no. 11, pp. 3981–3989, Mar. 2010.

[371] V.-E. Choong, Y. Park, Y. Gao, M. G. Mason, and C. W. Tang, "Photoluminescence quenching of Alq3 by metal deposition: A surface analytical investigation," *J. Vac. Sci. Technol. A Vacuum, Surfaces, Film.*, vol. 16, no. 3, p. 1838, Oct. 1998.

[372] M. S. Vezie *et al.*, "Exploring the origin of high optical absorption in conjugated polymers," *Nat. Mater.*, vol. 15, no. 7, pp. 746–753, Jul. 2016.

[373] S. M. Menke and R. J. Holmes, "Exciton diffusion in organic photovoltaic cells," *Energy Environ. Sci.*, vol. 7, no. 2, pp. 499–512, Jan. 2014.

[374] L. Dou, Y. Liu, Z. Hong, G. Li, and Y. Yang, "Low-Bandgap Near-IR Conjugated Polymers/Molecules for Organic Electronics," *Chem. Rev.*, vol. 115, no. 23, pp. 12633–12665, Dec. 2015.

[375] X. Fan, W. Zheng, and D. J. Singh, "Light scattering and surface plasmons on small spherical particles," *Light Sci. Appl.*, vol. 3, no. 6, p. e179, Jun. 2014.

[376] E. L. Lim, C. C. Yap, M. A. Mat Teridi, C. H. Teh, A. R. bin Mohd Yusoff, and M. H. Hj Jumali, "A review of recent plasmonic nanoparticles incorporated P3HT: PCBM organic thin film solar cells," *Org. Electron.*, vol. 36, pp. 12–28, 2016.

[377] B. Paci, A. Generosi, V. R. Albertini, G. D. Spyropoulos, E. Stratakis, and E. Kymakis, "Enhancement of photo/thermal stability of organic bulk heterojunction photovoltaic devices via gold nanoparticles doping of the active layer," *Nanoscale*, vol. 4, no. 23, p. 7452, Nov. 2012.

[378] G. D. Spyropoulos, M. M. Stylianakis, E. Stratakis, and E. Kymakis, "Organic bulk heterojunction photovoltaic devices with surfactant-free Au nanoparticles embedded in the active layer," *Appl. Phys. Lett.*, vol. 100, no. 21, p. 213904, May 2012.

[379] D. H. Wang *et al.*, "Enhanced light harvesting in bulk heterojunction photovoltaic devices with shape-controlled Ag nanomaterials: Ag nanoparticles versus Ag nanoplates," *RSC Adv.*, vol. 2, no. 18, p. 7268, Jul. 2012.

[380] S. Woo, J. Jeong, H. Lyu, Y. Han, and Y. Kim, "In situ-prepared composite materials of PEDOT: PSS buffer layer-metal nanoparticles and their application to organic solar cells," *Nanoscale Res. Lett.*, vol. 7, no. 1, p. 641, Nov. 2012.

[381] X. Chen, L. Zuo, W. Fu, Q. Yan, C. Fan, and H. Chen, "Insight into the efficiency enhancement of polymer solar cells by incorporating gold nanoparticles," *Sol. Energy*

Mater. Sol. Cells, vol. 111, pp. 1–8, Apr. 2013.

[382] D. Qu, F. Liu, Y. Huang, W. Xie, and Q. Xu, "Mechanism of optical absorption enhancement in thin film organic solar cells with plasmonic metal nanoparticles," *Opt. Express*, vol. 19, no. 24, p. 24795, Nov. 2011.

[383] H. Choi *et al.*, "Multipositional Silica-Coated Silver Nanoparticles for High-Performance Polymer Solar Cells," *Nano Lett.*, vol. 13, no. 5, pp. 2204–2208, May 2013.

[384] H.-L. Yip, S. K. Hau, N. S. Baek, H. Ma, and A. K.-Y. Jen, "Polymer Solar Cells That Use Self-Assembled-Monolayer- Modified ZnO/Metals as Cathodes," *Adv. Mater.*, vol. 20, no. 12, pp. 2376–2382, Jun. 2008.

[385] C.-C. Chang *et al.*, "Effects of cathode buffer layers on the efficiency of bulk-heterojunction solar cells," *Appl. Phys. Lett.*, vol. 96, no. 26, p. 263506, Jun. 2010.

[386] X. Li *et al.*, "Efficiency enhancement of polymer solar cells with Ag nanoparticles incorporated into PEDOT:PSS layer," *J. Mater. Sci. Mater. Electron.*, vol. 25, no. 1, pp. 140–145, Jan. 2014.

[387] C. C. D. Wang *et al.*, "Optical and electrical effects of gold nanoparticles in the active layer of polymer solar cells," *J. Mater. Chem.*, vol. 22, no. 3, pp. 1206–1211, Dec. 2012.

[388] K. Kim and D. L. Carroll, "Roles of Au and Ag nanoparticles in efficiency enhancement of poly(3-octylthiophene)/C60 bulk heterojunction photovoltaic devices," *Appl. Phys. Lett.*, vol. 87, no. 20, p. 203113, Nov. 2005.

[389] J.-Y. Lee and P. Peumans, "The origin of enhanced optical absorption in solar cells with metal nanoparticles embedded in the active layer," *Opt. Express*, vol. 18, no. 10, p. 10078, May 2010.

[390] Y.-F. Huang *et al.*, "Mitigation of metal-mediated losses by coating Au nanoparticles with dielectric layer in plasmonic solar cells," *RSC Adv.*, vol. 3, no. 36, p. 16080, Aug. 2013.

[391] F. Xie *et al.*, "Enhanced charge extraction in organic solar cells through electron accumulation effects induced by metal nanoparticles," *Energy Environ. Sci. Environ. Sci.*, vol. 6, no. 11, pp. 3372–3379, Oct. 2013.

[392] D. H. Wang *et al.*, "Enhancement of Donor-Acceptor Polymer Bulk Heterojunction Solar Cell Power Conversion Efficiencies by Addition of Au Nanoparticles," *Angew. Chemie*, vol. 123, no. 24, pp. 5633–5637, Jun. 2011.

[393] K. D. G. I. Jayawardena *et al.*, "'Inorganics-in-Organics': recent developments and outlook for 4G polymer solar cells," *Nanoscale*, vol. 5, no. 18, p. 8411, Aug. 2013.

[394] H. Hoppe *et al.*, “Nanoscale Morphology of Conjugated Polymer/Fullerene-Based Bulk- Heterojunction Solar Cells,” *Adv. Funct. Mater.*, vol. 14, no. 10, pp. 1005–1011, Oct. 2004.

[395] Daniel V. Leff, and Lutz Brandt, and J. R. Heath*, “Synthesis and Characterization of Hydrophobic, Organically-Soluble Gold Nanocrystals Functionalized with Primary Amines,” 1996.

[396] N. Kalfagiannis *et al.*, “Plasmonic silver nanoparticles for improved organic solar cells,” *Sol. Energy Mater. Sol. Cells*, vol. 104, pp. 165–174, 2012.

[397] T. K. S. Wong, “Effect of embedded nanoparticle surface chemistry on plasmonic organic photovoltaic devices,” *Mater. Renew. Sustain. Energy*, vol. 6, no. 1, p. 4, Feb. 2017.

[398] G. Haidari, M. Hajimahmoodzadeh, H. R. Fallah, A. Peukert, A. Chanaewa, and E. von Hauff, “Thermally evaporated Ag nanoparticle films for plasmonic enhancement in organic solar cells: effects of particle geometry,” *Phys. status solidi - Rapid Res. Lett.*, vol. 9, no. 3, pp. 161–165, Mar. 2015.

[399] G. Haidari, M. Hajimahmoodzadeh, H. R. Fallah, and M. G. Varnamkhasti, “Effective medium analysis of thermally evaporated Ag nanoparticle films for plasmonic enhancement in organic solar cell,” *Superlattices Microstruct.*, vol. 85, pp. 294–304, Sep. 2015.

[400] A. J. Morfa, K. L. Rowlen, T. H. Reilly, M. J. Romero, and J. van de Lagemaat, “Plasmon-enhanced solar energy conversion in organic bulk heterojunction photovoltaics,” *Appl. Phys. Lett.*, vol. 92, no. 1, p. 013504, Jan. 2008.

[401] Y. Takahashi, T. Yasuda, K. Yonezawa, and Y. Moritomo, “Carrier injection dynamics in heterojunction solar cells with bipolar molecule,” *Appl. Phys. Lett.*, vol. 106, no. 12, p. 123902, Mar. 2015.

[402] J. C. Wang, S. Q. Shi, C. W. Leung, S. P. Lau, K. Y. Wong, and P. K. L. Chan, “Short circuit current improvement in planar heterojunction organic solar cells by multijunction charge transfer,” *Appl. Phys. Lett.*, vol. 100, no. 5, p. 053301, Jan. 2012.

[403] V. Travkina, P. Stuzhinb, A. Okhapkinac, S. Korolyova, and G. Pakhomovac, “Organic tandem Schottky junction cells with high open circuit voltage,” *Synth. Met.*, vol. 212, pp. 51–54, Feb. 2016.

[404] A. Singh, A. Dey, D. Das, and P. K. Iyer, “Improvement of charge carrier dynamics in P3HT:PC61BM based solar cell in presence of organic cathode interfacial layers,” in *2016 3rd International Conference on Emerging Electronics (ICEE)*, 2016, pp. 1–3.

[405] F. Bussolotti, S. Kera, K. Kudo, A. Kahn, and N. Ueno, “Gap states in Pentacene Thin

Film Induced by Inert Gas Exposure," *Phys. Rev. Lett.*, vol. 110, no. 26, p. 267602, Jun. 2013.

[406] V. D. Mihailetchi, P. W. M. Blom, J. C. Hummelen, and M. T. Rispens, "Cathode dependence of the open-circuit voltage of polymer:fullerene bulk heterojunction solar cells," *J. Appl. Phys.*, vol. 94, no. 10, pp. 6849–6854, Nov. 2003.

[407] J. X. Tang, K. M. Lau, C. S. Lee, and S. T. Lee, "Substrate effects on the electronic properties of an organic/organic heterojunction," *Appl. Phys. Lett.*, vol. 88, no. 23, p. 232103, Jun. 2006.

[408] H. Ishii *et al.*, "Kelvin probe study of band bending at organic semiconductor/metal interfaces: examination of Fermi level alignment," *Phys. status solidi*, vol. 201, no. 6, pp. 1075–1094, May 2004.

[409] J. Endres, I. Pelczer, B. P. Rand, and A. Kahn, "Determination of Energy Level Alignment within an Energy Cascade Organic Solar Cell," *Chem. Mater.*, vol. 28, no. 3, pp. 794–801, Feb. 2016.

[410] M.-F. Lo, Z.-Q. Guan, C.-Y. Chan, T.-W. Ng, and C.-S. Lee, "Degradation of interface between boron subphthalocyanine chloride and fullerene," *J. Electron Spectros. Relat. Phenomena*, vol. 204, pp. 223–226, Oct. 2015.

[411] Q.-Y. Bao *et al.*, "Correlation between the electronic structures of transition metal oxide-based intermediate connectors and the device performance of tandem organic light-emitting devices," *J. Mater. Chem.*, vol. 21, no. 43, p. 17476, Oct. 2011.

[412] J.-X. Tang, M.-K. Fung, C.-S. Lee, and S.-T. Lee, "Interface studies of intermediate connectors and their roles in tandem OLEDs," *J. Mater. Chem.*, vol. 20, no. 13, pp. 2539–2548, Mar. 2010.

[413] M. Mingebach, C. Deibel, and V. Dyakonov, "Built-in potential and validity of the Mott-Schottky analysis in organic bulk heterojunction solar cells," *Phys. Rev. B*, vol. 84, no. 15, p. 153201, Oct. 2011.

[414] A. Nigam, M. Premaratne, and P. R. Nair, "On the validity of unintentional doping densities extracted using Mott–Schottky analysis for thin film organic devices," *Org. Electron.*, vol. 14, no. 11, pp. 2902–2907, Nov. 2013.

[415] M. Morsli, J. C. Bernède, L. Cattin, F. Dahou, and A. Khelil, "On the Exciton Blocking Layer at the Interface Organic/Cathode in Multiheterojunction Organic Solar Cells," *Energy Procedia*, vol. 31, pp. 74–80, Jan. 2012.

[416] P. Peumans and S. R. Forrest, "Very-high-efficiency double-heterostructure copper phthalocyanine/C[sub 60] photovoltaic cells," *Appl. Phys. Lett.*, vol. 79, no. 1, p. 126, Jul. 2001.

[417] S. Yogev, R. Matsubara, M. Nakamura, U. Zschieschang, H. Klauk, and Y. Rosenwaks, “Fermi Level Pinning by Gap States in Organic Semiconductors,” *Phys. Rev. Lett.*, vol. 110, no. 3, p. 036803, Jan. 2013.

[418] N. C. Giebink, G. P. Wiederrecht, M. R. Wasielewski, and S. R. Forrest, “Ideal diode equation for organic heterojunctions. I. Derivation and application,” *Phys. Rev. B*, vol. 82, no. 15, p. 155305, Oct. 2010.

[419] G. Garcia-Belmonte, A. Guerrero, and J. Bisquert, “Elucidating Operating Modes of Bulk-Heterojunction Solar Cells from Impedance Spectroscopy Analysis,” *J. Phys. Chem. Lett.*, vol. 4, no. 6, pp. 877–886, Mar. 2013.

[420] T. Kuwabara, M. Nakamoto, Y. Kawahara, T. Yamaguchi, and K. Takahashi, “Characterization of ZnS-layer-inserted bulk-heterojunction organic solar cells by ac impedance spectroscopy,” *J. Appl. Phys.*, vol. 105, no. 12, p. 124513, Jun. 2009.

[421] J. J. Kelly and R. Memming, “The Influence of Surface Recombination and Trapping on the Cathodic Photocurrent at p-Type III-V Electrodes,” *J. Electrochem. Soc.*, vol. 129, no. 4, p. 730, Apr. 1982.

[422] H. Gerischer, “Photoassisted interfacial electron transfer,” *Surf. Sci.*, vol. 101, no. 1–3, pp. 518–530, Dec. 1980.

[423] T. Ripolles-Sanchis, A. Guerrero, J. Bisquert, and G. Garcia-Belmonte, “Diffusion-Recombination Determines Collected Current and Voltage in Polymer:Fullerene Solar Cells,” *J. Phys. Chem. C*, vol. 116, no. 32, pp. 16925–16933, Aug. 2012.

[424] M. M. Mandoc, F. B. Kooistra, J. C. Hummelen, B. de Boer, and P. W. M. Blom, “Effect of traps on the performance of bulk heterojunction organic solar cells,” *Appl. Phys. Lett.*, vol. 91, no. 26, p. 263505, Dec. 2007.

[425] B. Liu, F. Xu, X. Zhang, D. Yan, and D. Lu, “Numerical simulations of the role of a ferroelectric polymer interfacial layer in organic solar cells,” *Phys. Chem. Chem. Phys.*, vol. 18, no. 7, pp. 5412–5418, Feb. 2016.

[426] F. Rice, “Introductory Electronics Laboratory: Impedance and frequency response,” *California Institute of Technology*, 2017. [Online]. Available: http://www.sophphx.caltech.edu/Physics_5/Experiment_2.pdf. [Accessed: 24-Jan-2018].

[427] M. Bazant, “Electrochemical Energy Systems Lectures: Impedance of Electrodes,” *Massachusetts Institute of Technology*, 2014. [Online]. Available: https://ocw.mit.edu/courses/chemical-engineering/10-626-electrochemical-energy-systems-spring-2014/lecture-notes/MIT10_626S14_S11lec06.pdf. [Accessed: 24-Jan-2018].

[428] K. K. Lian, J. Zhang, R. Li, H. Wang, and W. Hsi, “Printed Organic Memory Devices,” in *ECS Transactions*, 2009, vol. 16, no. 20, pp. 35–41.

[429] R. Steim, *The impact of interfaces on the performance of organic photovoltaic cells*. KIT Scientific Publ, 2010.

[430] H. Wang *et al.*, “Charge Carrier Conduction Mechanism in PbS Quantum Dot Solar Cells: Electrochemical Impedance Spectroscopy Study,” *ACS Appl. Mater. Interfaces*, vol. 8, no. 28, pp. 18526–18533, Jul. 2016.

[431] V. Gupta, A. K. K. Kyaw, D. H. Wang, S. Chand, G. C. Bazan, and A. J. Heeger, “Barium: An Efficient Cathode Layer for Bulk-heterojunction Solar Cells,” *Sci. Rep.*, vol. 3, no. 1, p. 1965, Dec. 2013.

[432] H. Yan *et al.*, “Increasing Polymer Solar Cell Fill Factor by Trap-Filling with F4-TCNQ at Parts Per Thousand Concentration,” *Adv. Mater.*, vol. 28, no. 30, pp. 6491–6496, Aug. 2016.

[433] M. Abdel Naby, A. Zekry, F. El Akkad, and H. F. Ragaie, “Dependence of dark current on zinc concentration in ZnxCd1−xS/ZnTe heterojunctions,” *Sol. Energy Mater. Sol. Cells*, vol. 29, no. 2, pp. 97–108, Mar. 1993.

[434] T.-H. Lai, S.-W. Tsang, J. R. Manders, S. Chen, and F. So, “Properties of interlayer for organic photovoltaics,” *Mater. Today*, vol. 16, no. 11, pp. 424–432, Nov. 2013.

[435] I. G. Hill and A. Kahn, “Energy level alignment at interfaces of organic semiconductor heterostructures,” *J. Appl. Phys.*, vol. 84, no. 10, p. 5583, Nov. 1998.

[436] A. Hayakawa, O. Yoshikawa, T. Fujieda, K. Uehara, and S. Yoshikawa, “High performance polythiophene/fullerene bulk-heterojunction solar cell with a TiOx hole blocking layer,” *Appl. Phys. Lett.*, vol. 90, no. 16, p. 163517, Apr. 2007.

[437] H. Gommans, S. Schols, A. Kadashchuk, P. Heremans, and S. C. J. Meskers, “Exciton Diffusion Length and Lifetime in Subphthalocyanine Films,” *J. Phys. Chem. C*, vol. 113, no. 7, pp. 2974–2979, Feb. 2009.

[438] T. Kim *et al.*, “Hybrid tandem quantum dot/organic photovoltaic cells with complementary near infrared absorption,” *Appl. Phys. Lett.*, vol. 110, no. 22, p. 223903, May 2017.

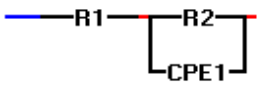
Appendices

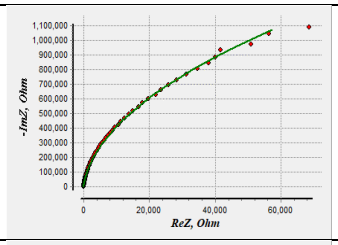
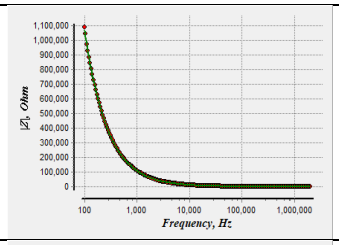
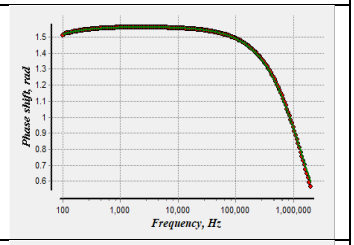
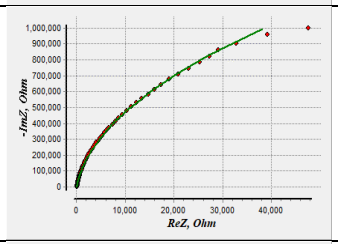
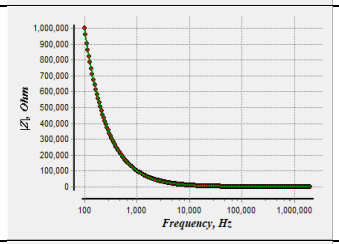
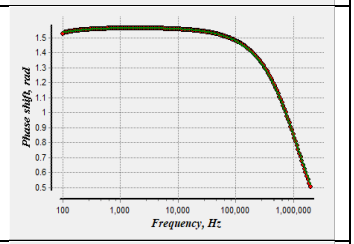
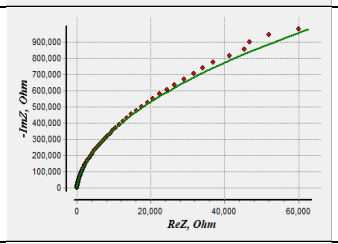
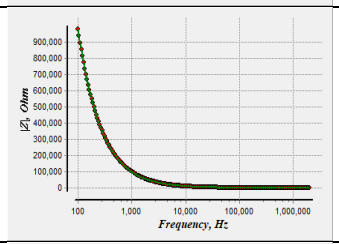
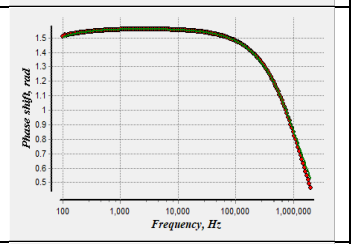
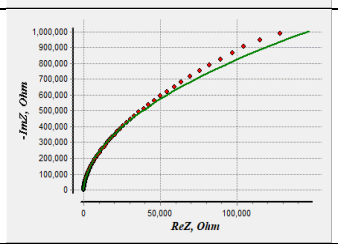
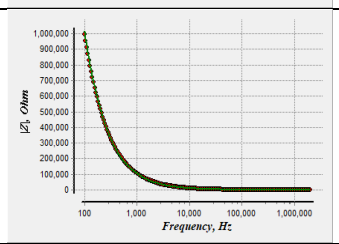
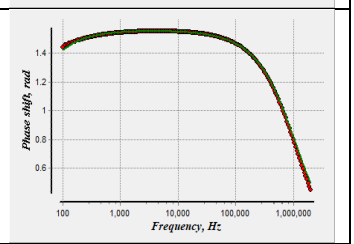
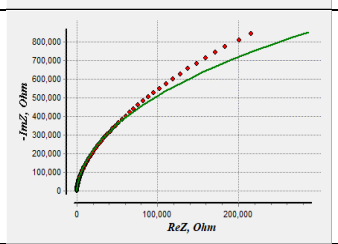
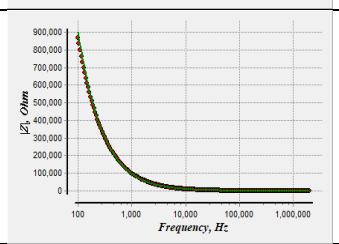
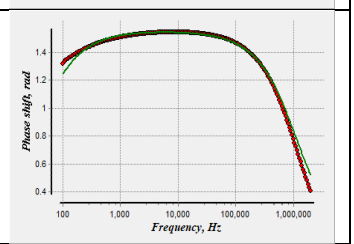
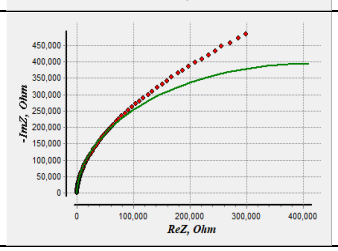
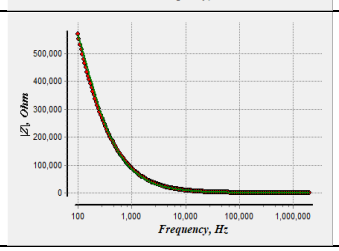
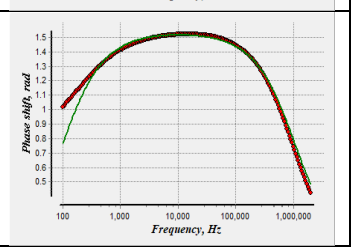
A. Appendix to Chapter 4

A.1 AC Impedance ECM Results

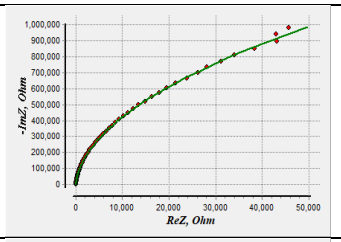
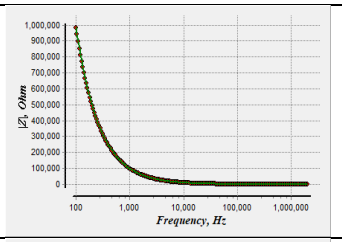
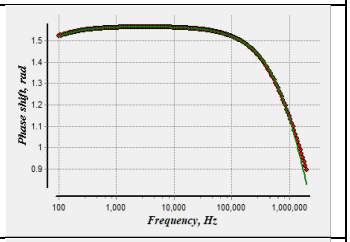
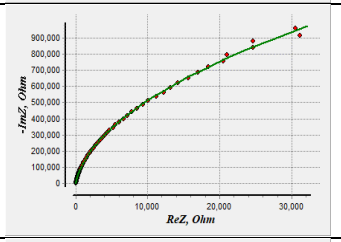
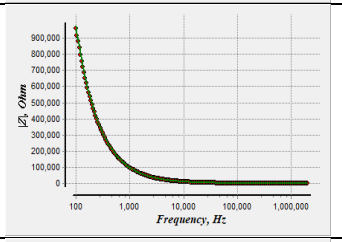
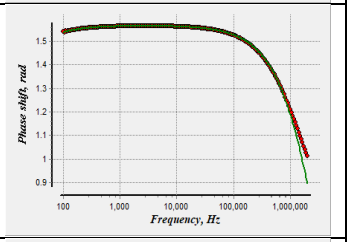
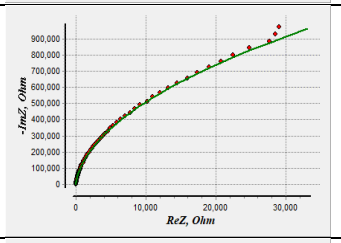
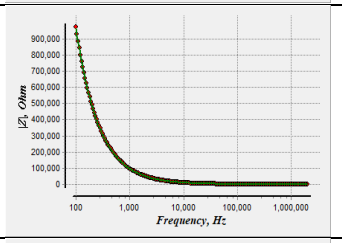
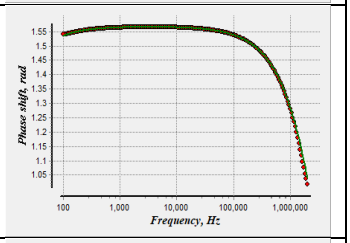
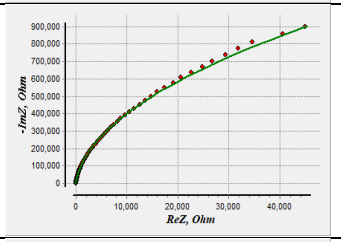
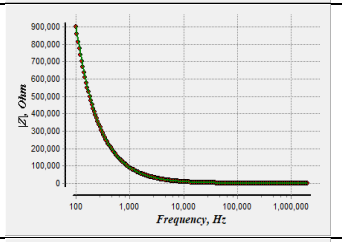
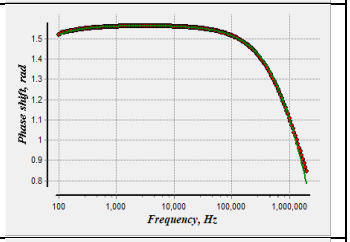
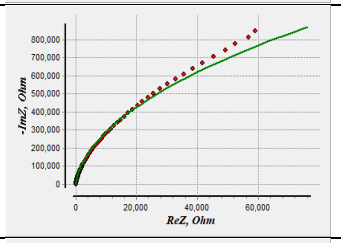
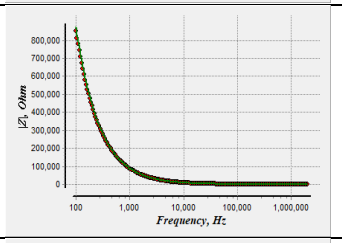
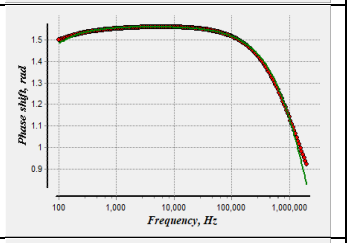
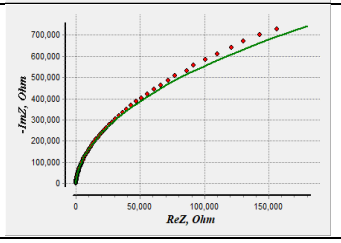
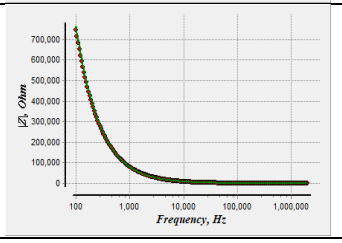
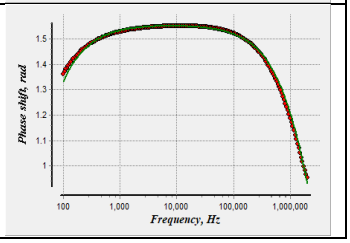
The tables below show the raw impedance data (red circles) overlaid with the fitted model trace (green line) for a representative pixel at each nominal thickness. The average fitting parameters are also presented in the subsequent tables, with error values calculated as the standard deviation across three pixels. The data is shown for both Au and Ag NPs at DC biases of +2 V and 0 V, as indicated in the top left cell of each table.

Equivalent circuit model used:

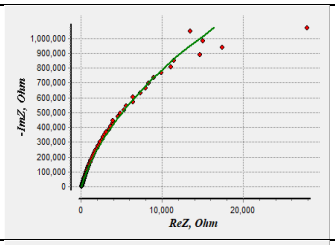
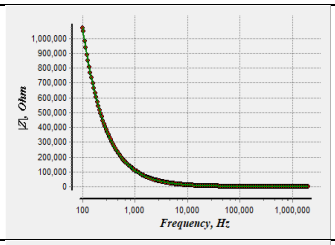
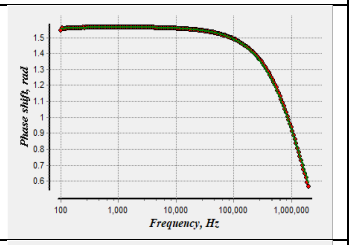
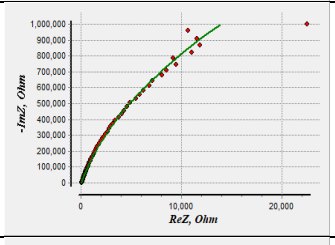
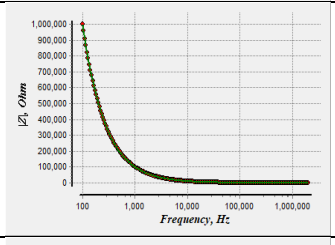
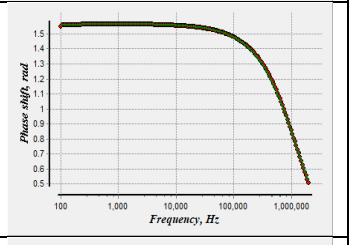
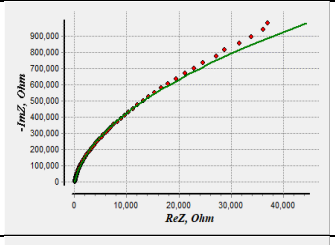
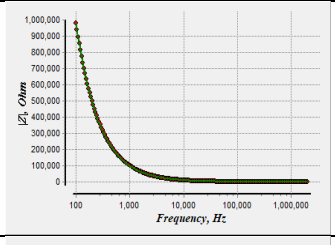
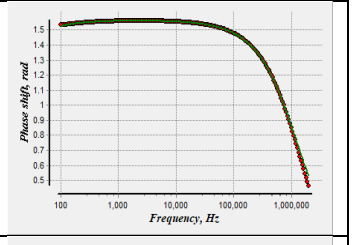
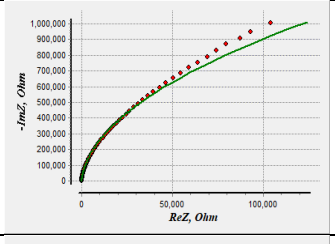
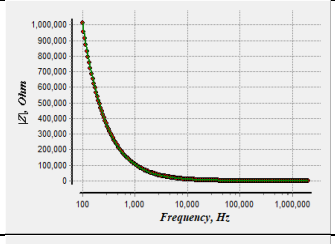
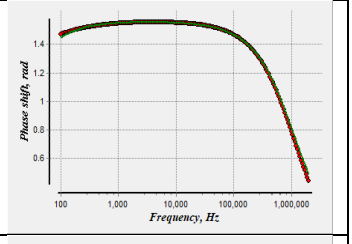
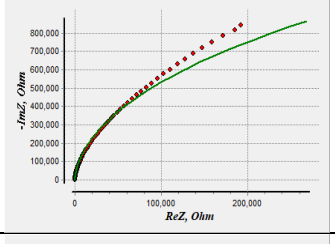
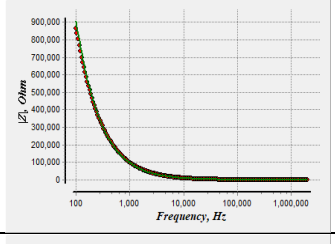
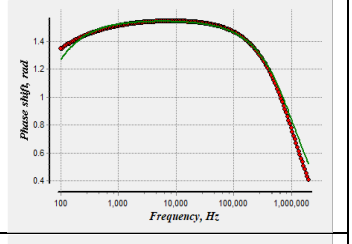
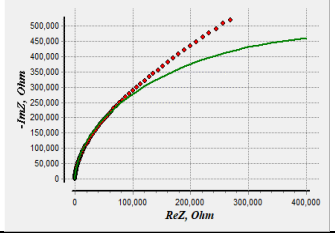
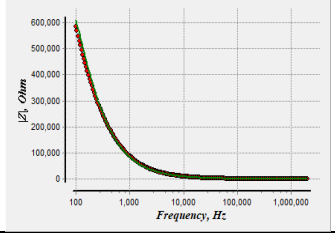
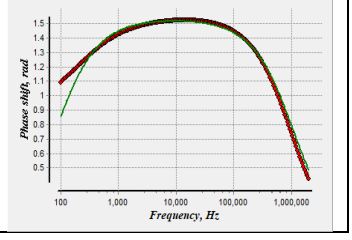


+2 V Au NP	Nyquist Plot	Bode Plot - Magnitude	Bode Plot - Phase
0 nm			
1 nm			
2 nm			
3 nm			
4 nm			
5 nm			

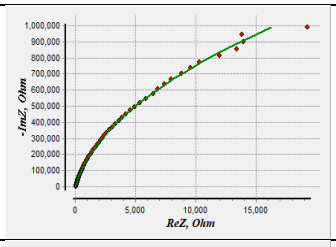
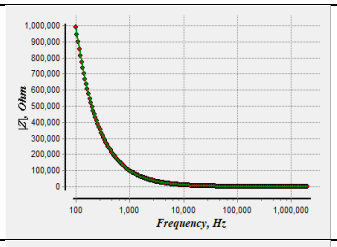
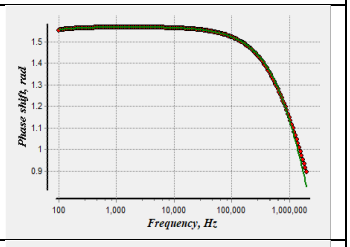
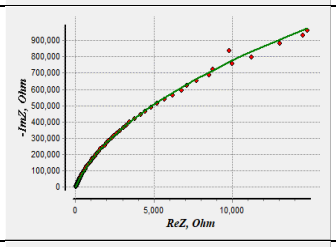
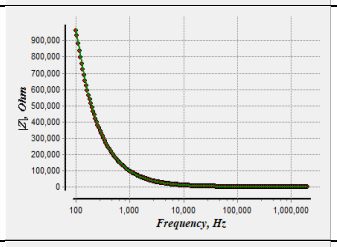
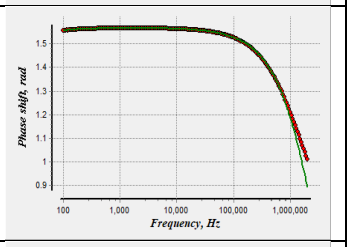
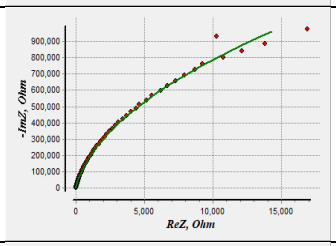
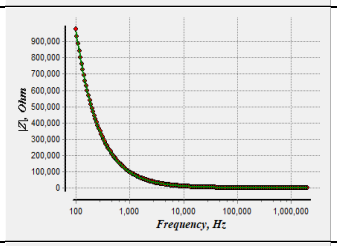
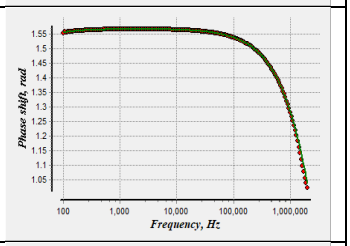
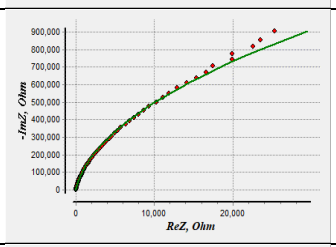
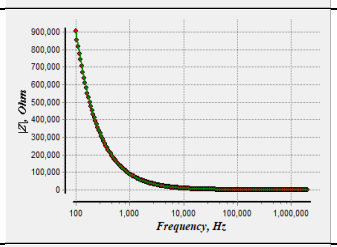
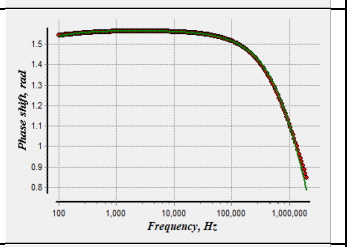
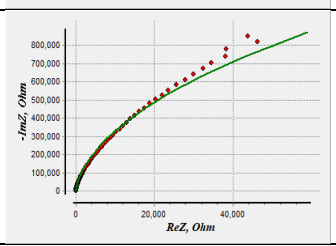
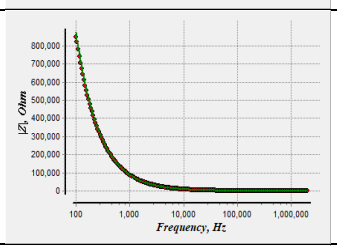
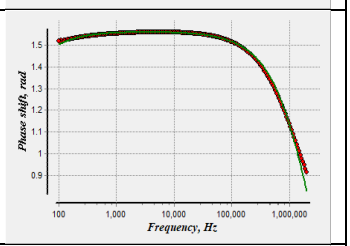
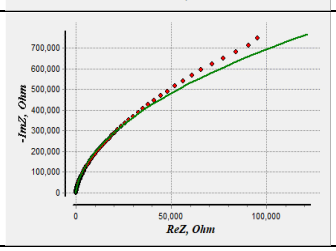
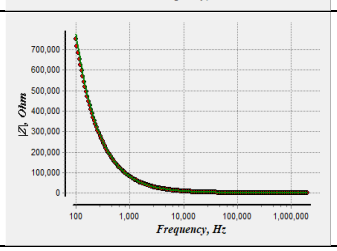
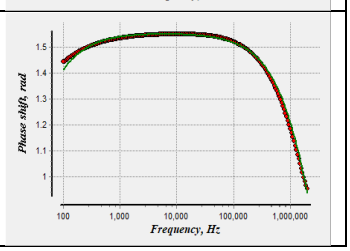
+2 V Au NP	***R1*** **(Ω)**		***R2*** **(Ω)**	***C1*** **(F)**	***τ1*** **(s)**
0 nm	145 ± 141		$2.5 \times 10^{7} \pm 1.7 \times 10^{6}$	$1.5 \times 10^{-9} \pm 1.3 \times 10^{-11}$	$3.7 \times 10^{-2} \pm 2.6 \times 10^{-3}$
1 nm	82 ± 7		$3.0 \times 10^{7} \pm 4.3 \times 10^{5}$	$1.6 \times 10^{-9} \pm 3.0 \times 10^{-11}$	$4.9 \times 10^{-2} \pm 1.2 \times 10^{-3}$
2 nm	80 ± 19		$1.6 \times 10^{7} \pm 1.7 \times 10^{6}$	$1.7 \times 10^{-9} \pm 3.6 \times 10^{-11}$	$2.6 \times 10^{-2} \pm 3.0 \times 10^{-3}$
3 nm	91 ± 43		$7.5 \times 10^{6} \pm 1.2 \times 10^{4}$	$1.6 \times 10^{-9} \pm 5.9 \times 10^{-11}$	$1.2 \times 10^{-2} \pm 4.5 \times 10^{-4}$
4 nm	119 ± 107		$2.1 \times 10^{6} \pm 6.3 \times 10^{5}$	$1.8 \times 10^{-9} \pm 2.3 \times 10^{-10}$	$3.8 \times 10^{-3} \pm 1.3 \times 10^{-3}$
5 nm	114 ± 39		$8.3 \times 10^{5} \pm 1.4 \times 10^{4}$	$2.0 \times 10^{-9} \pm 4.9 \times 10^{-11}$	$1.6 \times 10^{-3} \pm 4.9 \times 10^{-5}$

+2 V Ag NP	Nyquist Plot	Bode Plot - Magnitude	Bode Plot - Phase
0 nm			
1 nm			
2 nm			
3 nm			
4 nm			
5 nm			

+2 V Ag NP	***R1*** **(Ω)**		***R2*** **(Ω)**	***C1*** **(F)**	***τ1*** **(s)**
0 nm	46 ± 20		$2.0 \times 10^{7} \pm 1.1 \times 10^{6}$	$1.6 \times 10^{-9} \pm 2.8 \times 10^{-11}$	$3.3 \times 10^{-2} \pm 1.9 \times 10^{-3}$
1 nm	44 ± 11		$3.2 \times 10^{7} \pm 1.7 \times 10^{6}$	$1.7 \times 10^{-9} \pm 4.7 \times 10^{-11}$	$5.4 \times 10^{-2} \pm 3.3 \times 10^{-3}$
2 nm	38 ± 13		$2.9 \times 10^{7} \pm 2.4 \times 10^{6}$	$1.7 \times 10^{-9} \pm 4.5 \times 10^{-11}$	$4.8 \times 10^{-2} \pm 4.2 \times 10^{-3}$
3 nm	47 ± 17		$1.6 \times 10^{7} \pm 5.3 \times 10^{6}$	$1.8 \times 10^{-9} \pm 2.4 \times 10^{-11}$	$2.8 \times 10^{-2} \pm 9.4 \times 10^{-3}$
4 nm	37 ± 14		$6.0 \times 10^{6} \pm 4.3 \times 10^{6}$	$1.8 \times 10^{-9} \pm 2.4 \times 10^{-11}$	$1.1 \times 10^{-2} \pm 8.0 \times 10^{-3}$
5 nm	26 ± 11		$3.3 \times 10^{6} \pm 1.0 \times 10^{6}$	$2.1 \times 10^{-9} \pm 3.8 \times 10^{-11}$	$6.9 \times 10^{-3} \pm 2.1 \times 10^{-3}$

0 V Au NP	Nyquist Plot	Bode Plot - Magnitude	Bode Plot - Phase
0 nm			
1 nm			
2 nm			
3 nm			
4 nm			
5 nm			

0 V Au NP	***R1*** **(Ω)**		***R2*** **(Ω)**	***C1*** **(F)**	***τ1*** **(s)**
0 nm	146 ± 141		$1.1 \times 10^{8} \pm 3.0 \times 10^{6}$	$1.5 \times 10^{-9} \pm 1.5 \times 10^{-11}$	$1.7 \times 10^{-1} \pm 4.9 \times 10^{-3}$
1 nm	83 ± 7		$1.2 \times 10^{8} \pm 8.1 \times 10^{6}$	$1.6 \times 10^{-9} \pm 2.6 \times 10^{-11}$	$2.1 \times 10^{-1} \pm 1.4 \times 10^{-2}$
2 nm	80 ± 19		$2.3 \times 10^{7} \pm 3.2 \times 10^{6}$	$1.7 \times 10^{-9} \pm 3.7 \times 10^{-11}$	$3.8 \times 10^{-2} \pm 5.4 \times 10^{-3}$
3 nm	91 ± 43		$8.9 \times 10^{6} \pm 1.5 \times 10^{5}$	$1.6 \times 10^{-9} \pm 6.2 \times 10^{-11}$	$1.4 \times 10^{-2} \pm 6.0 \times 10^{-4}$
4 nm	63 ± 22		$3.2 \times 10^{6} \pm 6.8 \times 10^{4}$	$1.7 \times 10^{-9} \pm 4.8 \times 10^{-11}$	$5.5 \times 10^{-3} \pm 1.9 \times 10^{-4}$
5 nm	113 ± 39		$9.9 \times 10^{5} \pm 2.9 \times 10^{4}$	$2.0 \times 10^{-9} \pm 5.2 \times 10^{-11}$	$2.0 \times 10^{-3} \pm 7.7 \times 10^{-5}$

0 V Ag NP	Nyquist Plot	Bode Plot - Magnitude	Bode Plot - Phase
0 nm			
1 nm			
2 nm			
3 nm			
4 nm			
5 nm			

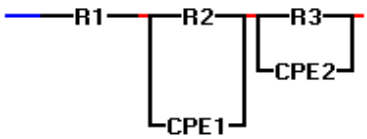
0 V Ag NP	***R1*** **(Ω)**		***R2*** **(Ω)**	***C1*** **(F)**	***τ1*** **(s)**
0 nm	45 ± 20		$7.5 \times 10^{7} \pm 1.6 \times 10^{6}$	$1.6 \times 10^{-9} \pm 2.9 \times 10^{-11}$	$1.2 \times 10^{-1} \pm 3.4 \times 10^{-3}$
1 nm	45 ± 11		$8.4 \times 10^{7} \pm 4.8 \times 10^{6}$	$1.7 \times 10^{-9} \pm 4.7 \times 10^{-11}$	$1.4 \times 10^{-1} \pm 9.0 \times 10^{-3}$
2 nm	38 ± 13		$8.3 \times 10^{7} \pm 5.5 \times 10^{6}$	$1.7 \times 10^{-9} \pm 4.4 \times 10^{-11}$	$1.4 \times 10^{-1} \pm 9.9 \times 10^{-3}$
3 nm	47 ± 17		$3.2 \times 10^{7} \pm 4.6 \times 10^{5}$	$1.8 \times 10^{-9} \pm 2.3 \times 10^{-11}$	$5.7 \times 10^{-2} \pm 1.1 \times 10^{-3}$
4 nm	39 ± 12		$1.3 \times 10^{7} \pm 2.1 \times 10^{6}$	$1.9 \times 10^{-9} \pm 3.9 \times 10^{-11}$	$2.4 \times 10^{-2} \pm 3.9 \times 10^{-3}$
5 nm	25 ± 11		$6.3 \times 10^{6} \pm 8.7 \times 10^{5}$	$2.1 \times 10^{-9} \pm 3.5 \times 10^{-11}$	$1.3 \times 10^{-2} \pm 1.8 \times 10^{-3}$

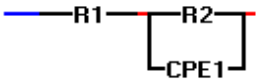
B. Appendix to Chapter 5

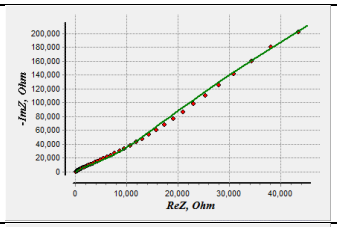
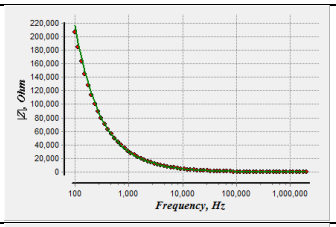
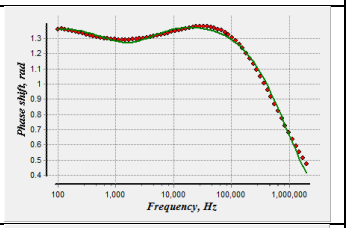
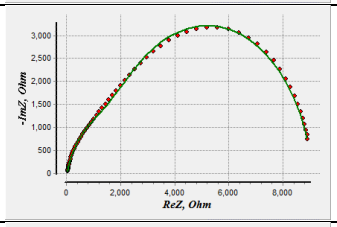
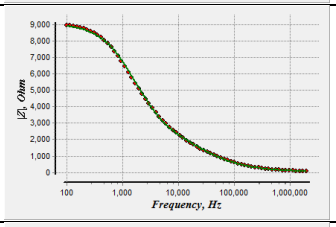
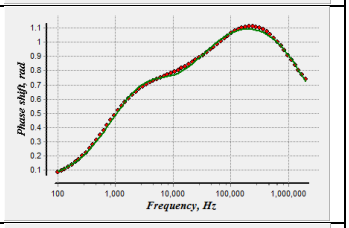
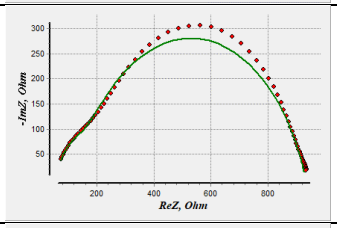
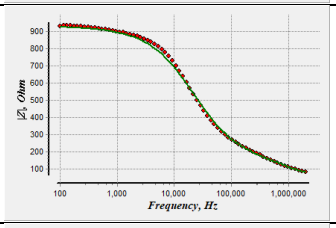
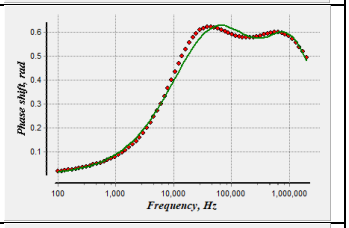
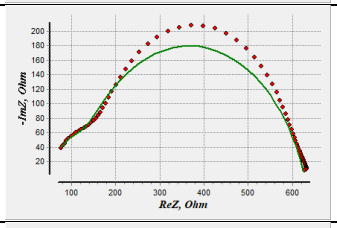
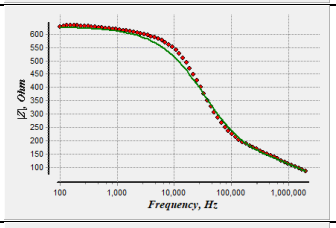
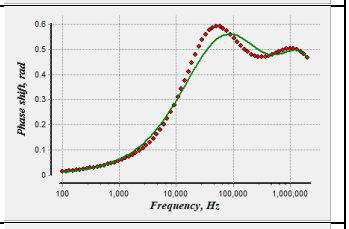
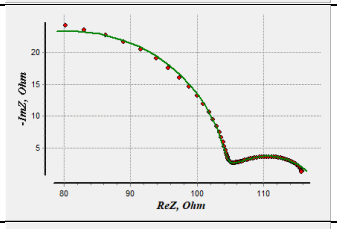
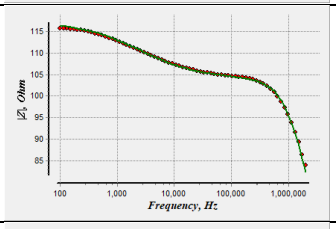
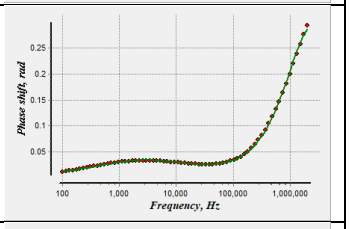
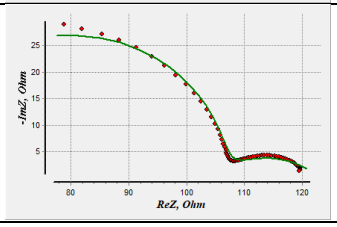
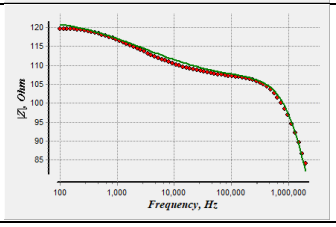
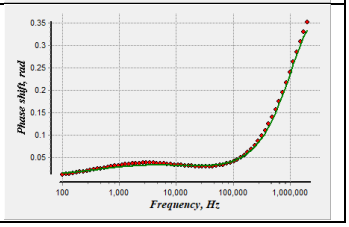
B.1 AC Impedance ECM Results

The tables below show the raw impedance data (red circles) overlaid with the fitted model trace (green line) for a representative pixel at each nominal thickness. The average fitting parameters are also presented in the subsequent tables, with error values calculated as the standard deviation across three pixels. The data is shown for DC biases of +2 V, 0 V and -2 V in turn, as indicated in the top left cell of each table.

Equivalent circuit models used:

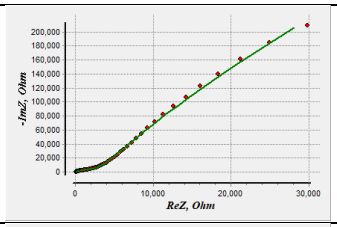
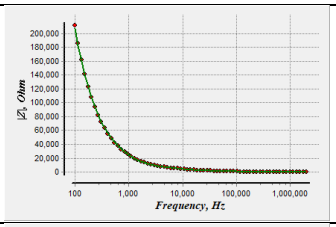
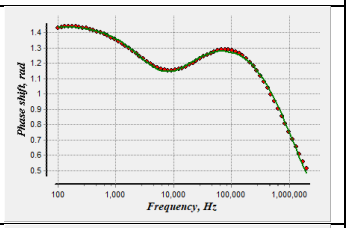
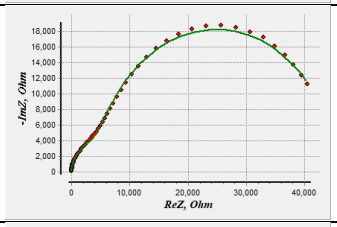
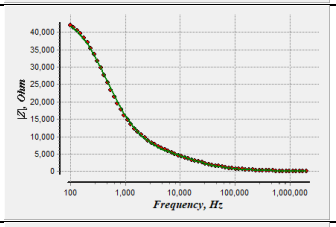
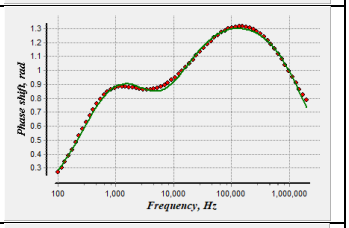
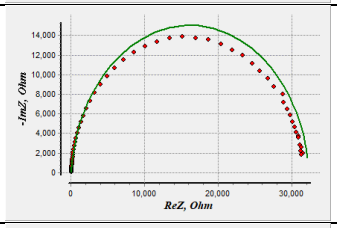
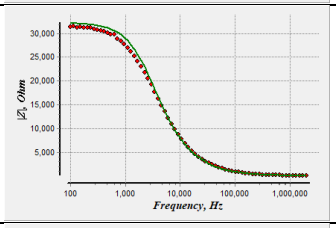
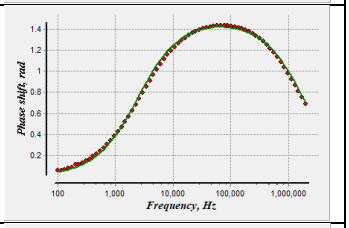
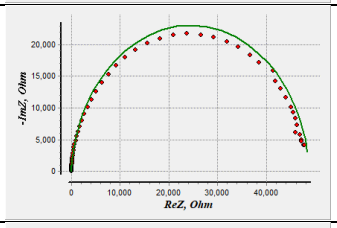
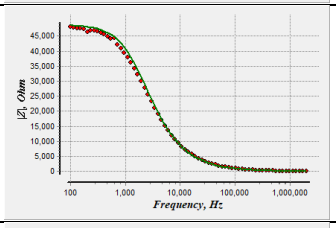
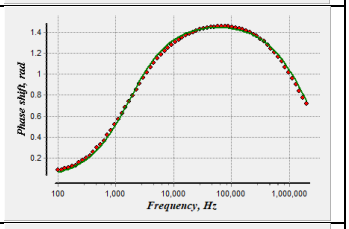
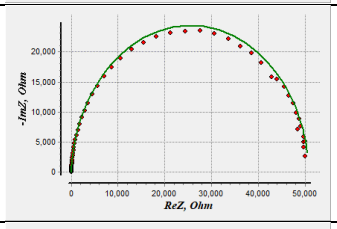
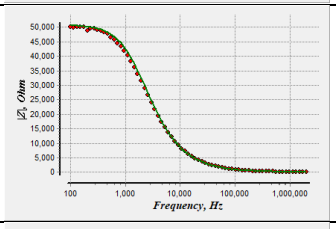
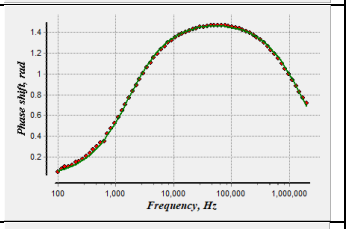
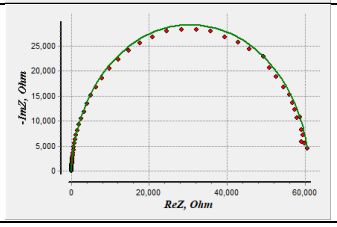
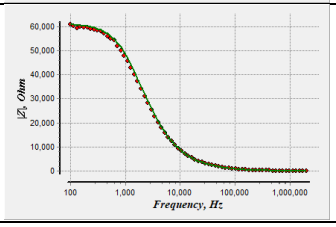
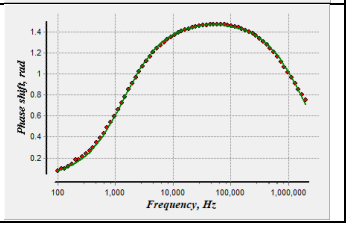




+2 V	Nyquist Plot	Bode Plot - Magnitude	Bode Plot - Phase
0 nm		|Z|, Ohm Frequency, Hz	
0.5 nm		|Z|, Ohm Frequency, Hz	
1 nm		|Z|, Ohm Frequency, Hz	
2 nm		|Z|, Ohm Frequency, Hz	
4 nm		|Z|, Ohm Frequency, Hz	
5 nm		|Z|, Ohm Frequency, Hz	

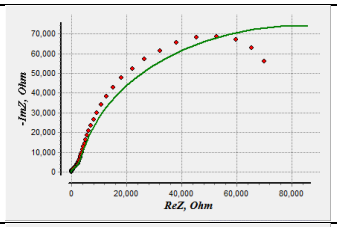
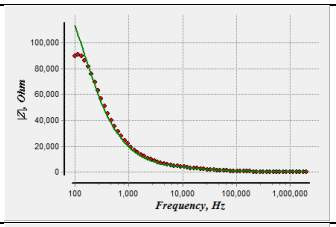
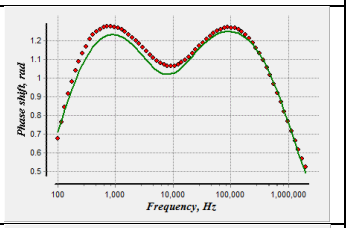
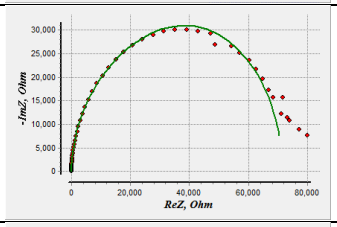
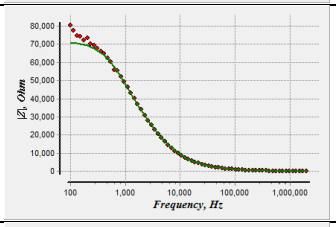
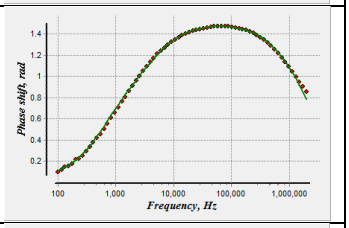
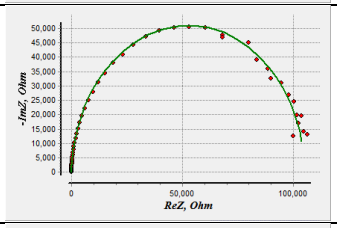
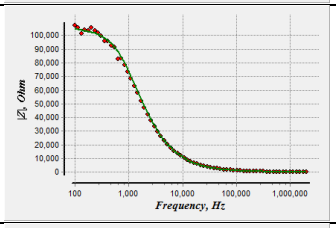
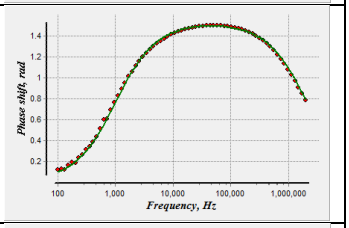
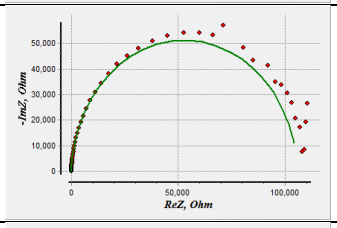
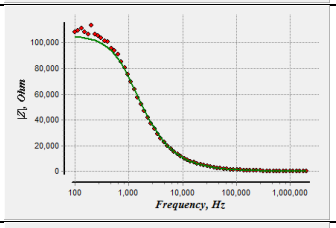
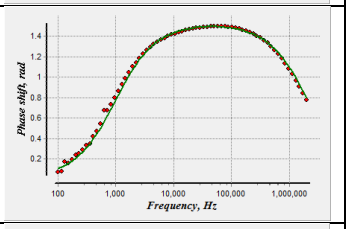
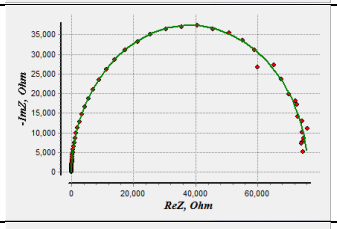
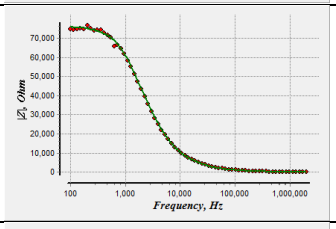
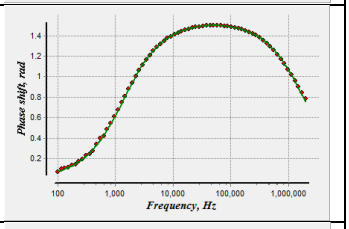
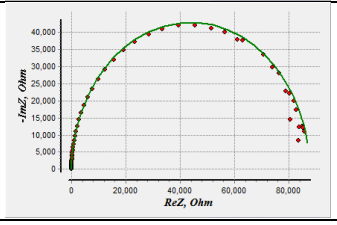
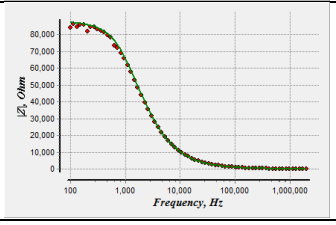
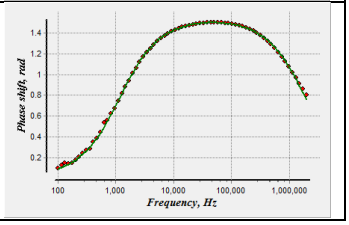
+2 V	***R1*** **(Ω)**		***R2*** **(Ω)**	***C1*** **(F)**	***τ1*** **(s)**
0 nm	73 ± 39		$5.5 \times 10^{3} \pm 6.3 \times 10^{2}$	$1.4 \times 10^{-8} \pm 2.3 \times 10^{-9}$	$7.6 \times 10^{-5} \pm 1.6 \times 10^{-5}$
0.5 nm	46 ± 26		$1.6 \times 10^{3} \pm 8.7 \times 10^{1}$	$4.1 \times 10^{-9} \pm 6.5 \times 10^{-10}$	$6.6 \times 10^{-6} \pm 1.1 \times 10^{-6}$
1 nm	35 ± 30		$9.3 \times 10^{1} \pm 6.7 \times 10^{0}$	$2.7 \times 10^{-9} \pm 1.8 \times 10^{-9}$	$2.5 \times 10^{-7} \pm 1.7 \times 10^{-7}$
2 nm	52 ± 30		$5.6 \times 10^{1} \pm 1.7 \times 10^{0}$	$2.5 \times 10^{-9} \pm 1.8 \times 10^{-10}$	$1.4 \times 10^{-7} \pm 1.1 \times 10^{-8}$
4 nm	46 ± 20		$5.9 \times 10^{1} \pm 2.3 \times 10^{1}$	$1.3 \times 10^{-9} \pm 2.6 \times 10^{-10}$	$7.8 \times 10^{-8} \pm 3.4 \times 10^{-8}$
5 nm	46 ± 9		$6.2 \times 10^{1} \pm 2.5 \times 10^{1}$	$1.4 \times 10^{-9} \pm 5.0 \times 10^{-10}$	$8.7 \times 10^{-8} \pm 4.7 \times 10^{-8}$

+2 V	***R3*** **(Ω)**	***C2*** **(F)**	***τ2*** **(s)**
0 nm	$6.0 \times 10^{6} \pm 4.1 \times 10^{5}$	$1.0 \times 10^{-8} \pm 6.1 \times 10^{-10}$	$6.1 \times 10^{-2} \pm 5.6 \times 10^{-3}$
0.5 nm	$7.4 \times 10^{3} \pm 4.7 \times 10^{2}$	$1.7 \times 10^{-8} \pm 8.5 \times 10^{-10}$	$1.2 \times 10^{-4} \pm 1.0 \times 10^{-5}$
1 nm	$7.9 \times 10^{2} \pm 4.0 \times 10^{0}$	$1.3 \times 10^{-8} \pm 1.4 \times 10^{-9}$	$1.0 \times 10^{-5} \pm 1.1 \times 10^{-6}$
2 nm	$5.2 \times 10^{2} \pm 7.5 \times 10^{0}$	$1.3 \times 10^{-8} \pm 5.1 \times 10^{-10}$	$6.5 \times 10^{-6} \pm 2.8 \times 10^{-7}$
4 nm	$1.4 \times 10^{1} \pm 1.8 \times 10^{0}$	$4.9 \times 10^{-6} \pm 1.7 \times 10^{-6}$	$6.8 \times 10^{-5} \pm 2.5 \times 10^{-5}$
5 nm	$1.6 \times 10^{1} \pm 2.2 \times 10^{0}$	$4.9 \times 10^{-6} \pm 6.5 \times 10^{-6}$	$7.8 \times 10^{-5} \pm 1.1 \times 10^{-4}$

0 V	Nyquist Plot	Bode Plot - Magnitude	Bode Plot - Phase
0 nm			
0.5 nm			
1 nm			
2 nm			
4 nm			
5 nm			

0 V	***R1*** **(Ω)**		***R2*** **(Ω)**	***C1*** **(F)**	***τ1*** **(s)**
0 nm	70 ± 40		$3.0 \times 10^{3} \pm 5.9 \times 10^{2}$	$5.9 \times 10^{-9} \pm 1.4 \times 10^{-9}$	$1.8 \text{ E-}5 \pm 5.6 \times 10^{-6}$
0.5 nm	52 ± 26		$4.2 \times 10^{3} \pm 3.6 \times 10^{2}$	$3.1 \times 10^{-9} \pm 2.6 \times 10^{-10}$	$1.3 \text{ E-}5 \pm 1.6 \times 10^{-6}$
1 nm	245 ± 346		$3.1 \times 10^{4} \pm 8.6 \times 10^{2}$	$2.1 \times 10^{-9} \pm 7.4 \times 10^{-10}$	$6.6 \text{ E-}5 \pm 2.3 \times 10^{-5}$
2 nm	52 ± 25		$4.8 \times 10^{4} \pm 2.8 \times 10^{3}$	$1.9 \times 10^{-9} \pm 6.8 \times 10^{-11}$	$9.0 \text{ E-}5 \pm 6.2 \times 10^{-6}$
4 nm	60 ± 27		$5.1 \times 10^{4} \pm 4.7 \times 10^{3}$	$1.9 \times 10^{-9} \pm 3.7 \times 10^{-11}$	$9.6 \text{ E-}5 \pm 9.0 \times 10^{-6}$
5 nm	58 ± 21		$5.7 \times 10^{4} \pm 1.1 \times 10^{4}$	$1.9 \times 10^{-9} \pm 2.7 \times 10^{-11}$	$1.1 \text{ E-}4 \pm 2.1 \times 10^{-5}$

0 V	***R3*** **(Ω)**	***C2*** **(F)**	***τ2*** **(s)**
0 nm	$8.1 \times 10^{6} \pm 1.5 \times 10^{6}$	$9.7 \times 10^{-9} \pm 7.2 \times 10^{-10}$	$7.9 \times 10^{-2} \pm 1.6 \times 10^{-2}$
0.5 nm	$4.1 \times 10^{4} \pm 3.1 \times 10^{3}$	$1.2 \times 10^{-8} \pm 6.3 \times 10^{-10}$	$4.8 \times 10^{-4} \pm 4.4 \times 10^{-5}$

-2 V	Nyquist Plot	Bode Plot - Magnitude	Bode Plot - Phase
0 nm			
0.5 nm			
1 nm			
2 nm			
4 nm			
5 nm			

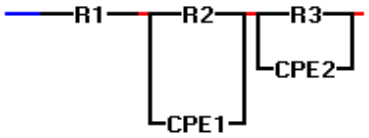
-2 V	***R1*** **(Ω)**	***R2*** **(Ω)**	***C1*** **(F)**	***τ1*** **(s)**
0 nm	69 ± 40	$2.8 \times 10^{3} \pm 1.2 \times 10^{2}$	$4.6 \times 10^{-9} \pm 5.2 \times 10^{-10}$	$1.3 \times 10^{-5} \pm 1.6 \times 10^{-6}$
0.5 nm	53 ± 31	$2.1 \times 10^{4} \pm 1.0 \times 10^{4}$	$3.2 \times 10^{-9} \pm 4.1 \times 10^{-10}$	$6.5 \times 10^{-5} \pm 3.4 \times 10^{-5}$
1 nm	42 ± 15	$1.0 \times 10^{5} \pm 3.1 \times 10^{3}$	$1.5 \times 10^{-9} \pm 7.3 \times 10^{-12}$	$1.5 \times 10^{-4} \pm 4.7 \times 10^{-6}$
2 nm	52 ± 26	$1.2 \times 10^{5} \pm 1.2 \times 10^{4}$	$1.5 \times 10^{-9} \pm 1.3 \times 10^{-11}$	$1.8 \times 10^{-4} \pm 1.8 \times 10^{-5}$
4 nm	60 ± 28	$7.4 \times 10^{4} \pm 2.2 \times 10^{3}$	$1.5 \times 10^{-9} \pm 1.9 \times 10^{-11}$	$1.1 \times 10^{-4} \pm 3.6 \times 10^{-6}$
5 nm	60 ± 22	$7.7 \times 10^{4} \pm 1.5 \times 10^{4}$	$1.5 \times 10^{-9} \pm 5.5 \times 10^{-11}$	$1.2 \times 10^{-4} \pm 2.3 \times 10^{-5}$

-2 V	***R3*** **(Ω)**	***C2*** **(F)**	***τ2*** **(s)**
0 nm	$2.0 \times 10^{5} \pm 4.1 \times 10^{4}$	$9.6 \times 10^{-9} \pm 2.5 \times 10^{-9}$	$1.9 \times 10^{-3} \pm 6.2 \times 10^{-4}$
0.5 nm	$5.4 \times 10^{4} \pm 1.4 \times 10^{4}$	$4.2 \times 10^{-9} \pm 1.3 \times 10^{-9}$	$2.2 \times 10^{-4} \pm 9.3 \times 10^{-5}$

B.2 Universal PV-Interface Fitting Test

The graphs below show the results of fitting the PV-interface model to all nominal thicknesses of NPs to investigate interface effects. This test was conducted on a single representative pixel for each nominal thickness, hence individual results are presented without a standard deviation error bar. The multiple fit solutions possible for each nominal thickness are shown, they are grouped into fit A, B or C depending on the parameter magnitude and resultant capacitance trend. The individual solutions are slightly offset from each other along the x-axis for visual clarity, note this does not indicate a higher nominal thickness.

Equivalent circuit model used:

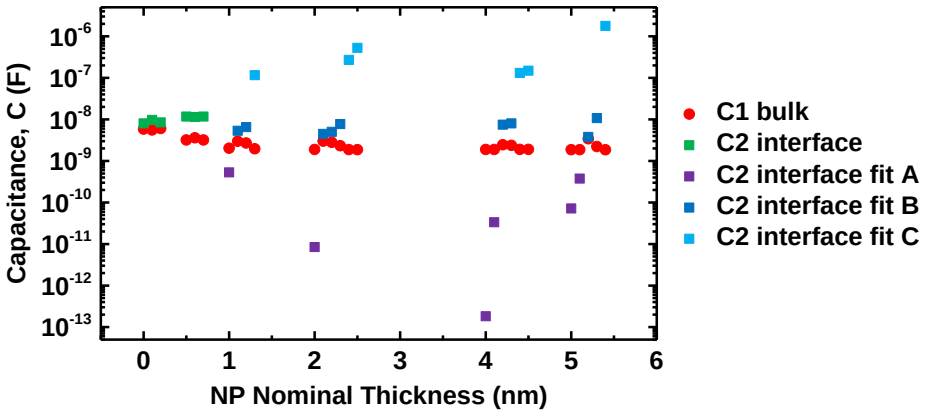


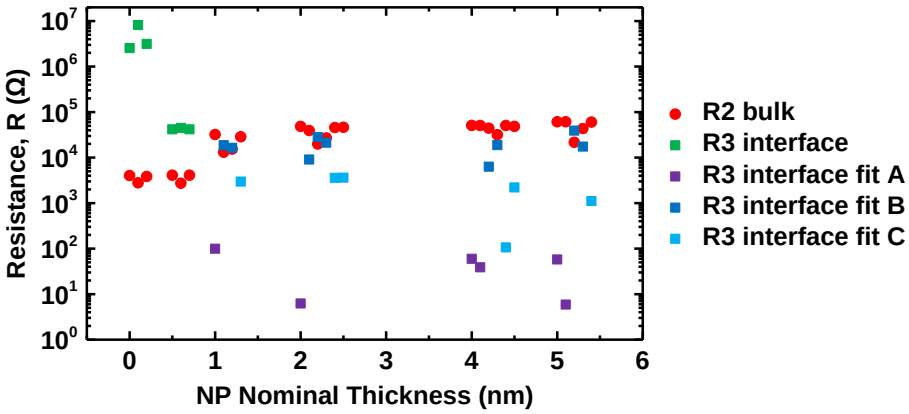
For 1 to 5 nm nominal thickness devices, where a single impedance feature is observed, the data was not constraining enough to provide a consistent fit solution and a wide range of possible parameter values were found for the additional interface extraction element. Despite the multiple solutions available, the bulk parameters (*R2, C1*) remained relatively unchanged. The same bulk trends were observed for all possible solutions, suggesting the two models are not essentially different and providing the same interpretation of bulk behaviour change. All

solutions showed the interface resistance *R3* to decrease substantially at higher nominal thicknesses, giving the consistent interpretation of interface extraction limits being reduced. This indicates fitting with and without an addition element to model the interface extraction processes is a faithful representation of the underlying interface behaviour.

However, for the interface capacitance *C2*, increasing, decreasing or invariant trends were possible depending on the solutions chosen, suggesting a variety of divergent trapping phenomena could potentially be occurring. The range of possible *C2* values exists due to the nature of the ECM fitting analysis. With a low *R3* value the majority of carriers pass through the resistor element, the parallel capacitor element is therefore not probed substantially and so the data does not constrain the *C2* values tightly to produce consistent solutions. The data does not provide any justification to select one set of *C2* solutions over another in order to reveal a particular capacitance trend, so further insight into the interface trapping behaviour cannot be gained by fitting with the more complex PV-interface model.

These results demonstrate that it is appropriate to apply the PV-conventional model to 1-5 nm devices and the PV-interface model to 0-0.5 nm devices, as no further mechanistic insights can be reasonably gained by fitting additional elements for higher nominal thicknesses devices.




Resistance, R (Ω)
10^7
10^6
10^5
10^4
10^3
10^2
10^1
10^0
0
1
2
3
4
5
6
NP Nominal Thickness (nm)
R2 bulk
R3 interface
R3 interface fit A
R3 interface fit B
R3 interface fit C